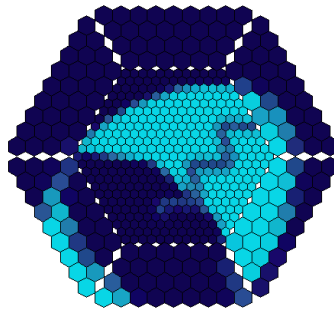


Observations of PG 1553+113 with the MAGIC telescope



Dissertation zur Erlangung des
naturwissenschaftlichen Doktorgrades
der Bayerischen Julius-Maximilians-Universität Würzburg

DANIELA DORNER

aus

Amberg

Würzburg 2008

Abstract

Blazars are among the most luminous sources in the universe. Their extreme short-time variability indicates emission processes powered by a supermassive black hole. With the current generation of Imaging Air Cherenkov Telescopes, these sources are explored at very high energies. Lowering the threshold below 100 GeV and improving the sensitivity of the telescopes, more and more blazars are discovered in this energy regime. For the MAGIC telescope, a low energy analysis has been developed allowing to reach energies of 50 GeV for the first time. The method is presented in this thesis at the example of PG 1553+113 measuring a spectrum between 50 GeV and 900 GeV.

In the energy regime observed by MAGIC, strong attenuation of the gamma-rays is expected from pair production due to interactions of gamma-rays with low-energy photons from the extragalactic background light. For PG 1553+113, this provides the possibility to constrain the redshift of the source, which is still unknown.

Well studied from radio to x-ray energies, PG 1553+113 was discovered in 2005 in the very high energy regime. In total, it was observed with the MAGIC telescope for 80 hours between April 2005 and April 2007.

From more than three years of data taking, the MAGIC telescope provides huge amounts of data and a large number of files from various sources. To handle this data volume and to provide monitoring of the data quality, an automatic procedure is essential. Therefore, a concept for automatic data processing and management has been developed. Thanks to its flexibility, the concept is easily applicable to future projects. The implementation of an automatic analysis is running stable since three years in the data center in Würzburg and provides consistent results of all MAGIC data, i.e. equal processing ensures comparability. In addition, this database controlled system allows for easy tests of new analysis methods and re-processing of all data with a new software version at the push of a button. At any stage, not only the availability of the data and its processing status is known, but also a large set of quality parameters and results can be queried from the database, facilitating quality checks, data selection and continuous monitoring of the telescope performance. By using the automatic analysis, the whole data sample can be analyzed in a reasonable amount of time, and the analyzers can concentrate on interpreting the results instead.

For PG 1553+113, the tools and results of the automatic analysis were used. Compared to the previously published results, the software includes improvements as absolute pointing correction, absolute light calibration and improved quality and background-suppression cuts. In addition, newly developed analysis methods taking into account timing information were used. Based on the automatically produced results, the presented analysis was enhanced using a special low energy analysis. Part of the data were affected by absorption due to the Saharan Air Layer, i.e. sanddust in the atmosphere. Therefore, a new method has been developed, correcting for the effect of this meteorological phenomenon. Applying the method, the affected data could be corrected for apparent flux variations and effects of absorption on the spectrum, allowing to use the result for further studies. This is especially interesting, as these data were taken during a multi-wavelength campaign.

For the whole data sample of 54 hours after quality checks, a signal from the position of PG 1553+113 was found with a significance of 15 standard deviations. Fitting a power law to the combined spectrum between 75 GeV and 900 GeV, yields a flux of $(1.4 \pm 0.1) \cdot 10^{-6}/\text{TeV}/\text{m}^2/\text{s}$ at 200 GeV and a spectral slope of 4.1 ± 0.2 . Due to the low energy analysis, the spectrum could be extended to below 50 GeV. Fitting down to 48 GeV, the flux remains the same, but the slope changes to 3.7 ± 0.1 .

The determined daily light curve shows that the integral flux above 150 GeV is consistent with a constant flux. Also for the spectral shape no significant variability was found in three years of observations.

In July 2006, a multi-wavelength campaign was performed. Simultaneous data from the x-ray satellite Suzaku, the optical telescope KVA and the two Cherenkov experiments MAGIC and H.E.S.S. are available. Suzaku measured for the first time a spectrum up to 30 keV. The source was found to be at an intermediate flux level compared to previous x-ray measurements, and no short time variability was found in the continuous data sample of 41.1 ksec. Also in the gamma regime, no variability was found during the campaign.

Assuming a maximum slope of 1.5 for the intrinsic spectrum, an upper limit of $z < 0.74$ was determined by deabsorbing the measured spectrum for the attenuation of photons by the extragalactic background light. For further studies, a redshift of $z = 0.3$ was assumed. Collecting various data from radio, infrared, optical, ultraviolet, x-ray and gamma-ray energies, a spectral energy distribution was determined, including the simultaneous data of the multi-wavelength campaign. Fitting the simultaneous data with different synchrotron-self-compton models shows that the observed spectral shape can be explained with synchrotron-self-compton processes. The best result was obtained with a model assuming a log-parabolic electron distribution.

Zusammenfassung

Blazare gehören zu den leuchtstärksten Quellen im Universum. Ihre extreme Kurzzeitvariabilität deutet auf Strahlungsprozesse hin, die von einem supermassereichen schwarzen Loch mit Energie versorgt werden. Mit der aktuellen Generation von abbildenden Luft-Cherenkov Teleskopen werden diese Quellen bei sehr hohen Energien erforscht. Durch das Absenken der Schwellenenergie auf unter 100 GeV und aufgrund verbesserter Sensitivitäten werden immer mehr Blazare in diesem Energiebereich entdeckt. Für das MAGIC Teleskop wurde eine Analysemethode entwickelt, die es erlaubt zum ersten mal zu niedrigen Energien im Bereich von 50 GeV vorzudringen. Mit dieser Methode wurde am Beispiel von PG 1553+113 ein Spektrum zwischen 50 GeV und 900 GeV bestimmt.

Im dem von MAGIC beobachteten Energiebereich wird eine starke Abschwächung des Gammalichts aufgrund von Paarproduktion in Wechselwirkungen mit niederenergetischen Photonen des extragalaktischen Hintergrundlichts erwartet. Für PG 1553+113 ergibt sich daraus eine Möglichkeit um die noch unbekanntete Entfernung der Quelle einzuschränken.

Während die Quelle PG 1553+113 im Radio- bis Röntgenbereich gut untersucht ist, wurde sie im Hochenergiebereich erst 2005 entdeckt. Zwischen April 2005 und April 2007 wurde sie mit dem MAGIC Teleskop insgesamt 80 Stunden lang beobachtet.

Aus mehr als drei Jahren Datennahme liefert das MAGIC Teleskop riesige Mengen an Daten und eine große Anzahl von Dateien. Um dieses Datenvolumen zu bewältigen und für die Überwachung der Datenqualität ist eine automatische Verarbeitung unverzichtbar. Darum wurde ein Konzept zur automatischen Datenverwaltung und -verarbeitung entwickelt. Aufgrund seiner Flexibilität kann dieses Konzept auch leicht auf zukünftige Projekte übertragen werden. Die Umsetzung für MAGIC läuft seit drei Jahren stabil im Datenzentrum in Würzburg und liefert konsistente Ergebnisse von allen Daten, d.h. die identische Verarbeitung sorgt für Vergleichbarkeit. Ausserdem ermöglicht das datenbankbasierte Konzept einfache Tests neuer Analysemethoden und die Neuanalyse aller Daten mit einer neuen Software auf Knopfdruck. Man kann nicht nur jederzeit die Verfügbarkeit und den Verarbeitungsstatus aller Daten aus der Datenbank abfragen, sondern auch Qualitätsparameter und Ergebnisse, was die Qualitätskontrolle und Auswahl von Daten sowie die Überwachung des Teleskopstatus erleichtert. Durch die Verwendung der automatischen Analyse kann die riesige Menge an Daten in einem vernünftigen Zeitrahmen analysiert werden und man kann sich stattdessen auf die Interpretation der Ergebnisse konzentrieren.

Für PG 1553+113 wurden die Werkzeuge und Resultate der automatischen Analyse verwendet. Verglichen mit den zuvor veröffentlichten Ergebnissen wurde eine Software Version verwendet, die verschiedene Verbesserungen enthält, wie zum Beispiel eine absolute Pointing-Korrektur, eine absolute Lichtkalibration und verbesserte Schnitte zur Qualitätssicherung und Untergrundunterdrückung. Ausserdem wurde eine neu entwickelte Analysemethode, welche die Zeitinformation mit einbezieht, benutzt. Basierend auf den Ergebnissen der automatischen Analyse wurde das Ergebnis mit einer speziell für niedrige Energien optimierten Analyse verbessert. Ein Teil der Daten wurde beeinträchtigt

durch Absorption aufgrund Sandstaub in der Atmosphäre, der sogenannten Calima. Eine neue Methode wurde entwickelt, um den Effekt dieses meteorologischen Phänomens zu korrigieren. Auf diese Weise konnten scheinbare Flussänderungen und Einflüsse auf das Spektrum ausgeglichen werden, wodurch die Daten für weiterführende Studien verwendet werden können. Dies ist hier von besonderer Bedeutung, da die betroffenen Daten simultan mit Daten aus anderen Wellenlängenbereichen genommen wurden.

Für den kompletten Datensatz wurde ein Signal aus der Richtung von PG 1553+113 mit einer Signifikanz von 15 Standardabweichungen gemessen. Fittet man ein Potenzgesetz an das kombinierte Spektrum, so erhält man einen Fluss von $(1.4 \pm 0.1) \cdot 10^{-6} / \text{TeV}/\text{m}^2/\text{s}$ bei 200 GeV und einen Spektralindex von 4.1 ± 0.2 . Mit Hilfe der Niederenergieanalyse konnte das Spektrum bis unter 50 GeV erweitert werden. Fittet man es bis 48 GeV, so bleibt die Flussnormierung gleich, aber der Index ändert sich auf 3.7 ± 0.1 .

Die berechnete Lichtkurve auf Tagesbasis zeigt, dass der integrale Fluss oberhalb von 150 GeV mit konstanten Fluss konsistent ist. Auch für die Form des Spektrums wurde in den drei Jahren, in denen beobachtet wurde, keine Variabilität gefunden.

Im Juli 2006 wurden simultane Beobachtungen des Röntgensatelliten Suzaku, des optischen Teleskops KVA und der Cherenkovexperimente MAGIC und H.E.S.S. koordiniert. Mit Suzaku wurde zum ersten Mal ein Röntgenspektrum bis 30 keV vermessen. Die Quelle befand sich, verglichen mit früheren Röntgenmessungen, in einem mittleren Flusszustand, und während der kontinuierlichen Datennahme von 41.1 ksec wurde keine Variabilität gemessen. Auch im Gammabereich wurden keine Veränderungen während der Beobachtungen festgestellt.

Nimmt man für das intrinsische Spektrum der Quelle einen maximalen Index von 1.5 an, so lässt sich für die Rotverschiebung eine obere Grenze von $z < 0.74$ bestimmen, indem man das gemessene Spektrum mit verschiedenen angenommenen Rotverschiebungen auf die Abschwächung durch das extragalaktische Hintergrundlicht korrigiert. Für weitere Studien wird eine Rotverschiebung von $z = 0.3$ angenommen.

Aus einer Sammlung von Daten aus dem Radio-, Infrarot-, optischen, Ultraviolett-, Röntgen- und Gammabereich wurde eine spektrale Energieverteilung bestimmt, die auch die simultanen Daten aus der Multiwellenlängenkampagne enthält. Fittet man die simultanen Daten mit einem Synchrotron-Selbst-Compton Modell, so sieht man, dass die spektrale Form mit Synchrotron-Selbst-Compton Prozessen erklärt werden kann. Das beste Ergebnis konnte mit einem Modell erzielt werden, das eine Elektronenverteilung annimmt, die in doppelt logarithmischer Darstellung eine Parabelform hat.

Contents

Abstract	3
Zusammenfassung	5
1. Multi-Wavelength Astronomy	11
1.1. Active Galactic Nuclei	11
1.1.1. Classification	12
1.1.2. Unified scheme	13
1.1.3. Blazars	13
1.2. Multi-wavelength astrophysics	17
1.2.1. Historical overview	17
1.2.2. Electromagnetic spectrum and earth's atmosphere	18
1.2.3. Observations and observatories	19
1.3. Gamma-ray astronomy	23
1.3.1. Space experiments	24
1.3.2. Ground-based experiments	26
1.4. Imaging Air Cherenkov Technique	29
1.4.1. Atmosphere as detector	29
1.4.2. Analysis principles	30
2. The MAGIC experiment	33
2.1. Telescope system	33
2.1.1. Central control	35
2.1.2. Drive system	36
2.1.3. Active mirror control	36
2.1.4. Camera	38
2.1.5. Calibration system	40
2.1.6. Trigger	41
2.1.7. Read-out chain - data acquisition	41
2.1.8. Auxiliary devices	42
2.1.9. Optical data	43
2.2. Data management	43
2.2.1. Data taking	43
2.2.2. Data flow	45
2.2.3. Data center	46
2.2.4. Analysis steps	47
2.2.5. Data quality issues	50

2.2.6. Simulated data	53
3. Concept for the automatic analysis	57
3.1. Requirements	57
3.2. Realization	58
3.2.1. Concept	58
3.2.2. Status tables	58
3.2.3. Database	60
3.2.4. Scripts	61
3.2.5. Configuration and setup	62
3.2.6. Example from the MAGIC analysis	63
3.3. Features, achievements and results	65
3.3.1. Consistent results for all data	65
3.3.2. Optical data	66
3.3.3. Simulated data	66
3.3.4. Tools for monitoring and data selection	66
3.3.5. Easy tests and re-processing	68
3.4. Flexibility and future prospects	69
4. MAGIC observations	71
4.1. Observations and data quality	71
4.1.1. Observation cycle I	72
4.1.2. Observation cycle II	73
4.2. Analysis	74
4.2.1. General analysis chain	74
4.2.2. Low energy analysis	79
4.2.3. Correction of atmospheric absorption due to the Saharan Air Layer	83
4.2.4. Effect of the inhomogeneous camera	84
4.3. Results and discussion	86
4.3.1. Single data sets	87
4.3.2. Combined data set	91
4.3.3. Light curves	92
4.3.4. Low energy results	95
4.3.5. Comparison to H.E.S.S. results	95
5. PG 1553+113	99
5.1. Discovery and first observations	99
5.2. X-ray observations	100
5.3. Gamma-ray observations	102
5.4. Other observations	102
5.5. Redshift	103
5.6. Multi-wavelength studies	103
5.7. Variability	105

5.8. Intrinsic spectrum	107
5.8.1. Metagalactic Radiation Field	107
5.8.2. Constraints on the redshift	107
5.9. Broadband spectral energy distribution	108
5.10. Summary	112
List of Figures	117
List of Tables	119
Bibliography	123
A. PG 1553+113	133
A.1. The source	133
A.2. Selection of MAGIC data	133
A.3. Additional Results from Single Data Sets	144
B. Additional Information on the Automation Package	153
C. Correction of atmospheric absorption due to the Saharan Air Layer	177

Contents

1. Multi-Wavelength Astronomy

*Multiwellenlängenkunde
Spektakuläre, neue Funde
Gamma, optisch, Radio
Aktive Kerne sieht man so
Gammastrahlen, andre Teilchen
Cherenkovblitze fast wie Veilchen
— Daniela Dorner.*

PG 1553+113 is an **Active Galactic Nucleus** (AGN) at unknown redshift. This work summarizes historical observations and includes new **Very High Energy** (VHE) data recorded with the **Major Atmospheric Gamma-Ray Imaging Cherenkov** (MAGIC) telescope.

AGNs are very energetic objects, emitting radiation over 19 decades of energy. Consequently, they are observed in the complete spectral range. From these **Multi-WaveLength** (MWL) observations conclusions on the physics mechanisms in AGNs can be drawn. To study the strong variability of these objects, MWL data are ideally taken simultaneously. At the example of AGNs, MWL astronomy is discussed and selected telescopes are presented, putting the main focus on telescopes of which data of PG 1553+113 are available and used within this work.

As a big part of the electromagnetic spectrum is absorbed in the earth's atmosphere, both satellite and ground based telescopes are needed to explore the whole spectral range. For technical reasons, e.g. limited detector size in space, some parts of the spectrum are not yet explored, or the sensitivity of the current experiments is still too low for conclusive studies. One of these gaps is at GeV energies in the gamma-ray regime. To close it, on the one hand space experiments like GLAST are built approaching from lower energies. On the other hand ground-based telescopes, using an indirect detection technique, bridge the gap coming from the TeV energies. Some selected gamma-ray telescopes and experiments are explained, and the principles of the **Imaging Air Cherenkov Technique** (IACT) are discussed.

1.1. Active Galactic Nuclei

Among other objects like **Gamma Ray Bursts** (GRBs), **Super Nova Remnants** (SNRs) and **Pulsar Wind Nebulae** (PWN), one of the main targets observed by the MAGIC telescope are AGNs.

After a brief description, the historical classification and the later introduced scheme unifying these objects are explained. From this overview, the focus will go to the subclass of

1. Multi-Wavelength Astronomy

blazars, which are AGNs observable in the VHE range ^a.

In general, galaxies showing a prominent core luminosity and evidence for relativistic particle acceleration are called active.

According to the canonical model, an AGN hosts a super-massive black hole in its center, surrounded by a hot accretion disk and a dust torus. Gas clouds showing line emission can be found around the center. Perpendicular to the accretion disk two relativistic jets extend from the black hole ending in large lobes.

1.1.1. Classification

Historically AGN were classified according to their properties [Lawrence, 1987], i.e. radio-loudness, broad and narrow line emission, continuum emission, variability and polarization. The main distinguishing features are radio-loudness and emission lines. Depending on these

	Type 0 (unusual)	Type 1 (broad line)	Type 2 (narrow line)
Radio quiet	BAL QSO	Seyfert 1 QSO	Seyfert 2 NELG IR Quasar
Radio loud	Blazars: BL Lac objects FSRQ (Blazar)	BLRG SSRQ FSRQ	NLRG: FR I FR II (NLRG)

Table 1.1.: Empirical classification of AGN ordered horizontally by their emission line properties and vertically by radio-loudness, adopted from Lawrence [1987] and Urry and Padovani [1995].

features, AGNs are known under different names, as listed in table 1.1. AGNs are divided into radio quiet and radio loud galaxies. For both types a classification is done according to the appearance of line emission: either no or unusual lines (Type 0) or broad liner (Type 1) or narrow (Type 2) lines are observed [Urry and Padovani, 1995].

Type 1 is characterized by bright continua and broad emission lines. For the radio quiet case, this includes Seyfert 1 galaxies and radio-quiet quasars (Quasar = **Q**uasi **S**tellar **O**bjects, QSO), for the radio loud **B**road-**L**ine **R**adio **G**alaxies (BLRG) at low luminosities and **S**teep and **F**lat **S**pectrum **R**adio **Q**uasars (SSRQ and FSRQ) at high luminosities.

Compared to this, Type 2 AGNs have weak continua and narrow emission lines. In the group of radio quiet AGNs, this summarizes Seyfert 2 galaxies and **N**arrow-**E**mission-**L**ine **X**-ray **G**alaxies (NELG) at low luminosities and infrared luminous galaxies at high luminosities. The radio loud group of this type, often called **N**arrow-**L**ine **R**adio **G**alaxies (NLRG), include low- and high luminosity **F**anaroff-**R**iley type radio galaxies (FR I and FR II).

^ainformation from Weekes [2003] if not stated otherwise

Galaxies having very unusual spectral characteristics are summarized as Type 0. For the radio quiet case, these are **Broad Absorption Line** (BAL) quasars, for the radio loud case blazars, which summarize BL Lac type objects and FSRQs including also objects empirically known as **Optically Violently Variable** (OVV) quasars, **Highly Polarized Quasars** (HPQ) and **Core-Dominated Quasars** (CDQ).

All these objects are characterized by very rapid variability, unusually high and variable polarization, high brightness-temperatures and superluminal velocities of compact radio cores [Urry and Padovani, 1995].

1.1.2. Unified scheme

Although AGNs were classified primarily just by their observed characteristics, unifying models suggest that the different characteristics come mainly from different viewing angles of the observer. This means that the various classes of objects are mainly the same type of object, but seen from different directions, as shown in figure 1.1.

If the AGN is observed edge-on, the emission from the lobes in the radio is dominant, as the core is obscured by the dust torus. The other extreme, when watching the AGN along the jet axis, producing very strong emission due to relativistic beaming, is seen as a blazar ('blazing quasar'). In this case the emission from the core exceeds the emission from the rest of the galaxy and also emission lines from the gas clouds are hardly seen due to that. For viewing angles in between emission lines from the gas clouds can be observed.

1.1.3. Blazars

To be detectable in the gamma-ray regime, high luminosities are needed. Therefore blazars are the best candidates among the variety of the observable appearances of an AGN.

The two forms of blazars, BL Lac objects and FSRQs, are mainly distinguished by the fact that the latter show emission lines. A possible explanation is a slight difference in the viewing angle. For FSRQs, a small angle between jet and line of sight remains. In case of a BL Lac object, the observer is looking directly along the jet axis.

While FSRQs are mainly detected in the high energy regime, e.g. by EGRET, BL Lac objects dominate the observations of AGNs at very high energies.

Jets From the center of the AGN, a highly colimated outflow of particles extends up to 2 Mpc into the surrounding medium. The collision with the medium creates a shockfront in the jet, e.g. [Rosswog and Brügggen, 2007]. In these shocks, particles are accelerated to relativistic energies. In magnetic fields, relativistic particles emit synchrotron radiation.

Due to the small angle between the jet axis and the line of sight, the radiation emitted by the nucleus and further beamed in the jet exceeds the emission from the host galaxy.

The relativistic beaming is characterized by the bulk Lorentz factor $\Gamma = (1 - \beta^2)^{-1/2}$ and the Doppler factor $\delta = 1/(\Gamma \cdot (1 - \beta \cdot \cos\theta))$ where $\beta = v/c$ is the velocity of the object moving and θ its angle with the line of sight. With this, several observed peculiarities can be explained. For example the dimension of the source extension estimated from short time

1. Multi-Wavelength Astronomy

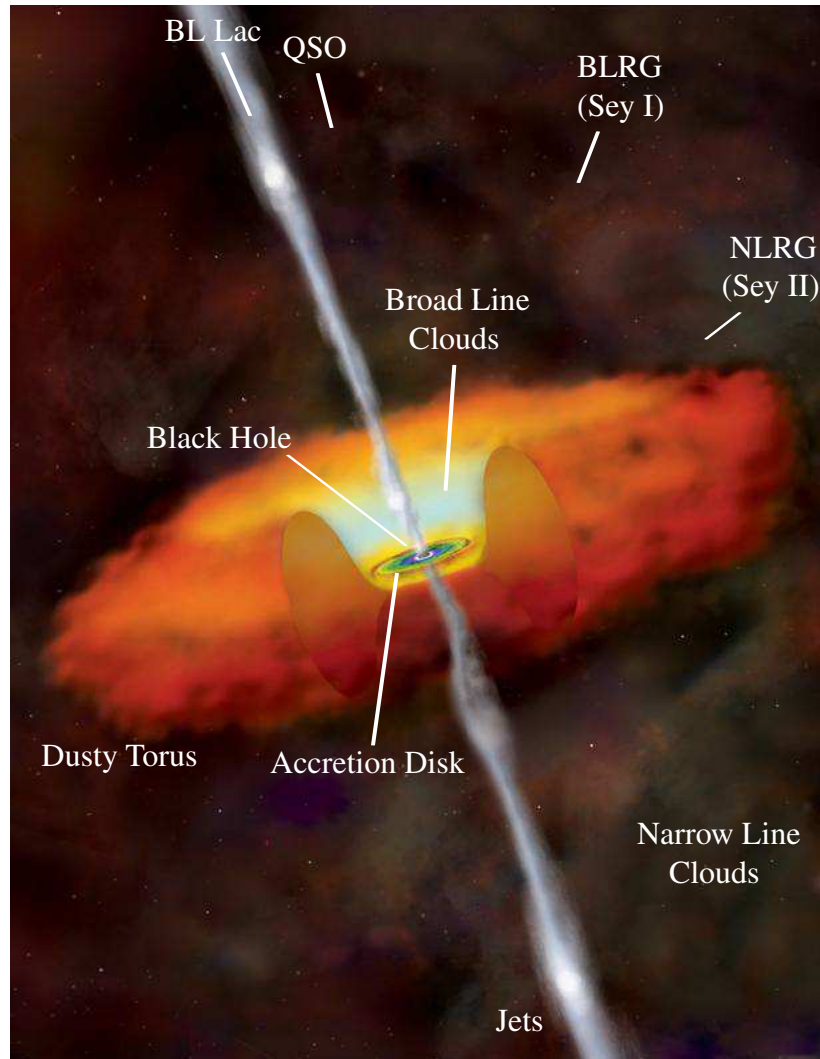


Figure 1.1.: Illustration of an Active Galactic Nucleus and its environment [Weiss, 2006]. The measured spectral characteristics depend on the observation direction. In parentheses the names in the radio-quiet case are given.

variabilities is not $D = dt_{obs} \cdot c$ but $D = t_{source}/\delta \cdot c$. The observed frequency ν_{obs} equals $\delta \cdot \nu_{source}$ and the observed luminosity is even more dramatically reduced: $L_{obs} = \delta^4 \cdot L_{source}$. With Doppler factors of 10 to 20 the observed luminosity can be a factor 10^3 to 10^4 larger than the intrinsic luminosity.

Without relativistic beaming, the luminosity of blazars would not be high enough to be observable in the VHE. Consequently, these objects have to be gigantic particle accelerators providing the possibility to study relativistic phenomena.

Variability The most striking feature of BL Lac objects is their extreme variability of the VHE emission. Strong flux variations are observed in time scales between minutes and years. From the duration of the variability conclusions can be drawn on the extension of the emission region. With the flux level also the spectral slope might change. The best studied objects in this context are Markarian 421 [Albert et al., 2007a] and Markarian 501 [Albert et al., 2007b]. For the first time variability in the VHE was detected in 1994 by Whipple, when observing Markarian 421 [Kerrick et al., 1995]. Recently flares with very short doubling times have been observed from Markarian 501 [Albert et al., 2007b] and PKS 2155-304 [Aharonian et al., 2007].

To probe the various AGN models, it is important to measure the complete spectral energy distribution including the VHE part. Due to the strong variability of blazars, simultaneous MWL data is important to correlate the data of the different wavelength. Tight and strict schedules of the telescope often result in only quasi-simultaneous data. In this case only few constraints on the models can be made, if strong variability is observed.

Spectral Energy Distribution Apart from the variability, another striking feature of blazars is that their Spectral Energy Distribution (SED) extends over 19 decades in energy. To determine a complete SED, MWL observations are carried out. Being non-thermal emitters, AGNs show broad band SEDs with two peaks. The first is located in the infrared to x-ray regime, the second in the x-ray to gamma regime. The varying peak position is the origin of the earlier classification of blazars: BL Lacs detected in radio surveys were called **Radio-selected BL Lac** (RBLs) and those detected in x-ray surveys **X-ray-selected BL Lacs** (XBLs). This historical classification has been generalized to **Low-frequency BL Lacs** (LBLs) and **High-frequency BL Lacs** (HBLs) according to the peak position of the emission. Some AGNs with peak energies in between are referred to as **Intermediate BL Lacs** (IBLs) [Nieppola et al., 2006], and the discovery of more BL Lac type sources reveals a continuum of peak energies.

The two peaks at different energies originate in different emission processes. While the low energy peak is synchrotron radiation from electrons accelerated in the magnetic fields along the jet axis, the origin of the second peak is still discussed in various models: The two main possibilities are lepton and proton models, in which either electrons from the synchrotron emission or protons are accelerated. Both types of models can be subdivided.

Synchrotron peak Electrons accelerated in the magnetic field of a jet emit synchrotron radiation, producing the first peak in the spectral energy distribution. In different approaches the photon flux is modeled with different formulae. The simplest approach is a power law:

$$F(E) = K \cdot E^{-\alpha} \quad (1.1)$$

Another possibility is a broken power law with different slopes α_1 and α_2 before and after the break energy E_{break} . A more complex approach is a log-parabolic law where r is the curvature and s the slope at an energy γ_0 :

$$F(E) = K \cdot E^{-(s+r \cdot \text{Log}(E))} \quad (1.2)$$

1. Multi-Wavelength Astronomy

These different formulae are also used for modeling the electron distributions. For more details see Tramacere et al. [2007] and Massaro et al. [2006].

Lepton models In leptonic models the second peak is assumed to be produced by inverse Compton scattering of the same electrons producing the synchrotron peak. According to this the second peak is named inverse Compton (IC) peak. The existing models differ concerning the origin of the photons interacting with the electrons. If the photons originate from the same electron population, the models are called **Synchrotron-Self-Compton (SSC)** models. Other models consider also photons from outside, for example from the surrounding gas clouds. Such models are called **External Radiation Compton (ERC)** models. An overview of different leptonic model is given for example in [Sikora and Madejski, 2001]. The simplest models are one-component models, where the Compton scattering is assumed in only one emission region.

Proton models In hadronic models, the photons are synchrotron radiation from secondary electrons of hadronic processes. Such electrons have higher energies than directly accelerated electrons. An overview is given e.g. in [Sikora and Madejski, 2001]. The accelerated protons interact with soft photons and produce mesons by photoproduction initiating pion cascades. Proton models can also explain extragalactic CRs and neutrinos. For a compact jet with relativistic electrons and protons the name 'proton blazar' has been coined [Mannheim, 1993].

Very high energy peak While the synchrotron peak is well measured for many blazars, only for few objects VHE data is available. Only with the current generation of IACTs the number of measurements increased. For some LBLs, measurements of previous gamma-ray space experiments are available.

By measuring more blazars at VHE, the knowledge about this type of objects can be increased and the available models can be probed. By fitting the whole SED, parameters describing the blazar can be constrained, e.g. magnetic field. From the determined parameters also conclusions on the black hole mass can be drawn.

1.2. Multi-wavelength astrophysics

Astronomy is a popular and well-studied branch in science since thousands of years. While in the beginning all observations were made in the visible range of the electromagnetic spectrum, the discovery of other parts of the spectrum enlarged the observation window. New techniques and telescopes have been developed to explore the universe in all wavelengths. A short overview of the history is given and the astronomical approach for the different wavelengths is presented. Selected telescopes and experiments are briefly explained ^b.

1.2.1. Historical overview

Although astronomy is a very old branch in science, it was restricted for a long time to the part of the electromagnetic spectrum visible by eye. Already ancient civilizations in Mesopotamia, Egypt, Persia, Middle and South America, Greece and India made astronomical observations. For example in 1054 Chinese and Arab astronomers recorded the observation of the **Super Nova** (SN) leaving as well-know remnant the Crab Nebula, considered stable and therefore as standard candle in Cherenkov astronomy.

While observations were primarily done only by eye, the invention of lenses allowed a big step forward as telescopes could be built enabling a deeper look into space.

Another important approach in astronomy, the spectroscopy, was pioneered by Isaac Newton who used prisms to disperse the light of the Sun. With this technique, emission and absorption lines could be detected in the spectra of sources.

The discovery of other parts of the electromagnetic spectrum opened new windows for the observers:

Radio Predicted in 1865 by James Clerk Maxwell, the first radio waves were generated 1887 by Heinrich Hertz in Karlsruhe. The first astronomical source was discovered by chance in 1931 in the Bell Laboratories by Karl Guthe Jansky, who identified a repeating signal to come from the direction of the Milky Way. Starting from 1937 the first astronomical measurements in the radio band were performed.

Infrared The first observations of **InfraRed** (IR) radiation were made in 1800 by William Herschel, who found it in the light of the sun, and Charles Piazzi Smyth, who detected it in the light of the moon. Starting from 1915 William Coblentz measured IR radiation from 110 stars and pioneered IR spectroscopy. Modern infrared astronomy started in the 1960s to 1970s partly with ground-based telescopes and partly with balloon and space experiments.

Ultraviolet First observation of **UltraViolet** (UV) radiation were made in 1801 by the German physicist Johan Wilhelm Ritter. Astronomical observation started with observations from balloons and starting from 1962 with satellites from space.

^binformation and numbers from *www-10* or Dahlem [2007] if not stated otherwise

1. Multi-Wavelength Astronomy

X-ray In 1895 Wilhelm Conrad Röntgen published his work about the discovery of x-rays in Würzburg, for which he received the first Nobel Prize for Physics in 1901. As x-rays are absorbed in the earth's atmosphere, the first astronomical observations in this range of the spectrum were only done with balloon experiments, rocket flights and space telescopes. In 1962 Riccardo Giacconi succeeded in discovering the first x-rays from an astronomical object, namely Scorpius X-1, and received the Nobel Prize for Physics in 2002.

Gamma-ray Similar to x-ray astronomy, this branch of astronomy developed only with the first satellites in the 1960s and 1970s as gamma-rays are absorbed in the earth's atmosphere. At the same time a spectacular discovery was made by defense satellites observing the earth to detect gamma-rays from nuclear bomb blasts: they recorded gamma-ray bursts from space instead.

Cosmic rays The existence of cosmic rays was discovered by Victor Hess in 1912 in a balloon experiment. He received the Nobel Prize for Physics in 1936. The first **Extensive Air Showers (EAS)** were detected in 1934 by Bruno Rossi and three years later again by Pierre Auger who investigated this phenomenon more detailed.

Neutrinos Postulated in 1930 by Wolfgang Pauli, the first neutrinos were detected in 1956, awarded with the Nobel Prize for Physics in 1995. Detection of solar neutrinos and from SN 1987A in 1987 marked the beginning of neutrino astronomy (Nobel Prize for Physics in 2002).

Combining all the information of these different parts of astronomy and astrophysics, multi-wavelength astronomy and multi messenger astrophysics were born. Also the connection to particle physics is given, as VHE radiation needs powerful acceleration processes to be generated. In the new born field of astroparticle physics, experimental results from astronomical observations are used to probe theories and models from particle physics.

1.2.2. Electromagnetic spectrum and earth's atmosphere

Ranging from several femto-electronvolt (extreme low frequency radio band) to several terra-electronvolt (VHE gamma-rays), the electromagnetic spectrum can be divided in the radio, IR, optical, UV, X-ray and gamma-ray regime. In gamma astronomy numbers are given mainly in electronvolt (eV), while in radio hertz (Hz) and in IR, optical and UV meter (m) are the preferably used units.

Due to its composition, the opacity of the earth's atmosphere depends on the wavelength of the radiation. As shown in figure 1.2, there are only a few windows in which ground-based observations are possible: the optical window (300 nm to 1100 nm), the radio window (1 cm to 11 m) and several windows in the IR. For observations in other ranges balloon experiments or space telescopes have to be launched.

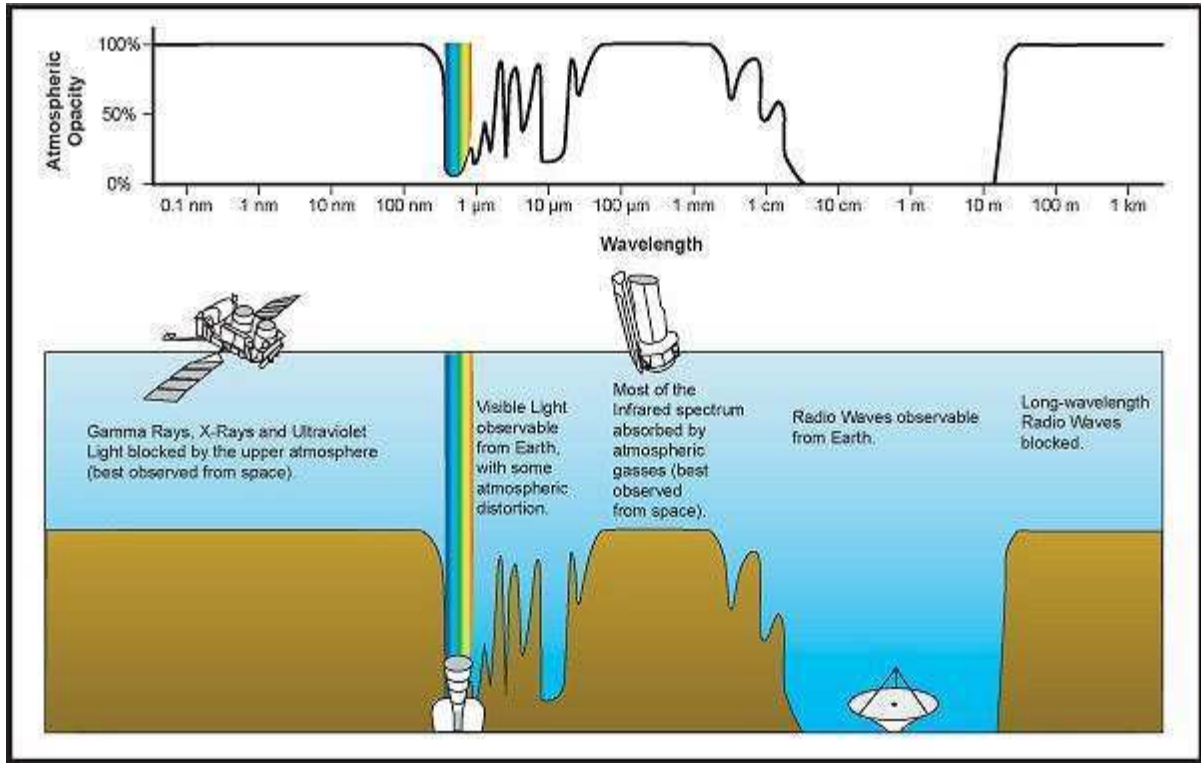


Figure 1.2.: Opacity of the earth's atmosphere versus wavelength. Courtesy NASA/JPL-Caltech.

1.2.3. Observations and observatories

Spectra of astronomical sources are marked by different features: Continuum spectra, caused by thermal or non-thermal emission of astronomical objects, can be superimposed by emission and absorption lines created in the medium between object and observer. Studying these features, the observed spectra allow for conclusions on the physics in the objects and their surrounding medium.

Especially for AGN, observations in the whole energy range are needed to measure the complete SED. From emission and absorption lines, the redshift, i.e. the distance, of an object can be determined.

In the following the different branches of astronomy and astrophysics are shortly discussed and examples for telescopes and experiments are given.

Radio astronomy Profiting from the fact that long-wavelength radiation penetrates extremely deep through intervening matter, radio astronomy has two advantages: Objects, which are obscured by dust along the line of sight in the optical light, can be observed. In addition no space telescope is needed, as the radiation is not absorbed in the atmosphere (radio window, figure 1.2).

1. Multi-Wavelength Astronomy

Due to technical developments in the past century, radio astronomy suffers from an enormous background, e.g. from radio or television broadcasts and especially mobile phones.

In radio astronomy the concept of interferometry is very important to increase the angular resolution. For example the **Very Large Array** (VLA) of the National Radio Astronomy Observatory uses this for its 27 antennas, which can be moved on a Y-shaped rail system, providing a maximum baseline of 36 km. With an angular resolution of about four arcseconds for example the jet structure of AGNs can be resolved [Rector et al., 2003]. But even **Very Long Baseline Interferometry** (VLBI) is done using single radio telescopes across the whole world, e.g. the 100 m telescope in Effelsberg and the Green Bank radio telescope. The **Very Long Baseline Array** (VLBA) consisting of ten radio telescopes around the world reaches accuracies of 0.01 arcseconds.

From AGNs, synchrotron emission is measured in the radio band forming the rising edge of the first peak in the SED.

Infrared astronomy Ranging from several micro-meter (μm) to several hundred nanometer (nm) the IR waveband is usually split into three sub-bands: **Near IR** (NIR, 700 nm - 4 μm), **Mid IR** (MIR) and **Far IR** (FIR). The pass bands in IR astronomy are named I (1.05 μm), J (1.25 μm), H (1.65 μm), K (2.2 μm), L (3.45 μm), M (4.7 μm), N (10 μm) and Q (20 μm).

Considering that the equipment at room temperature (300 K) emits IR radiation itself, measurements at ground-based telescopes have to be done very carefully. Despite of that, ground-based observations in the IR are performed in the above mentioned IR windows with detectors cooled with liquid nitrogen. Observations in the FIR are done with aircrafts or balloons from high in the atmosphere or with space telescopes. Many optical telescopes are capable to measure in the IR band as well. For example the **Hubble Space Telescope** (HST) or the **Very Large Telescope** (VLT) are therefore equipped with additional instruments like the **Spectrograph for INtegral Field Observations in the Near Infrared** (SINFONI) at the VLT. As IR radiation is absorbed by water vapor in the atmosphere, most IR telescopes are built at very dry places at high altitudes, e.g. the Mauna Kea (4205 m) or the ALMA site in Chile (5000 m).

From 1997 to 2001 the **Two Micron All Sky Survey** (2MASS) measured the whole sky at wavelengths of 1.25 μm (J-band), 1.65 μm (H-band) and 2.17 μm (K_s -band). The **InfraRed Astronomical Satellite** (IRAS) provided an almost complete (96 %) sky survey in the MIR and FIR at 12 μm , 25 μm , 60 μm and 100 μm .

Like in radio synchrotron emission from AGNs is measured. Observations in the IR range are important to determine the position of the first peak in the SED. From emission or absorption lines in the IR spectra the redshift can be determined.

Optical astronomy Although optical observations can be done with ground based telescopes, high and dry places or the space are preferred to improve the observation conditions, data quality and precision. Thanks to the variety and large number of telescopes, including also many amateur astronomers, the possibility of time variability studies is used

more often than in other wavebands. For example the optical telescope KVA monitors blazars in the optical to trigger MAGIC observations in case of an flare and to provide data simultaneous to MAGIC observations [Albert et al., 2006b].

Depending on the peak position, optical measurements of AGNs are at the synchrotron peak or its rising edge. Consequently, the observations in this spectral range are important for the determination of the peak. However only from the optical data no big conclusion can be draw, but also data at neighboring wavelenths is needed to constrain the peak position.

In addition emission and absorption lines measured in the optical range can be used to determine the redshift of an AGN.

Ultraviolet astronomy Ranging approximately from 10 nm to 380 nm, UV astronomy can be subdivided into **Near UV** (NUV, 200 nm - 380 nm), **Far UV** (FUV, 100 nm - 200 nm) and **Extreme UV** (EUV, 10 nm - 100 nm). While observations in the NUV waveband can be done with optical telescopes, the rest of the UV band is absorbed in the atmosphere and observations have to be performed from space. In the beginning observations in the FUV were done with balloon experiments, which reached heights of 45 km. Starting from 1962 UV observation of the sun were done from space (Orbiting Solar Observatory). Ten years later several other satellites, observing also other objects, followed. For UV astronomy the **International Ultraviolet Explorer** (IUE, 1978 to 1996) and the UV instruments on-board the HST play an important role.

Being between the optical and x-ray range, the UV is also important for the determination of the position of the first peak in the SED of an AGN.

X-ray astronomy This energy range (0.1 keV - 500 keV) can be subdivided to soft and hard x-rays at 2 keV. As x-rays are absorbed in the atmosphere, satellite experiments are needed for this branch of astronomy, consequently only developed with the launch of space experiments. In the beginning the experiments were done with rocket and balloon flights. While the first are limited in time and field of view, the second still suffer from absorption. Despite of that, the first cosmic x-rays were detected in 1949 from the corona of the sun during a flight of a V2 rocket. An important step was the discovery of x-rays from Scorpius-X-1 with an experiment on board of an Aearobee rocket. In 1971 the Uhuru Satellite detected 339 sources during the first x-ray sky survey. From 1978 to 1981 the **High Energy Astronomy Observatory 2** (HEAO-2, named Einstein Observatory after its launch) observed between 0.15 keV and 20 keV with improved sensitivity and angular resolution compared to previous experiments. More recent experiments were the German **ROentgenSATellit** (ROSAT) and the BeppoSAX satellite (1996-2003). Equipped with several instruments, ROSAT performed an all-sky survey and detected 125,000 new x-ray sources and 479 EUV sources between 1990 and 1999. BeppoSAX, an Italian-Dutch project, observed the sky in x-rays between 0.1 keV and 300 keV with five instruments: While the **Medium Energy Concentrator Spectrometer** (MECS) covered the energy range between 1.3 keV and 10 keV, the **Low Energy Concentrator Spectrometer** (LECS) was

1. Multi-Wavelength Astronomy

measuring down to 0.1 keV. The **Wide Field Camera** (WFC) operated between 2 keV and 30 keV. The **High Pressure Gas Scintillation Proportional Counter** (HPGSPC) could detect photons up to 120 keV and the **Phoswich Detector System** (PDS) up to 300 keV. From these observations, for example a catalog of 157 x-ray spectra and 84 spectral energy distributions of blazars have been compiled [Giommi et al., 2002].

The main current x-ray satellites are the Chandra X-Ray Observatory (since 1999), the **X-ray Multi-Mirror Mission Newton** (XMM-Newton), the **Rossi X-ray Timing Explorer** (RXTE) and the Suzaku satellite. Launched in 2005, Suzaku is equipped with three experiments. While the **X-Ray Spectrometer** (XRS) broke, the **X-ray Imaging Spectrometer** (XIS) and the **Hard X-ray Detector** (HXD) are measuring between 0.3 keV and 600 keV. Operational since 1996, the RXTE satellite has three instruments: the **Proportional Counter Array** (PCA), the **High-Energy X-ray Timing Experiment** (HEXTE) and an **All Sky Monitor** (ASM).

In the x-ray regime the falling edge of the first peak in the SED of AGNs is observed. Compared to the other wavelengths a relatively large energy range is observed allowing for constraints on the curvature of the peak.

Astroparticle physics The new field of astroparticle physics pools **Cosmic Ray** (CR) physics, neutrino physics and gamma-ray astronomy and deals with the research of dark matter ^c.

CRs are charged particles with energies ranging from 1000 eV to more than 10^{20} eV coming from space and hitting the earth. For energies up to 10^{15} eV, it can be measured with space detectors or balloon experiments, but for higher energies the rate of particles is too low, necessitating ground-based, indirect measurements. CRs consist of 85% protons, 12% helium nuclei, 2% heavy nuclei and 1% electrons.

As CR particles are charged, they are deflected in magnetic fields in space several times, losing any information about the direction of their origin. Despite of that, useful information can be gained like the abundance of elements in cosmic rays and their energy spectrum. Ground-based measurements are for example done with the large detector array of the Auger-Experiment in Argentina and the **KARlsruhe Shower Core and Array DETector** (KASCADE). Balloon experiments, e.g. the **ISOtope Magnet EXperiment** (ISOMAX), and space experiments, e.g. the **Alpha Magnetic Spectrometer** (AMS), are performing direct measurements of CRs.

Other particles being observed for astronomical purposes are neutrinos. Due to their small crosssection, these weak interaction particles are difficult to detect, on the other hand they can travel long distances without interaction. Being neutral they carry information about the direction of their origin. Several experiments in neutrino physics are exploring the neutrinos coming from the sun. To search for neutrinos from other astronomical sources, new large neutrino telescopes have been built using on the one hand the ice of Antarctica (**Antarctic Muon And Neutrino Detector Array** (AMANDA), IceCube Neutrino Observatory) on the other hand the water of the Mediterranean Sea (**Astronomy with a Neutrino**

^cinformation and numbers from www-15

Telescope and Abuss environmental RESEARCH (ANTARES), KM3Net) as detector for muons from neutrino interaction in the water or ice. The main problem for these neutrino telescopes is the large background from atmospheric neutrinos which is suppressed by looking only to neutrinos coming from the ground. Consequently, from Antarctica the northern hemisphere and from the Mediterranean Sea the southern hemisphere is observed. The low rate of neutrino interactions makes it difficult to correlate measured neutrinos with sources. Therefore either long observation times or strong outbursts of a source are needed.

Multi-wavelength and multi messenger astrophysics As discussed in the previous paragraphs the first peak of the SED of an AGN is measured in the radio, IR, optical, UV and x-ray regime. The gamma-ray energy range, discussed in the next section, adds information about the second peak. With this, conclusions on the mechanisms in the AGN, the jet and the medium between source and observer can be drawn. Consequently, MWL astronomy helps to understand the physics in these energetic objects.

But not only photons, but also CR in general carry information from the objects to the observer. As charged particles are deflected by magnetic fields, another important candidate are neutrinos, as they allow for conclusions on the acceleration processes in the HE astrophysics.

As it is assumed that there are neutrinos coming from extragalactic objects like AGNs, the correlation of neutrino and gamma-ray observation is an important goal in astroparticle physics. To allow for correlating neutrino events and gamma-ray measurements, simultaneous and complete data set is needed. Therefore the Cherenkov telescope DWARF (**D**edicated **m**ulti-**W**avelength **AGN** **R**esearch **F**acility) is planned to be assembled [Bretz et al., 2007] on the Canary Island of La Palma to do long-term monitoring of the brightest AGN in the gamma-ray regime. This allows for correlating flares in the gamma-ray emission of AGNs and neutrinos coming from the source.

Collecting information not only from various wavelength, but also from CR particles, this so-called multi messenger astrophysics allows to enhance the knowledge of astrophysical sources further.

1.3. Gamma-ray astronomy

Ranging from a few keV to several hundred EeV the gamma-ray regime can be subdivided into several parts [Weekes, 2003]: **Low to Medium Energies** (LE/ME, 0.1 keV - 30 MeV) and **High Energies** (HE, 30 MeV - 100 GeV) are observed from space, as photons with these energies do not reach ground. For higher energies, the photon statistics is too low for the small detector volumes possible in space. Therefore **Very High Energies** (VHE, 100 GeV to 100 TeV) and **Ultra High Energies** (UHE, 100 TeV to > 100 EeV) are observed from ground.

Next, a selection of satellite and ground-based gamma-ray experiments is presented ^d.

^dinformation and numbers from www-10 if not stated otherwise

1. Multi-Wavelength Astronomy

1.3.1. Space experiments

Although cosmic gamma-ray emission had already been predicted in the 1940s and 1950s, their existence was only confirmed with the first gamma-ray satellite Explorer XI. Since then several gamma-ray satellites have been launched.

Compton Gamma-Ray Observatory The Compton Gamma-Ray Observatory (CGRO) was the first big satellite mission observing in the gamma-ray regime from 1991 to 2000. With its four instruments it covered an energy range from 20 keV to 30 GeV. The **Burst And Transient Source Experiment** (BATSE) was searching for **Gamma-Ray Bursts** (GRBs) between 20 keV and 600 keV. With approximately one burst per day, it detected in total more than 2700 GRBs equally distributed in the sky. From these bursts, two populations were found: While short duration GRBs last less than two seconds, long duration bursts are longer than ten seconds, considering the time T_{90} in which the burst emits 90 % of its counts [Kaneko et al., 2006; Meegan et al., 1998]. The **Oriented Scintillation Spectrometer Experiment** (OSSE) was observing between 0.05 MeV and 10 MeV, while the **Imaging COMpton TELEscope** (COMPTEL) covered the range between 1 MeV and 30 MeV. The **Energetic Gamma-Ray Experiment Telescope** (EGRET), measuring between 20 MeV and 30 GeV, provided an all-sky map at gamma energies above 100 MeV. From this a source catalog of 271 sources was compiled (figure 1.3), of which 170 were unidentified. The instrument achieved an energy resolution of about 15 % and a position accuracy of about 1° [www-12].

HETE The **High Energy Transient Explorer** (HETE), a satellite mission for MWL studies of GRBs, is able to localize a GRB with approximately 10 arcsec accuracy. After the failure of the first mission, HETE2 was launched in 2000. It was equipped with gamma- and x-ray instruments to detect and observe GRBs from 8 keV to 500 keV, from 2 keV to 25 keV and from 0.5 keV to 14 keV.

The position information is directly transmitted to the **GRB Coordination Network** (GCN) providing the information to all telescopes observing GRBs to allow for MWL observations of these extremely short events.

Swift Gamma-Ray Burst Mission The Swift Satellite, another mission to detect GRBs, was launched in 2004. Equipped with a **Burst Alert Telescope** (BAT, 15-150 keV), a **X-Ray Telescope** (XRT, 0.2-10 keV) and an **UV/Optical Telescope** (UVOT, 170-650 nm), GRBs are observed in several wavelengths and their spectra are measured. Apart from that, also **Target-of-Opportunity** (ToO) observation of other objects are performed. In addition the UVOT and XRT are used for regular observations of sources.

On September 4th 2005 with $z=6.29$ the farthest and on February 18th 2006 with 2000 seconds the longest GRB was detected with Swift.

AGILE In 2007 another gamma and x-ray satellite was launched: **Astro-rivelatore Gamma a Imagini LEggero** (AGILE). Apart from GRBs, it aims to detect diffuse galactic

1. Multi-Wavelength Astronomy

GLAST The **G**amma-ray **L**arge **A**rea **S**pace **T**elescope (GLAST), a new Gamma-ray satellite, will be launched in 2008. With its **L**arge **A**rea **T**elescope (LAT) it will observe a field of view of two steradians in the energy range between 20 MeV and 300 GeV with the aim to close the gap between previous Gamma-ray space telescopes and the current IACTs. Apart from this the **GLAST Burst Monitor** (GBM) will search the whole sky for GRBs in the energy range between 10 keV and 25 MeV.

1.3.2. Ground-based experiments

In the VHE regime the photon statistics is low or rather the detector volumes feasible in space are too small to measure the flux of the sources. Consequently, indirect ground-based measurements are preferred.

Comparing the source map above 100 MeV (figure 1.3) to the VHE sky map (figure 1.4), a large difference in the number of sources is found. While EGRET saw almost 300 sources, in 2003 less than 15 sources were known to emit at energies above 500 GeV. The reason for this discrepancy is supposed to be the attenuation of high energetic photons in the **M**etagalactic **R**adiation **F**ield (MRF). To investigate this, the current generation of **I**maging **A**ir **C**herenkov **T**elescopes (IACTs) has been built lowering the energy threshold and enhancing the sensitivity by increasing the light collection efficiency. In the past four years, many new sources have been detected above 100 GeV, raising the number of known VHE sources to 59 (figure 1.4, lower plot). These sources include also new source types like binary systems or **L**ow-frequency **BL Lac** objects (LBLs).

In the following different ground based experiments will be explained, of which most are using the **I**maging **A**ir **C**herenkov **T**echnique (IACT, section 1.4).

First Cherenkov detectors The first images of Cherenkov showers were recorded by Jelley and Porter [1963]. Between 1960 and 1964 a group from the Lebedev Institute operated in Crimea twelve light detectors measuring the Cherenkov light of air showers. Although no source was detected, this was the base of the next developments in the field.

Whipple 10 m telescope The first large reflector used for ground-based gamma-ray observations was the 10 m telescope at the Fred Lawrence Whipple Observatory [Weekes, 2003]. Operating since 1968, it was the first IACT which detected a source: In 1989, gamma-ray emission from the Crab Nebula was significantly detected above 700 GeV [Weekes et al., 1989]. In 1992 the first VHE emission from an extragalactic object was found. Markarian 421 was detected at a flux level of 30% of the Crab flux above 500 GeV [Punch et al., 1992].

Since 2005 the Whipple 10 m telescope is monitoring five known TeV blazars, namely 1ES 2344+514, 1ES 1959+650, Markarian 421, H 1426+428 and Markarian 501 [www-03].

HEGRA The HEGRA (**H**igh **E**nergy **G**amma-**R**ay **A**stronomy) experiment, operational from 1992 to 2002 on the Canary Island of La Palma, consisted of an array of IACTs, the

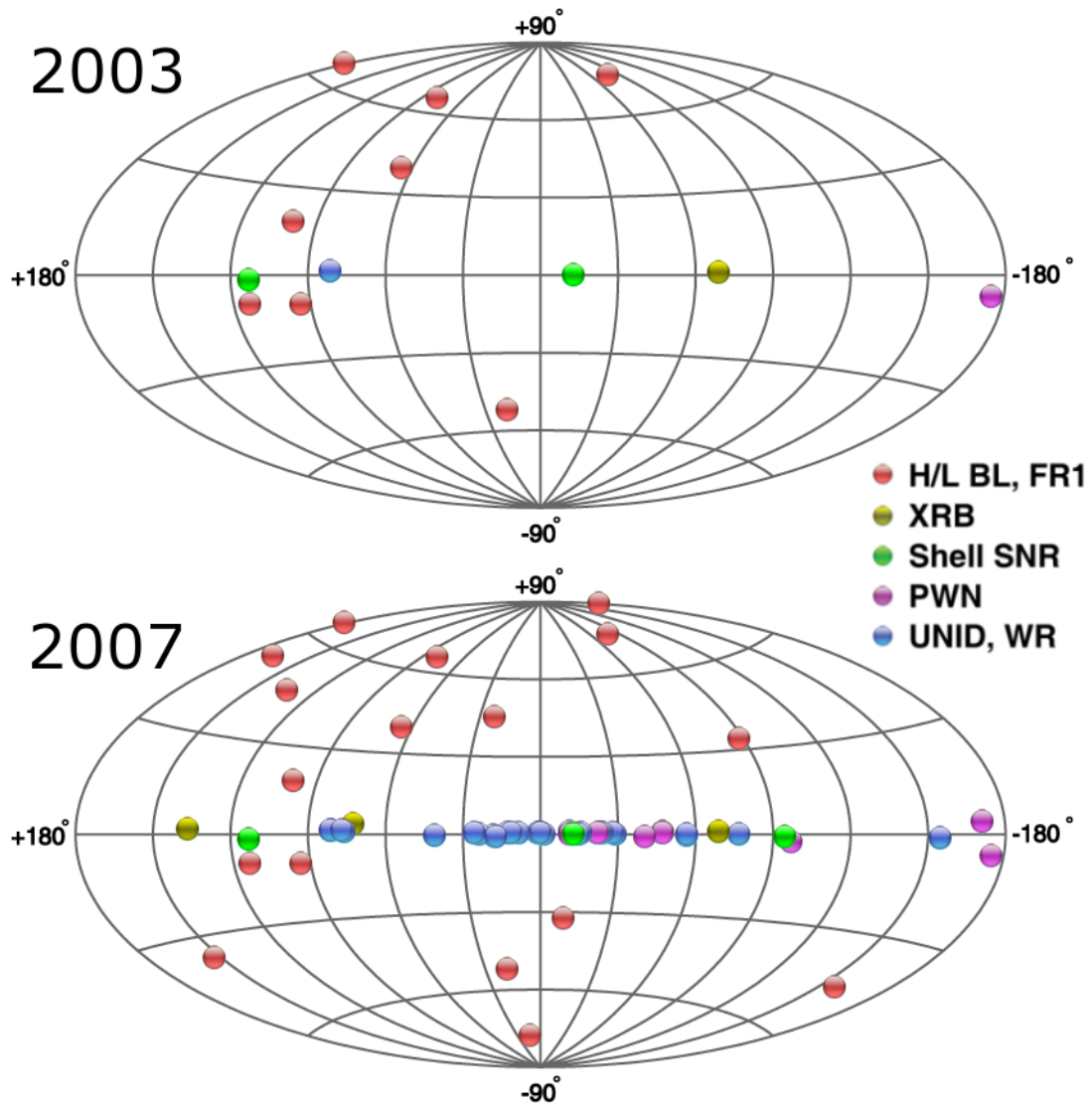


Figure 1.4.: Map of VHE sources known in 2003 (upper plot) and 2007 (lower plot) [Wakely and Horan, 2008]. Different source types are indicated with different colors, as given in the legend.

AIROBIC array (**A**IRshower **O**bservation **B**y angle **I**ntegrating Cherenkov Counters), the CRT (**C**osmic **R**ay **T**racking) and the Cherenkov **L**ight **U**ltraviolet **E**xperiment (CLUE). Observations between 500 GeV and 10,000 TeV were performed [www-11]. With the Cherenkov Telescope (CT) system, observations of 54 AGNs have been performed. Apart from Markarian 421 and Markarian 501 also VHE emission was found from 1ES 1959+650, H 1426+428, 1ES 2344+514 and M 87 [Aharonian et al., 2004].

1. Multi-Wavelength Astronomy

CANGAROO The CANGAROO project (Collaboration between Australia and Nippon for a Gamma Ray Observatory in the Outback) started in 1999 with a single 3.8 m telescope in 1999 [www-01] and was enlarged to a four telescope system with 10 m each until 2004 [www-02], i.e. CANGAROO III. Situated in Australia at 165 m a.s.l., it is observing on the southern hemisphere.

H.E.S.S. The High Energy Stereoscopic System (H.E.S.S.), situated at 1800 m a.s.l. in Namibia, consists of four telescopes observing in stereoscopic mode since 2003 [www-06]. Situated on the southern hemisphere the galactic plane is one of its major targets. During the performed galactic plane scan, plenty of new gamma-ray sources were detected by H.E.S.S.

VERITAS The Very Energetic Radiation Imaging Telescope Array System (VERITAS), successor of the Whipple 10 m telescope, consists of four 12 m telescopes and is observing between 50 GeV and 50 TeV. VERITAS is situated on the northern hemisphere at 1268 m a.s.l. in the Fred Lawrence Whipple Observatory.

Solar power stations Due to their large mirror area solar power stations may be used as Air Cherenkov Telescopes for observations between 30 GeV and 100 GeV [Weekes, 2003]. Examples for such experiments are the Solar Tower Atmospheric Cherenkov Effect Experiment (STACEE), the Converted Atmospheric Cherenkov Telescope Using Solar-2 (CACTUS) and the Cherenkov Low Energy Sampling and Timing Experiment (CELESTE). STACEE has detected gamma-ray emission from the Crab Nebula [STACEE Collaboration: S. Oser et al., 2000] and also observed AGN [www-04].

Other ground-based detectors Apart from IACTs, which observe single sources, there are also different ground-based gamma-ray detectors monitoring the visible sky continuously. For example the Multiple Institution Los Alamos Gamma Ray Observatory (MILAGRO) observes the northern sky in the energy range between 100 GeV and 100 TeV [Atkins et al., 2004]. To improve the sensitivity a similar, bigger experiment is planned at an altitude of 4300 m a.s.l.: the High Altitude Water Cherenkov (HAWC) Observatory [Dingus, 2007]. At high altitudes even direct detection of high energetic gammas is possible. For example the Tibet AS-gamma Experiment, located at an altitude of 4300 m a.s.l., is measuring with scintillation counters at energies larger than 3 TeV [www-05].

Future IACTs As shown in figure 1.4, the number of known sources in the gamma-ray regime increased a lot with the observations of current IACTs. There are several projects planning to enhance the capabilities of the current gamma-ray experiments. The upgrade of H.E.S.S. and MAGIC are already underway. While the MAGIC experiment is building a second telescope to improve the background suppression, H.E.S.S. phase II plans an additional single telescope with about 600 m² mirror area [www-06].

Although already now guest observer proposals are possible to some extent, the current

projects are mainly operated as experiments and not as observatories. Consequently, one of the next steps is a big Cherenkov observatory. There are two projects aiming this: the US-American **A**dvanced **G**amma-ray **I**maging **S**ystem (AGIS) and the European Cherenkov **T**elescope **A**rray (CTA). The goals are to extend the energy range well below 100 GeV and above 100 TeV, as well as to improve the sensitivity in the current energy range by at least an order of magnitude [www-07; www-08]. While these projects aim to explore new ranges, another approach is long-term monitoring of known, bright AGN to gain new information about the physics of these variable sources [Bretz et al., 2007]. The DWARF (**D**edicated **M**ulti-**W**avelength **A**GN **R**esearch **F**acility) project plans to upgrade the old CT3 telescope of the HEGRA experiment with new technology and operate it fully robotic. Multi-wavelength observations of the following blazars are intended: Markarian 421, Markarian 501, 1ES 2344+514, 1ES 1959+650, H 1426+428 and PKS 2155-304. Building more such small, low-cost telescopes around the globe, would allow for 24 hours monitoring of the sources.

1.4. Imaging Air Cherenkov Technique

The name Imaging Air Cherenkov Technique originates from the fact that *images* of *Cherenkov* light distributions of *air* showers are recorded. In this section, first the indirect detection technique, then the analysis principle is explained.

1.4.1. Atmosphere as detector

As explained in section 1.2.2, the atmosphere is not transparent in all parts of the electromagnetic spectrum. In the GeV to TeV regime gamma photons and CRs interact with nuclei in the atmosphere. In the initiated cascade all particles traveling faster than the speed of light in the medium emit Cherenkov light. The Cherenkov effect, awarded with the Nobel Price in 1958, is described e.g. in Dorner [2003].

If a photon enters the atmosphere, an electromagnetic shower is produced. The electrons and positrons created in pair production emit bremsstrahlung. While the first interaction typically takes place at 20 km a.s.l., the maximum of a shower is around 10 km a.s.l. When the energy of the particles falls below a critical value of 81 MeV, the shower dies out. Consequently, it has an elongated, cigar-like shape.

In case of a hadronic interaction the secondary particles are mainly pions, but also other particles like K-mesons or anti-nuclei. Decaying, they produce for example gamma photons ($\pi^0 \rightarrow 2\gamma$) or muons and neutrinos ($\pi^+ \rightarrow \mu^+\nu_\mu$, $\pi^- \rightarrow \mu^-\bar{\nu}_\mu$). Consequently, a hadronic shower consists of electromagnetic, muonic and hadronic components, e.g. [Klapdor-Kleingrothaus and Zuber, 1997]. As the secondary particles may have larger transversal momentum, these showers are broader than gamma induced showers and may contain several electromagnetic sub-showers.

The Cherenkov light emitted by these particles is measured by the telescope, if it is inside the light pool. The light hits the mirror surface and is reflected into the camera, where it

1. Multi-Wavelength Astronomy

is recorded by photon detectors. As showers last only a few nano-seconds, the exposure time is very short compared to optical measurements for example. To suppress artificial coincidences from the night sky background, a trigger system is used.

Although being equipped with a mirror, IACTs are different from normal optical telescopes. Measuring not the star light directly, but the Cherenkov light from shower cascades in the atmosphere instead, the angular resolution is less accurate than in optical astronomy. For the detector design this includes several consequences: To the optical quality less strict requirements are made. A tessellated mirror is used to achieve the large mirror area needed to collect enough photons at low energies. For the photon detectors a pixel size between 0.1° - 0.2° diameter is chosen to resolve the shower morphology. Taking into account the focussing accuracy and pixel size, also no arc-second accuracy for the pointing and tracking is required. Another difference is that for IACTs, compared to for example IR telescopes, no detector cooling with liquid nitrogen is needed, as the cameras can be operated at temperatures between 20°C and 40°C .

1.4.2. Analysis principles

To determine signal, spectrum and light curve from a source, the following information is calculated from the events:

Time To study the variability of the sources, the arrival time information of the events is needed for the determination of a light curve.

Particle identity As charged particles are deflected in intergalactic magnetic fields, only photons contain information on the source direction. Consequently, the background, consisting of hadronic showers and muons, has to be rejected. The ratio between gammas and background is approximately 1/1000. Thanks to the different interaction processes in the showers, the recorded images can be distinguished based on their morphology. For energies below 100 GeV the similarity of gammas and background showers complicates the discrimination.

The image is first cleaned, i.e. the noise is removed leaving only pixels containing signal. This can be done by rejecting pixels below an absolute value or by cutting in the signal-to-noise ratio. In addition, the arrival time information of the single pixels can be included in the image cleaning [Bretz, 2008].

On the cleaned shower image a statistical analysis is performed. Various parameters are calculated [Hillas, 1985]. The most important are listed here:

SIZE total number of measured photo electrons in the image

LENGTH standard deviation along the major axis of the light distribution

WIDTH standard deviation along the minor axis of the light distribution

COG Center of gravity of the light distribution

DIST distance of the COG from the position of the target source in the camera

By cutting in the distributions of these parameters, background events are rejected.

Shower origin Similar to meteors, the showers point towards their origin in the picture. To determine a sky map, the origin of each shower has to be reconstructed. There are different approaches for this:

ALPHA α is the angle between the major axis of the shower image and the line between the COG and the target source position.

Theta ϑ is the distance from the target source position to the reconstructed source position, which is determined as described in Riegel and Bretz [2005].

In both cases a value around zero indicates that the event may come from the source. For the signal determination, one of the values is histogrammed for both ON and OFF events. The signal is calculated from the excess events, i.e. difference of signal and background events in the signal region, which is α or ϑ smaller than a certain value.

Energy of the primary particle To determine a spectrum, the energy of the excess events has to be reconstructed. As the interaction processes in the atmosphere are well understood, they can be simulated. From the comparison of real events to simulated showers, the energy of the primary particle can be reconstructed.

1. *Multi-Wavelength Astronomy*

2. The MAGIC experiment

*Die Magie des Cherenkovlichts
Durch die Atmosphäre bricht's
Trifft Spiegel und trifft Kamera
Zu Niederenergien strebt man da
100 GeV und drunter
Da werden neue Quellen munter
— Daniela Dorner.*

One approach to close the gap between 30 GeV and 300 GeV, was to enlarge the energy range of IACTs to lower energies. For this purpose a new generation of telescopes has been built consisting of four major experiments distributed around the globe. On the southern hemisphere, the stereoscopic systems of CANGAROO III and H.E.S.S. are observing. On the northern hemisphere, the new generation of IACTs is completed by VERITAS and the **Major Atmospheric Gamma-Ray Imaging Cherenkov** (MAGIC) telescope. While the other experiments rely mainly on established technologies, MAGIC is focused on the aim to detect gammas at energies down to 30 GeV [Moralejo et al., 2003], to discover plenty of new sources, and to observe GRBs. To meet these challenges, several new techniques have been developed and are used in MAGIC. Inaugurated in October 2003 and taking data routinely since summer 2004, the telescope is continued to be equipped with new subsystem components to optimize the performance of the telescope for low energy observations. Not only the numerous new sources that are observed by MAGIC, but also the enhancements of the telescope and its ability to observe during moonlight, require an automatic and failsafe processing of all data to obtain consistent results for all observations and a continuous monitoring of the data quality.

To point out the precise requirements, which an automation concept had to fulfill, the MAGIC telescope, its subsystems, the data flow and the analysis software are described in the following sections.

2.1. Telescope system

The MAGIC telescope is situated at 2200 m a.s.l. on the Canary Island of La Palma. For the observation of GRBs, fast repositioning of the telescope is essential, as the duration of these energetic phenomena is very short (see section 1.3). To realize this, the telescope has been equipped with a lightweight space frame, built from carbon fiber epoxy composite tubes, reaching a low weight of only 60 tons. The drawback of this lightweight structure

2. The MAGIC experiment



Figure 2.1.: MAGIC site in March 2006 during sunset with both telescopes pointing to zenith. View in north-north-eastern direction with Magic II in the middle. In the background there are other telescope facilities of the Observatorio Roque de los Muchachos, the moon (right) and Magic I (left).

is the bending of the telescope frame, especially during movements in elevation, affecting the pointing accuracy and the focusing.

To reach lower energies, fainter showers have to be recorded. To detect more photons, the MAGIC telescope has been equipped with a higher quantum efficiency camera and a larger mirror, leading to a larger total light collection efficiency and thus a larger collection area. Furthermore, the aim to observe during moonlight makes certain requirements on the camera, which has to cope with a higher background light. Different observation conditions and changing hardware require a monitoring of the data quality.

To improve the sensitivity, the construction of a second telescope was started in 2006 (see figure 2.1). Including some technical improvements, it is planned to be finished in 2008. Already the first telescope made certain requirements on the data processing and management. Depending on the used techniques (camera layout, data acquisition and trigger configuration), least the same amount of data is expected with the second telescope.

In the following section, the different subsystems of the MAGIC telescope are presented to show not only how they contribute to reach the physics goals, but also how their performance can influence the data quality. The produced output (files) are mentioned, to show the initial situation for the data management and the requirements on the automation concept.

2.1.1. Central control

To coordinate all subsystems a **Central Control (CC)** has been installed, which not only sends commands to all subsystems to operate the telescope, but also collects reports from the subsystems. Once every ten seconds, the reports and some more information, e.g. the average discriminator thresholds, are stored into text files. There is one file with the most important information for each raw data file and there are files with all reports, one file for each raw data file and one summary file for the whole night. In addition, the CC takes care of the electronic runbook, to which the shift crew can add comments via an insert mask. This runbook text file and a log file complete the output of the CC.



Figure 2.2.: MAGIC telescope during daytime in park position. In the center of the dish two panels are left out to provide space for the calibration box (section 2.1.5) and some CCD cameras for the active mirror control (section 2.1.3) and the calibration and monitoring of the pointing (section 2.1.2).

2. The MAGIC experiment

2.1.2. Drive system

Having an Alt-Az mount, the MAGIC telescope is equipped with three 11 kW servo motors (one for the elevation and two for the azimuth axis) and three 14bit shaft encoders (one for the azimuth and two for the elevation axis) [Bretz et al., 2008]. This setup allows the drive system on the one hand to move the more than 60 tons weighing telescope 180° in less than 25 seconds [Bretz et al., 2003] and on the other hand to reach a tracking accuracy of 1.1 arcminutes which is better than the required 3 arc-min. Details on the technical implementation of the drive system can be found in Bretz [2006].

The disadvantage of the lightweight telescope frame, its bending, causes not only a deformation of the mirror surface, but affects also the pointing of the telescope. To correct for this, the pointing has been calibrated using an analytic model describing the differences between an ideal and a real telescope, called pointing model [Dorner, 2003]. As the effects of the mirror control on the optical axis cannot be disentangled, the pointing has to be monitored taking regularly data sets for a pointing model. In case of changes, which can be introduced for example by a new calibration of the active mirror control (see section 2.1.3), a new pointing model is calculated and implemented.

To check the tracking accuracy and record possible mispointing or misfocusing, a starguiding system has been installed, consisting of a CCD camera situated at the center of the dish (see figure 2.2) and several **L**ight **E**mitting **D**iodes (LEDs) mounted around the MAGIC camera to determine the camera center. The starguider calculates the relative mispointing by comparing the star position from a CCD picture (see fig 2.3) to those from a catalog online. For offline use in the analysis, the relative mispointing as well as the number of identified spots in the CCD picture, the number of correlated stars and a number representing the sky brightness in arbitrary units are sent to the CC. To obtain the absolute mispointing, a pointing model for the starguider has to be performed. This calibration of the starguider is not done online, but the measurements are stored and the correction is done offline in the analysis.

As oscillations of the MAGIC camera with respect to the telescope frame, e.g. due to wind gusts, had been expected, in 2002-2003 an additional device, named camera oscillation monitor, had been installed. Measurements, presented in Dorner [2003], show that this subsystem is not needed, as the oscillations of the camera are smaller than 5 mm, which is negligible compared to the 15 mm diameter of a pixel of the MAGIC camera (see section 2.1.4).

Drive system and starguider send reports to the CC (see section 2.1.1) containing the pointing position and the above mentioned values from the starguider. Apart from that, log files are written and the data sets of the two pointing models are stored.

2.1.3. Active mirror control

The 17 m diameter mirror surface of the MAGIC telescope, described in more detail in Garczarczyk [2007], consists of 964 mirror segments (50 cm x 50 cm), made from aluminum and having a diamond-milled, coated surface. 223×4 and 24×3 (at the outer rim of the

2.1. Telescope system

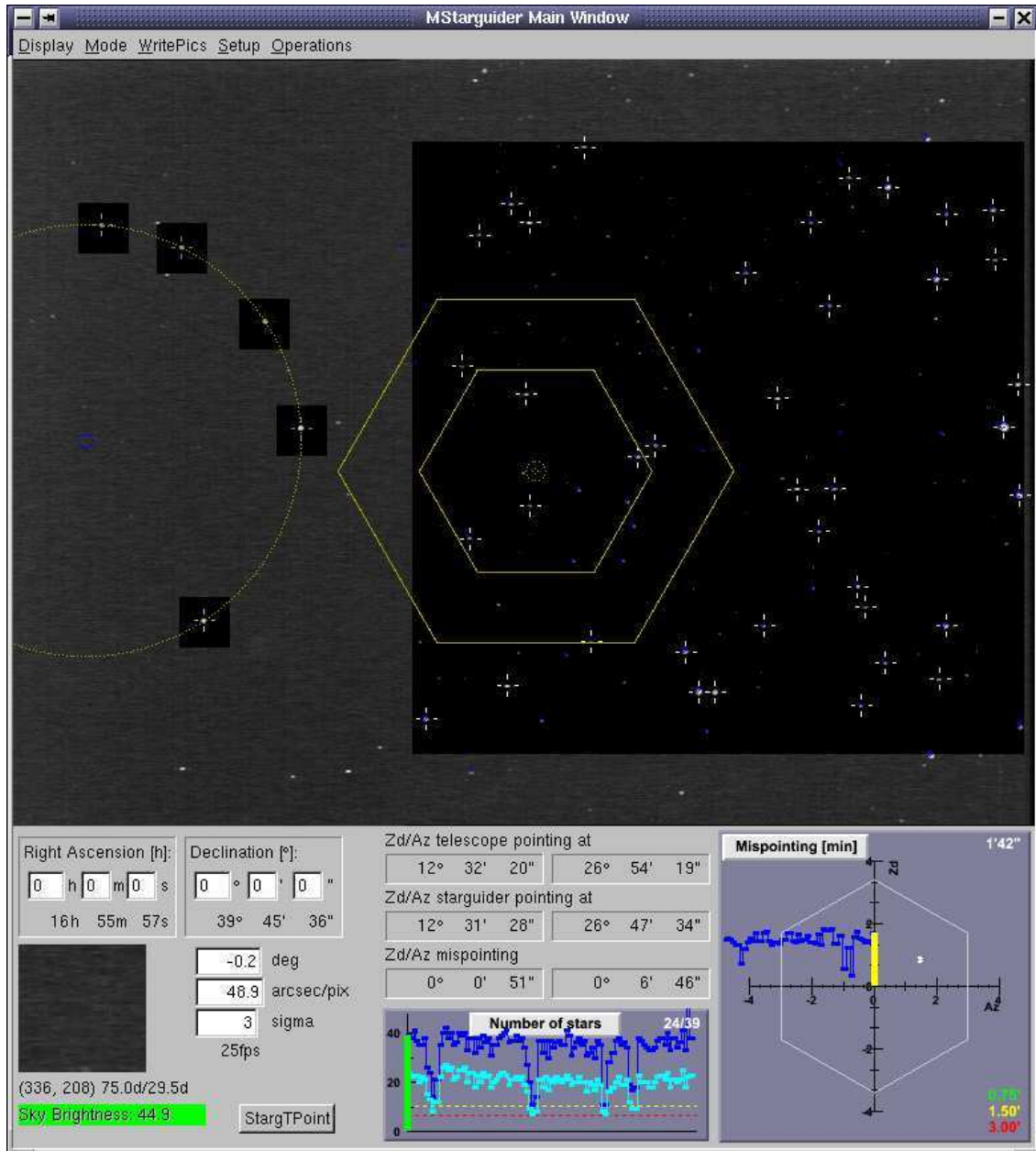


Figure 2.3.: Screen-shot of the starguider program. Upper part: picture of the CCD camera, showing a star-field (right) and the MAGIC camera with the LEDs (left). In the star-field white crosses mark the recognized spots and blue circles the star positions from the catalog. The number of recognized spots and the number of correlated stars, is shown in the starguider display (bottom) in the lower middle panel. From these correlations the relative mispointing is calculated and displayed (bottom right panel).

2. The MAGIC experiment

dish and near the axes) of these segments are grouped on light-weight aluminum panels, on which they have been pre-aligned in the laboratory. The total reflecting surface of 236 m^2 helps to collect enough light from lower energy showers. While the single segments have a spherical surface with different radii, the overall shape of the mirror is parabolic, i.e. isochronous to provide the possibility to use the timing information to discriminate different shower types. The aluminum components have been chosen to reduce the weight of the dish for faster repositioning. To remove ice and dew from the mirrors, each of the 247 panels is equipped with a heating. It is fixed to the frame with a 3-point mount, where one point is fixed and the other two are actuators enabling a panel movement to correct the focusing for the deformation of the dish and hence guarantee a stable **P**oint **S**pread **F**unction (PSF). This system, which is the first of its kind used in an IACT, is called **A**ctive **M**irror **C**ontrol (AMC) and allows not only for correcting misfocusing, but enables also to focus to different focal lengths. The optical quality of the mirrors is chosen such that the PSF is less than the diameter of one pixel of the MAGIC camera (section 2.1.4). There are three different possibilities to align the mirrors. The so-called laser adjust, which is done with the help of lasers mounted in the center of each panel and four LEDs fixed on the lid of the MAGIC camera. This is a possible option for normal operation, but needs a calibration of the system, which can be done with one of the other two methods. The first uses an artificial light source, which is mounted in about one kilometer distance on the top of the mountain. The second, the so-called star adjust, is done by focusing a star to the camera lid. As the laser adjust takes at least three minutes, it is inappropriate especially for GRB observations. To speed up the procedure **L**ook**U**p **T**ables (LUTs) have been produced allowing for re-focusing in ten seconds already during the repositioning. As this method does not need the lasers and the LEDs on the camera lid, it is also used during normal data taking every 5° in zenith.

For the star adjust, a sensitive camera has been installed in the center of the telescope dish (see figure 2.2), which is also used to measure the PSF and the reflectivity of the mirror for longterm degradation studies. The pictures of this camera are analyzed offline and do not enter the automatic data flow directly, but the results can be compared for example to the PSF obtained from the muon analysis (see section 2.2.4).

From the AMC only the LUTs and some log files are stored.

2.1.4. Camera

To record lower energy events not only the mirror surface, but also the photon detection efficiency of the camera is an important issue. For the camera of the MAGIC telescope several photo sensors have been considered. While **P**hoto **M**ultiplier **T**ubes (PMTs) have been chosen for the first phase of MAGIC, **H**ybrid **P**hoto **D**etectors (HPDs) or Geigermode **A**valanche **P**hoto **D**iodes (APDs) might be used in later phases of the experiment. Tests on these new technologies are ongoing.

The PMTs chosen for MAGIC I have a **Q**uantum **E**fficiency (QE) close to 25% in the spectral range between 350 nm and 450 nm, which could be enhanced by more than 20% by coating the PMTs with a special lacquer including a wave length shifter. The installation

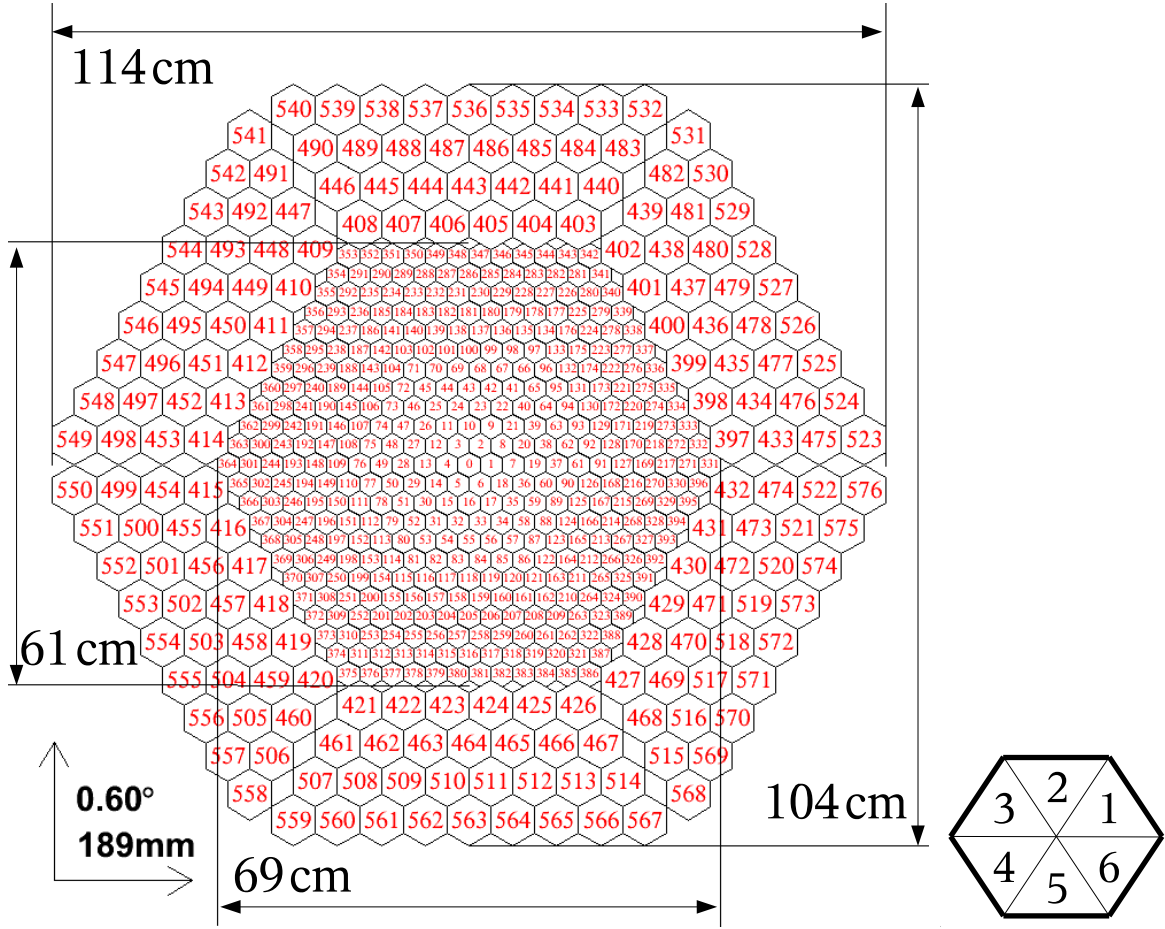


Figure 2.4.: Scheme of the MAGIC camera giving the measures of the inner and outer camera (left) and the sectors (right).

of light collectors around the pixels additionally improved the QE [Paneque et al., 2003]. In total, the camera consists of 577 pixel where the central one is a PMT dedicated for optical measurements needed for pulsar studies. The inner part of the camera is formed by 396 PMTs of 3 cm diameter (corresponding to 0.1° in the sky) each, including the light collector. Four rows of larger PMTs (diameter 6 cm), in total 180, build the outer part of the camera. The camera has a hexagonal shape with a total diameter of 3.5° to 3.8° (2° to 2.3° for the inner part). The layout of the camera is shown in figure 2.4 including measures, sectors and pixel numbering. The design with two different pixel sizes was done as an optimization between cost and performance. In the inner camera a fine pixelization was needed to resolve the showers. A diameter of 0.1° was sufficient as the expected fluctuations in the shower are in that range [Barrio et al., 1998]. For the outer camera, no low energy showers are expected. In addition, effects like coma blur the shower image at the outer part of the camera. A pixel size of 0.2° was chosen.

2. The MAGIC experiment

To allow for observations during moonlight, the gain of the PMTs is about 5×10^4 instead of the standard gains of $10^6 - 10^7$ [Armada, 2005]. This reduces the current in the last dynode, and observations with higher night sky background are possible. With a maximum anode current of $8 \mu\text{A}$, MAGIC can observe sources with an angular distance $> 50^\circ$ to the moon up to three or four days before and after full moon, leaving only a small degradation of the last dynode. To compensate this ageing effect of the PMTs, a readjust of their **H**igh **V**oltages (HVs) is needed once or twice a year [Albert et al., 2007c]. To correct also for changes in the camera response due to changes in the hardware, this procedure has been done about six times a year since the inauguration of the telescope.

For pixels having electronic problems the HV may be set to zero until the pixel can be exchanged or repaired during the next access to the camera. For such pixels a special treatment in the analysis is needed.

To provide a stable and homogenous behavior for the whole camera, it is equipped with a cooling system taking care that the conditions inside the camera are constant no matter what the conditions (temperature, humidity, etc.) outside the camera are. To be able to check the camera status afterwards, the values describing the state of the camera, e.g. the temperature at different parts of the camera, are reported to the CC (see section 2.1.1). The **C**amera **C**ontrol (CaCo), the subsystem steering all components of the camera, sends not only these reports to the CC, but it also stores the values of the currents at the anode of the PMTs into a text file two to five times per second. The CC triggers the record of a new file each time a new raw file is started. Consequently, there should be one file with currents for each raw file. However, there are sometimes problems resulting in the fact that the currents of several raw files are stored in one file. The automatic procedure has to take care that the correct files are used.

2.1.5. Calibration system

Due to gain fluctuations, changing behavior of several components in the readout chain with changing extrinsic influences, e.g. the temperature, the PMT signals have to be calibrated. Therefor several methods have been implemented [Gaug, 2006]: the F-factor method, providing only a relative calibration, the pin diode method and the blinded pixels method. As the possibilities of these latter, new methods are still under investigation, currently muons are used for an absolute calibration [Goebel et al., 2005].

The hardware needed for the calibration is installed in the so-called calibration box, which is located in the center of the dish (see figure 2.2). From there light pulses of different intensity and different wavelength are emitted, illuminating the camera, and a signal is sent to the trigger.

The calibration system provides several scripts triggering simultaneously the light emission and the readout. Either a whole file with only calibration events or interleaved calibration events during normal data taking are stored at a certain frequency.

The steering of the calibration box is implemented in the CaCo program. No extra log files are written.

2.1.6. Trigger

As continuous data storage is not possible, a trigger system is needed. The trigger of the MAGIC telescope includes 325 pixels in the inner camera grouped to 19 so-called macro cells. It has three levels:

Level 0 A discriminator is operating on the signal of single pixels. The threshold of this discriminator can be set from the CC.

Level 1 With a pattern recognition algorithm, neighboring pixels are checked for coincidences in closed packages. The configuration, two to five next neighbors, can be chosen from the CC.

Level 2 Consisting of programmable modules this level of the trigger allows to do online pattern recognition. The possibilities of this tool are still under investigation.

The time synchronization of the trigger signal is done at discriminator level by using programmable devices allowing to finely adjust the relative delays. This procedure is routinely repeated during the year to ensure an efficient performance of the trigger system [Paoletti et al., 2007].

The trigger sends reports to the CC, containing e.g. trigger rates of the macro cells. No log files are stored.

2.1.7. Read-out chain - data acquisition

After being converted into an optical pulse in the camera with **V**ertical **C**avity **S**urface **E**mitting **L**asers (VCSELs), the signal is transmitted via approximately 170 m long optical fibers from the PMTs to the counting house, where it is converted back to electrical pulses in receiver boards. The signal is split: One half is going to the trigger, the other to the **F**ast **A**nalog to **D**igital **C**onverter (FADC) system, which digitizes the signal and writes it into a ring-buffer. When the trigger sends a signal, the data stream is copied into a first-in-first-out (FiFo) buffer. From there it is read out and stored to disk.

To make better use of the timing information, the so-called MUX FADC system [Goebel et al., 2007] has been installed in April 2006. To ensure a failsafe transition, the old and new system were running in parallel until end of January 2007, when the new system was put into full operation. During this time inbetween, the signal was provided via splitters to both systems. For MAGIC II the implementation of the domino chip [Pegna et al., 2006] is foreseen, and it is planned to equip the first telescope with this system when it has proven to be successful.

This means that in total three different FADC systems have been or will be used in the MAGIC experiment. The properties affecting the data processing are given in table 2.1. Details about the systems can be found in Bartko et al. [2005], Bartko [2006] Albert et al. [2008] and Pegna et al. [2006].

For the old FADC system, the first half of the 30 slices is the high gain signal. In case, this saturated, the low gain signal is read out in the second 15 slices.

2. The MAGIC experiment

characteristics	FADCs	MUX	Domino3
amplitude resolution	8 bit	10 bit	12 bit
number of slices	30 (15 + 15)	80	n.a.
time per slice	0.5 ns	3.33 ns	n.a.
timing resolution	1.3 ns	0.35 ns	n.a.
average FWHM of pulse (cosmic event)	6.3 ns	3.2 ns	n.a.
event size	17.3 kB	92 kB	n.a.
sampling rate	300 MHz	2 GHz	1.5-4.5 GHz
data amount per month	1.5 TB	7.5 TB	n.a.
possible compression	30-40%	≈60%	n.a.

Table 2.1.: Characteristics of the different FADC systems used or planned to be used in the MAGIC experiment [Bartko et al., 2005; Pegna et al., 2006]. For the domino chip, many information is not available (n.a.), as the system has not yet been tested at the telescope.

The **Data Acquisition** system (DAQ) stores the raw data and one log file per restart. Due to an original limitation of the file size, the DAQ starts a new raw data file, called 'run', every 1 GB, which corresponds to 53521 events for the old FADC system and 10775 events for the current FADC system. More detailed numbers are listed in table 2.1.

In some cases, the DAQ starts itself a new run, resulting in a bigger number of smaller raw data files.

The analysis software and automation package have to be capable to deal with changing hardware and the large number and big file size.

2.1.8. Auxiliary devices

For the monitoring of the conditions at the site several auxiliary devices have been installed.

Weather station The MAGIC weather station measures humidity, temperature, air pressure, wind speed and wind direction. For the shift crew, an online display is available. The weather station subsystem sends reports to the CC. Apart from that, all weather information is continuously written to files, which are transferred, read and inserted into a database at the Universidad Autònoma de Barcelona. From there all the information is available trough a web archive.

Cloud monitor A radiation pyrometer has been installed at the telescope to measure the infrared radiation of the sky, from which the temperature can be concluded. As clouds reflect part of the infrared radiation of the earth, they can be detected with this monitoring tool. The pyrometer is aligned along the axis of the telescope and has a field of view of 2° . The measured temperature is proportional to the thickness

of the clouds. Even high cirrus clouds can be detected. More details on the technical implementation and further results can be found in Fuchs [2005]. The values provided by the pyrometer will be included in the reports of the CC so that they are available for the data check and the analysis.

Lidar As the cloud monitor measures only the existence and thickness of clouds, a **L**ight **D**etection **A**nd **R**anging system (LIDAR) has been installed to measure the differential extinction of the atmosphere from the telescope (2 km a.s.l.) up to 14.5 km a.s.l. The lidar takes not yet data regularly, but results of first measurements can be found in Fuchs [2005].

2.1.9. Optical data

Collaboration members, the group of Tuorla Observatory, operate two optical telescopes on La Palma, which are steered remotely from Tuorla via internet. A 60 cm telescope is used mainly for polarimetry. With the second telescope, a 35 cm Celestron, photometric observations simultaneous to the MAGIC observations are performed. In addition, several blazars are monitored enabling triggers of ToO observations in case of an optical outburst. Apart from having simultaneous optical data for spectral studies, these observations provide information about the atmospheric conditions. Therefore, the result files with the optical magnitudes are transferred to the Würzburg data center. The values are inserted into the database. By comparison to the real magnitude, a relative extinction measurement can be performed providing an independent check of the atmospheric conditions.

2.2. Data management

Before the new generation of Cherenkov telescopes started operation, only few sources were known in the TeV energy range (see figure 1.4, upper plot). By lowering the energy threshold, the discovery of many new sources have been expected. After three years of observations with the new generation of Cherenkov telescopes the number of sources has reached 59 (see figure 1.4, lower plot).

This means not only more data, but also that there are more data samples due to the larger number of observed sources. In addition, the data rate increases due to the power law spectrum of the background. To guarantee consistent results, all data have to be analyzed in the same way. The big amount of data and files make automatic processing mandatory.

2.2.1. Data taking

In this section, some details on data taking will be explained: the different types of data, the different observation modes and some remarks on moon observation.

2. The MAGIC experiment

Data Events recorded by the DAQ can be classified in three types: calibration, pedestal and data events. The first have been explained in section 2.1.5. When taking pedestal events, the read out is triggered artificially with 500 Hz to measure the offset, which has to be subtracted from the signal. Both types of events are needed to process the data events. To distinguish such events in the software, they are flagged by the DAQ (trigger pattern). In the beginning of an observation, one run with 1000 pedestal events and one run with 5000 calibration events are taken. In case of an GRB alert, data taking is started of course immediately, and the calibration and pedestal run are taken later on. Apart from that, there is the possibility to take interleaved pedestal and calibration events, which is done since November 2004 for calibration and February 2007 for pedestal events. One block of data taking consist of a pedestal and a calibration run in the beginning and then a sequence of data runs. To be able to update the calibration not only interleaved calibration events are taken, but also a pedestal and calibration run every hour. Such a block of pedestal, calibration and data runs is called sequence.

Observation modes The MAGIC telescope observes in two different modes, the so-called On-Off mode and the so-called Wobble mode.

In the On-Off mode the source is observed such that it is in the center of the camera. The background is determined from a dedicated Off measurement, where a position in the sky with similar star field and **Night Sky Background (NSB)** is observed in the center of the camera.

The Wobble mode does not need a dedicated Off measurement, as the source is observed in a position 0.4° away from the camera center and the background can be determined from the so-called anti source position, which at 0.4° symmetric to the camera center. It is possible to take more than one Off position. Another method takes a ring around the center of the camera, of which everything but the source position is used for the background estimation [Bretz, 2005].

While for the Wobble mode no Off data is needed, the data selection for data taken in On mode is crucial. The chosen Off data has to have the same data quality, e.g. same PSF. To avoid spending too much data taking time for Off observations, the Off data is used for different sources. One just has to make sure that the data quality and telescope performance is the same for On and Off data.

The sensitivity for Wobble mode is less than 20% lower than for On observations [Bretz et al., 2005], but the observation time is longer as no Off observations are needed. The advantage of Wobble mode is that by definition the data quality and telescope performance is the same for On and Off data. For Wobble data, only inhomogeneities in the camera can cause problems.

Moon observations As explained in section 2.1.4, the MAGIC telescope is able to observe during moonlight due to the relatively low HV at the last dynode of the PMTs. To observe during moonlight no change in the HV settings is needed, but only the discriminator threshold of the trigger (see section 2.1.6) has to be adapted.

The increase of the background light due to the presence of the Moon depends on various factors including the source zenith angle, Moon phase, angular distance to the Moon, Moon zenith angle, and atmospheric composition as well as the aerosol content of the atmosphere [Albert et al., 2007c].

Although observations during moonlight are possible, there are a few days around full moon, when no observations are possible. The time between two full moons is called observation period.

2.2.2. Data flow

The information and data stored by the subsystems described in section 2.1 have to be combined into one data stream. As the amount of data is too big to process everything on-site, all files are transferred to the MAGIC data centers, i.e. to **Port d'Informació Científica** (PIC) in Barcelona and to the data center in Würzburg. In the following, the data stream for the Würzburg data center will be described.

Amount of data The two different FADC system, explained in section 2.1.7, produce different amounts of data: For the first FADC system, there are in average about 480 files per night, where about one third each are from raw files, cc files and caco files. AMC and drive have only a few files per night. For the drive system, there are more files in case there is data for the pointing model. When data is taken and AMC adjusts are performed the number of AMC log files is around 20.

As the event size is five times higher for the current FADC system than for the previous one, the number of raw files has increased by a factor of five since the commissioning of the new system. With the number of raw files, the total amount of data per night increased. The file size remained the same. Since the CC and the CaCo write one file per run, their number increased by the same factor. The number of the other subsystem log files is untouched by this change.

While for the old FADC system the amount of data per night was up to 170 GB depending on the weather, the season and the phase of the moon, with an average of about 90 GB, the amount is five times higher for the new system. This leads to 1.5 TB (old system) and 7.5 TB (new system) per month. These numbers do not take into account the compression of the data. As stated in table 2.1 the files of the new system can be compressed by about 60 %, while this number is 30 % to 40 % for raw data of the old system. The sizes of the subsystem log files are negligible, as the CC files have about 100 MB, the CaCo files about 270 MB and the AMC and drive files less than 10 MB per night in average.

Data transfer After gathering all files, which have to be transferred, on one machine in La Palma, small files, i.e. the subsystem files, are transferred directly from La Palma to the data center in Würzburg. Therefore, a `rsync`^a script is launched several times a day. As

^asynchronizing tool provided with standard linux distribution

2. The MAGIC experiment

soon as a file is copied without error, which is ensured by checking the md5 checksum^b, a script in the data center takes care of the correct processing. Depending on the information the file contains, it is either archived or processed further. Some information is already retrieved and inserted into a database before copying the file to its final destination in the data center.

The bigger files, the raw data files, are either copied via internet or sent by tape from La Palma to the data centers. Which option is chosen depends on the amount of raw data and the band width of the internet line from La Palma to central Europe. As the raw data should be accessible in more than only one place, and to have a backup, the raw data is transferred to both data centers (Würzburg and PIC). Due to the limited band width to and from the MAGIC site, the data is transferred from La Palma to PIC and from there to Würzburg. When not all data can be sent via internet, the remaining files are written to tape in La Palma and the tapes are sent via mail to PIC and Würzburg. In the beginning, in 2003, tapes were sent to Würzburg, then the line to La Palma was upgrade so that the transfer of the full amount of data via internet was possible. Since February 2007 the data is sent again via tape, as the new FADCs produce a bigger amount of data. After an upgrade of the line from the Canary Islands to Spain, which is planned for the next years, the transfer may be possible via internet again.

Storage and archiving No matter which way the files arrive in the data center in Würzburg, as soon as they have been copied successfully, they are moved into a structure which is optimized on the one hand for the handling with the software, on the other hand for the handling of the file system. Log files are archived. Files containing data or other useful information, e.g. about the status of a subsystem during data taking, are stored and further processed in the automatic analysis. For optimal use of the storage capacity, the raw data files are compressed with gzip^c.

The layout of the data center and its requirements on the data processing and the automation concept will be explained in the next section.

2.2.3. Data center

When the efforts to automate the data processing were started, the data center in Würzburg consisted of one server with a 6 TB disk array. Beginning of 2005, a new system with 15 TB SATA disks managed by a Veritas file system and eight 64-bit computing machines (16 CPUs) were installed. In addition, a tape library with 40 storage slots and two tape drives was included in this system. Middle of 2006, the system was upgraded. The tape library (upgraded to 80 storage slots and three drives), the SATA disk array (upgraded from 15 TB to 23 TB) and a new 3 TB fiber channel disk array were combined in a SAMFS^d. For computing four 32-bit and 27 64-bit CPUs were available. Beginning of 2008, another

^bmd5sum: tool to calculate and verify md5 hashes, provided with standard linux distribution

^cGNU zip: program used for file compression

^dStorage Archive Manager file system, Sun Microsystems, Inc.

upgrade with a L1400 tape library and another 8 TB of disk space enhanced the storage capacity. In addition, now 40 CPUs are available. To distribute the jobs to this computing cluster, the queueing system condor is used [Condor Team, 2008]. In the future Grid^e may be used, especially for the production and processing of the simulated data.

2.2.4. Analysis steps

A detailed description of the MAGIC analysis can be found in Bretz [2006]. In the following, just the important steps are listed to point out what has to be accomplished by the automatic analysis. The names of the programs are mentioned, as they are needed later on in the explanation of the automation concept.

The concept of the **M**AGIC **A**nalysis and **R**econstruction **S**oftware (MARS), which is based on the root-package [www-09], is explained in Bretz [2006]. There are two version of MARS in the MAGIC collaboration. This work refers to the version used and developed in the Würzburg data center (Mars V2.0).

In the following the steps of the automatic analysis performed in the Würzburg data center are explained. The first steps can be done already before the raw data files are available. As soon as the run information from the CC files has been inserted into the database, the runs are grouped to sequences. When the raw data files arrive in the data center, the data is calibrated. Next the image cleaning is done and the image parameters are calculated. Before the background suppression is done, the sequences are grouped to data sets to be able to analyze data of several nights together. This has to be done manually, as the data has different quality and maybe different observation modes. If a signal is found, a spectrum can be calculated.

In the following the single steps are described. The used programs, scripts and root macros are explained in tables B.1, B.3 and B.2

Run selection and data check Part of the data check on run basis can be done already as soon as the run information is available in the database. Runs with less than ten events, technical runs, test runs, etc. are excluded from the automatic data analysis. This exclusions are done automatically. In addition, there is the possibility to exclude runs manually, if they are known to have bad quality or a problem, e.g. written in electronic runbook.

After the arrival of the raw files, some additional checks are performed, e.g. verifying the integrity of the files. In case additional problematic runs are found, these runs have to be excluded from the sequences possibly already built (see next item).

Due to the diversity of available information (run information, run books, raw files), several programs share the data checking task, namely the scripts *dodatacheck* and *doexclusions*, which launch the root macros and programs *filldotraw.C*, *sinope* (**S**Imple **N**on **O**nline **P**ulse **E**valuation), *fillsinope.C* and *doexclusions.C*.

^e<http://www.gac-grid.org/>

2. The MAGIC experiment

Sequence building As the raw data itself is not needed to group runs to sequences, this step can be done as soon as the run information is available in the database. It is done by a root macro named *buildsequenceentries.C* launched by the shell script *buildsequenceentries*.

File availability Before the sequences can be processed automatically, the availability of the raw and the needed subsystem files has to be checked, which is done by *checkfileavail.C* launched by *checkfilesforsequenceavail*.

Calibration and signal extraction From the pedestal run (see section 2.2.1) and from the first events of the data runs, the pedestal is calculated. This is needed for the calculation of the calibration factors, which is done next with the calibration events from the calibration run. The pedestal is updated with values calculated either from the data events or from interleaved pedestal events. The calibration factors are updated by calculations from the interleaved calibration events.

When the calibration factors have been calculated, they are applied to the signal extracted from the data events. More about the signal extraction and the methods used there can be found in Albert et al. [2006c].

Apart from the calibration and signal extraction the program *callisto* (**CAL**ibrate **L**ight **S**ignals and **T**ime **O**ffsets) takes care of the treatment of bad pixels, described in Bretz [2006] and Rügamer [2006].

In the automatic analysis, the calibration step includes the merging of the subsystem information into the calibrated files. As there is one raw file, one CC report file and one camera currents file per run, this step is performed on run basis with the program *merpp* (**ME**rging and **P**reprocessing **P**rogram).

Callisto and *merpp* are launched by the script *runcallisto*. In a next step in the automatic analysis, the results of the calibration, e.g. information about bad pixels, are filled into the database (*fillcalib.C* and *fillsignal.C*, launched by *fillcallisto*).

The size of the calibrated files is about one third of the size of raw data files for the old FADCs. For the new FADCs, the size of the calibrated files remains the same.

Calculation of image parameters After having calibrated the signals including the arrival time of the pulses, a software trigger, which rebuilds the trigger described in section 2.1.6 in the software, is applied to remove events accidentally triggered [Bretz, 2006]. Next the noise in the image is removed so that only the pixels belonging to the shower remain. There are different methods for this so-called image cleaning [Bretz, 2006]. From the cleaned image the image parameter are calculated. While the classical image parameters [Hillas, 1985] were explained in section 1.4, more detailed information on additional image parameters can be found in Bretz [2006]. Apart from that, the muon analysis is done in this step performed by the program *star* (**ST**andard **A**nalysis and **R**econstruction, launched by *runstar*). Detailed information on the functionality and results of this analysis based on the shower images produced by single muons can be found in Meyer [2008]. The important results are values for the optical PSF and a factor for the absolute light calibration.

When *star* has been done successfully, interesting results like the rate after cleaning, some muon parameters and some information from the subsystems, e.g. trigger rate, temperature, the relative mispointing (see section 2.1.2), which are available after they have been merged into the files after the calibration of the data, are filled into the database by the root macro *fillstar.C* launched by the script *fillstar*. Compared to the raw and calibrated data, the size of the image parameter files is negligible.

Building of data sets As the data of one source is taken in several nights, depending on the amount of hours even in several periods, there are many sequences per source, which have to be grouped together to data sets. Depending on the observation mode (see section 2.2.1) this needs different efforts. For Wobble data, checks on the data quality and the telescope performance have to be done, to make sure that the data set does not contain data with bad quality, e.g. bad weather or camera inhomogeneities, and all sequences were taken with the same telescope performance, e.g. same PSF. For the data taken in On-Off mode, the data set building requires in addition checks, that the On and Off data has not only the same data quality and telescope performance, but also the same zenith angle and night sky background. More information on the quality parameters, that have to be checked, can be found in section 2.2.5.

As it is difficult to do all these checks automatically, this step is still done manually with the help of some tools, which will be in section 3.3.4. In addition to that, there are data sets for different purposes. Data sets for variability studies have different requirements than those for a spectrum study or for a detection. While for light curves small data sets are needed, spectral studies require enough statistics.

Background suppression The background suppression is done on data set basis by the program *ganymed* (**G**ammas **A**re **N**ow **Y**our **M**ost **E**xciting **D**iscovery), launched by the script *run_ganymed*. For the automatic analysis a file availability check (*checkstardone.C* launched by *checkstardone*) is performed to make sure that the image parameter files of all sequences belonging to the data set are available.

To separate the gamma candidates from the background consisting of hadronic showers and muons (see section 1.4), there are different methods implemented in MARS. It is not only possible to use static or dynamical cuts, but also statistical learning methods like neural net or random forest [Albert et al., 2007c; Kolodziejcki, 2005].

For the automatic analysis, robust, dynamical cuts have been developed [Riegel, 2005]. It is planned to implement the usage of random forest in parallel, as soon as this method has been studied in detail and provides a robust background suppression.

For completeness the program doing the spectrum calculation, *sponde* (**S**pectrum **O**N **D**Emand) is mentioned here. As the step needs simulated data (see section 2.2.6) for the reconstruction of the energy of the primary particle, which is not yet produced and processed fully automatic, also the determination of the spectrum has not been automated up to now. But there are some scripts performing the processing, i.e. *callisto* and *star*, of the simulated data. Depending on the data quality and telescope performance, simulated data

2. The MAGIC experiment

with the same conditions are needed. A script has been provided choosing the simulated data on run basis and grouping it to sequences and data sets as needed for the analysis. Apart from that, a script has been developed, providing spectra produced with different sets of cuts and different simulated spectra to study the systematic errors of the analysis in the spectrum.

2.2.5. Data quality issues

In this section, some issues affecting the data quality and some parameters describing it will be explained. These parameters are used for the data check when building data sets. There are two different types of influences on the data quality. On the one hand the data quality depends on the performance of the subsystems of the telescope, and on the other hand there are weather conditions, which can cause data with bad quality.

Telescope performance While the observer has no influence on the weather, the telescope performance can be monitored. When the data check reveals problems in the hardware, they can be solved.

As some problems cannot be solved instantaneously, they have to be faced in the analysis and solutions have to be found to handle them in the software. To identify and quantify the problems, several quality parameters have been developed. The most important ones are listed next. Many of them are calculated independently for the inner and outer camera, on the one hand as the pixels have different sizes, and on the other hand as only the inner camera is in the trigger.

Pulse position The position of the pulse is important for the signal extraction, especially for the old FADC system (see section 2.1.7), where 15 FADC slices are recorded. If a pulse is coming too early or too late, the signal cannot be extracted properly. The limits depend to some extent on the extractor and the extraction window.

As the trigger for calibration events is done differently than for data events (see section 2.1.5, the problem of too early or too late pulses can appear for data and calibration independently. This applies also for different regions in the camera depending on the time synchronization of the trigger (see section 2.1.6).

Mean pedestal RMS As the NSB light adds noise to the background, it increases the RMS of the pedestal (see section 2.2.1). For each sequence, the mean of the pedestal RMS is calculated for the inner and the outer camera.

Although the data is flagged, whether it was taken during moonlight or twilight, the mean pedestal rms gives a better representation of this information, as the NSB light level changes only then remarkable, when the moon rises above the mountain and not yet, when it rises above the horizon.

Apart from indicating the level of NSB light, extrinsic influences, like light from cars coming down or driving up the mountain, can also be seen in the mean pedestal RMS. Since for example a light flash from a car can fake a signal, this has to be

taken into account in the data check.

As a higher noise level produces more current, the mean currents show the same behavior as the mean pedestal RMS.

Bad pixels The calculation of the calibration constants may fail for individual pixels. The different reasons of failure are classified. Some make it impossible to calculate a calibration constant. Such pixels are called 'unsuitable'. If the results can be calculated, but some quality criteria is not fulfilled, the pixels are flagged as 'unreliable'. Both types of pixels are marked by the calibration and when calibrating the data the unsuitable pixels are interpolated by the signals and times of the surrounding pixels. If there is a cluster of unsuitable pixels, this can result in pixels which are not calibrated at all and a hole in the camera remains, where no signal is extracted. Such holes in the signal distribution can influence the background suppression. Consequently, sequences with such holes should be rejected.

Rate after cleaning As not all events survive software trigger and image cleaning, the rate after cleaning is lower than the mean trigger rate. Unaffected by artificial triggers, the pure shower rate remains. Therefore this rate is stable apart from extrinsic influences like weather.

Relative on-time By comparing the on-time after image cleaning and the uptime of all runs, a value for the relative on-time can be calculated. In case this value differs from the expected one, the reason for this has to be checked.

Non-physical events Although the software trigger removes accidentally triggered events, some non physical events survive. There are several types known with different characteristics. Due to the characteristics part of the events can be removed by simple cuts before the background suppression. One type are events, where a whole sector of the camera triggers. Another type are events, where one or a cluster of pixels triggers and saturates. These events are very small in WIDTH and LENGTH, but have a big SIZE. With the different telescope setups, their characteristic changed, requiring a careful study to remove as many of them as possible.

Camera inhomogeneity When looking at the distribution of the center of gravity of the showers, it turned out that the acceptance of the camera is inhomogeneous for some data. To describe this inhomogeneity, the rms of the fraction of the number of showers per sector is calculated. For the affected data, there are more showers in some sectors of the camera than in others. To find out where this inhomogeneity comes from, other plots were studied. In the plot of the pulse position similar distributions were found: in some regions of the camera the pulses come quite early and in others quite late. It seems that in a certain region of the camera, the pulses are so early that they are out of the extraction window. This results in showers that are recorded only partly or not at all, which leads to the described inhomogeneity. The reason for this might be an inaccurate synchronization of the delays in the trigger.

The effect of this inhomogeneity on the results is discussed in section 4.2.4.

2. The MAGIC experiment

PSF As the optical PSF has an impact on the reconstructed shape and structure of the showers, this value should be similar for all data combined in one set to make sure that appropriate simulated data can be used for the energy reconstruction. The PSF can be calculated by analyzing the triggered muon showers.

Other muon parameters Apart from the PSF some other parameter are calculated from the muon showers. From the ratio between the size of the data event and a simulated event, the values for the absolute calibration can be retrieved.

To get reliable values from the muon analysis the number of muons in a sequence should be larger than 180.

From the muon rate, conclusions on the weather can be made, but again no quantitative result is possible, as the light of the analyzed muons images comes from a different height compared to that of gamma showers.

Information from starguider As explained in section 2.1.2, the starguider provides some numbers calculated from the CCD pictures. From the number of identified spots and the number of correlated stars conclusions on the weather, i.e. clouds, can be drawn. The values of the relative mispointing from the starguider and the data for the pointing model show if there was some mispointing or misfocusing and they are needed to calculate a correction.

Extrinsic influences Outside influences on shower images come mainly from weather and NSB light. Weather includes not only clouds or fog, but also calima, which is sanddust in the air coming from the Sahara.

Weather The user has several possibilities to find out if the data is affected by bad weather.

In the runbook the shift-crew writes information about the status of the weather, and the weather station provides some values like temperature and humidity. If there is a closed cloud cover or a humidity of 100% at the site, no data is taken. In case, there are only few clouds or a thin layer, data is taken, but its quality is affected. Measurements of the atmosphere can be done with the lidar and cloud monitor. While the cloud monitor provides only information about the presence of clouds, the lidar measures also their vertical distribution. From the lidar, no measurements are available up to now, and also the data of the cloud monitor do not yet enter the normal data flow. But also the number of identified spots and correlated stars of the starguider can give a hint, as they are reduced when clouds are present. The rate after image cleaning is lower in case of thin clouds or calima.

Data with lower rate can be analyzed, but for the flux calculation in the spectrum it is difficult to estimate the effect of thin clouds or calima, especially as the light of the showers passes only part of the atmosphere while extinction measurements with optical telescopes take into account the whole atmosphere.

Night sky background light When building data sets, the NSB light has to be considered. The level of the diffuse NSB light has to be approximately the same for all sequences.

In On-Off observation mode one should in addition ensure that the star-field in the Off region is similar to that in the On region.

Apart from moon or twilight, depending on the observation time, and the star field, depending on the observed source position, zodiacal light and calima or haze may influence the level of the diffuse NSB light. While the zodiacal light is restricted to a certain region of the local sky, haze or calima increase the level by scattering light, which is relevant especially for observations during moon or twilight.

The level of NSB light corresponds to the pedestal, which means that the average of the pedestal rms over the camera is a good value to select data, when building data sets. In the database it is available as 'mean pedestal rms inner'.

Saharan Air Layer The **Saharan Air Layer** (SAL), also known as calima, is a layer in the atmosphere between 1.5 km and 5.5 km a.s.l., in which sand-dust from the Sahara is transported from Africa in western direction [Dunion and Velden, 2004]. Consequently, La Palma is affected by this meteorological phenomenon, as shown in figure 2.5. Data affected by calima has usually a lower rate, as the light traveling through the SAL gets scattered and less light reaches the telescope. The detected light from muons is less affected by calima, as it is emitted only few hundred meter above the telescope. As calima is visible also by eye, comments in the runbook can give a hint to find out, if data is affected by calima. Apart from that, extinction measurements from optical telescopes show the amount of atmospheric absorption. From the **Carlsberg Meridian Telescope** (CMT) extinction measurements are available. For each night an extinction value is given for the zenith [Carlsberg Meridian Telescope, 2007]. Also from the KVA (see section 2.1.9) measurements are available allowing for the calculation of the extinction.

While the NSB light influences mainly the threshold of the analysis, the weather influences the rate. This effect has to be considered in the flux calculation.

2.2.6. Simulated data

In Cherenkov astronomy, an energy calibration of the detector is not feasible, as there is no possibility to generate a shower of known energy. For this reason, simulated data is needed to reconstruct the energy.

The energy of the primary particle of a shower is reconstructed by comparing the image to that of simulated data, where the energy is known. As the shower image depends on weather conditions, geomagnetic field and telescope performance, e.g. PSF, a simulation adapted to the quality of the analysed data set is required. Not fitting simulated data could affect the shower image, and thus the analysis results, including the energy reconstruction. Consequently, a large pool of simulated data is needed. Especially for long-term monitoring appropriate simulations are mandatory for comparing flux levels and to study spectral changes.

2. The MAGIC experiment

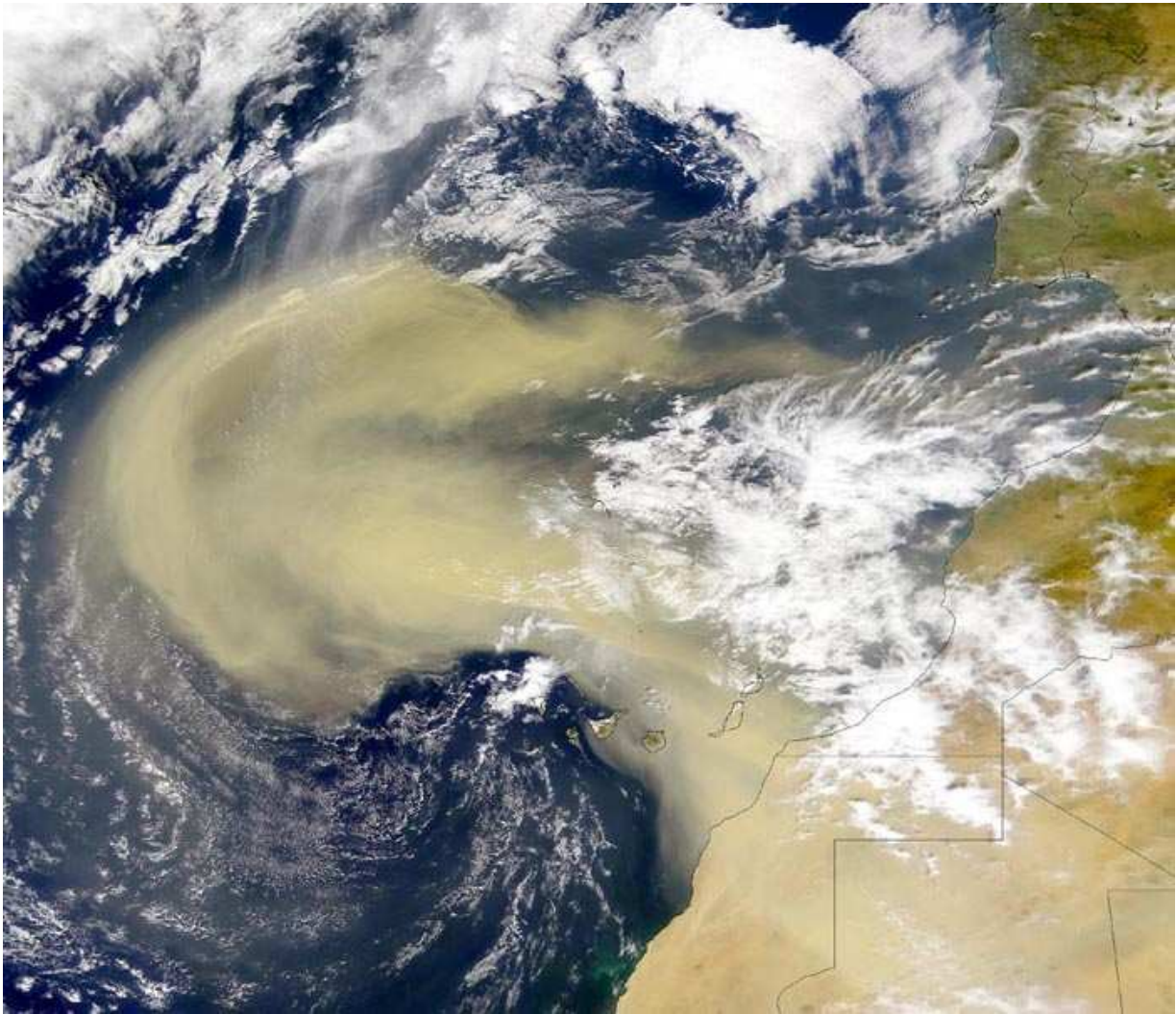


Figure 2.5.: Satellite image of the of the Saharan Air Layer. Credits: NOAA

For MAGIC, up to now not all effects and different settings have been simulated. This compromise had to be made to be able to cope with the amount of simulated data, as the production has not yet been automatized.

Production and processing For simulating the showers in the atmosphere, the **Magic Monte Carlo Simulation** (MMCS, based on CORSIKA [Knapp and Heck, 2004]) is used. The MAGIC mirror is simulated with the program *reflector* and the MAGIC camera with *camera*.

In the data center in Würzburg, all available simulated data are processed automatically. The files are treated equally to normal data and processed in the analysis chain up to image parameters. To allow for this in MARS, the naming of the files has been adapted.

For convenience for the users, the files names have been chosen such that they also give information about particle type, zenith angle and PSF.

Available set of simulated data For MAGIC, a set of simulated data with different zenith angles and PSFs is available. Up to now, different atmospheric conditions, which could be taken into account using different atmospheric models [Haffke, 2007], are neglected. For the simulations of the showers in the atmosphere in CORSIKA, the atmospheric model *US standard* is used. The difference in the atmospheric models, result in systematic underestimation of the energy of about 5% [Curtef et al., 2007]. For the azimuth, which is important for geomagnetic effects [Commichau, 2007], not the whole range but only two distinct azimuth angles are simulated. Effects like the inhomogeneous camera are also not considered in the simulation.

2. *The MAGIC experiment*

3. Concept for the automatic analysis

*Pro Monat viele Terabyte
Da hilft keine Handarbeit
Automatisierung heißt der Trick
Endlich Zeit für die Physik
Ein Konzept, verwendbar nach Belieben
Flexibilität ist groß geschrieben*
— Daniela Dorner.

As shown before, several Terabyte of data are recorded every month by the DAQ. To handle this enormous amount of data and the large number of files, a concept for automatic management and processing of data has been developed. Based on this, an automatic analysis has been realized for the MAGIC experiment.

After summarizing the requirements, the concept and its realization are explained. The results achieved with the automation package are shown and further features and achievements are discussed.

3.1. Requirements

With the new generation of Cherenkov telescopes, the amount of data has reached a dimension that cannot be handled any more by processing all files manually. An automatic procedure has become mandatory to ensure that all data is processed failsafe and treated equally. In addition, changing observation conditions require a monitoring of the data quality. By analyzing all data uniformly, long term studies of quality parameters become feasible, facilitating performance checks and revealing hardware problems.

In the previous chapter, the initial situation of the data processing has been shown. Each night about 500 files (about 2500 for the new FADC system) of different file types are produced. An automation concept has to provide tools managing this large number of files and big amount of data automatically and failsafe.

Apart from that, a future-oriented and pioneering experiment like MAGIC has some more demands on an automation concept. Not only due to enhancement or change of technologies, which accompanies changing hardware, the software is continuously modified. To analyze low energy events, new algorithms and methods are developed. Therefore an automation concept should allow for easy re-processing of all data with a new software version.

In addition, 'quick-look' results for all data and an easy handling of the results are required to realize possible detections quickly in order to schedule further observations in time and

3. Concept for the automatic analysis

trigger **Target-of-Opportunity** (ToO) observations of other telescopes.

3.2. Realization

Since beginning of 2004, a concept for automation has been developed and an automation package, consisting of root macros, shell and php scripts, has been designed for MAGIC and implemented in the MARS package.

Core part of the concept is a MySQL database [MySQL AB, 1997-2008], containing the status of the analysis, information about the data and results. The interaction between analysis software and database is done with shell scripts and root macros. To provide the user with results and information, including plots, root macros and php scripts have been written.

In this section, first the key idea of the concept is presented, then the database, the scripts and the configuration of the automation package are explained.

For illustration and better understanding, the calibration is used as example. In the automatic analysis, this step is composed of callisto (main step: called once for the whole sequence) and merpp update (sub-steps: called twice for each data run in the sequence, once for the CC report file and once for the CaCo currents file), resulting in a minimum of three calls per sequence.

3.2.1. Concept

The main idea of the concept is very simple. The status of the analysis is stored in a database, in which a status column for each step of the analysis is available. Consequently, only a script is needed that

1. queries from the database, for which data, the step has to be done
2. executes the step
3. inserts the new status into the database

A scheme of this core part is shown in figure 3.1. The script is called by a cronjob. The possible executed steps, either reading, processing and writing data or interaction with the database, are shown with dotted arrows.

In the next sections, the layout of the database, the scripts and the configuration of the software are described.

3.2.2. Status tables

The columns for the single steps are grouped in so-called status tables:

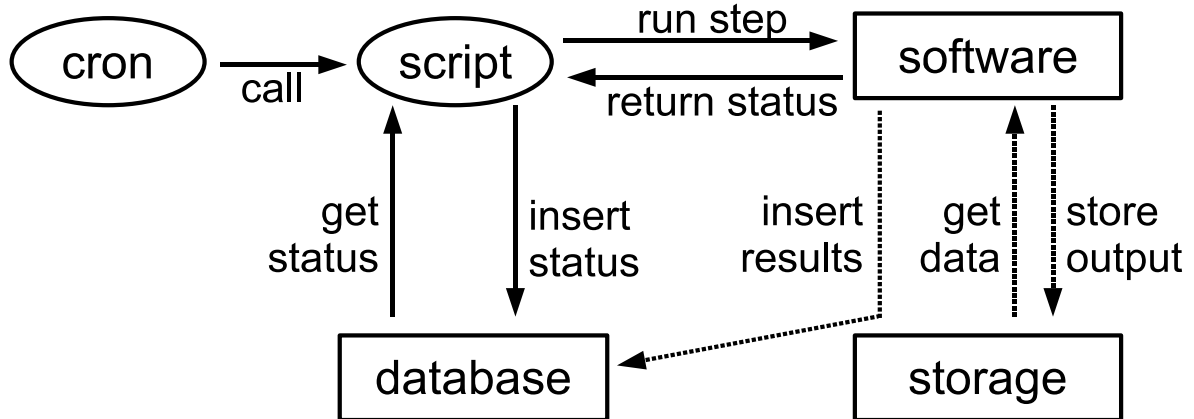


Figure 3.1.: Scheme of the automation concept.

Timestamp	Meaning
NULL	the step is not done
2007-03-01 11:00:16	example: step has been finished successfully at the given time
1970-01-01 00:00:00	the step does not have to be done

Table 3.1.: Overview of possible entries for an analysis step and their meaning.

Status columns Some steps in the chain of the automatic analysis have to be done per night, others per run, others per sequence and others per data set. Therefore, four status tables have been created. Depending on which basis a step has to be done, a column of the type *TIMESTAMP* in the according status table is implemented. The column either contains the date, when the step has been done, or nothing, i.e. NULL (see table 3.1). For special cases, when a step has to be done only for certain data, the timestamp '1970-01-01 00:00:00' is inserted, if the step is not needed. Looking to the entry, e.g. for a sequence, it is easy to see at what stage of the analysis the sequence is, e.g. if all needed files are already available in the data center, if the sequence is already calibrated or if the image parameters have already been calculated.

This concept provides an easy possibility to redo a step: The according column, e.g. the one for calibration, has to be set to NULL, e.g. for the sequence one wants to reanalyze (re-calibrate). When a step is finished the subsequent step is set to NULL to make sure that all available result files of one sequence are consistent.

Failure columns To provide more information in case of failure, each status table has five additional columns. Two columns contain start- and stop-time. The latter is only filled in case of failure. When a job is finished successfully the start-time is set back to NULL. Therefore, it is not only possible to realize when a job failed, but also when it hangs or crashed, e.g. if a power cut occurs. In this case, only a start time would be available in the

3. Concept for the automatic analysis

Column	Meaning
fStartTime	start-time, only not NULL if a job runs, hangs, crashed or failed
fFailedTime	stop-time, only not NULL if a job failed
fFailedCode	failure code, indicating the step which failed
fFailedCodeAdd	additional information at which e.g. run or sequence a step failed
fReturnCode	return value of failed program, depends on fFailedCode

Table 3.2.: Status tables: Overview of columns containing information about job failure.

database, but the job would not be running any more.

Apart from this timing information, there are three columns containing more information about the type of failure. The first column contains the return value of the program. The programs have been adapted to return different values depending on the kind of error (example see section 3.2.6). The second column contains a code telling which program or macro failed. This is necessary, as some steps include several programs, e.g. calibration includes also merging subsystem data into the files. In addition, this facilitates debugging, as it is more easily visible from the database which step failed. The third column contains only information, if a step includes sub-steps, done on a different basis, like the merpping of single runs in case of the calibration. So if for example merpping fails for one run, this run number is inserted into this column.

The content of those five columns is summarized in table 3.2.

3.2.3. Database

In appendix B the explicit structure of the database (tables B.8- B.45) and an explanation on the table content are presented. In the following, only the different types of tables are outlined. To classify the tables an identifier is given in []. In general, tables containing information are marked with [I].

Initial information [i] Information coming directly from the telescope site. In the case of MAGIC data, this is the table containing run information coming from the CC.

Information from processing [p] Information obtained during data processing. For MAGIC these are tables containing information and results generated when processing runs and building and processing sequences and data sets.

Tables with reappearing entries [K] Information that reappears and is outsourced in extra tables for technical reasons. For MAGIC several entries in the tables containing initial and processing information, e.g. the source name, reappear for different runs, sequences or data sets. To avoid storing such information many times, it is stored only once in an extra table and represented by a key in the information tables. This saves not only disk space, but also make the database access faster. Apart from that,

this provides the possibility to store additional information, e.g. an explanation for a certain HV setting in an additional column in the extra table.

Results from processing [R] Analysis results from various analysis steps, i.e. calibration, image cleaning, calculation of image parameters, muon analysis and background suppression. To some extent these tables also contain information from the subsystems, e.g. starguider, as this information is not merged into the files until calibrating the data.

Additional information [a] Information not needed for and not coming from the analysis. In the case of MAGIC, these are mainly tables containing additional information about the observed sources.

Status information [S] Information about the status of the analysis, see section 3.2.2. For MAGIC, there are four status tables: *SequenceBuildStatus*, *RunProcessStatus*, *SequenceProcessStatus* and *DataSetProcessStatus*.

In table B.7 all tables of the MAGIC database are classified according to this scheme.

3.2.4. Scripts

The interaction between database and analysis software is done with scripts. An overview of all scripts can be found in table B.1. In general, the automatic analysis includes several shell scripts, some for process and data management tasks and one for each step in the analysis.

Analysis steps These scripts have an identical structure as explained in section 3.2.1: First, the script queries from the database for which data, i.e. for which night, run, sequence or dataset, the step has to be done. Second, the step is executed and third, the return status is inserted into the database, using the coding explained in section 3.2.2. The big number of scripts is necessary due to the fact that different steps have different requirements, e.g. the script executing the calibration performs in addition the merpping of the subsystem data into the files and therefore a more complex script is needed.

For the interaction with the database some functions have been implemented.

Process management In addition to that, the analysis steps require different amounts of computing resources, making requirements at which frequency and how the according scripts are started, i.e. for one sequence or for all in a row. Therefore the automation package provides additional scripts ensuring that the computing power of the data center is optimally used. For analysis steps requiring a lot of computing power, either because they have to be executed for example for each run like the data check, or as they take a long time like the calibration, a script named *jobmanager* has been developed starting an appropriate number of jobs depending on the load of the system. Via setup file, the

3. Concept for the automatic analysis

Column	Needs	Influences
fSequenceFileWritten	-	fAllFilesAvail, fCallisto, fFillCallisto, fStar, fFillStar
fAllFilesAvail	fSequenceFileWritten	fCallisto, fFillCallisto, fStar, fFillStar
fCallisto	fSequenceFileWritten, fAllFilesAvail	fFillCallisto, fStar, fFillStar
fFillCallisto	fSequenceFileWritten, fAllFilesAvail, fCallisto	-
fStar	fSequenceFileWritten, fAllFilesAvail, fCallisto	fFillStar
fFillStar	fSequenceFileWritten, fAllFilesAvail, fCallisto, fStar	-

Table 3.3.: Example for dependencies: sequence based steps.

configuration for this script can be changed online, e.g. when new CPUs are added or the system has problems.

For steps which are done for all data in a row, the scripts are executed several times a day. Some of these scripts are preferably executed in a certain order. Therefore, a script named *scriptlauncher* has been developed, which can submit several scripts either at once and in a certain order.

Both, the *jobmanager* and the *scriptlauncher* distribute the jobs they start via the scheduling system condor to different CPUs to use the capacities of the system efficiently.

3.2.5. Configuration and setup

To provide the possibility to run the automation package easily on different systems, for different users or even several times on the same system, it has been equipped with several setup files.

This provides the possibility to make easily a copy of the complete automatic analysis either on another system like in La Palma or at the PIC, or on the same system, e.g. to run tests for a new analysis method on a large amount of data.

The configuration files steer the following parts of the automatic analysis:

Dependencies of the analysis steps One of the core parts of the automation concept is the setup file containing the dependencies of the analysis steps. To provide the scripts with the information on the correct order of the analysis, this resource file contains for each step the information which other steps it influences and on which steps it depends. This ensures that the steps are done in the correct order and it avoids

Column	Indicates
fSequenceFirst	- (primary key)
fSequenceFileWritten	if sequence file is written
fAllFilesAvail	if all files are available
fCallisto	if callisto and merpp updates were successful
fFillCallisto	if insert of calibration results were successful
fStar	if star was successful
fFillStar	if insert of image parameter information was successful
fStartTime	start time, in case job runs, hangs, crashed or failed
fFailedTime	stop time, in case job failed
fFailedCode	program in case of failure
fReturnCode	return code in case of failure
fFailedCodeAdd	run number in case the merpp update failed

Table 3.4.: Example for status table: sequence based steps.

needless attempts of execution, if steps can not be done yet. An example is shown in table 3.3 and illustrated in figure 3.2

Software To provide the information for the database access to the root macros and scripts, a resource file named `sql.rc` is included in the MARS package, while the php scripts get the information from the php script `db.php`.

Scripts Apart from the information for the database access other things like logging and output paths, root version and path, the setup for the *jobmanager* and mailing addresses for error and information messages are defined in an extra setup file for the scripts.

Cron The execution of scripts not started by the *jobmanager* is regulated via cronjob. Apart from that, the path to the MARS version is given here, allowing to have different setups for one user.

3.2.6. Example from the MAGIC analysis

To explain the concrete realization for MAGIC, the sequenced based steps are chosen: The table *SequenceProcessStatus* has the following columns: *fSequenceFileWritten*, *fAllFilesAvail*, *fCallisto*, *fStar*, *fFillCallisto* and *fFillStar*.

As first step the sequence file is written (*fSequenceFileWritten*), extracting the information from the database. To be able to run the analysis, it has to be checked first, if all needed files are available. The first analysis step done on sequence basis is the calibration. Therefore not only the raw data files have to be available, but also the report files from the CC and the current files from the CaCo are needed. To ensure the availability of all files, the execution

3. Concept for the automatic analysis

initial situation:

sequence building has inserted sequence information into database

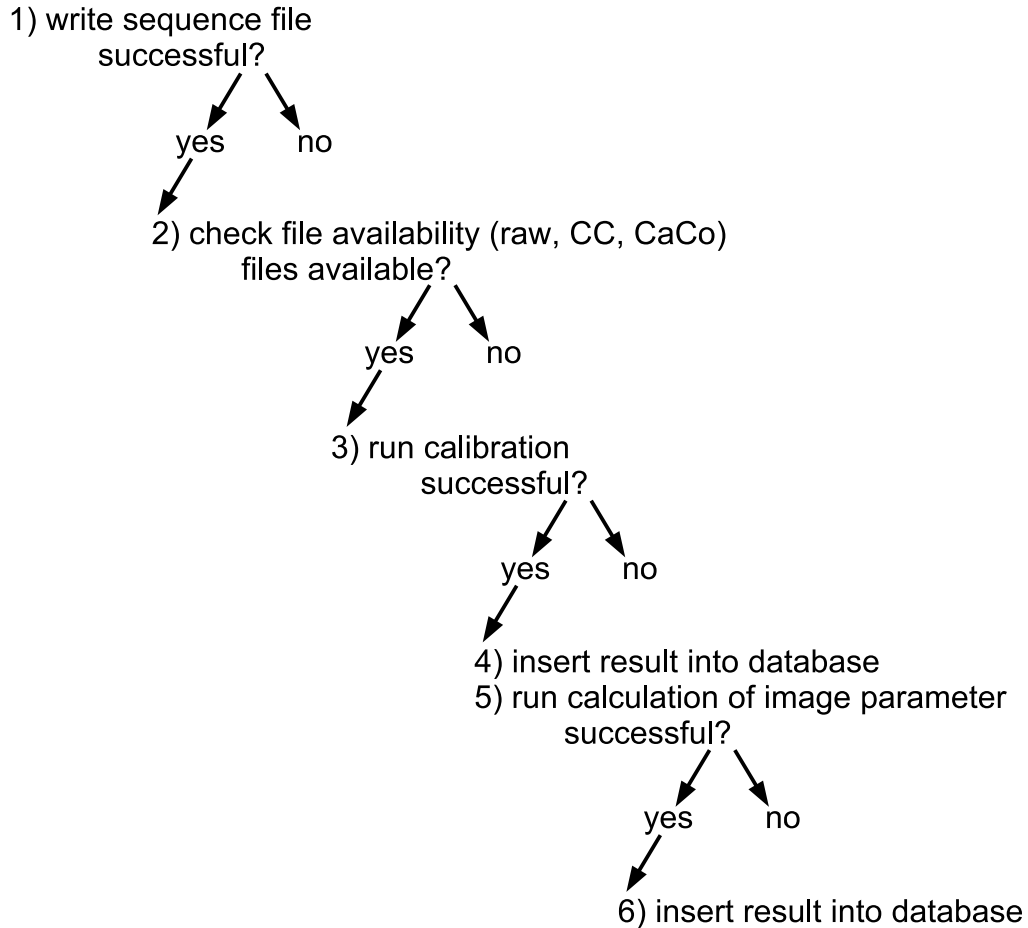


Figure 3.2.: Example for dependencies in the automatic analysis: sequence based steps.

of the script *checkfilesforsequenceavail* precedes the calibration, represented in the database by the column *fAllFilesAvail*. It checks from the table *RunProcessStatus* if all runs listed in the sequence file are available in the data center. Accordingly the dependencies in the setup file are the following: *fAllFilesAvail* has no dependencies, but influences the steps *fCallisto*, *fStar*, *fFillCallisto* and *fFillStar*, i.e. if *fAllFilesAvail* is reset also the other steps have to be reset. When a step is inserted as 'done successfully', the influenced steps are reset. For the next step, the calibration, the dependencies are the following: *fCallisto* depends on *fAllFilesAvail* and influences *fFillCallisto*, *fStar* and *fFillStar*. In case the calibration fails, one can see from *fFailedCode* (see table 3.2) what failed, i.e. if the calibration itself failed or the merpp update with the CC reports or the merpp update with the currents. In case the calibration itself does not work for a sequence the *callisto* returns a different

code depending on the type of error which occurred, e.g. there is a different error code if the calculation of the calibration constants fails or if the calibration of the data cannot be done. In case, one of the merpp updates fails, *fFailedCode* and *fReturnCode* are set accordingly and for *fFailedCodeAdd* the run number is inserted. If the calibration could be done successfully, the next steps are performed automatically. While *fStar* and *fFillCallisto* depend both on *fAllFilesAvail* and *fCallisto*, *fFillCallisto* does not influence any step, but *fStar* influences *fFillStar*.

Runcallisto and *runstar*, the scripts executing the calibration and calculation of image parameter, are launched by the *jobmanager*, while *checkfilesforsequenceavail*, *fillcallisto* and *fillstar* are launched by the *scriptlauncher*.

Apart from the steps on sequence basis, there is an equivalent structure for the steps on data set basis (table *DataSetProcessStatus*) and run basis (table *RunProcessStatus*).

The whole data flow of the automatic analysis is shown in figure B.1.

3.3. Features, achievements and results

Starting from April 2005 the results of the automatic processing are available in the data center in less than 24 hours after the raw files arrive. All data is reprocessed, when a new MARS version is available.

As soon as the concept of data sets had been implemented in MARS the automation of the background suppression was easily added, thanks to the flexibility of the concept. The only step which needs manual interaction is the building of data sets, as different observation modes, different weather conditions and changing telescope performance have to be taken into account for that (see more in section 2.2.4). For these data checking tasks, the automation package provides tools and plots to the user. Furthermore the automation concept has been enhanced by an error coding (see table 3.2) and some features to meet the requirements of the changing hardware and file system in the data center (see section 2.2.3). In the following the main features, achievements and results of the automation package are discussed.

3.3.1. Consistent results for all data

It has been shown that the handling of the large number of files and the automatic processing of the big amount of data is possible [Dorner and Bretz, 2005] and first quick-look results are available one or two days after the raw files arrived in the data center.

Processing all data with a defined software version makes sure that the results are consistent and reproducible. As one of the main goals of the software development is robustness, the provided results are comparable facilitating and accelerating the detection of hardware problems with the help of the monitoring tools described in the next section.

Apart from that, already several discoveries in the 100 GeV energy range could be achieved by this fast and robust automatic analysis package: 1ES 1218+304 [Albert et al., 2006a], PG 1553+113 [Albert et al., 2007] and BL Lac [Albert et al., 2007a].

3. Concept for the automatic analysis

3.3.2. Optical data

As explained in section 2.1.9, the data of optical observations on La Palma is copied to the data center. Like the subsystem files, files with optical data are sorted to the file system and the information is inserted into the database for further use. A relative value for the extinction is calculated and inserted as well into the database.

To study the atmospheric conditions, these values are plotted versus time and provided to the user.

3.3.3. Simulated data

As discussed in section 2.2.6, a large pool of simulated data with different conditions and settings is needed for the analysis. Analog to the data processing, it is planned to use the automation concept for the production of simulated data. First test setups have been made on clusters at the Technische Universität Dortmund and the Universidad Complutense de Madrid. For the automatic production, proper return values of the simulation programmes and some experience with the choice of parameters are still needed.

The aim is to simulate automatically all data needed to analyse the data incoming from the telescope. In addition a web interface providing production on demand for specific user requests is planned.

3.3.4. Tools for monitoring and data selection

The availability of consistent results for all data gives an ideal situation for the monitoring of the data quality. Therefore quality parameters, which are gained in the different analysis steps, are automatically filled into the database. From there, they can be queried by the user either via web interface or with root macros and used not only for monitoring but also for selecting data for an analysis.

In the following, a selection of useful tools provided by the automation package is explained:

runinfo-aio.php From this website, one can query all available information on run basis. Not only the run information from the CC is available, but also the results from the data check. In addition it is shown which rawfiles, CC report files and camera current files are available in the file system in the data center. The user can chose in a menu which of the above mentioned information should be displayed in a table.

queryrbk.php From this website, the user can query all entries of the electronic run book and it is possible to search the runbook entries via date and regular expression.

sequinfo-aio.php Displayed in a table, this website provides all available information about sequences: the information from the building of the sequences, the results from the calibration and the calculation of image parameters. This includes star-guider and weather information and results from the muon analysis. The status of the analysis of the sequences can be queried. Apart from that, the site has an insert

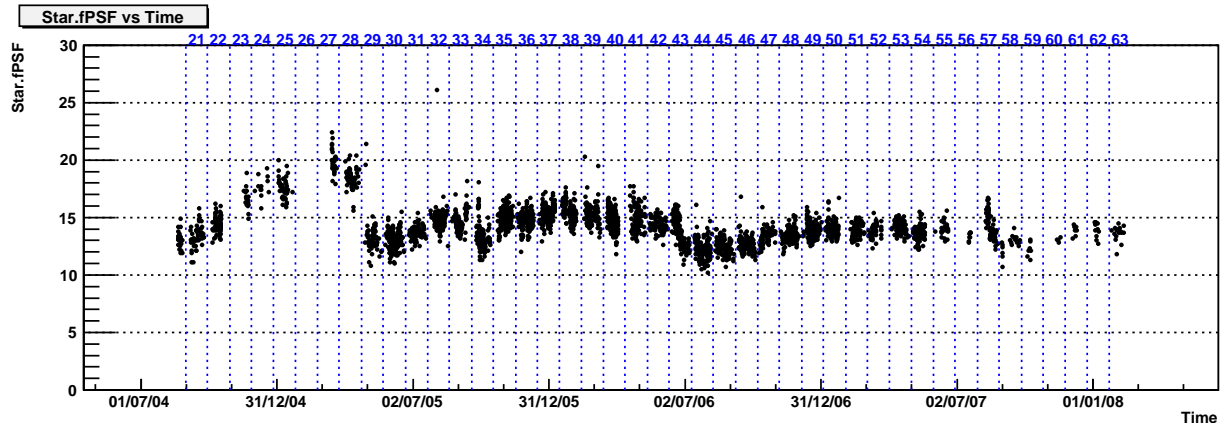


Figure 3.3.: Example for long-term monitoring: Evolution of the optical PSF between August 2004 and February 2008. Observation periods are marked in blue.

mask for limits for the quality parameters, resulting in a colored display of the values in the table from red (unsuitable data) in five steps to green (suitable data). For data which are taken in On-Off observation mode it provides the possibility to search only for On or only for Off data.

datasetinfo-aio.php On this website, the user can query all information about datasets: general information coming from the building of the datasets, status information and results of the background suppression are displayed in a table, e.g. observation mode, zenith distance range, significance of the signal.

builddatasets.php This website provides the possibility to write data sets for the automatic analysis. It has the same functionalities as sequinfo-aio.php. In addition, the user can choose the On and Off sequences for datasets by marking them in the table and insert the data set into the database.

showplots.php On this website, the user can go consecutively over all plots for one sequence, i.e. the result plots of *callisto* and *star*.

plotdb.php This website offers a plotting tool to the user. It is possible to plot all values from the information tables in the database either versus another value or versus the primary of the table, i.e. run, sequence or data set number. Two sets of primaries can be plotted overlaid in different colors. This provides the possibility to compare for example quality parameters of one data set to the ones of all data. Thus, for a On-Off data set, the On sequences can be displayed in one color and the Off sequences in another.

plotdb.C This macro is similar to plotdb.php, but it does not plot the values versus primary, and it plots only the sequence information. For each value the distribution,

3. Concept for the automatic analysis

the distribution versus zenith distance and versus time are plotted in a tab. As example the evolution of the optical PSF is shown in figure 3.3. Like the website, the macro has the possibility to plot values for data sets in color, the On data in blue and the Off data in red. Also plotting the values for a restricted time range, e.g. an observation period is possible.

plotrundb.C Similar to plotdb.C, this macro plots the quality parameter on run basis, i.e. the values from the data check.

plotoptical.C This macro plots the values from the optical data, including plots with daily, weekly, monthly and yearly averages.

plotstat.C The statistics of the automatic sequence processing, including one plot for all data and one for each observation period, can be plotted with this macro.

The root macros are available in the MARS package and the websites can be accessed from www-17.

Plots for the complete data taking time of the MAGIC telescope, produced automatically with the above mentioned tools, facilitate long term studies. For example the output of the macro plotdb.C is available in the web in root and postscript file format and the plots are implemented in a website for easy checking, updated every night. If plots are needed for certain data, e.g. for a period, the user can create the plots himself with the macro plotdb.C or the website plotdb.php depending on the format needed. Especially the parameters of the muon analysis are of big interest, as they allow not only for an absolute calibration, but they can also be used to crosscheck the values for the optical PSF obtained by the AMC.

A detailed study of the muon parameters, done with the output of the automatic analysis, can be found in Meyer [2008].

Furthermore the plots and values from the database can be used to check the telescope performance as for example hardware problems result in changes in the quality parameters. They can be seen more clearly if values for a long period with good statistics are available. Apart from long term studies and automatic quality checks, these tools serve the users when they are selecting data for a dedicated analysis.

3.3.5. Easy tests and re-processing

As explained in section 3.2.2, it is very easy to rerun the whole or part of the analysis for selected data. After the installation of the new software version and the adaption of the setup (path in cronjob), only a query to the database is needed resetting the according columns.

As shown in section 3.2.5, the whole setup for the automation package is stored in three configuration files. This facilitates not only re-processing, but also provides a possibility to do tests for selected data very easily. In addition to the MARS version which should

be tested, a copy of the database and enough disk space to store the analysis result are needed.

This easy duplication of the whole setup, facilitates tests of new algorithms. A new analysis method can be applied to all data. By comparison with the values (database and result plots) from the standard automatic analysis, it can be seen with good statistics if the method improves the results significantly.

Also for testing bug-fixes or general software improvements, this option has already been used in the data center to make sure that the software gives reliable results for all data and handles data with problems properly, e.g. too early pulses.

3.4. Flexibility and future prospects

As explained in section 3.2, each analysis step has one column in one of the status tables. Consequently, for implementing a new step in the automatic analysis chain one only needs to:

1. create column for the step in one of the status tables
2. include dependencies for the step in the dependencies setup file
3. write script executing the step
4. include the new script in the cronjobs

Having such an easy way of implementing new steps, means also that setting up an automatic analysis for a new experiment is very easy and can be done on a short timescale. Such, the presented automation concept lends itself for being used in the future experiments like CTA or DWARF, but can be used also for other experiments. An additional advantage is that it is already implemented in the software package MARS which is based on a flexible concept (Bretz [2006]) and can easily be adapted for any event based experiment.

An important advantage of this automation package is that it saves a lot of time, as the implementation of new steps is fast and easy. In addition the major part of the analysis is done automatically. Such, the physicist can concentrate on the interpretation of the results.

3. *Concept for the automatic analysis*

4. MAGIC observations

*Beobachtet 3 Jahre lang
80 Stunden Datenfang
Die guten Daten untersucht
Eine Detektion verbucht
Mit neuer Technik analysiert
Bis 50 GeV spektriert
— Daniela Dorner.*

In April 2005 the MAGIC telescope took data of PG 1553+113 for the first time. After a hint of signal had been detected, further observations were made in 2006 and 2007. In July 2006 MAGIC observations were coordinated in a multi-wavelength campaign. Part of the data, i.e. April 2005 to beginning of April 2006, were published in Albert et al. [2007]. In the following, the analysis results of all available MAGIC data are presented, including a re-analysis of the already published data. While for a first quick-look analysis (detection of the hint of signal in 2005) the sequences of the automatic analysis have been used, for this thesis a more detailed quality check of the data has been performed, using the tools shown in section 3.3.4. Some of the data have been rejected due to bad quality, detailed reasons are given. Additional data, not included automatically, were added. The results of the analyzed data sets are discussed with respect to their data quality and compared to the published results.

4.1. Observations and data quality

In total about 78 hours of data of PG 1553+113 were taken with the MAGIC telescope between April 16th 2005 and April 25th 2007. An overview of the data taken is shown in table 4.1.

The data from April 2005 until beginning of April 2006 (observation cycle I) were taken in On-Off observation mode. Starting from end of April 2006, the data were taken mainly in Wobble mode as requested in the proposal for the observation cycle II. Detailed information on the observation modes can be found in section 2.2.1.

The data were grouped to sets according to their different observation modes and the changing telescope performance. Data with bad quality have been excluded. A detailed list of chosen and discarded sequences can be found in table A.2. The added and excluded runs are also given in the appendix (tables A.4 and A.3). In the following, the single data sets are discussed and the selected data are summarized in table 4.2.

4. MAGIC observations

Obs.Dates	Duration	Zd Range	Obs.Mode	FADC System
Apr/May 2005	8.91 h	18° - 29°	On	old
Jan-Apr 2006	28.49 h	18° - 54°	On	old
Apr-Jun 2006	16.35 h	18° - 36°	Wobble	old, splitter
Jul 2006	9.53 h	18° - 35°	Wobble	old, splitter
Mar/Apr 2007	14.68 h	18° - 30°	Wobble	new

Table 4.1.: Overview of all data of PG 1553+113. No quality cuts are applied for the given numbers. The first three columns list date, duration and zenith range of the observation. The fourth and fifth column contain information in which observation mode (see section 2.2.1) and with which FADC system (see section 2.1.7) the data were taken.

4.1.1. Observation cycle I

In the first MAGIC observation cycle, about 37.5 hours of data have been taken: about 8.9 hours in 2005 and about 28.5 hours from end of January 2006 to beginning of April 2006. Due to different observation conditions, telescope performance and the big gap in time these data have been divided into two sub-samples: one for the data of 2005 (Set 1) and one for the data of 2006 (Set 2).

The zenith distance (zd) for the observations ranges from 18° to 54° (2006) and from 18° to 29° (2005), where 18° is at the culmination of the source. As the data are taken in On mode, appropriate Off data have to be found for the analysis.

In 2005 almost simultaneous data from the H.E.S.S. telescope array, which observed PG 1553+113 in May and August 2005, are available.

Set 1 The data of 2005 can be split again into two sub-samples: While the data of April (≈ 1.7 hours) have an optical PSF of about 20 mm, those of May (≈ 7.2 hours) have one of about 14 mm. Apart from the worse PSF, the data of April have a good quality, while the data of May are affected by several problems, such as slight camera inhomogeneity (see section 2.2.5), mispointing and a misfocusing of 0.059° (0.048° in x-direction in the camera and 0.034° in y-direction). As the misfocusing was corrected in the hardware just after the period in May, only few Off observations with the same telescope performance are available. Also On data of a strong source with the same telescope performance for the optimization of cuts for the background suppression are missing.

Despite of its good quality the data of April are excluded in the here presented analysis, as on the one hand its duration is too short to analyze it independently, but on the other hand its quality is too different from that in May to analyze all data in one set, especially the different PSF which influences the collection area, needed for the spectrum determination.

Set 2 From January 2006 to April 2006 some data are affected by bad weather or atmospheric absorption due to the SAL (see section 2.2.5). Sequence 81024 has a broken pixel in the inner camera. Apart from that, the data with a z_d larger than 35° have been excluded, as no big flux is expected for these data due to the steep spectrum of the source. In total 16.5 hours with good quality and z_d smaller than 35° are available.

Off data have been chosen from the same time period. As not enough dedicated Off data are available, Wobble data of sources showing no signal were used in addition, resulting in a scale factor 0.31 for the Off data.

4.1.2. Observation cycle II

From the second observation cycle about 40.5 hours of data are available: about 16 hours from mid of April 2006 to end of June 2006, about 9.5 hours from July 2006 and about 15 hours from March 2007 and April 2007. For more details see table 4.1. Only 2.5 hours in the time slot between April 2006 and July 2006 have been taken in On mode, the rest in Wobble mode. The data in July 2006 were taken during a MWL campaign with H.E.S.S. and Suzaku.

The data of cycle II have been split into three sub-samples. One consists of the data taken directly after the installation of the splitters (Set 3), the second is the data taken in July 2006 (Set 4). This division is not only motivated by the fact that Set 4 is taken during a MWL campaign, but also by the different problems of the data (Set 3: inhomogeneous camera, Set 4: calima). Furthermore, the data are taken with a different optical PSF (April-June about 12 mm, July: about 14.5 mm). Due to the gap in time and the different telescope performance (new FADC system starting from February 2007) the data of 2007 are analyzed independently (Set 5) as well.

Set 3 Starting from mid of April 2006 the data were taken with the old FADC system but including the splitters (see section 2.1.7). In the first two to three months after their installation the camera was inhomogeneous (see section 2.2.5). About 2.5 hours are taken in On mode with a high level of NSB light, as the moon was above the horizon during the observation. As the different observation modes require slightly different analyses and the On sample has only 2.5 hours, these data are excluded here. The data of the night of 3./4. May 2006 having a hardware problem are also rejected. One sequence (95036) has a significantly higher pedestal rms, as the data were taken during moon. To ensure similar NSB, this one hour of data is excluded as well.

Although the remaining data suffer from an inhomogeneous camera, they are analyzed, as the set covers 11 hours. The effect of inhomogeneity is checked and discussed in section 4.2.4.

Set 4 Beginning of July the problem of the inhomogeneous camera was solved resulting in a better telescope performance (smaller PSF, less inhomogeneous camera) for the data of July 2006. Compared to the previous observations the optical PSF was improved. In the

4. MAGIC observations

days, when the data for the MWL campaign were taken, there was atmospheric absorption due to the SAL affecting the data quality. Especially the flux measurement is influenced by this and the data need a special treatment, as discussed in detail in section 4.2.3 and in Dorner et al. [2008]. For one sequence the calibration was not working, which was excluded due to that. This results in 8.5 hours of data with good telescope performance.

Set 5 The data of 2007 were taken after the installation of the new FADCs. Two sequences have to be excluded due to bad weather, resulting in 12 hours of data with good quality, one hour from March and the rest from April.

Set	Obs.Dates	Analyzed	Zd Range	Remarks
1	May 2005	6.0 h	18°-29°	various problems (see text)
2	Jan-Apr 2006	16.5 h	18°-35°	-
3	Apr-Jun 2006	11.0 h	18°-26°	inhomogeneous camera
4	Jul 2006	8.5 h	18°-35°	MWL campaign, SAL
5	Mar/Apr 2007	12.0 h	18°-30°	-

Table 4.2.: Overview of data sets used for the presented analysis. In the first column the number is given under which the data set is referred to in the following sections. In the next columns the date, the duration and the zenith range of the observation are given. The last column lists remarks on the data and their quality. More information on the data selection is given in the text.

4.2. Analysis

The data is analyzed with the Mars release V2.0. For the calibration and the calculation of the image parameter, the automatic analysis in the Würzburg data center has been used. For some runs, which could not be analyzed automatically for technical reasons (table A.4), sequences were written manually and processed with the same setup as in the automatic analysis. From some sequences few runs were excluded (table A.3), either due to bad weather or high zenith angle.

Compared to Albert et al. [2007] the presented analysis includes several changes. The major differences and also some improvements in the software are explained hereafter

4.2.1. General analysis chain

First differences and improvements in some general parts of the analysis chain are discussed.

Calibration In contrary to Albert et al. [2007], in the presented analysis an absolute light calibration with muons is done providing a correction of long-term changes in the light detection efficiency of the telescope.

In addition the used calibration includes several improvements and bug-fixes: The signal extraction has been rewritten, the calibration code simplified, and the treatment of bad pixels and the hi-/lo-gain calibration have been improved [www-13].

Pointing Corrections for mispointing and misfocusing have been applied, as this is done automatically for all data. These corrections were not applied in Albert et al. [2007]. Additionally a starguider calibration is implemented since version V2.0 providing an absolute pointing correction resulting in a smaller gamma-ray point spread function.

Timing information With the new FADC system (section 2.1.7) a better timing resolution for the pulse position is achieved. To profit from this, new methods using the timing information have been implemented. In the presented analysis, it is used for image cleaning and background suppression, not only for the data taken with the new, but also for those taken with the old FADC system.

For the image cleaning, first an absolute cleaning with lowered cleaning levels is done. Consequently, pixels not belonging to the shower survive. These pixels are removed from the shower image in two iterative steps removing pixels having no neighboring pixel with a signal coincident in a time window of 1.5 ns - 2.0 ns [Bretz, 2007]. This results in a better shower reconstruction allowing for an improved background suppression.

Additionally, the slope of the arrival time along the reconstructed major shower axis is used in the background suppression for parameterizing the Disp [Bretz, 2007].

With these methods, a total sensitivity with the new FADC system of 1.5 % Crab for five sigma in 50 hours is achieved. The improvement compared to the analysis without timing information is about 35 %. The new FADC system improves the sensitivity by 10 % - 20 % compared to the old FADCs [Bretz, 2008, 2007; Tesaro et al., 2007].

In Albert et al. [2007] no timing information was used in the analysis.

Quality cuts Compared to Albert et al. [2007] improved quality cuts have been used. With the previously used quality cuts remaining non-physical events (see section 2.2.5) were found. A fake signal from these events cannot be excluded, therefore they have to be removed thoroughly.

The new set of cuts has been developed in a detailed study comparing parameter distributions and correlations of simulated gammas to those of real data. The study included many different parameters and correlations. In addition data with different telescope setup (FADCs, splitter, see section 2.1.7) was used. The aim of the study was to cut away as many non-physical events as possible without rejecting gamma events. Different populations of non-physical events have been found.

The outcome of the study are the following cuts. To survive, an event has to fulfill all of the following conditions:

4. MAGIC observations

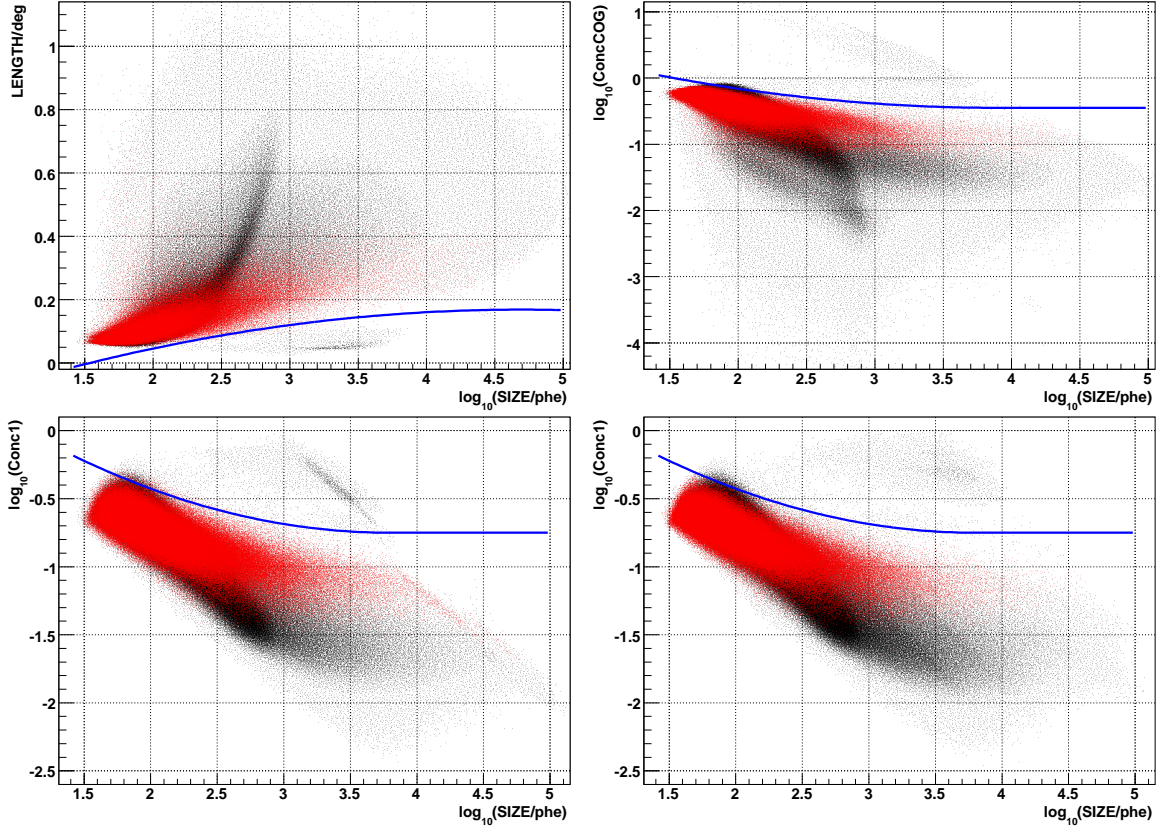


Figure 4.1.: Distributions in $LENGTH$, $Conc1$ and $ConcCOG$ versus $SIZE$. In red simulated gammas and in black real data are shown. The corresponding quality cuts are plotted as blue lines. For $LENGTH$ the events above the line survive, for $Conc1$ and $ConcCOG$ those below. In the left plots, simulated gammas and real data events for Set 5 are shown. The upper right plot is for Set 1, the lower right for Set 3.

- less than three islands of pixels
- more than five pixels after cleaning
- $Leakage1^a$ smaller than 0.3
- cut in the distribution $ConcCOG^b$ versus $SIZE$ (figure 4.1, upper right plot):

$$\log_{10}(ConcCOG) < -0.45 + 0.08 \cdot (\log_{10}(SIZE) - 3.9)^2 \cdot H(-\log_{10}(SIZE) + 3.9) \quad (4.1)$$

^aphotons in outermost ring of pixels divided by $SIZE$

^bconcentration ratio: phe of the three pixels next to COG divided by $SIZE$

where $H(n)$ is the discrete form of the Heaviside step function:

$$H(n) = \begin{cases} 0 & : n < 0 \\ 1 & : n \geq 0 \end{cases} \quad (4.2)$$

- cut in the distribution $Conc1^c$ versus $SIZE$ (figure 4.1, lower plots):

$$\log_{10}(Conc1) < -0.75 + 0.10 \cdot (\log_{10}(SIZE) - 3.8)^2 \cdot H(-\log_{10}(SIZE) + 3.8) \quad (4.3)$$

- cut in the distribution $LENGTH$ [°] versus $SIZE$ (figure 4.1, upper left plot):

$$LENGTH > -5 \cdot (\log_{10}(SIZE) - 4.7)^2 + 50 \quad (4.4)$$

The first three conditions remove events which are probably no gammas or would be removed with later cuts anyhow. The other three cuts (formulas 4.1, 4.3 and 4.4) reject the above mentioned non-physical events. The origin of these events is unclear. Showing very much light in a small area, they can be seen when plotting $LENGTH$, $Conc1$ or $ConcCOG$ versus $SIZE$ (figure 4.1). The lower two plots show that the characteristics of these showers images changed with the telescope setup. The performed study takes these changes into account for data up to mid of 2007. The cuts are done such that more than 99 % of the gammas survive. For small energies, the cuts are made as close as possible to the gamma distribution to remove the non-physical events as good as possible. For higher energies, where the event statistics is low, the cut is chosen such that all gammas survive. These cuts are used as standard quality cuts since Mars V2.0.

Background suppression While in Albert et al. [2007] the background suppression was done with Random Forest (RF) [Albert et al., 2007c], here dynamical cuts were used. The parameterization of these cuts is discussed in detail in Riegel and Bretz [2005]; Rügamer [2006] and Riegel [2005]. As the cuts in ϑ and $Area$ ($Area = \pi \cdot WIDTH \cdot LENGTH$) are varied here, they are explained (formula 4.5 and 4.6) and the coefficients for the different sets of used cuts are given in table 4.3.

$$\vartheta^2 < c_1^2 \quad (4.5)$$

$$Area < c_2 \cdot (1 - c_4 \cdot (\log_{10}(SIZE) - c_3)^2) \quad (4.6)$$

To get the coefficients, the cuts have been optimized on data of the Crab Nebula using three data sets, one for each FADC setup. The obtained results were almost identical with the outcome of an extensive study, done for the new methods using the timing information [Bretz, 2007]. The result of this study, including also better coefficients for the disp parameterization, has been implemented as standard cuts in Mars V2.0.

^cconcentration ratio: phe of the highest pixel divided by $SIZE$

4. MAGIC observations

Set	Purpose	c1	c2	c3	c4
A	standard	0.215	0.215468	5.63973	0.0836169
B	signal detection	0.2	0.215468	5.58973	0.0836169
C	light curve	0.215	0.215468	5.58973	0.0836169
	spectrum:				
D	inhomogeneous data	0.215	0.215468	5.53973	0.0836169
E	inhomogeneous data	0.215	0.215468	5.5	0.0836169
F	good data, low energy analysis	0.215	0.3	6.2	0.042

Table 4.3.: Coefficients for the cuts in *Area* and ϑ for different purposes: standard automatic analysis (A), signal detection in case of PG 1553+113 (B), light curve (C), spectrum calculation for data with inhomogeneous camera (D,E) and good data with a low energy analysis (F), which includes an additional cut in *Area* (see section 4.2.2). The definition of the coefficients can be found in formula 4.5 and 4.6.

Signal determination To account for the steeper spectrum of PG 1553+113 compared to the one of the Crab Nebula, the cuts used for the signal determination are looser than the standard cuts, i.e. coefficients set B in table 4.3.

Depending on the observation mode (section 2.2.1), either Off data, or in case of Wobble mode three off regions in the camera, were used to determine the background. For Wobble mode this results in a scale factor of one third, for On-Off mode it depends on how much Off data with the same quality and telescope performance is available.

The significance is determined according to formula 17 in Li and Ma [1983].

Spectrum A detailed description of the algorithms to calculate the spectrum can be found in Bretz [2006]. For this analysis apart from the RF energy reconstructor a parameterization for the energy reconstruction has been developed:

$$\begin{aligned}
 E_{est} &= SIZE^{0.906} \cdot 10^x & (4.7) \\
 x &= -0.831 \cdot (DIST - 0.161)^2 \cdot H(DIST - 0.161) \\
 &\quad + 2.21 \cdot (DIST - 0.493)^2 \cdot H(DIST - 0.493) \\
 &\quad + 8.18 \cdot 10^{-6} \cdot Zd^{2.82} \\
 &\quad - 0.1 \cdot Leakage1^{0.2}
 \end{aligned}$$

where $H(n)$ is again the discrete form of the Heaviside step function.

Both the RF regression, trained on $\log_{10}(E_{mc})/\log_{10}(SIZE)$, and the parameterization (formula 4.7) give comparable results with respect to the resolution and bias of the energy reconstruction.

For the determination of the spectrum the cut in *Area* is loosened (coefficients set D, E or F in table 4.3). This enhances the efficiency of the cuts, especially for low energies, and

lowers the energy threshold, i.e. the peak energy of the distribution of simulated gammas surviving the cuts. Consequently, not only more gamma, but also more background events survive. This lowers the significance of the signal, but the spectrum determination at low energies is improved due to better statistics. More details concerning a special low energy analysis can be found in the next section (4.2.2).

To study the systematics of the analysis, spectra are determined with different simulated spectral slopes and different cut coefficients. In the result plots for the single data sets in appendix A.3, these sets of spectra are shown as gray band in the spectral plots.

For the interpretation, two different fits to the spectra are made:

- Power law:

$$dN/dE = N_0 \cdot (E/200 \text{ GeV})^{-\Gamma} \quad (4.8)$$

where Γ is the slope in a logarithmic representation and N_0 the flux at 200 GeV.

- Power law with cutoff:

$$dN/dE = N_0 \cdot (E/200 \text{ GeV})^{-\Gamma} \cdot e^{-E/E_c} \quad (4.9)$$

where E_c is the cutoff energy.

Light curve As there is no special program to determine a light curve, this is done by building a data set for each bin in the light curve, e.g. one per night, and producing a spectrum with appropriate binning, i.e. three bins and the middle one for the energy range needed for the light curve. From the single spectra the integral flux in the central energy bin, which is between 150 GeV and 1 TeV for the presented analysis, is retrieved and plotted versus **Modified Julian Date** (MJD). The coefficients for the used cuts are given as set C.

Stacking Due to different telescope performance not all data can be analyzed together. For example the different FADC systems and PSFs require different sets of simulated data. Therefore the complete sample is subdivided into several sets (for PG 1553+113 see section 4.1) which are analyzed independently. Afterwards the signal can be combined and a spectrum of the whole sample can be determined. For this stacking, the χ^2 distributions are added up. To calculate the spectrum correctly, the collection area is weighted with the observation time of the samples. From the added excess, the weighted collection area and the total observation time the combined spectrum is calculated.

4.2.2. Low energy analysis

Background At energies around 100 GeV the background suppression is getting more difficult. On the one hand, hadronic showers become more similar to gammas, as with smaller energies less electromagnetic subshowers are generated. On the other hand, muonic background is dominating at small energies: If the telescope is not completely inside the Cherenkov light pool emitted by the muon, the image is no ring anymore. Instead, the

4. MAGIC observations

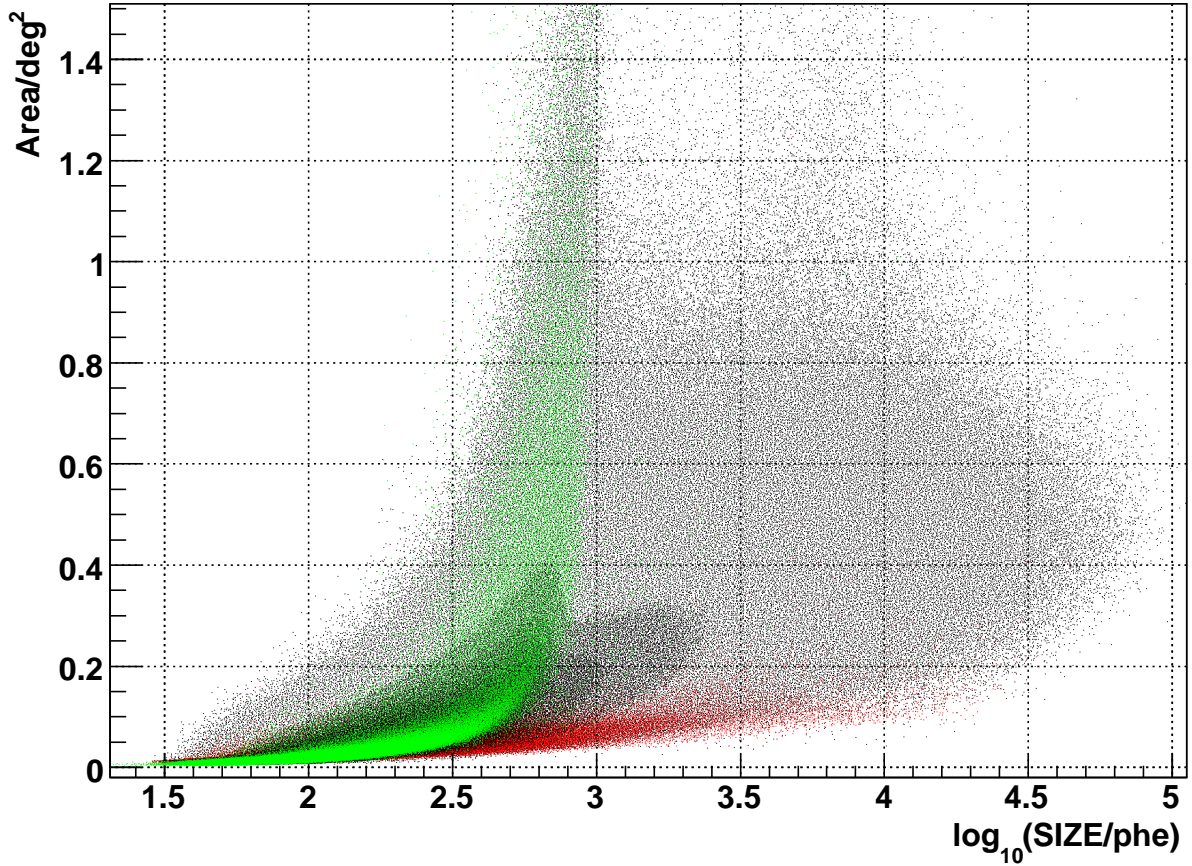


Figure 4.2.: *Area* versus *SIZE* for real data (black), simulated gammas (red) and simulated muons (green).

remaining small fraction of a ring resembles the image from a gamma shower. Consequently, it gets difficult to reject this background. This can be seen for example, when plotting the *Area* of these different image types (figure 4.2). The distribution of muonic images (green) overlaps with that of gamma showers (red). The muons can also be seen in the distribution of real data (black).

To get rid of the background, the cut has to be chosen very tight at small energies, resulting in a small gamma efficiency below the energy threshold. The consequently small event statistics can result in a wrong determination of the flux in the low energy bins.

New cuts To extend the spectra to lower energies, the cut efficiency in this range has to be increased. Therefore the cut in *Area* (formula 4.6) has been chosen so loose (table 4.3, coefficients set F) that more than 99% of all gamma showers survive. The parameters have been chosen by plotting the cut efficiency for simulated gamma events in *Area* versus *SIZE*.

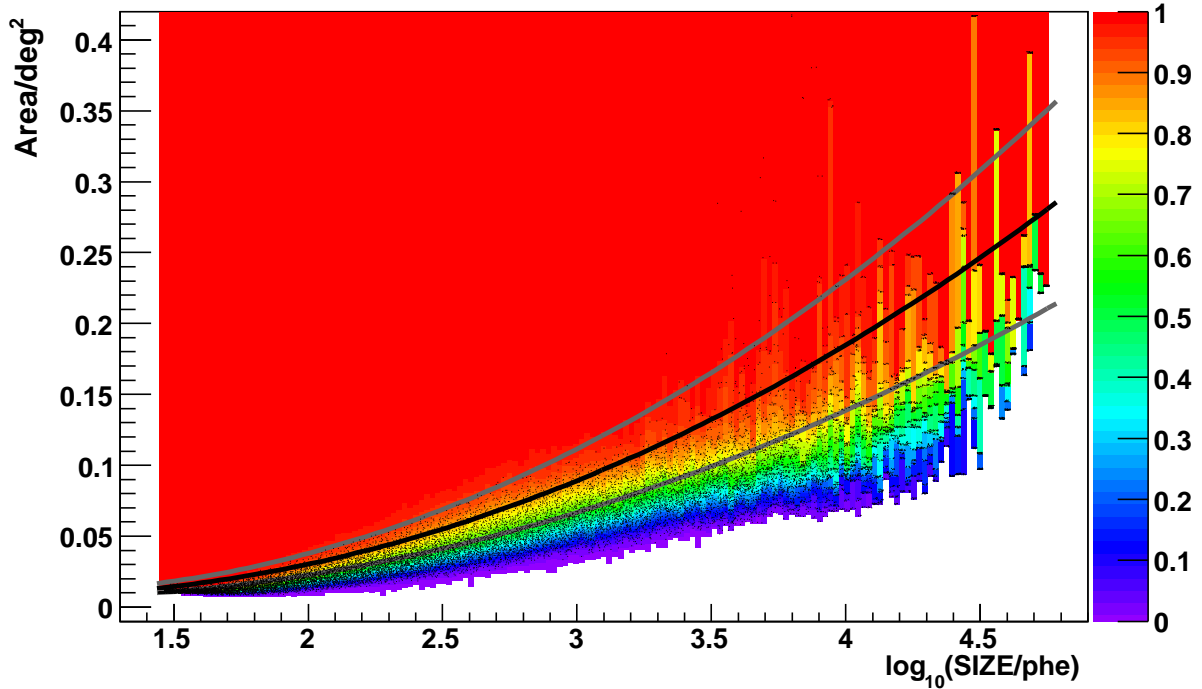


Figure 4.3.: Efficiency in an *Area* versus *SIZE* distribution. Overlaid to a scatter plot of simulated events, the efficiency is plotted as color scale: red means that all gammas survive, violet indicates an efficiency of 0%. The black line shows the cut in *Area* used for the low energy analysis (formula 4.10) with $x = 0.008$. The dark gray lines show the cuts for $x = 0.006$ and $x = 0.01$ respectively.

With the same method a new parameterization for the cut in *Area* was developed:

$$Area < (2.3 \cdot (\log_{10}(SIZE) - 0.9)^2 + 1) \cdot x \quad (4.10)$$

where x is varied between 0.005 and 0.01 to study the dependence of the spectrum from the cut efficiencies. For the shown spectra a value of 0.008 or 0.009 was chosen. For $x=0.009$ an overall cut efficiency of >35% for energies above 75 GeV is achieved as shown in figure 4.4. Going down to 60 GeV the cut efficiency is still almost 30%.

Data quality This low energy analysis can be used only for data with good quality. For loose cuts, the problem of the inhomogeneous camera gets more pronounced than for tight cuts. Especially for data with bad quality, the agreement between On and Off data has to be checked in the ϑ^2 distributions. To make sure that the flux is calculated correctly for the spectrum, these distributions have to be checked in single *SIZE* or energy bins. If the distributions agree well, the method can be used. Else the cuts can be loosened just as much as On still fits the Off in the ϑ^2 distributions, e.g. coefficients set D or E in table 4.3.

4. MAGIC observations

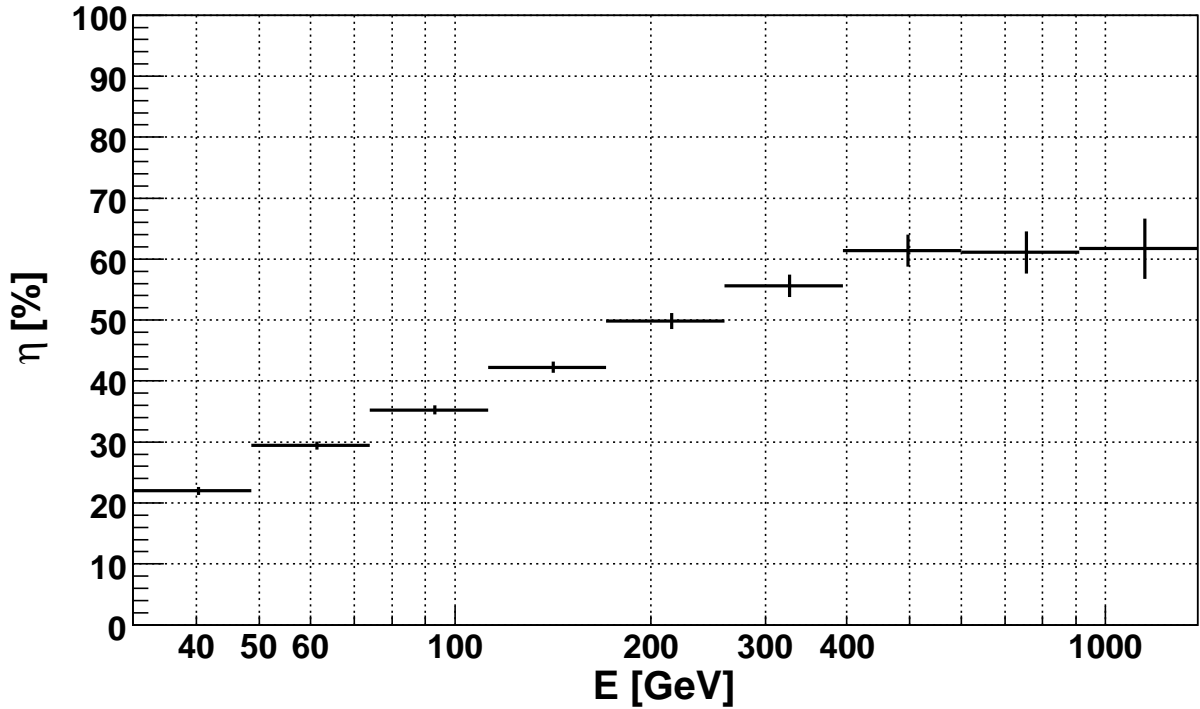


Figure 4.4.: Overall cut efficiency of the low energy analysis, including all cuts after the calculation of the image parameter.

Discussion For the first time energy spectra down to 50 GeV are shown and PG 1553+113 is the first source to which the presented low energy analysis has been applied.

In Albert et al. [2008] a spectrum of the Crab Nebula between 60 GeV and 9 TeV was shown. The position of the IC-peak was determined to be at (77 ± 47) GeV. Consequently, the Crab Nebula is not the ideal candidate for studying this low energy analysis.

Lacking a source with a flux high enough in this energy range, it cannot be excluded that for example bad fitting simulated data results in a wrong energy reconstruction for the low energy showers.

To check for possible fake signals, e.g. due to the large number of muons at the small energies (see figure 4.2), a low energy analysis has been performed with Off data. Although the majority of tested Off samples showed a signal with a significance between -1σ and 1σ , there were outliers showing significances up to 7σ . But for those outliers, it was obvious from the χ^2 distributions that On and Off did not agree, confirming that a quality check is mandatory when applying the low energy analysis.

Further studies on the agreement between simulated and real data at these low energies are needed. In addition the method should be tested on other sources with either steep spectrum or extremely high flux, if available, e.g. with flares of bright AGN [Hadasch, 2008].

4.2.3. Correction of atmospheric absorption due to the Saharan Air Layer

Night	CMT extinction [mag]	KVA extinction	CMT [%]	KVA [%]	Size [%]	Muon [%]
15./16.	0.096 ± 0.014 (12)	5.237 ± 0.003	99.4 ± 1.3	92.3 ± 0.3	95	101
16./17.	0.338 ± 0.009 : (3)	5.880 ± 0.059	79.6 ± 0.7	51.1 ± 2.7	94	100
17./18.	0.214 ± 0.006 (9)	5.271 ± 0.004	89.2 ± 0.5	89.5 ± 0.3	87	101
18./19.	0.084 ± 0.005 (12)	5.149 ± 0.006	100.6 ± 0.5	100.1 ± 0.6	-	-
19./20.	0.074 ± 0.006 (11)	5.157 ± 0.003	101.5 ± 0.6	99.4 ± 0.3	-	-
20./21.	0.265 ± 0.061 : (11)	5.229 ± 0.011	85.1 ± 4.7	93.0 ± 0.9	-	-
21./22.	0.320 ± 0.020 : (11)	5.382 ± 0.004	80.9 ± 1.5	80.8 ± 0.3	74	96
22./23.	0.605 ± 0.001 : (3)	6.110 ± 0.225	62.2 ± 0.1	41.3 ± 7.7	-	-
23./24.	0.408 ± 0.017 (8)	5.441 ± 0.003	74.6 ± 1.2	76.5 ± 0.2	81	98
24./25.	0.336 ± 0.009 (6)	-	79.7 ± 0.7	-	78	98
25./26.	0.310 ± 0.005 (7)	5.381 ± 0.004	81.7 ± 0.4	80.8 ± 0.3	81	99
26./27.	0.088 ± 0.007 (7)	-	100.2 ± 0.6	-	92	101
27./28.	0.099 ± 0.005 (9)	5.179 ± 0.007	99.2 ± 0.5	97.4 ± 0.6	-	-
average good night	0.09	5.16	100	100	100	100

Table 4.4.: Atmospheric extinction and transmission for the nights between July 15th 2006 and July 28th 2006. The second column shows the extinction measurement of the CMT, where ':' marks nights with variable extinction, and the number of photometric frames is given in parenthesis. In column three the extinction determined from the optical data of KVA are given. From these two columns the transmission (column four and five) is calculated with formula 1 from Dorner et al. [2008]. The last two columns give corresponding numbers determined from the *SIZE* distributions and the muon rings of the MAGIC data. In the last row the numbers for an average good night without absorption for zenith (i.e. airmass $X = 1$) are given, which is needed for the calculation of the transmission from the extinction.

As part of the here presented data of PG 1553+113 is affected by atmospheric absorption due to the SAL, a correction method has been developed. In my publication [Dorner et al., 2008] the feasibility of the method is studied in detail. From extinction measurements of the Carlsberg Meridian Telescope [Carlsberg Meridian Telescope, 2007] and the optical telescope KVA, listed here in table 4.4, the transmission is calculated using formula 1 of the paper. From the MAGIC data itself, the transmission is determined by comparing the *SIZE*

4. MAGIC observations

distributions of affected data to one of good quality data. In addition, an estimation of the transmission from muon rings has been done. The different measurements are compared. The correction method itself and the results after applying the correction factor to the data are discussed. For completeness, the publication is appended to this thesis.

4.2.4. Effect of the inhomogeneous camera

To study the effect of the inhomogeneous camera (section 2.2.5) on the signal and spectrum, the COG distributions of the showers were investigated. Figure 4.5 shows these distributions for different *SIZE* ranges after cuts (including the cut in ϑ) for data Set 3. The inhomogeneity appears in the upper right part of the COG distributions as lack of events. From the distribution for the complete *SIZE* range (upper left plot) the effect on the signal can be checked, while comparing the distributions for different *SIZE* bins (upper right plot and lower plots) allows to conclude on the effect on the spectrum.

Although the plots give an impression of the effect, calculations are needed to infer the errors on the signal, flux and spectrum. Similar to the inhomogeneity parameter in the database, the loss L of events is estimated as follows:

$$L = \frac{n_{med} - n_{min}}{n_{sum}} \quad (4.11)$$

where n_{med} is the median of the number of events per sector, n_{min} the number of events in the sector with the fewest events and n_{sum} the sum of events in all six sectors. This way of estimating the fraction of missing events is feasible, as the affected part of the camera is located almost completely in one sector. For the calculation only events after cuts including the cut in ϑ were used to get the correct numbers for the signal and spectrum.

For all five data sets and for comparison also for a data set of simulated data, the loss of events is calculated (table 4.5). Depending on whether a low energy analysis was used, the *SIZE* ranges were chosen accordingly, and the same cuts like in the analyses were used.

Signal The loss calculated for the whole energy range shows that Set 3 is strongly affected by an inhomogeneous camera ($\approx 8\%$) and also Set 1 shows a remarkable effect ($\approx 6.5\%$). For the other three data sets the effect does not disappear, but the loss stays below 4%. This slight inhomogeneity gets also obvious when plotting the according COG distributions. Calculating the values for simulated gammas (On mode) results in a loss of less than 2% in all energy ranges. Gammas simulated in Wobble mode show that also the shifted source position can cause an apparent loss of up to 4%. As the MC data set does not include Off events, this effect is less pronounced in real data and depends on the strength of the source.

While for data taken in Wobble mode, the choice of the Wobble positions and the ratio of observation time between the different Wobble positions influences the effect of the inhomogeneity on the ϑ^2 distributions and therefore the determined signal, it depends in the On-Off mode on the fact whether the inhomogeneity was the same during On and

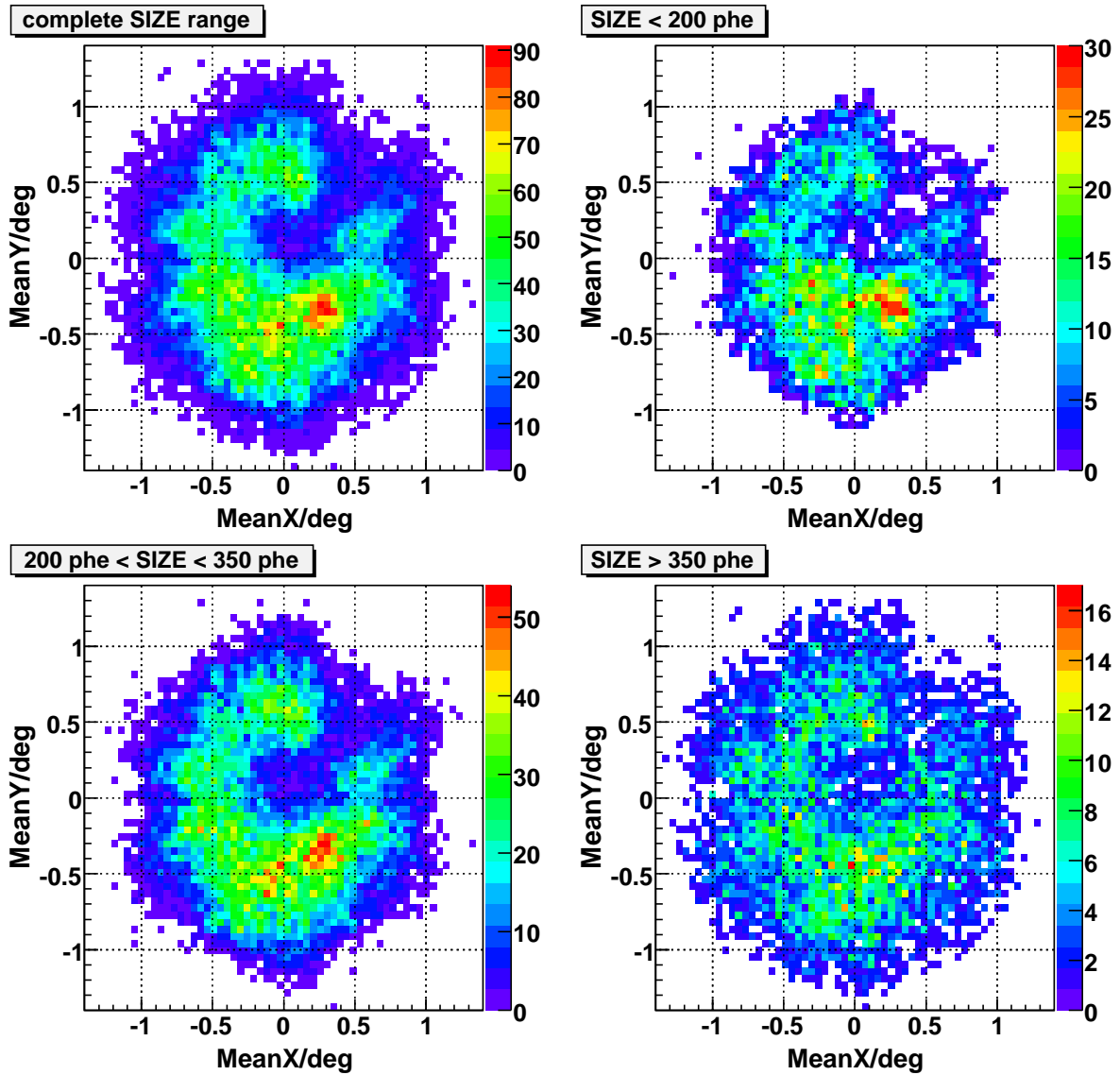


Figure 4.5.: Center of gravity distributions after cuts in $Area$ and ϑ for Set 3 for the whole $SIZE$ range (upper left), below 200 phe ($\approx 120 GeV$, upper right), between 200 phe and 350 phe (lower left) and above 350 phe ($\approx 200 GeV$, lower right).

Off observations. In both cases differences between On and Off can result in an over- or underestimation of the signal.

Light curves To estimate the effect of the inhomogeneity on the flux in the light curves, the calculations were also done for $SIZE$ larger than 150 GeV. Here, Set 1 shows a loss of

4. MAGIC observations

Set	1	2	3	4	5	MC	MC
Set of coefficients	E	F	E	F	F	E	F
$E < 75 \text{ GeV}$	-	4.4 %	-	3.1 %	4.2 %	-	0.4 %
$75 \text{ GeV} < E < 120 \text{ GeV}$	-	2.9 %	-	3.5 %	1.8 %	-	0.4 %
$E < 120 \text{ GeV}$	7.7 %	-	9.4 %	-	-	1.4 %	-
$120 \text{ GeV} < E < 200 \text{ GeV}$	5.8 %	3.3 %	8.7 %	2.1 %	0.9 %	0.4 %	0.5 %
$E > 200 \text{ GeV}$	6.8 %	2.8 %	8.3 %	0.9 %	0.9 %	0.6 %	0.6 %
complete E range	6.5 %	3.9 %	8.3 %	2.8 %	2.6 %	0.4 %	0.5 %
$E > 150 \text{ GeV}$	6.5 %	2.6 %	6.9 %	2.3 %	2.6 %	0.5 %	0.5 %

Table 4.5.: Fraction of events lost due to camera inhomogeneity calculated with formula 4.11. For the different data sets, the cuts for spectrum (complete energy range and energy bins; set of coefficients E or F as given in second row) and lightcurve (energy $> 150 \text{ GeV}$, last row, set of coefficients C) were used for the COG distributions from which the loss was calculated. For comparison, the same calculations were done for simulated data (MC, last two columns) with the same cuts as for the data.

about 6.5 %, Set 3 about 7 % and the other three sets about 2.5 %. For a more detailed light curve Set 3 is divided in two sub-sets, where the first set (April, May) shows 9.3 % and the second one (June) only 4.7 %. This improvement was due to a hardware intervention at the telescope.

Spectrum To study the effect on the spectrum, only the events surviving the spectrum cuts were used. Consequently, for the different data sets, different *SIZE* ranges were investigated. The bins were chosen such that the shown spectral range is covered and the number of events per bin is similar. The numbers for the different sets and *SIZE* bins are given in table 4.5.

With 4.2 % at low energies and 0.9 % at higher energies, the data of 2007 show the largest dependence on energy. For the other data sets the difference is smaller. For the data having the strongest inhomogeneity (Set 3), the difference is about 1 %. For the coefficients set E, also the MC set shows the largest inhomogeneity in the lowest energy bin.

Although differences in the loss per *SIZE* bins are found and the loss tends to be larger at small energies, no significant correlation is found.

4.3. Results and discussion

With the improved methods described in chapter 4.2, the five data sets have been analyzed. In the following the obtained results of the single data sets and the combined data set are presented and discussed. A comparison with the H.E.S.S. results [Aharonian et al., 2008]

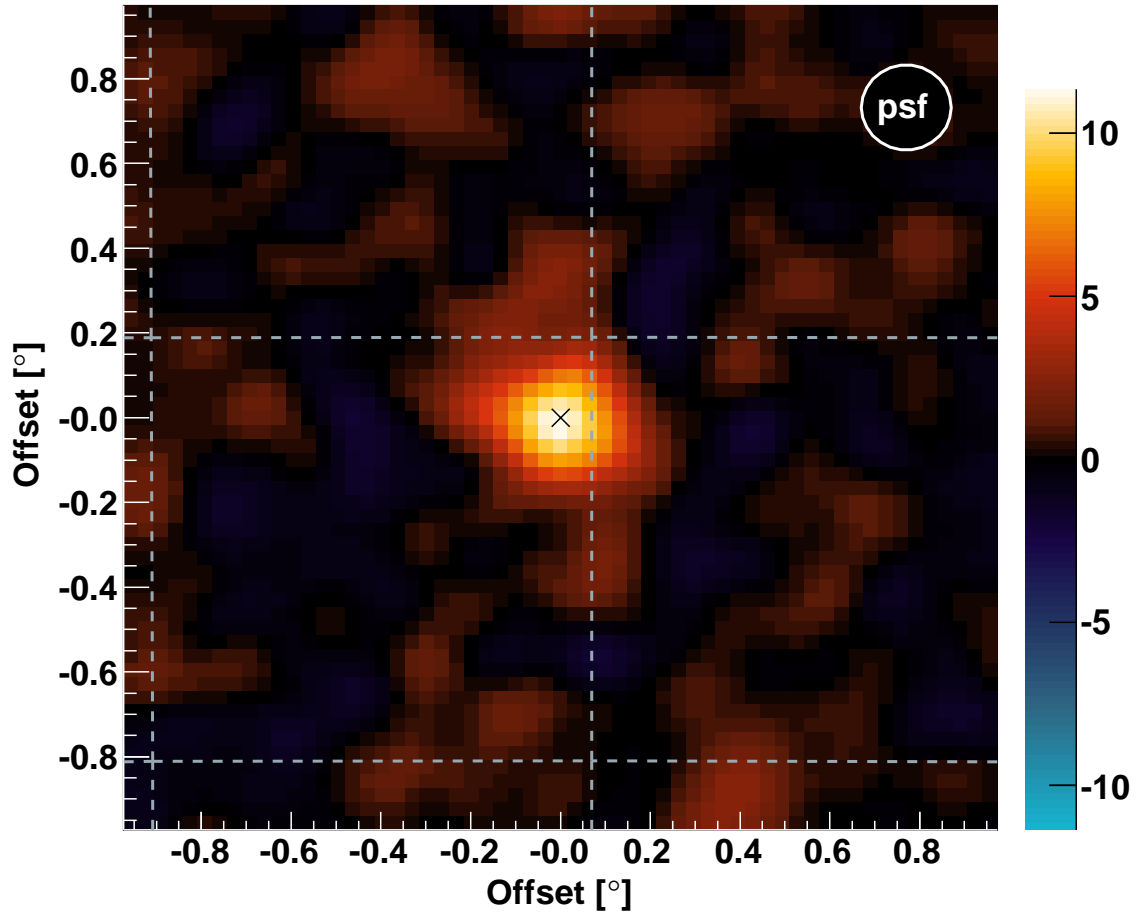


Figure 4.6.: Sky map for the data of January to April 2006 showing the number of equivalent excess events in events per 3.1 arcminutes².

is done for the combined set and the set of July 2006. Light curves of the complete sample with different time binnings are shown.

4.3.1. Single data sets

For each data set, the signal and the spectrum are determined. In the following these results are discussed. The χ^2 distributions and spectra are shown in appendix A.3. In these spectra the systematics of the analysis, explained in 4.2.1, is given as gray band.

For the two data sets of the first observation cycle, i.e. Set 1 and 2, a comparison with the already published results [Albert et al., 2007] is done. The differences are discussed and possible reasons are given. The results of the single data sets and the combined data set are discussed.

4. MAGIC observations

Set	Observation Dates	Effective On-Time	Off-Scale Factor	Signif.	Integr. Flux >150 GeV	Flux at 200 GeV	Spectral Slope
1	May 2005	6.0 h	0.48	5.2σ	3.1 ± 0.6	2.3 ± 0.4	4.9 ± 0.5
2	Jan-Apr 2006	16.5 h	0.31	9.4σ	2.9 ± 0.3	1.3 ± 0.2	4.2 ± 0.3
3	Apr-Jun 2006	11.0 h	0.33	6.5σ	2.2 ± 0.6	1.6 ± 0.3	4.7 ± 0.4
4	Jul 2006	8.5 h	0.33	5.0σ	2.4 ± 0.8	1.5 ± 0.3	4.1 ± 0.3
5	Mar/Apr 2007	12.0 h	0.33	8.1σ	2.5 ± 0.4	1.4 ± 0.2	3.9 ± 0.3
all	2005-2007	54.0 h	0.33	15.0σ	2.6 ± 0.2	1.4 ± 0.1	4.1 ± 0.2

Table 4.6.: Results of all data sets. The second, third and fourth column list the observation time, the duration of the analyzed data set (first column) and the scale factor between On and Off data. The next columns give the significance of the signal, the integral flux above 150 GeV in $10^{-7}/\text{m}^2/\text{s}$, the flux at 200 GeV in $10^{-6}/\text{TeV}/\text{m}^2/\text{s}$ and the spectral slope from a power-law fit between 75 GeV and 900 GeV (600 GeV respectively for Set 1 and 2).

Set 1: May 2005 As explained in section 4.1, the data of May 2005 suffer from various problems: While the inhomogeneous camera was a persisting problem, the mispointing and misfocusing was only from April 28th to May 21th 2005. To ensure the same telescope performance and quality, the Off data for the background determination have been chosen also from this period, resulting in a scale factor between On and Off data of 0.48. With the signal cuts (table 4.3, coefficients set B) a signal has been detected with a significance of 5.2σ from a total observation time of 6 hours (figure A.1, upper plot).

Despite of the careful choice of Off data, they do not fit optimal to the On data, due to the slightly inhomogeneous camera. Consequently, the low energy analysis could not be applied to determine the spectrum. Instead the same cut coefficients like for the signal detection (set B) were applied. To study the systematics of the analysis, also spectra were calculated using the coefficients set A, D and E and spectra simulated with different slopes. The range of obtained spectra is shown as gray band in figure A.1 (lower plot). Fitting a power law to the spectrum yields a flux of $(2.3 \pm 0.4) \cdot 10^{-6} \text{ ph}/\text{TeV}/\text{s}/\text{m}^2$ at 200 GeV and a slope of 4.9 ± 0.5 . Due to the tight cuts, the points at 91 GeV and 139 GeV are too high, resulting in a steeper spectrum and a higher flux in the low energy part. The effect of the inhomogeneous camera has been studied. The values for the loss of events, given in table 4.5, vary between 5.8% and 7.7% and show no clear dependence on the energy. Compared to the statistical errors and systematic uncertainties of the analysis, the effect of the inhomogeneous camera is negligible. Consequently, the determined results can be used for a combined analysis.

Albert et al. [2007] quotes a significance of 6.7σ for 7.0 hours of 2005 data. The difference in the observation time is mainly due to the fact that the analysis in the paper includes the data of April. The remaining difference comes probably from different quality criteria in the data selection. In addition, in the paper not only Off data from the same time, but

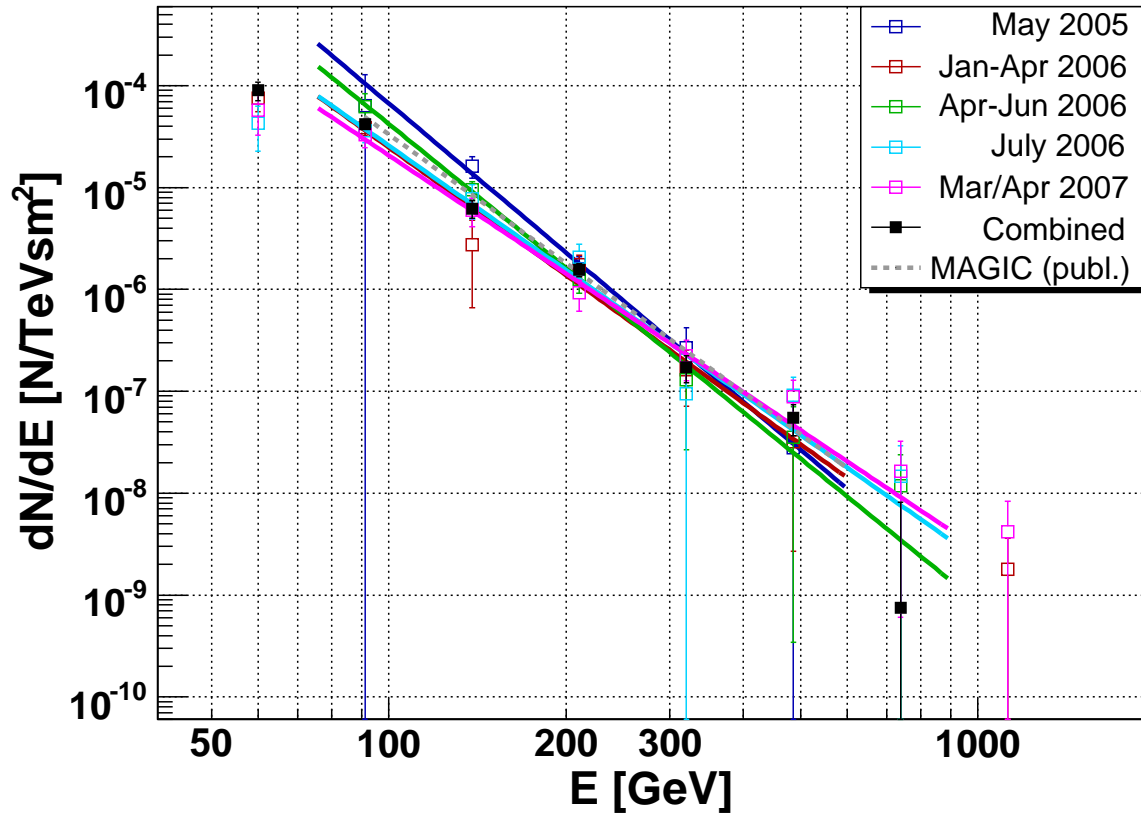


Figure 4.7.: Differential spectra of all data sets. The spectra and the according power law fits of the single data sets are plotted in different colors (see legend). The fit results are given in table 4.6. For comparison the result of Albert et al. [2007] is plotted as gray dotted line. In addition the combined spectrum is shown (black filled squares).

also from 2006 were used. Taking into account the larger observation time and the smaller scale factor (0.2), the 6.7σ correspond to 5.5σ , which is comparable to the here obtained result. Considering on the other hand, that due to the timing information the 5.2σ come from an analysis with a better sensitivity (see results of Set 2 and section 4.2.1), a higher significance would be expected. Also the applied mispointing and misfocussing correction should increase the signal, as it is better centered then. Despite of these two effects, the significance in the presented analysis stays below the one of the paper. The reason for this might be an overestimation of the flux in the paper due to unsuitable Off data.

The spectral index, which was determined to 4.31 ± 0.45 in the paper, as well as the flux at 200 GeV ($(2.0 \pm 0.6) \cdot 10^{-6}$ ph/TeV/s/m²) agree within the errors with the presented results.

Set 2: January to April 2006 From the 16.5 hours of data with good quality and zenith distance smaller than 35° a signal was found with a significance of 9.4σ (coefficients set

4. MAGIC observations

B in table 4.3, upper plot in figure A.2). For these data the low energy analysis could be applied and spectral points at 91 GeV and 60 GeV have been determined. Fitting a power law to this spectrum between 75 GeV and 600 GeV a slope of 4.2 ± 0.3 is obtained. Fitting down to 48 GeV the slope is smaller with 3.6 ± 0.2 . The flux at 200 GeV is $(1.4 \pm 0.3) \cdot 10^{-6}$ ph/TeV/s/m² and $(1.3 \pm 0.2) \cdot 10^{-6}$ ph/TeV/s/m² respectively (lower plot in figure A.2).

From the analysis presented in Albert et al. [2007] a signal was found with 7.0σ for 11.8 hours of data. The scale factor between On and Off is approximately the same in both analyses: 0.31 here and 0.30 in the paper. The difference in the observation time comes mainly from the fact that a different zenith angle range ($18^\circ - 30^\circ$) was used. Taking into account the observation time the 7.0σ would correspond to 8.2σ neglecting the fact that these additional hours of data are only from zd between 30° and 35° . The difference in the significance can be explained by the fact that here the timing information was used providing an improved sensitivity. Also the absolute mispointing correction might slightly improve the result.

Combined set: April 2005 to April 2006 For Albert et al. [2007] the combined data set of 18.8 hours with zd smaller than 30° has been analyzed. While from the single data sets a signal was found with 6.0σ (2005) and 7.6σ (2006), the analysis of the combined data set yields 8.8σ . This is not consistent with summing up the significances quadratically, as for the single data sets the complete Off data sample of 14.5 hours in total (6.5 hours of 2005 and 8.0 hours of 2006) was used. According to the paper the two Off data samples are in good agreement.

For this thesis, the two sets have not been analyzed together due to the bad quality of the data of May 2005 and the fact that the two samples have different telescope performance. Summarizing, the results of Set 2 agree well, considering the improvement due to the timing information. On the contrary the results of Set 1 do not agree, if the better sensitivity is taken into account. It may be that the flux was overestimated due to unsuitable Off data. Compared to Albert et al. [2007], where the lowest energy bin ranges from 85 GeV to 112 GeV, the here presented analysis shows a point at 60 GeV (bin: 49 GeV - 74 GeV). With the low energy analysis (section 4.2.2) the spectrum could be extended down to 50 GeV.

Set 3: April to June 2006 For this set the ϑ^2 distributions of signal and background do not agree anymore for the low energy cuts (table 4.3, cuts F) due to the inhomogeneous camera. Consequently, the low energy analysis cannot be applied. Instead only a slightly loosened cut in *Area* (coefficients set E) is used for the spectrum determination. With the cuts for the signal detection (coefficients set B) a signal was found with 6.5σ from the 11 hours remaining after the data selection (figure A.2, upper plot). Despite of the tight cuts, the On distribution does not agree completely with the Off distribution due to the inhomogeneous camera. This is visible in the ϑ -distribution, where the On is above the Off up to $\vartheta \approx 0.1^\circ$.

The spectrum covers the energy range between 75 GeV and 600 GeV (figure A.2, lower plot). Fitting a power law to the spectrum yields a flux of $(1.3 \pm 0.2) \cdot 10^{-6}/\text{TeV}/\text{m}^2/\text{s}$ at 200 GeV and a spectral slope of 4.5 ± 0.5 . Although the loss of events is around 8%, the error in the flux due to inhomogeneity stays well below the statistical one. As the dependence on the energy is negligible, the spectrum is included in the combined data set.

Set 4: July 2006 To these data the method presented in Dorner et al. [2008] has been applied to correct the flux for the atmospheric absorption due to SAL. Using the signal detection cuts (table 4.3, coefficients set B) in both cases, a signal has been detected with 5.0σ (figure A.4, upper plot) from the 8.5 hours of data, compared to 3.2σ (figure A.5, upper plot) found without correcting the data. The spectrum has been determined between 48 GeV and 600 GeV (coefficients set F). Fitting a power law to the spectrum yields a flux of $(1.4 \pm 0.3) \cdot 10^{-6}/\text{TeV}/\text{m}^2/\text{s}$ at 200 GeV and a spectral slope of 4.1 ± 0.3 (figure A.4, lower plot). Before applying the correction the result of a power law fit was a flux of $(9.5 \pm 2.3) \cdot 10^{-7}/\text{TeV}/\text{m}^2/\text{s}$ and a spectral slope of 4.6 ± 0.3 (figure A.5, lower plot). Although the low energy analysis could be applied thanks to the good quality of the data, for the low energy point an effect of the absorption can not be excluded, as for small energies events might be lost.

Set 5: March/April 2007 The data taken with the new FADC system have very good quality and from the 12 hours of good weather data a signal was found with 8.1σ significance (figure A.6, upper plot). A spectrum between 50 GeV and 900 GeV has been determined (figure A.6, upper plot). Fitting a power law to the spectrum between 75 GeV and 900 GeV, yields a flux of $(1.4 \pm 0.2) \cdot 10^{-6}/\text{TeV}/\text{m}^2/\text{s}$ and a spectral slope 3.8 ± 0.4 . Fitting the whole range down to 50 GeV the slope changes to 3.4 ± 0.2 .

4.3.2. Combined data set

The results of the single data sets are summarized in table 4.6 and the plots and spectral points are given in the appendix (tables A.5, A.6, A.7, A.8 and A.9 and figures A.1, A.2, A.3, A.4, A.5 and A.6). To compare the spectra of the single data sets, they are plotted together in figure 4.7 with different colors. Also the fits, quoted in table 4.6, are plotted in the corresponding colors. It is obvious that the spectra agree well within the errors, apart from the two data sets without low energy analysis. The spectra agree also well with the spectrum from Albert et al. [2007], which is indicated as dotted line in the figure.

Consequently the ϑ^2 distributions are combined and also a spectrum is determined with the stacking method described in 4.2.1. The combined ϑ^2 distribution yields 2282.3 excess events, 16286.7 background events and a scale factor of 0.35 (figure 4.8). From this a signal is obtained with 15.0σ significance, which is consistent with the 15.7σ obtained when adding the significances quadratically.

The combined spectrum is shown in figure 4.9 and also in figure 4.7 (black filled squares) for comparison. Fitting a power law between 75 GeV and 900 GeV yields a flux of $(1.4 \pm$

4. MAGIC observations

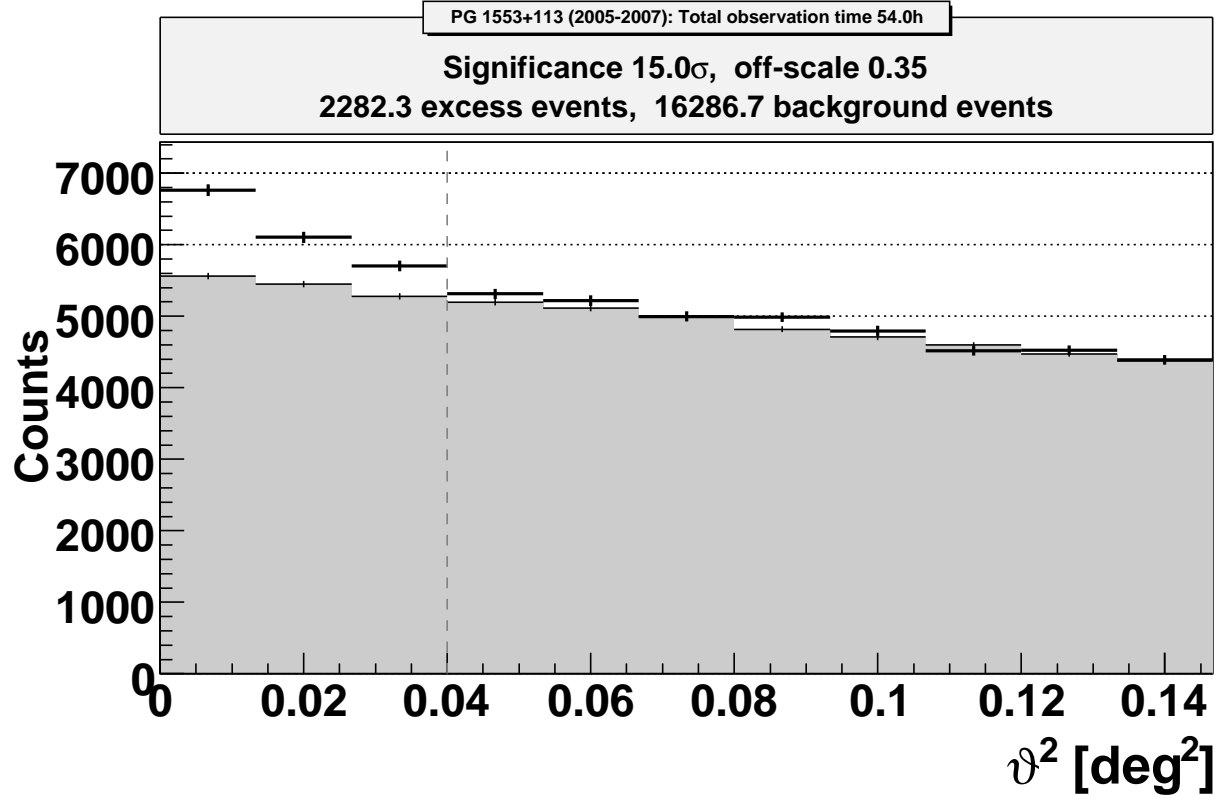


Figure 4.8.: ϑ^2 distributions (black crosses: signal, gray shaded area: background) for the complete data set of 54.0 hours. The cut in ϑ is indicated with a vertical gray dashed line.

$0.1) \cdot 10^{-6}/\text{TeV}/\text{m}^2/\text{s}$ at 200 GeV and a spectral slope of 4.1 ± 0.2 . Fitting down to 48 GeV the flux at 200 GeV stays the same, but the slope is determined to 3.7 ± 0.1 . In addition a power law with an exponential cutoff is fitted yielding a flux of $(9.4 \pm 7.8) \cdot 10^{-6}/\text{TeV}/\text{m}^2/\text{s}$, a slope of 2.5 ± 0.6 and a cutoff energy of (123 ± 60) GeV. The large errors of the latter fit result from the larger error of the high energy point.

4.3.3. Light curves

To study the VHE variability light curves with different time binning have been determined as described in section 4.2.1. Three light curves with the integral flux above 150 GeV are shown in figure 4.10.

The upper plot is a light curve where each bin corresponds to one data set, resulting in one bin in 2005 and 2007 each and three bins in 2006. Fitting a constant yields an integral flux of $(2.6 \pm 0.2) \cdot 10^{-11} \text{ cm}^{-2}\text{s}^{-1}$ above 150 GeV. The fit probability for fitting a constant is 73 %.

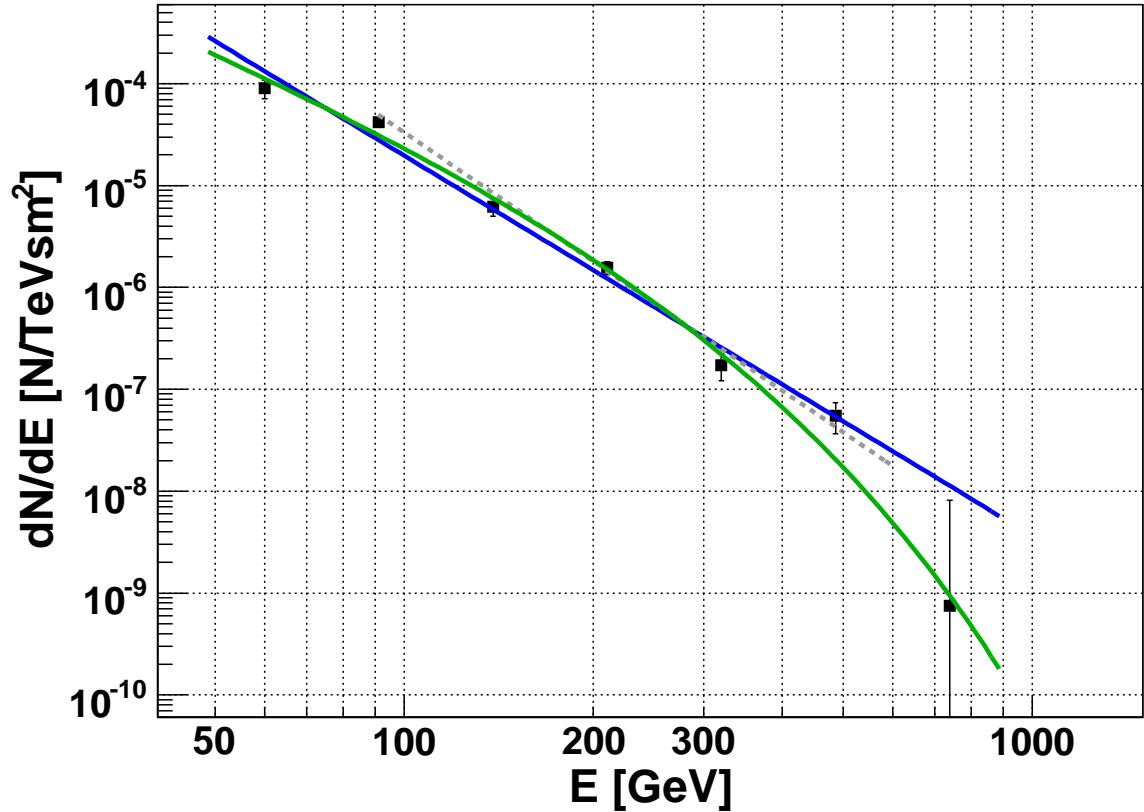


Figure 4.9.: Combined differential spectrum from 54 hours of data. A power law fit between 48 GeV and 900 GeV is plotted in blue. For comparison the result of Albert et al. [2007] is plotted as gray dotted line. In addition a fit of a power law with an exponential cutoff is plotted (green).

For the middle plot, the two bigger data sets in 2006 have been subdivided yielding significances of five to six σ . Set 2 is splitted in three and Set 3 into two data sets. From the latter, the first set is the data with the strongest inhomogeneity. Therefore the slightly lower flux might be due to the loss of events of almost 10 %. Also here, the data is consistent with a constant flux (probability 78 %). The fit gives a flux of $(2.5 \pm 0.2) \cdot 10^{-11} \text{ cm}^{-2}\text{s}^{-1}$.

To check if the source shows internight variability or a strong flare of only one of the two days, a daily light curve is determined (lower plot). For this, the five data sets have been subdivided such that each small data set includes the sequences of one night. For the first two sets, the Off data was chosen such that for each small set the scale factor is approximately the same and the Off data is close in time to the On data. Not for all sets Off data from the same night is available, but apart from some exceptions the Off data is from within one or two nights around the On data. In total the daily light curve includes 44 nights. The fit probability for fitting a constant is 82 %.

4. MAGIC observations

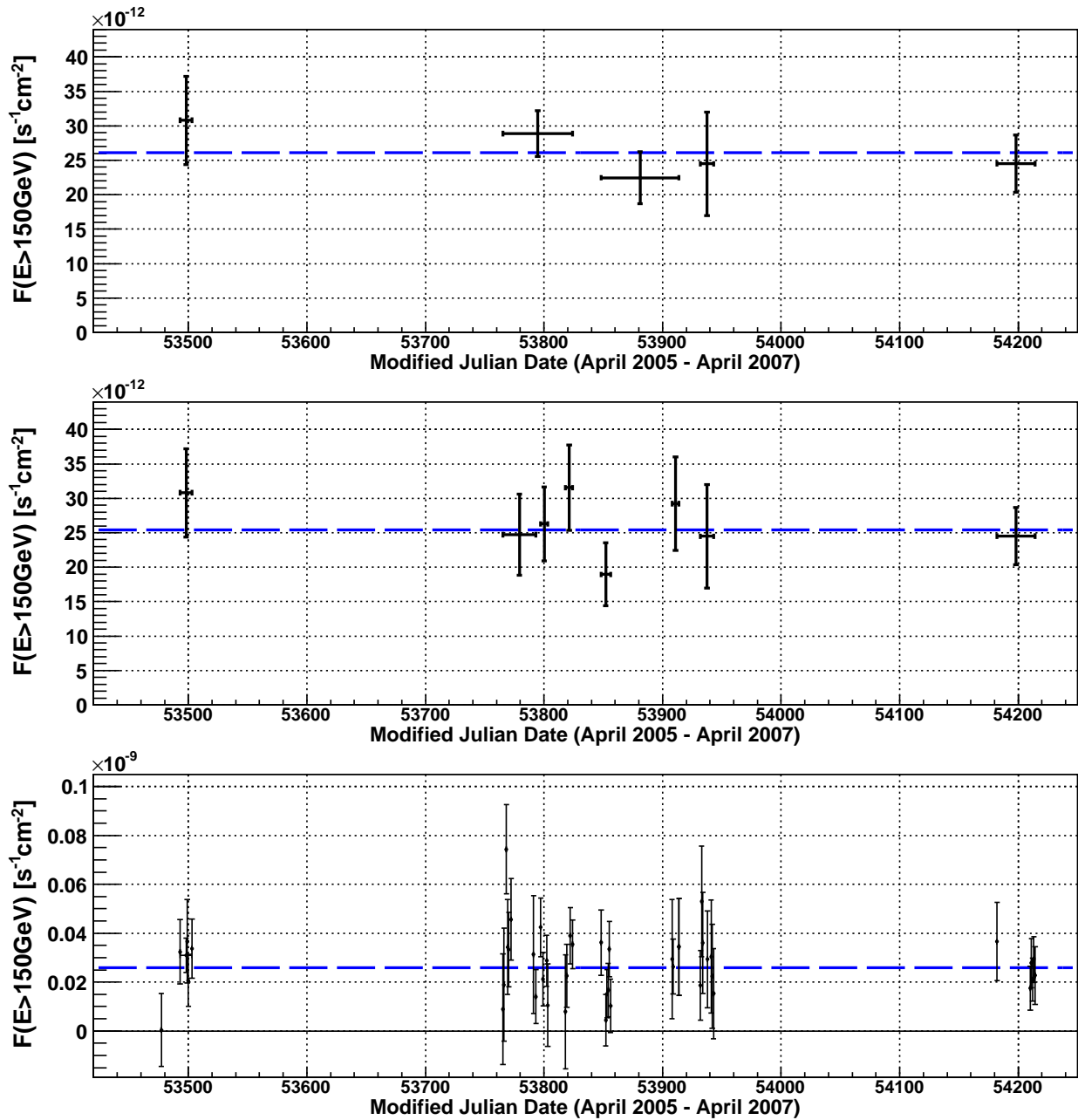


Figure 4.10.: Integral flux above 150 GeV. The upper light curve shows one point per data set, for the middle one Set 2 and 3 have been subdivided and the lower plot shows a daily light curve. The error bars in the x-direction represent the observation time. A fit is plotted as blue dashed line.

4.3.4. Low energy results

As explained in section 4.2.2, the low energy cuts can be applied only if the data has a good quality. For three of five data sets, the low energy analysis could be performed and spectra down to 50 GeV could be determined, providing the first results at these energies. Also the combined spectrum, which will be used for further studies covers the energy range between 50 GeV and 900 GeV.

Compared to the power law fit between 75 GeV and 900 GeV the point at 60 GeV is lower. Consequently, the slope decreases from 4.1 ± 0.2 to 3.7 ± 0.1 , if the point is included in the fit.

4.3.5. Comparison to H.E.S.S. results

From 2005 and 2006 also H.E.S.S. measurements are available [Aharonian et al., 2008]. In 2005 observations in May and August were done, and in 2006 in April/May and July.

Combined data set From 24.8 hours of data in total a signal with 10.2σ significance was found, and a combined spectrum between 225 GeV and 1.3 TeV was determined. Above 1 TeV three upper limits are given. A power law fit yields a flux of $(4.68 \pm 0.49) \cdot 10^{-7} \text{ m}^{-2}\text{s}^{-1}$ at 300 GeV and a slope of 4.46 ± 0.34 . Assuming a constant flux and slope, this flux corresponds to $(2.86 \pm 0.31) \cdot 10^{-6} \text{ m}^{-2}\text{s}^{-1}$ at 200 GeV, which is about twice the flux determined from a fit to the MAGIC data (see table 4.6). To compare the two spectra, they are shown in figure 4.11 (upper plot). At 300 GeV the H.E.S.S. points (blue) are slightly above the MAGIC points (black). Apart from that, the two spectra agree well and can be fitted together. A power law fit yields a flux of $(1.7 \pm 0.1) \cdot 10^{-6} \text{ m}^{-2}\text{s}^{-1}$ at 200 GeV and a slope of 3.7 ± 0.1 including the low energy point at 60 GeV. Assuming this slope for an extrapolation of the H.E.S.S. fit a flux at 200 GeV of $(2.1 \pm 0.2) \cdot 10^{-6} \text{ m}^{-2}\text{s}^{-1}$ is obtained. This is slightly above the fit result of the combined spectrum. The reason for this might be systematic errors in the energy reconstruction due to simulated data (see section 2.2.6) not fitting properly the real data. Fitting a power law with an exponential cutoff between 48 GeV and 900 GeV to the combined spectrum yields a flux of $(5.7 \pm 2.3) \cdot 10^{-6} / \text{TeV}/\text{m}^2/\text{s}$, a slope of 2.8 ± 0.3 and a cutoff energy of $(203 \pm 72) \text{ GeV}$.

Simultaneous data Both MAGIC and H.E.S.S. have observed PG 1553+113 in 2005 and 2006. Part of the data were taken simultaneously.

May 2005 From May 2005 quasi-simultaneous data of MAGIC and H.E.S.S. is available. H.E.S.S. measured for almost five hours and found a signal with 5.5σ significance. A spectrum has been determined only from the combined set of May and August 2005 (7.6 hours, 6.0σ). The slope of 4.0 ± 0.6 determined with a power law fit agrees within the errors with the MAGIC result.

4. MAGIC observations

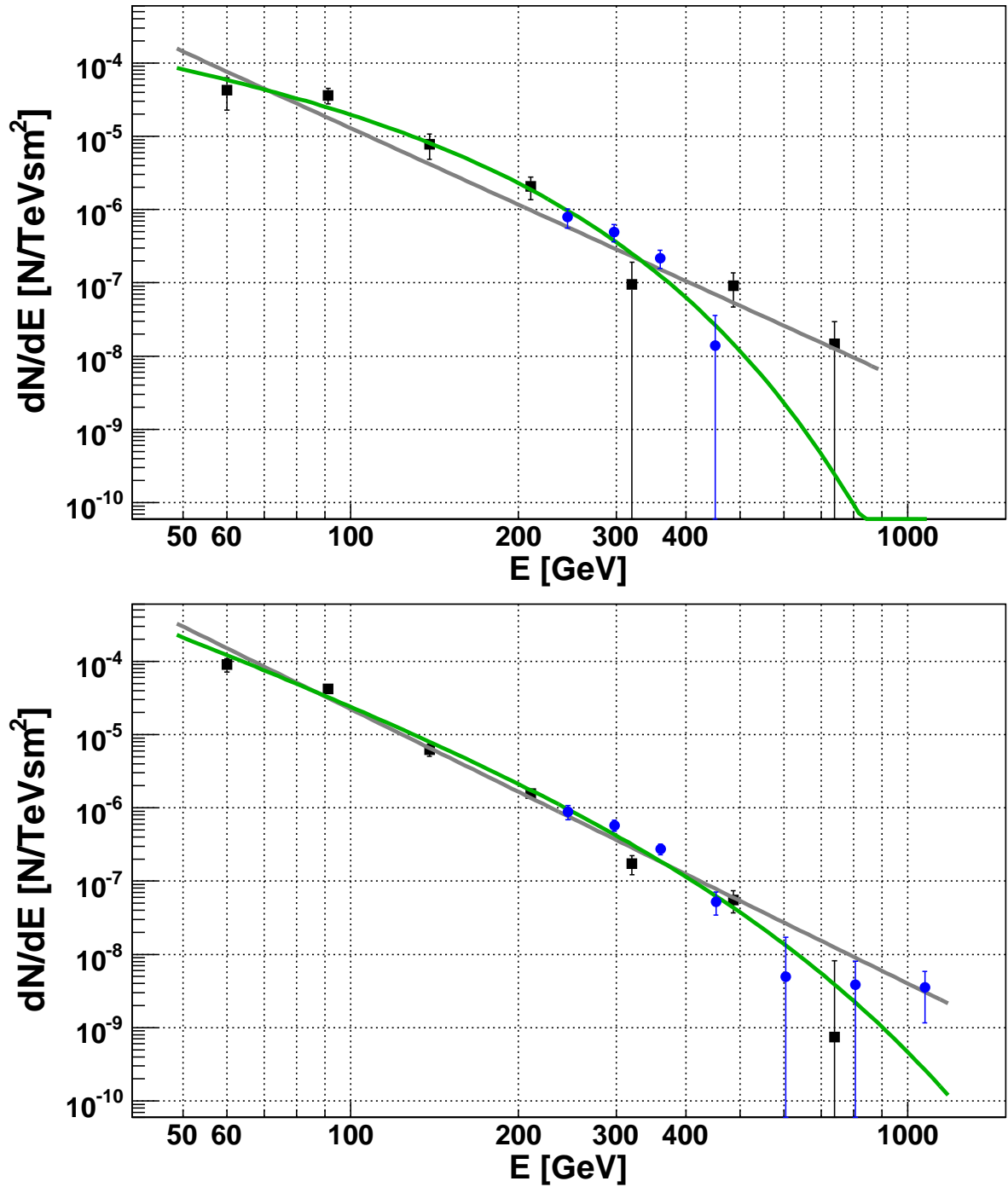


Figure 4.11.: Comparison of H.E.S.S. (blue points) and MAGIC (black squares) differential spectra. The lower plot shows the combined spectra, the upper those of July 2006. A power law (dark gray line) and a power law with cutoff (green line) are fitted to the combined spectrum (MAGIC and H.E.S.S.).

July 2006 Like MAGIC also H.E.S.S. observed PG 1553+113 during the MWL campaign in July 2006 [Aharonian et al., 2008]. From 10.1 hours in total, 3.1 hours were taken simultaneously with the x-ray data yielding a signal of 3.9σ significance. To have enough statistics the whole sample of July was used to determine a spectrum between 225 GeV and 535 GeV. In addition three upper limits are given, ranging up to 1.3 TeV. Fitting a power law to this spectrum yields a slope of 5.0 ± 0.7 and a flux of $(3.6 \pm 0.6) \cdot 10^{-7}$ /TeV/m²/s at 300 GeV, corresponding to $(2.7 \pm 0.5) \cdot 10^{-6}$ /TeV/m²/s at 200 GeV. This is again almost a factor two higher than the result of the fit to the MAGIC data. Therefore also for this set of data, the comparison between the MAGIC (black dots) and the H.E.S.S. spectrum (blue dots) is shown in figure 4.11 (lower plot). Apart from the three points with very large errors, the spectra agree within the errors. The larger slope and flux of the H.E.S.S. fit comes probably from the lower point at 450 GeV. A power law fit between 48 GeV and 900 GeV yields a flux of $(1.2 \pm 0.2) \cdot 10^{-6}$ /TeV/m²/s at 200 GeV and a slope of 3.5 ± 0.1 , but it does not fit the data very well (probability 0.3%): apart from the low energy point and two points with very large errors, all points are above the fit. Although fitting a power law with an exponential cutoff to the combined spectrum yields a better probability (10%), the fit parameters are not well determined with a flux of $(4.1 \pm 4.8) \cdot 10^{-5}$ /TeV/m²/s at 200 GeV, a slope of 1.0 ± 0.8 and a cutoff energy of (69 ± 24) GeV. Both telescope have observed a quite short time in July 2006. The low statistics in the spectra might be a reason for the bad quality of both fits.

4. *MAGIC* observations

5. PG 1553+113

*Variabel ist die Quelle nicht
Im neuerschlossnen Gammalicht
Radio, optisch, Röntgenstrahlen
Den ersten Peak des Blazars malen
Ähnlich den Synchrotronverwandten
Zeichnen den zweiten Gammaquanten
Die Rotverschiebung nimmt man an
Damit man modelieren kann*

— Daniela Dorner.

Its unknown redshift suggested the HBL PG 1553+113 as target for many observations. From different wavelengths and various surveys PG 1553+113 is also known under different names, e.g. HB89 1553+113, 1ES 1553+11.3 or RX J1555.7+1111. An extended list of names is given in table A.1. A selection of results from various observations is presented. Since 2005, the source is also studied in the VHE range. The above shown results are included in the set of historical data.

5.1. Discovery and first observations

PG 1553+113 was discovered in the Palomar-Green Survey of UV-excess stellar objects [Green et al., 1986]. Measurements with the multichannel spectrometer at the 5-meter Hale telescope revealed no discrete spectral features. The optical flux in a historical light curve since 1900, obtained from archival photo plates, ranges from 15.0 mag to 13.2 mag. In 1940 the most rapid variation was observed: 0.7 mag within two days. According to these findings the source was suggested to be a BL Lacertae object [Miller et al., 1988]. Therefore PG 1553+113 was observed with the IUE in 1982, 1986, 1987 and 1988 [Falomo and A. Treves, 1990; Miller et al., 1988]. Two different flux levels were measured and for part of the data simultaneous measurements in the NIR and optical are available. A spectrum from the NIR to the UV is given showing a spectral break around 10^{15} Hz. By comparing its spectral characteristics to samples of radio and x-ray selected BL Lac objects, PG 1553+113 was found to be closer to the latter group [Falomo and A. Treves, 1990]. In Nieppola et al. [2006] it was classified as IBL due to a estimated peak frequency of $\log(\nu_{peak}) = 16.49$.

5.2. X-ray observations

In the last ten years various x-ray observations of PG 1553+113 were done.

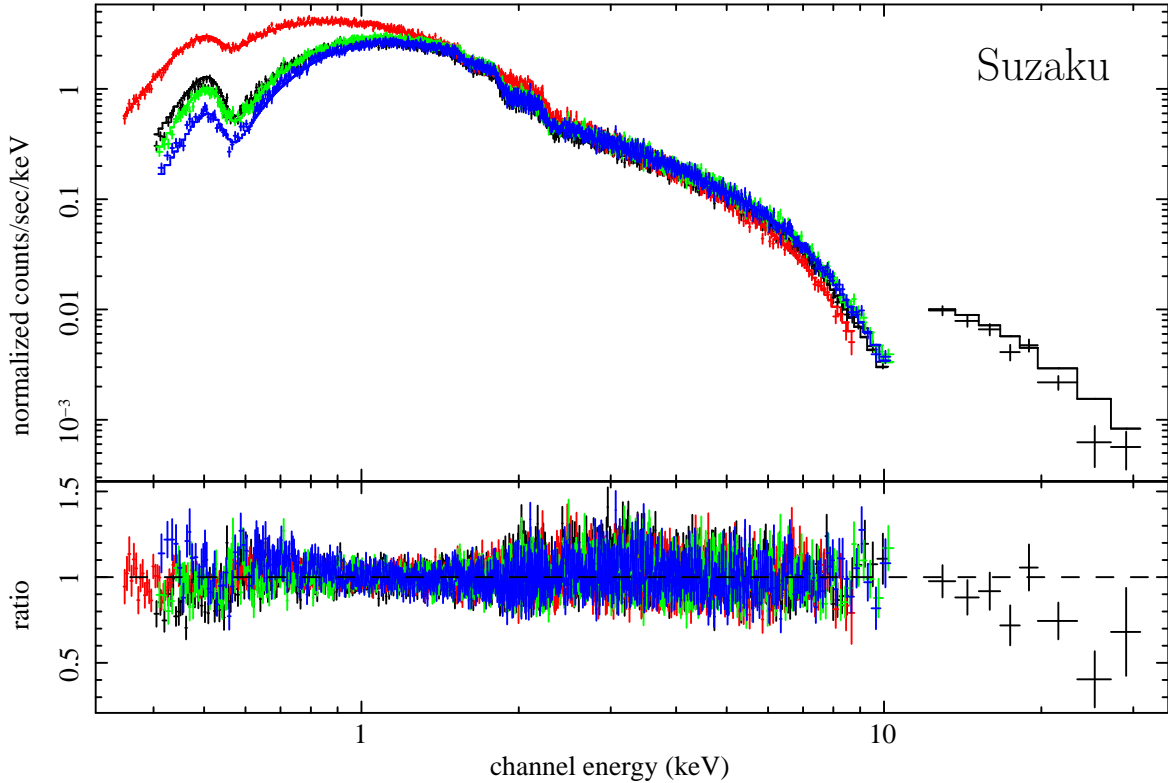


Figure 5.1.: Suzaku spectrum of the MWL campaign in July 2006 [Reimer et al., 2008].

BeppoSAX On February 5th 1998, the source was observed by the BeppoSAX satellite for 4.5 ksec with the LECS, 10.6 ksec with the MECS and 4.7 ksec with the PDS. From the last no signal could be determined, the LECS measured 26.38 ± 0.76 counts/sec and the MECS 15.3 ± 0.39 counts per second. Fitting a broken power law to the spectrum yields slopes of $\Gamma_1 = 1.96$ and $\Gamma_2 = 2.79$ and a break energy of 1.01 keV [Donato et al., 2005].

RXTE Triggered by an optical flare, ToO observations were done with the satellite RXTE. Two to three observations of 3 ksec each were carried out between April 21st and May 12th 2003, 46 observations in total. During the campaign, a flare was observed, beginning on April 29th/30th and peaking on May 10th. While the flux was $0.5 \cdot 10^{-11}$ erg cm⁻²s⁻¹ before the flare, it reached $1.2 \cdot 10^{-11}$ erg cm⁻²s⁻¹ at the peak [Osterman et al., 2006].

Swift In 2005 PG 1553+113 was observed twice by the Swift satellite. On April 20th data were taken with the XRT in x-rays and with the UVOT in optical and UV. From October 6th

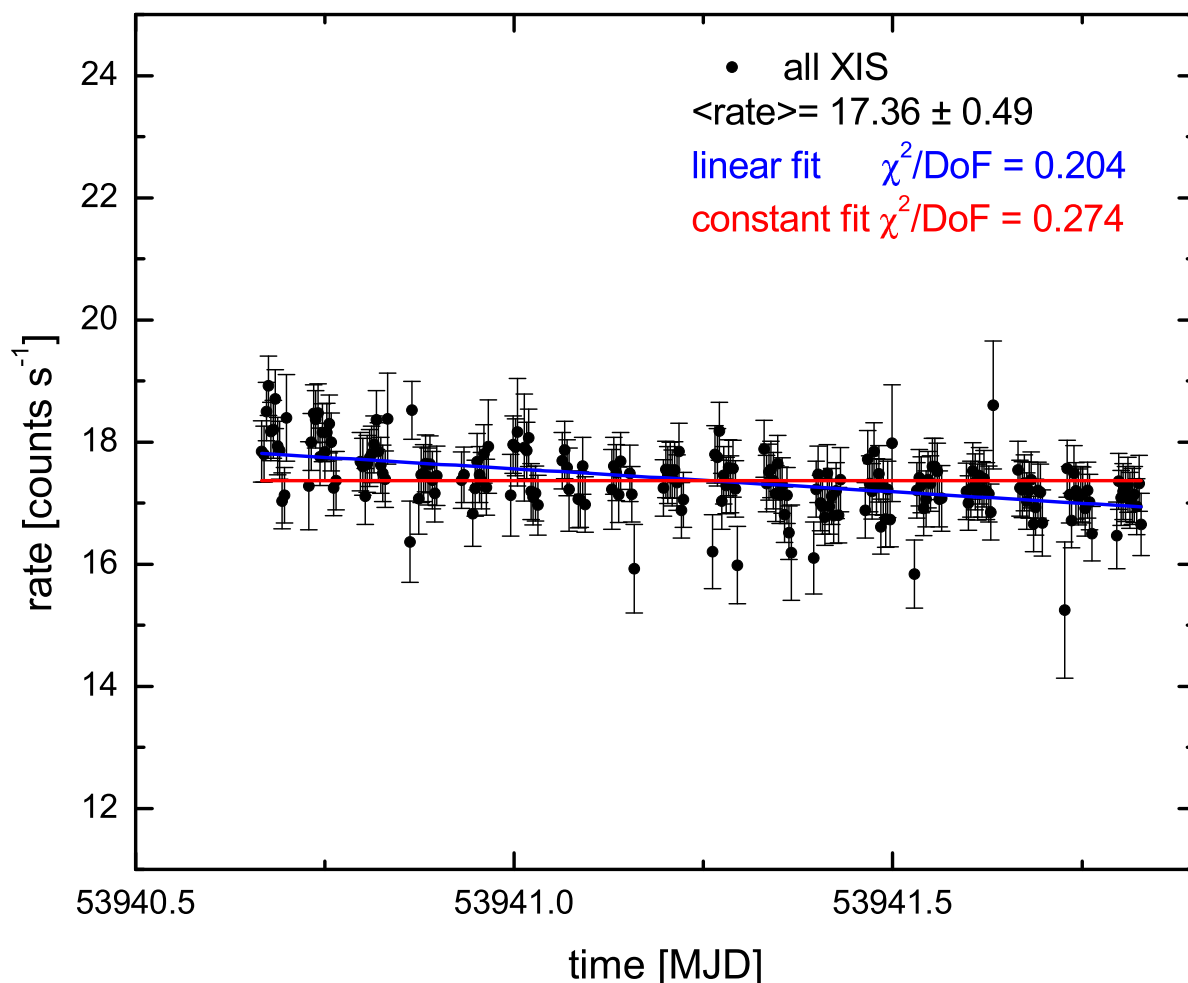


Figure 5.2.: Suzaku light curve of the MWL campaign in July 2006 [Reimer et al., 2008].

and 8th, x-ray and UV data are available. While in April a flux of $2.1 \cdot 10^{-11} \text{ erg cm}^{-2}\text{s}^{-1}$ was measured between 2 keV and 10 keV, the flux was more than three times higher in October with $6.9 \cdot 10^{-11} \text{ erg cm}^{-2}\text{s}^{-1}$ (6.10.2005) and $6.7 \cdot 10^{-11} \text{ erg cm}^{-2}\text{s}^{-1}$ (8.10.2005). The determined break energy of the spectrum depends on whether the UV and optical data is included in the fit. Considering only the x-ray data, the curvature determined from a log-parabolic fit is comparable for the measurement in April and the first in October and slightly smaller for the second in October. If the UV data is included in the fit, the curvature is significantly lower [Tramacere et al., 2007].

Suzaku PG 1553+113 was observed by the Suzaku satellite in July 2006 for 41.1 ksec with the XIS and HXD instruments. For the first time a spectrum up to 30 keV was determined (figure 5.1), which is the highest ever measured energy point in x-rays. Compared to

5. *PG 1553+113*

previous x-ray data for the first time a long set of continuous data was taken, but no short time variability was found (see figure 5.2). The flux level, $3.4 \cdot 10^{-11}$ erg cm⁻²s⁻¹, is between the high flux measured by Swift in October 2005 and the low flux seen with RXTE in 2003 [Reimer et al., 2008].

5.3. Gamma-ray observations

The first observations of PG 1553+113 in the gamma-ray regime were done in 1991 and 1992 with the EGRET experiment on board the CGRO. The source was not detected, but an upper limit of 1.8 photons/GeV/cm²/s above 100 MeV has been determined from measurements of the all sky survey.

From the first VHE observations, done in April to May 2002 by the Whipple 10 m telescope, also only an upper limit of $1.62 \cdot 10^{-11}$ erg cm⁻²s⁻¹ (corresponding to 19% Crab flux) above 390 GeV was obtained.

As described in section 4.3.5, the source was observed again in the VHE range with the current generation of IACTs in April and May 2005. From these data a hint of signal was found. Consequently, further observations were scheduled in August 2005 (H.E.S.S.) and January 2006 (MAGIC), and the detection of the source was confirmed [Aharonian et al., 2006; Albert et al., 2007]. A re-analysis of these first MAGIC data and the new results of the data starting from April 2006 have been presented in section 4.3. During the observations of three years no significant variability in the flux or the spectral shape was found.

5.4. Other observations

In the IR range, observation from 2MASS are available. Also the observations with the SINFONI instrument at the VLT aiming at the determination of the redshift were in the IR range.

In the radio regime measurements at various energies are available, among others from the Metsähovi radio telescope, the VLA and the Green Bank telescope. In Rector et al. [2003] the radio structure is studied from the VLA and VLBA data. While the VLBA 5 GHz data of May 17th 1997 show a faint, diffuse lobe, in the deep VLA map (1.4 GHz) no jet structure is found.

Naturally there are plenty of optical observations. Here only the KVA data is mentioned, as they are taken simultaneously with the MAGIC data and therefore used for the studies. With its 35 cm telescope the KVA is monitoring the AGN observed by the MAGIC telescope providing simultaneous optical data.

5.5. Redshift

The originally determined redshift of $z = 0.36$ [Miller and Green, 1983] turned out to be a misinterpretation [Falomo and A. Treves, 1990]. In all following measurements no emission or absorption lines could be found, and also the host galaxy is not resolved [Scarpa et al., 2000]. After the detection in the VHE range, dedicated observations in the NIR have been carried out with the SINFONI spectrometer at the VLT, but also here no lines were found [Aharonian et al., 2008].

Consequently, up to now no redshift could be determined for PG 1553+113, but lower limits have been calculated from the absence of lines and the fact that the host galaxy could not be resolved; and upper limits from the measured VHE spectra and assumptions on the intrinsic spectrum of the source.

Lower Limits In [Carangelo et al., 2003] a lower limit was determined from an optical spectrum measured at the **E**uropean **S**outhern **O**bservatory (ESO). From the absence of lines (EW of $\approx 0.1 \text{ \AA}$) and the assumption that the source is hosted by a typical BL Lac galaxy, it was calculated to $z < 0.3$.

In Sbarufatti et al. [2005] a lower limit of $z = 0.78$ was given using the HST images. More recent results report a lower limit of $z = 0.09$ [Sbarufatti et al., 2006]. Here the EW_{min} from the absence of lines and assumptions on the luminosity of the host galaxy are used. A reanalysis of the HST images to constrain the magnitude of the host galaxy leads to an lower limit of $z = 0.25$ [Treves et al., 2007].

With similar methods slightly different results are obtained, which are all in the range between $z = 0.09$ and $z = 0.3$.

Upper Limits With the detection of PG 1553+113 at VHE, upper limits got possible by the constraints from the **M**etagalactic **R**adiation **F**ield (MRF) and assumptions on the intrinsic spectrum of the source. The first upper limit has been determined from the measured VHE spectrum and the assumption that the slope of the intrinsic spectrum is not smaller than 1.5 in Aharonian et al. [2006] with $z < 0.74$. With the same method a limit of $z < 0.68$ has been determined using the combined MAGIC and H.E.S.S. spectrum [Mazin and Goebel, 2007]. A stricter upper limit has been inferred assuming that there is no spectral break in the intrinsic spectrum. With this method an upper limit of 0.42 has been determined [Mazin and Goebel, 2007].

5.6. Multi-wavelength studies

To study the **S**pectral **E**nergy **D**istribution (SED) of the source, MWL observations are very important. Due to the extreme variability of blazars, these data should be taken simultaneously.

For PG 1553+113, in the past already two MWL campaigns have been carried out. In 2003 the source was not yet discovered in the VHE, but the first peak of the SED was

5. PG 1553+113

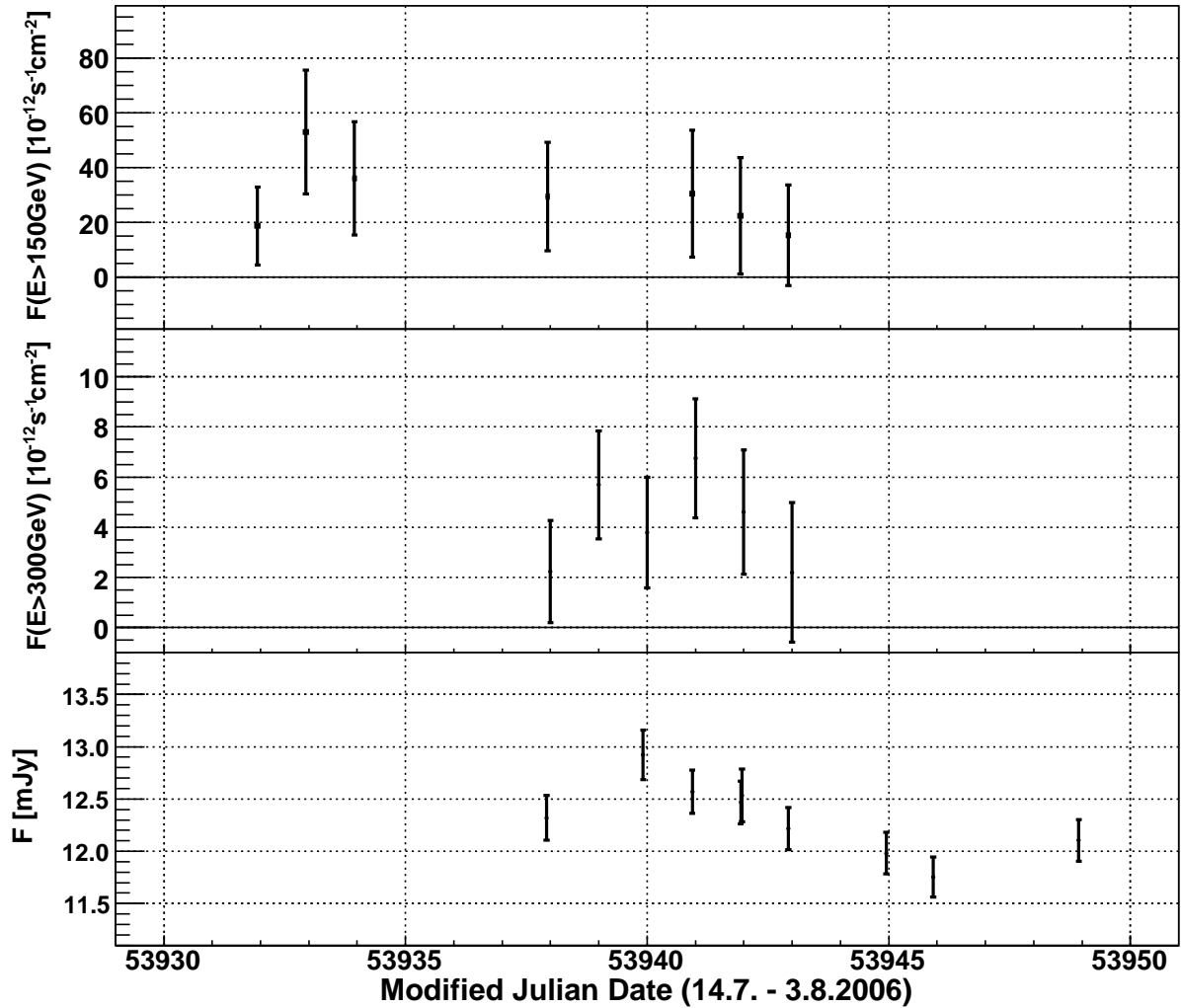


Figure 5.3.: Daily light curves of a MWL campaign in July 2006: MAGIC integral flux above 150 GeV (upper plot), HESS integral flux above 300 GeV (middle plot) and optical light curve (lower plot).

measured at radio, optical and x-ray energies. After the detection by IACTs, a campaign was conducted, including measurements at optical, x-ray and VHE.

Campaign 2003: X-ray, optical and radio observations In April and May 2003 a MWL campaign of three weeks was performed. During this time PG 1553+113 was observed with the x-ray satellite RXTE between 2 keV and 10 keV, in the optical B- and R-band and in the radio at 37 GHz, 14.5 GHz and 4.8 GHz. The optical observations were done with several telescopes (Abastumani Observatory, Lowell Observatory and Braeside Observatory). In the radio, high frequency observations were done by the Metsähovi Radio Observa-

tory, lower frequency observations were obtained with the 26 m dish at the **University of Michigan Radio Astronomy Observatory (UMRAO)**.

The x-ray observations were triggered by an optical flare. Subsequently, a x-ray flare of about two weeks was observed. While the x-ray flux more than tripled in that time, the optical flux was lower than before. After the end of the x-ray campaign another optical flare occurred. In the radio observations no significant changes in the flux were observed. The optical data showed no intraday variability.

After the MWL campaign the radio observations were continued until September with UMRAO. In late July a slight rise in the radio flux was observed, which was coincident with a higher flux in the optical R-band [Osterman et al., 2006].

Campaign July 2006: X-ray, optical and VHE observations In July 2006 x-ray, VHE and optical observations were coordinated in a MWL campaign [Reimer et al., 2008]. In the x-ray regime, the Suzaku satellite took continuously 41.1 ksec of data on July 24th and 25th. The VHE data are taken between July 15th and July 27th (MAGIC) and July 22nd and July 27th (H.E.S.S.). In addition, optical data of the KVA are available simultaneously to the MAGIC data. As described in section 4.3.5, the data of the two VHE experiments agree well with each other and also with previous VHE results. In a daily light curve, no significant variability is found (see figure 5.3), neither in the integral flux above 300 GeV (H.E.S.S., middle plot) nor in that above 150 GeV (MAGIC, upper plot). Only part of the VHE data is simultaneous with the x-ray data. These sets of 3.1 hours (H.E.S.S.) and 2.1 hours (MAGIC) are too small to determine a reliable spectrum. As there are no changes in the spectral shape and in the flux, the whole VHE sets of 8.5 hours (MAGIC) and 10.1 hours (H.E.S.S.) can be used for MWL studies.

5.7. Variability

The results of these MWL campaigns can be used to study the variability of PG 1553+113. In addition, the VHE flux can be studied for the complete set of MAGIC and H.E.S.S. data.

In July 2006, for the first time a long, continuous observation was carried out in the x-ray regime [Reimer et al., 2008]. As shown in figure 5.2, the x-ray data of Suzaku shows no short time variability. On the other hand, variability in the x-ray regime is known from the fact that different measurement from BeppoSAX, Swift and RXTE show different flux levels. In addition, RXTE recorded a flare during the MWL campaign in 2003 [Osterman et al., 2006]. In the radio, flux variations have been observed in summer 2003 as discussed above.

From the MWL measurements no correlation between different energy ranges could be found. Consequently, no conclusions on the origin of the high energy photons can be drawn.

Figure 5.4 shows daily light curves from April 2005 to April 2007, i.e. the time range in which MAGIC data are available. The VHE flux above 150 GeV (MAGIC, upper most

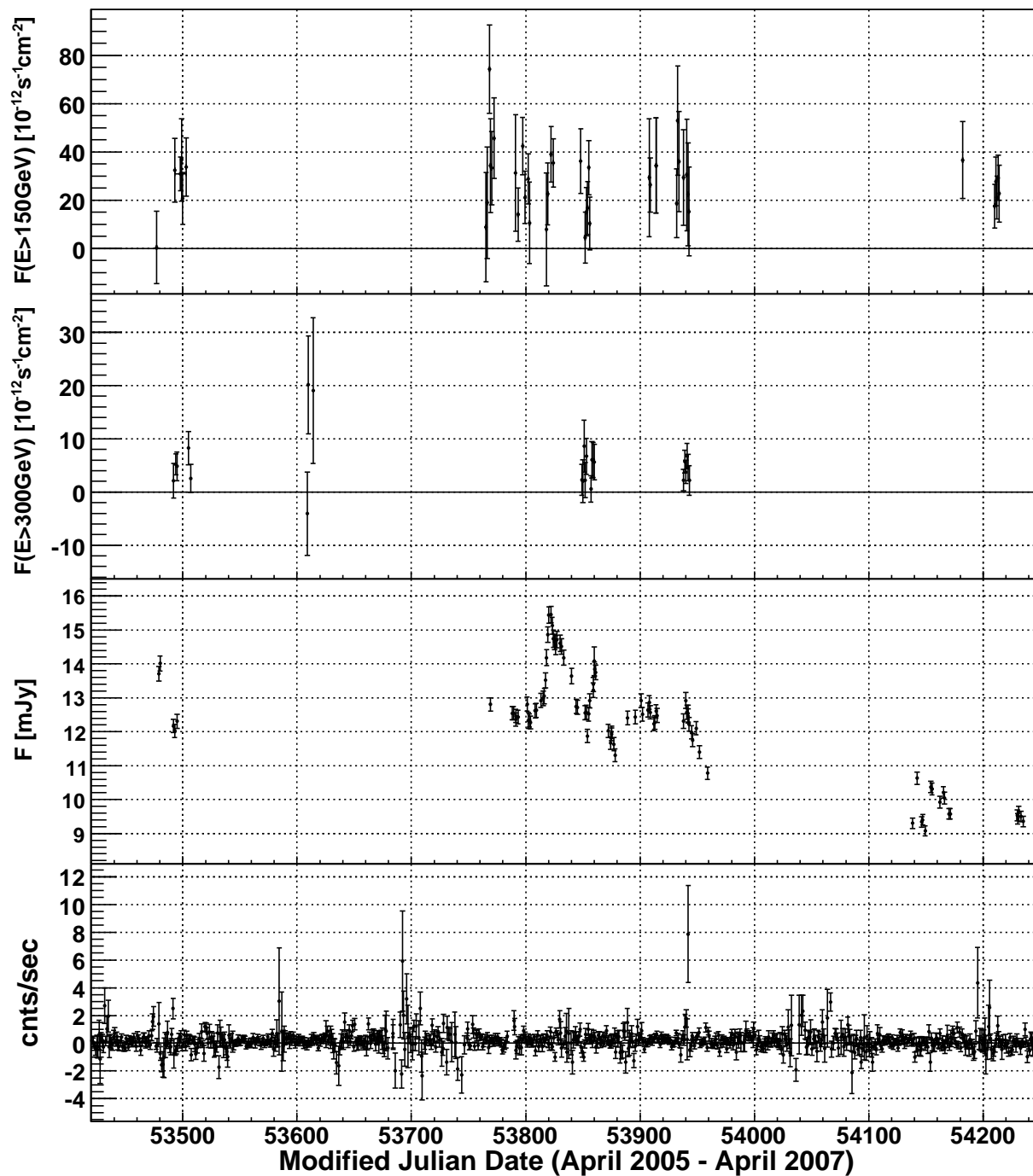


Figure 5.4.: Daily light curves of integral flux above 150 GeV (uppermost panel, MAGIC), above 300 GeV (second panel from the top, H.E.S.S.), optical light curve from the KVA (second panel from the bottom) and x-ray count rates of ASM on board RXTE (bottom panel).

panel), above 300 GeV (H.E.S.S., second panel from the top), the optical flux (KVA, second panel from the bottom) and count rate of the ASM of the RXTE satellite (bottom panel) are plotted. Only the optical light curve shows variability. The ASM measurements shows neither a significant flux nor a significant variability. Also for the VHE measurements, the statistics on daily basis is low, but strong flares and inter-night variability can be excluded. As discussed in section 4.3.3, also the flux determined from larger time intervals is consistent with a constant flux. While from other AGN VHE variability is known, PG 1553+113 shows neither a significant variability nor a spectral change during the observations between April 2005 and April 2007.

5.8. Intrinsic spectrum

The intrinsic spectrum of a source can be determined taking into account the influence of the Metagalactic Radiation Field.

5.8.1. Metagalactic Radiation Field

On their way from the source to the observer, high energy photons interact with low energy photons of the extragalactic background radiation. Consequently, the VHE radiation of blazars is attenuated. To calculate the intrinsic spectrum, a correction for this absorption has to be applied to the observed spectrum.

The MRF at $z = 0$ is commonly referred to as **Extragalactic Background Light** (EBL). There are several models available discussing the effect on the passing photons.

In Kneiske et al. [2002] a semi-empirical model for the MRF is described taking into account the stellar light produced and reprocessed in evolving galaxies. Based on this, the gamma-ray attenuation due to pair production in photon-photon scattering can be calculated. Using on the one hand data from galaxy number counts at optical and IR wavelengths and on the other hand direct measurements of the EBL, a set of models is computed [Kneiske et al., 2004]. From these models, the optical depth for pair creation $\tau_{\gamma\gamma}(E, z)$ along the line of sight is calculated. The impact on the spectrum can be described as follows:

$$F_{obs}(E) = F_{int}(E) \cdot e^{-\tau_{\gamma\gamma}(E, z)} \quad (5.1)$$

As the optical depth depends on the redshift, for PG 1553+113 a redshift has to be assumed before applying the correction.

For deabsorbing the observed spectrum of PG 1553+113, the best-fit model presented in [Kneiske, 2007] has been used. Figure 5.5 shows the measured spectrum and several spectra deabsorbed with different assumed redshifts. The different spectra with redshifts between 0 and 0.7 are plotted in different colors.

5.8.2. Constraints on the redshift

While usually the measured spectra of VHE Blazars are used to draw conclusions on the EBL, here assumptions on the intrinsic spectrum and the EBL help to constrain the

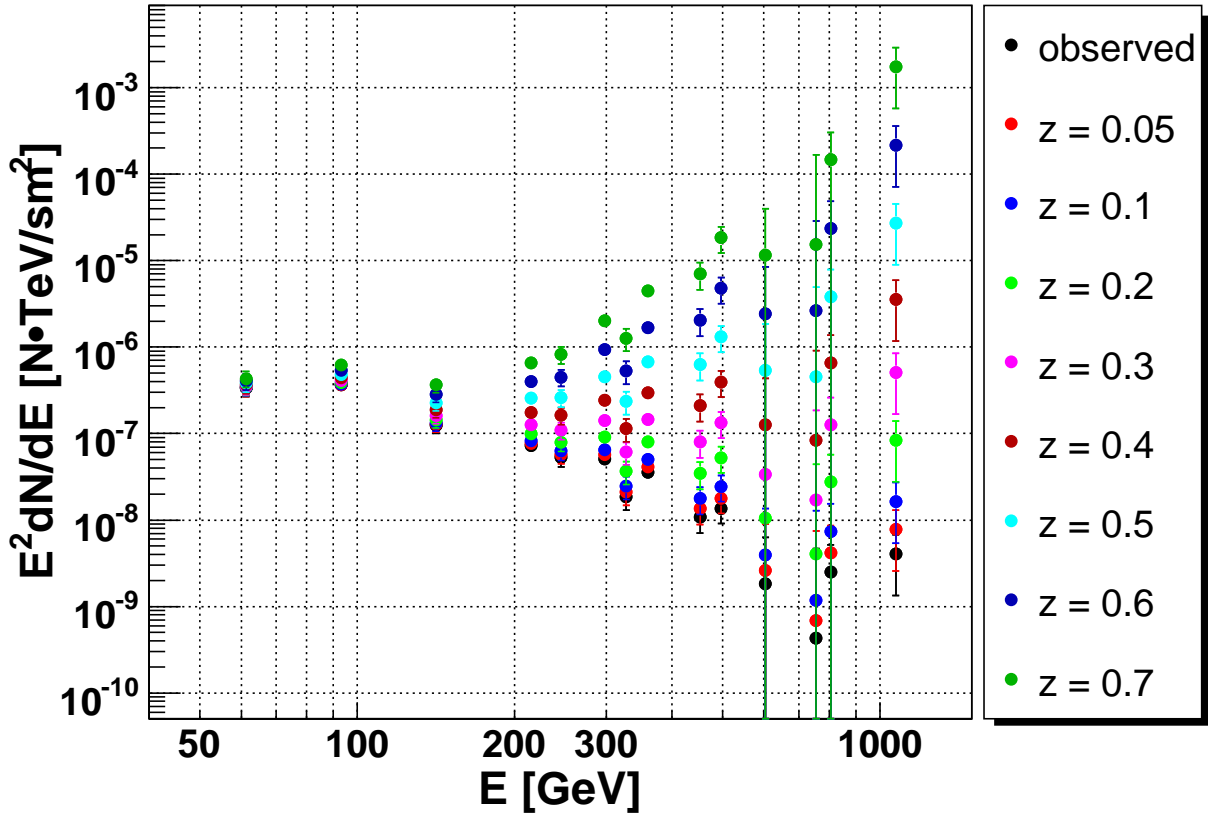


Figure 5.5.: Deabsorbed spectra of the combined MAGIC and H.E.S.S. data sets with the assumption of redshifts between 0.05 and 0.7. The measured spectrum is plotted in black.

redshift of the source. Therefore, the deabsorption is done with different assumed redshifts, as shown in figure 5.5, but with finer binning in redshift (0.01 steps). To the deabsorbed spectra a power law is fitted. The determined intrinsic photon index Γ is plotted versus redshift (figure 5.6). Assuming that the intrinsic photon index should not be harder than 1.5, an upper limit on the redshift of $z < 0.74$ (95% confidence level) can be deduced. Using the other five models from Kneiske et al. [2004], the upper limit for the redshift is between 0.64 and 0.87. Obviously the determined redshift depends on the one hand on the EBL model used and on the other hand on the limit assumed for the intrinsic slope.

5.9. Broadband spectral energy distribution

Summarizing all data from radio to VHE in a νF_ν versus ν plot, provides a broad band Spectral Energy Distribution (SED). In figure 5.7 the SED including the combined VHE spectra is shown.

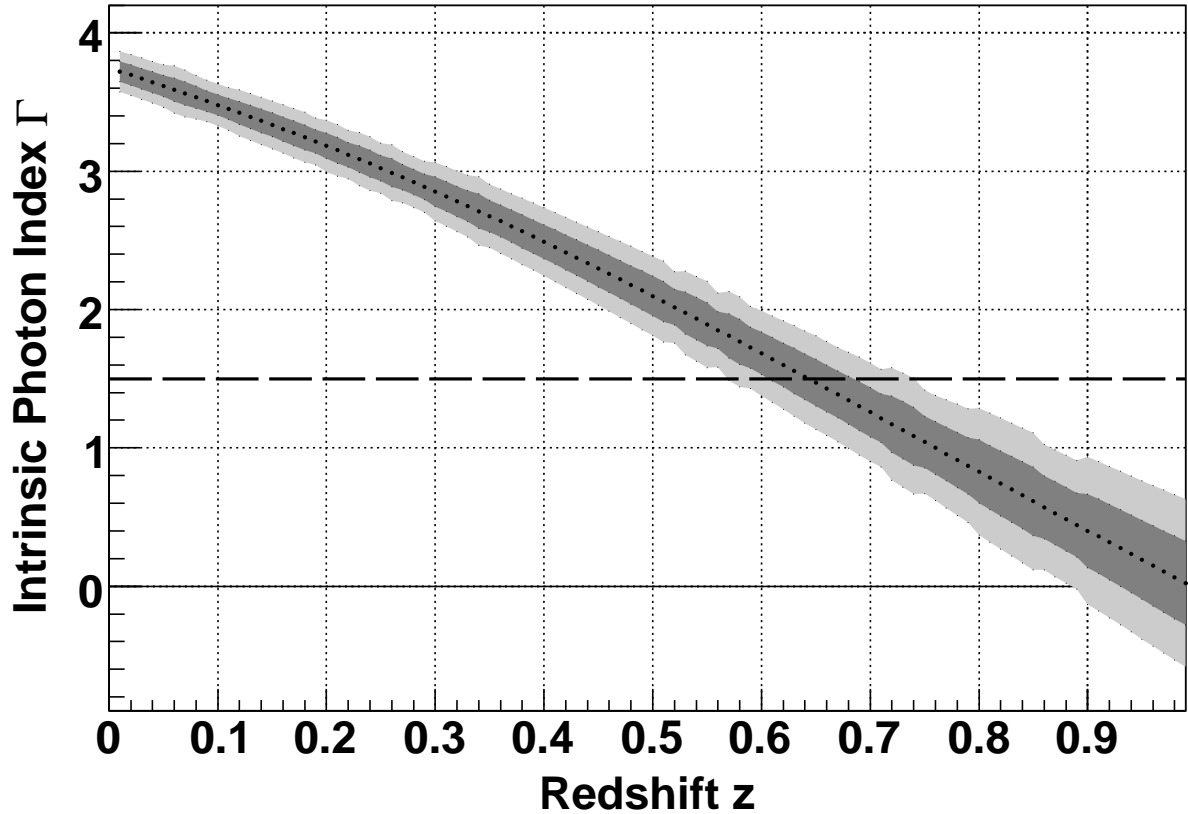


Figure 5.6.: Constraints on the redshift of PG 1553+113. The intrinsic photon index Γ , determined by deabsorbing the measured spectrum, is plotted versus the assumed redshift z . The gray shaded areas represent the one (dark gray) and two (light gray) sigma confidence belts. $\Gamma = 1.5$ is marked with a dotted line.

Apart from the VHE data, the SED includes x-ray data of Suzaku and BeppoSAX (described in section 5.2). In addition to the simultaneous data from KVA, there are data of the GSC2 in the optical [Morrison et al., 2001]. In the IR, data in the J, H and K band from 2MASS are available [Chen et al., 2005]. The radio regime comprises data from various surveys between 74 MHz and 22 GHz [Cohen et al., 2007; Dallacasa et al., 2000; Douglas et al., 1996; Gorshkov et al., 2003; Griffith et al., 1991; Neumann et al., 1994; Voges et al., 1999; White and Becker, 1992].

For fitting the data with different models, not the combined, but only the VHE data of July 2006 are used. The simultaneous data of KVA, Suzaku, MAGIC and H.E.S.S. are fitted. For comparison, three different SSC models are used:

Model 1 One component SSC model, described in Ruger [2007]. The method assumes a broken power law for the electron distribution. The development of the electron

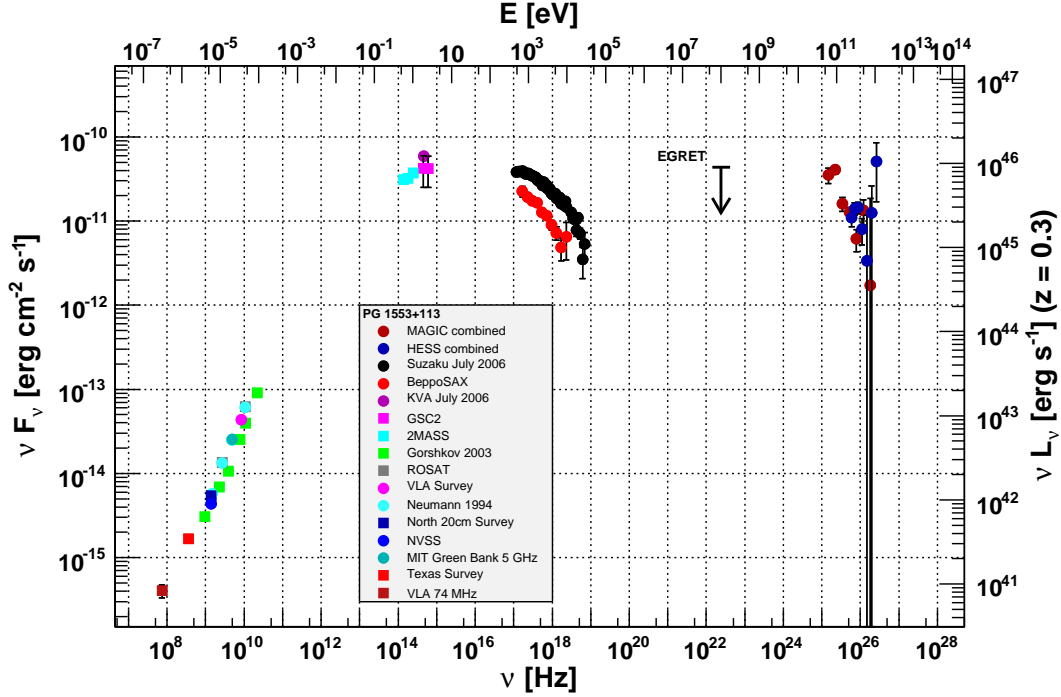


Figure 5.7.: Broadband spectral energy distribution including the combined VHE spectra.

distribution is calculated self-consistent. As no variability is observed, the variability time scale is assumed to one day to estimate the extension of the emission region.

Model 2 SSC model provided by Giommi [2008]. Also here the electron distribution is simulated with a broken power law spectrum.

Model 3 SSC model provided by Tramacere [2008]. In the web interface, spectra can be calculated for different electron distributions. As input, a power law, a power law with cutoff, a broken power law (BKN) or a log-parabolic (LP) distribution can be chosen. In Massaro et al. [2006] the model with a log-parabolic distribution is discussed in detail and applied to Markarian 501.

The parameters, which produce a spectral curve fitting the simultaneous data well, are listed in table 5.1. Like for deabsorbing the VHE spectra, a redshift of $z = 0.3$ has been used for all models.

With all three models, the SED can be fitted more or less. While Model 1 fits the x-ray data well, it is too low in the optical and IR range. An additional thermal component may

5.9. Broadband spectral energy distribution

Parameter	Model 1	Model 2	Model 3	
			BKN	LP
Magnetic field B [Gauss]	1.2	2	0.2	0.25
Doppler factor δ	10	22	12	15
Extension of emission region $\log_{10}(R)[cm]$	16.11	15.67	16.47	16.28
Normalizing constant $\log_{10}[cm^{-3}]$	5.52			
Normalized electron distribution $\log_{10}[cm^{-3}]$		1.6	1.3	1.3
Minimum energy $\log_{10}(\gamma_{min})$			1	1
Maximum energy $\log_{10}(\gamma_{max})$	5.15		6	5.8
Break Energy $\log_{10}(\gamma_{break})$	4.95	4	3.9	
Slope before break α_1	2.4	1.3	1.5	
Slope after break α_2	3.4	5.1	3.25	
curvature r				0.45
Energy $\log_{10}(\gamma_0)$				3.1
Slope s at energy γ_0				1.8

Table 5.1.: Parameters of the different models.

be considered to fit this. Compared to fits to the data of other sources [Huber, 2007] the parameters give reasonable values.

Although it fits the VHE, optical and IR data well, Model 2 does not describe the spectral shape of the Suzaku data properly. The slope of the model in the x-ray regime is too steep compared to the data. A two-zone model might be considered to fit the x-ray data better.

With the log-parabolic and broken power law shapes for the electron distributions in Model 3, all data are described quite well. In both cases, the spectral shape of the x-ray data is not fitted optimal, but this can be neglected taking into account the uncertainties of the Suzaku analysis ($< 0.7 keV$) and flux determination (larger errors at energies $> 10 keV$). For the log-parabolic fit, the x-ray data is below the fit at the smallest and highest energies. For the broken-power law, the data is above the fit for the smallest x-ray energies. Considering the uncertainties of the Suzaku analysis and data, the model with the log-parabolic electron distribution fits the data best. While in Massaro et al. [2004b] and Massaro et al. [2004a] the log-parabolic fit is applied only to the synchrotron peak of Markarian 421 and Markarian 501, the latter is fitted in the complete energy range in Massaro et al. [2006]. The obtained fit parameters are comparable. The smaller curvature for PG 1553+113 is obviously due to the wider peak.

Also compared to 1ES 1218+304, PG 1553+113 shows wider peaks. In Bretz [2006], a SED was fitted with Model 2. The determined parameters are comparable. For PG 1553+113 the higher peak fluxes are fitted with larger magnetic field and higher normalization factor.

5.10. Summary

The blazar PG 1553+113, discovered in the Palomar-Green survey, is well studied from the radio to the x-ray regime. Only in 2005, it was discovered in the VHE range. From 2005 to 2007, in total almost 80 hours of VHE data are available, about 25 hours taken with the H.E.S.S. array and 54 hours with the MAGIC telescope. Part of the data were taken simultaneously allowing for an independent check. The obtained MAGIC spectra agree with both the H.E.S.S. and the previously published MAGIC results. With the here presented low energy analysis, a spectrum down to 50 GeV was determined. Reaching such low energies marks a break through in the analysis of IACTs. In addition, another newly developed method has been used in the analysis of the MAGIC data. For the first time data affected by the SAL are corrected for the loss of light due to atmospheric absorption. From the whole set of VHE data, spreading over three years, neither changes in the spectral slope nor flux variations were found. In the same time, the optical flux shows a maximum difference of a factor 1.7.

During a MWL campaign in 2003, some variability in the radio and optical range was found and a flare in the x-ray was observed, in which the flux changed by a factor 3. In total from the x-ray measurements in 2003, 2005 and 2006, differences of a factor 13 in the flux are measured. From April 2005, where Swift data are available, the almost simultaneous MAGIC data sample is too short to detect a signal. The only simultaneous data in x-ray and gamma-ray are from the MWL campaign in July 2006, including optical (KVA), x-ray (Suzaku) and VHE data (H.E.S.S. and MAGIC). For the first time, the x-ray spectrum of PG 1553+113 was measured up to 30 keV. In the x-ray regime, the source was found to be at an intermediate flux level compared to previous measurements. Neither in the x-ray nor in the gamma-ray regime, flux variations were observed during the campaign. To study, if there is a correlation between the two spectral peaks in energy, more simultaneous data in both energy ranges are needed. Especially VHE data during a x-ray flare could help to constrain the models.

As neither the host galaxy is resolved, nor emission or absorption lines could be found, the redshift of PG 1553+113 is still unknown. Up to now, only lower and upper limits were determined. The lower limits range between 0.09 and 0.3 and the upper limits between 0.42 and 0.74. From the combined MAGIC and H.E.S.S. spectrum, an upper limit of $z < 0.74$ has been determined. For further studies a redshift of $z = 0.3$ was assumed.

Together with non-simultaneous data in the IR and radio, a spectral energy distribution was determined from the data of the MWL campaign in July 2006. The simultaneous data were fitted with different SSC models. Although the data could be fitted more or less, the models have either problems to describe the shape of the x-ray spectrum or the curve is too low in the IR to optical part of the broad-band SED. Consequently, more complex models have to be considered, for example two-zone models or a model taking into account an additional thermal component.

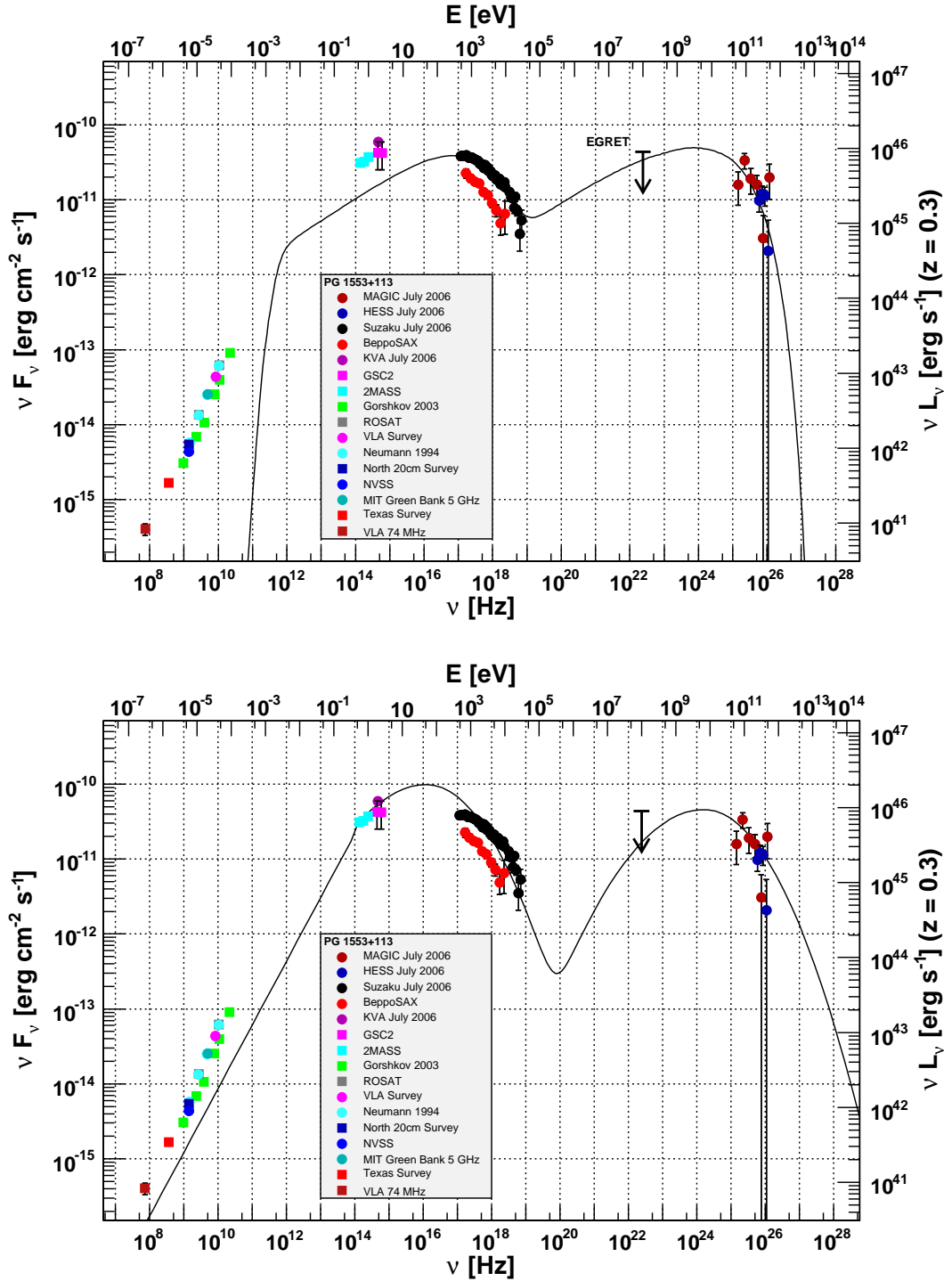


Figure 5.8.: Broadband spectral energy distributions of July 2006 with different SSC models. The upper plot shows Model 1, the lower Model 2.

5. PG 1553+113

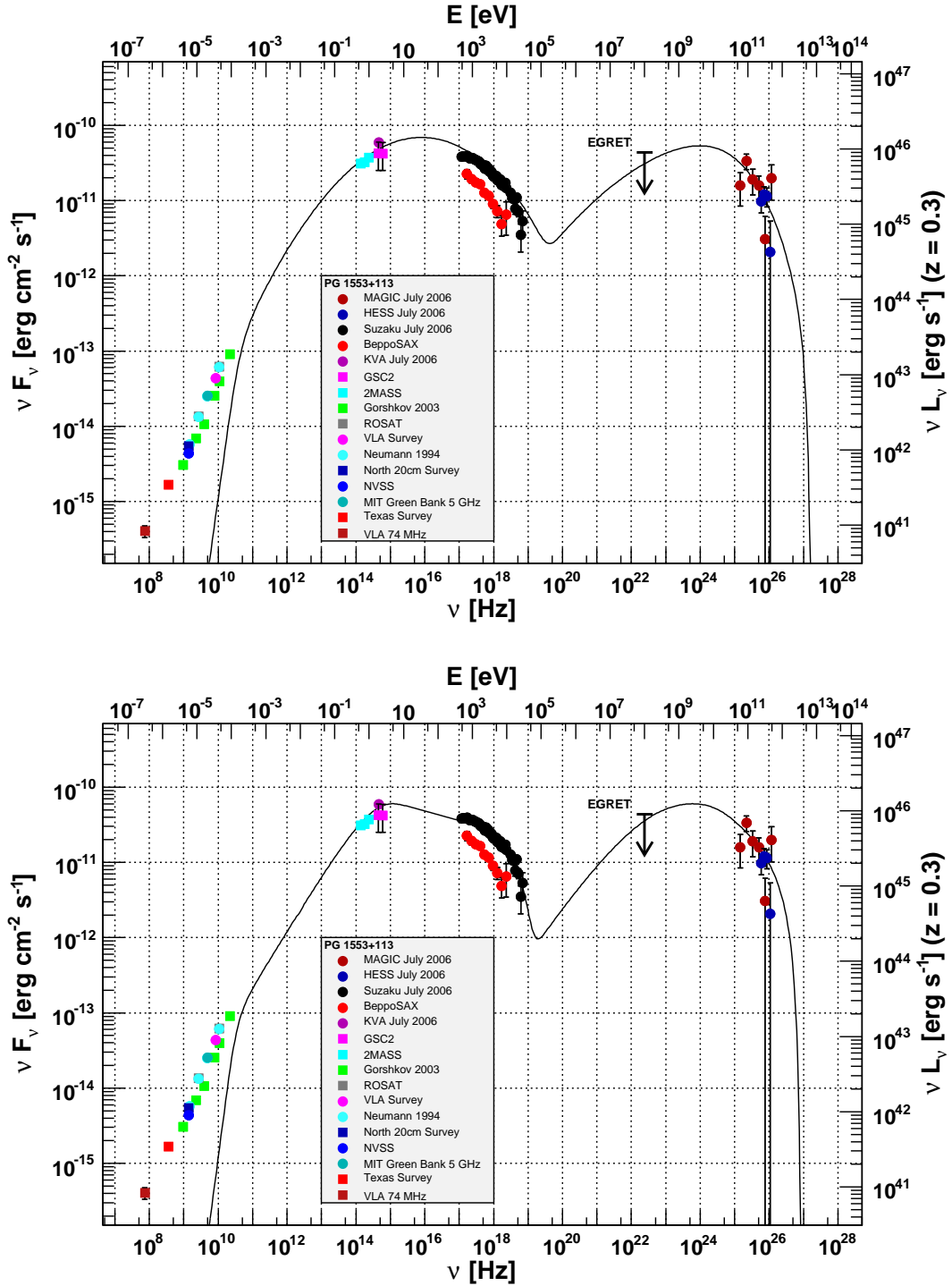


Figure 5.9.: Broadband spectral energy distributions of July 2006 with different SSC models. Both plots show Model 3: upper plot LP and lower plot BKN.

Acknowledgements

Above all I thank Prof. Dr. Karl Mannheim for his support, for the possibility to work in this interesting field and for having the confidence to put me in charge of the datacenter. Special thanks to my boyfriend Thomas Bretz, not only for his moral support, but also for developing a robust analysis software Mars and for the fruitful discussion especially in the context of the data center and automatic analysis.

I would like to thank the Instituto de Astrofísica de Canarias for the excellent working conditions at the Observatorio del Roque de los Muchachos in La Palma. The support of the German BMBF is gratefully acknowledged. Apart from that I would like to thank the MAGIC collaboration for their effort in planning, building and maintaining this powerful experiment.

Furthermore I thank the groups in Würzburg, Dortmund, Tuorla and Madrid for the friendly atmosphere and good working conditions, especially Victoria Fonseca and Leo Takalo for giving me the possibility to work with the groups in Madrid and Tuorla.

Thanks to Daniela Hadasch and Igor Oya for crosschecking my analysis results. I also thank Anita Reimer and Wytan Benbow for providing me the results of Suzaku and H.E.S.S., and Michael Rieger and Tanja Kneiske for providing me their models. Thanks to Kari Nilsson and Dafydd Wyn Evans for the fruitful discussions about the effects of atmospheric absorption.

In particular, I would like to thank my family including my very best friends Steffi and Swepi for their moral support.

5. *PG 1553+113*

List of Figures

1.1. Unified scheme of Active Galactic Nuclei	14
1.2. Atmospheric opacity	19
1.3. 3rd EGRET Catalog	25
1.4. VHE maps 2003 and 2007	27
2.1. Picture of the MAGIC telescopes	34
2.2. Picture of the MAGIC telescope	35
2.3. Starguider	37
2.4. Scheme of the MAGIC camera	39
2.5. Saharan Air Layer	54
3.1. Scheme of the automation concept	59
3.2. Example for dependencies	64
3.3. Long-term evolution of PSF	67
4.1. Quality cuts	76
4.2. Muons: Area versus SIZE	80
4.3. Low energy analysis: cut efficiency	81
4.4. Low energy analysis: overall cut efficiency	82
4.5. Camera Inhomogeneity: COG distributions	85
4.6. Sky map for January to April 2006	87
4.7. Differential spectra of all data sets	89
4.8. Combined ϑ^2 distribution	92
4.9. Combined differential spectrum	93
4.10. VHE light curve	94
4.11. Comparison of H.E.S.S. and MAGIC spectra	96
5.1. Suzaku spectrum of MWL campaign in July 2006	100
5.2. Suzaku light curve of MWL campaign in July 2006	101
5.3. Daily light curves of MWL campaign in July 2006	104
5.4. Daily VHE and optical light curves	106
5.5. Deabsorbed spectra	108
5.6. Constraints on the redshift	109
5.7. Broadband spectral energy distribution	110
5.8. Broadband spectral energy distributions	113
5.9. Broadband spectral energy distributions	114

List of Figures

A.1. Results May 2005	147
A.2. Results January-April 2006	148
A.3. Results April-June 2006	149
A.4. Results July 2006	150
A.5. Results July 2006 without correction	151
A.6. Results March/April 2007	152
B.1. Data flow in the automatic analysis	154

List of Tables

1.1. Empirical classification of Active Galactic Nuclei	12
2.1. Parameters of the different FADC systems	42
3.1. Overview of possible entries in a status table	59
3.2. Overview of additional columns in the status tables	60
3.3. Example for dependencies	62
3.4. Example for status table	63
4.1. Overview of data taken between April 2005 and April 2007	72
4.2. Overview of data sets used for the analysis	74
4.3. Coefficients for cut in Area	78
4.4. Transmission measurements of CMT, KVA and MAGIC	83
4.5. Camera Inhomogeneity: Loss of Events	86
4.6. Overview of results of all data sets	88
5.1. Parameters of the different models	111
A.1. List of identifiers of the source	134
A.2. List of sequences for the analysis of PG 1553+113	135
A.3. List of excluded runs	144
A.4. List of added runs	144
A.5. Spectral points Set 1	145
A.6. Spectral points Set 2	145
A.7. Spectral points Set 3	145
A.8. Spectral points Set 4	145
A.9. Spectral points Set 5	146
A.10. Spectral points combined data set	146
B.1. List of scripts of the MAGIC automation package	155
B.2. List of ROOT macros in the automation package	157
B.3. List of programs in the MARS package	158
B.4. List of input and output files of the analysis	159
B.5. List of files needed in the analysis	160
B.6. List of files coming from the telescope	161
B.7. Classification of tables in MAGIC database	162
B.8. Structure of table Band	164

List of Tables

B.9. Structure of table CCD	164
B.10. Structure of table Calibration	164
B.10. Structure of table Calibration (continued)	165
B.11. Structure of table CalibrationScript	165
B.12. Structure of table DataCheck	165
B.13. Structure of table DataSetProcessStatus	165
B.13. Structure of table DataSetProcessStatus (continued)	166
B.14. Structure of table DataSetSequenceMapping	166
B.15. Structure of table DataSets	166
B.16. Structure of table DiscriminatorThresholdTable	166
B.16. Structure of table DiscriminatorThresholdTable (continued)	167
B.17. Structure of table ExcludedFDA	167
B.18. Structure of table Filter	167
B.19. Structure of table FitsFile	167
B.20. Structure of table Ganymed	167
B.20. Structure of table Ganymed (continued)	168
B.21. Structure of table HvSettings	168
B.22. Structure of table L1TriggerTable	168
B.23. Structure of table L2TriggerTable	168
B.24. Structure of table LightConditions	168
B.25. Structure of table MagicNumber	168
B.26. Structure of table MarsVersion	169
B.27. Structure of table Object	169
B.28. Structure of table ObservationMode	169
B.29. Structure of table OpticalData	169
B.29. Structure of table OpticalData (continued)	170
B.30. Structure of table Project	170
B.31. Structure of table RunBook	170
B.32. Structure of table RunData	170
B.32. Structure of table RunData (continued)	171
B.33. Structure of table RunProcessStatus	171
B.34. Structure of table RunType	172
B.35. Structure of table SequenceBuildStatus	172
B.36. Structure of table SequenceProcessStatus	172
B.37. Structure of table Sequences	172
B.37. Structure of table Sequences (continued)	173
B.38. Structure of table Source	173
B.39. Structure of table SourceType	174
B.40. Structure of table Star	174
B.41. Structure of table Status	174
B.42. Structure of table Telescope	174
B.43. Structure of table TestFlag	175
B.44. Structure of table TriggerDelayTable	175

B.45. Structure of table User 175

List of Tables

Bibliography

- F. Aharonian, A. Akhperjanian, M. Beilicke, et al. Observations of 54 Active Galactic Nuclei with the HEGRA system of Cherenkov telescopes. *A&A*, 421:529–537, July 2004. doi: 10.1051/0004-6361:20035764.
- F. Aharonian, A. G. Akhperjanian, A. R. Bazer-Bachi, et al. Evidence for the γ -ray emission from the distant bl lac 1553+113. *A&A*, 448:L19, January 2006.
- F. Aharonian, A. G. Akhperjanian, A. R. Bazer-Bachi, et al. An Exceptional Very High Energy Gamma-Ray Flare of PKS 2155-304. *ApJ*, 664:L71–L74, August 2007. doi: 10.1086/520635.
- F. Aharonian, A. G. Akhperjanian, U. Barres de Almeida, et al. HESS observations and VLT spectroscopy of PG 1553+113. *A&A*, 477:481–489, January 2008. doi: 10.1051/0004-6361:20078603.
- J. Albert, E. Aliu, H. Anderhub, et al. Discovery of Very High Energy Gamma Rays from 1ES 1218+30.4. *ApJ*, 642:L119–L122, May 2006a. doi: 10.1086/504845.
- J. Albert, E. Aliu, H. Anderhub, et al. Discovery of Very High Energy γ -Rays from Markarian 180 Triggered by an Optical Outburst. *ApJ*, 648:L105–L108, September 2006b. doi: 10.1086/508020.
- J. Albert, E. Aliu, H. Anderhub, et al. Signal Reconstruction for the MAGIC Telescope. *ArXiv Astrophysics e-prints*, December 2006c.
- J. Albert, E. Aliu, H. Anderhub, et al. Observations of Markarian 421 with the MAGIC Telescope. *ApJ*, 663:125–138, July 2007a. doi: 10.1086/518221.
- J. Albert, E. Aliu, H. Anderhub, et al. Variable Very High Energy γ -Ray Emission from Markarian 501. *ApJ*, 669:862–883, November 2007b. doi: 10.1086/521382.
- J. Albert, E. Aliu, H. Anderhub, et al. Implementation of the Random Forest Method for the Imaging Atmospheric Cherenkov Telescope MAGIC. *ArXiv e-prints*, 709, September 2007c.
- J. Albert, E. Aliu, H. Anderhub, et al. Detection of very high energy radiation from the bl lacertae object pg 1553+113 with the magic telescope. *ApJ*, 654:L119–L122, January 2007.

Bibliography

- J. Albert, E. Aliu, H. Anderhub, et al. Discovery of Very High Energy γ -Ray Emission from the Low-Frequency-peaked BL Lacertae Object BL Lacertae. *ApJ*, 666:L17–L20, September 2007a. doi: 10.1086/521550.
- J. Albert, for the MAGIC Collaboration, J. Ellis, N. E. Mavromatos, et al. Probing Quantum Gravity using Photons from a Mkn 501 Flare Observed by MAGIC. *ArXiv e-prints*, 708, August 2007b.
- J. Albert, E. Aliu, H. Anderhub, et al. VHE γ -Ray Observation of the Crab Nebula and its Pulsar with the MAGIC Telescope. *ApJ*, 674:1037–1055, February 2008. doi: 10.1086/525270.
- J. Albert et al. Very high energy gamma-ray observations during moonlight and twilight with the MAGIC telescope. *Astroparticle Physics*, 12345:stillmiss, February 2007c.
- A. Armada. Characterization and some applications of the anode current monitoring system of the magic telescope. Master's thesis, Universitat Autònoma de Barcelona, aug 2005.
- R. Atkins, W. Benbow, D. Berley, et al. Limits on Very High Energy Emission from Gamma-Ray Bursts with the Milagro Observatory. *ApJ*, 604:L25–L28, March 2004. doi: 10.1086/383414.
- J.A. Barrio et al. The MAGIC Telescope - Design study for the construction of a 17 m Cherenkov telescope for Gamma-Astronomy above 10 GeV. *MPI-PhE*, March 1998.
- H. Bartko. *Observations of Galactic Sources of Very High Energy Gamma-Rays with the MAGIC Telescope*. PhD thesis, Ludwig-Maximilian-Universität München, Dec 2006.
- H. Bartko, F. Goebel, R. Mirzoyan, W. Pimpl, and M. Teshima. Tests of a prototype multiplexed fiber-optic ultra-fast FADC data acquisition system for the MAGIC telescope. *Nuclear Instruments and Methods in Physics Research A*, 548:464–486, August 2005. doi: 10.1016/j.nima.2005.05.029.
- A. J. Bird, A. Malizia, A. Bazzano, et al. The Third IBIS/ISGRI Soft Gamma-Ray Survey Catalog. *ApJS*, 170:175–186, May 2007. doi: 10.1086/513148.
- T. Bretz. *Observations of the Active Galactic Nucleus 1ES 1218+304 with the MAGIC-Telescope*. PhD thesis, Bayerische Julius-Maximilians-Universität Würzburg, 2006.
- T. Bretz. Sensitivitätsverbesserung bei MAGIC durch Berücksichtigung der Signalankunftszeit in der Analyse. In *Verhandlungen der Deutschen Physikalischen Gesellschaft*, 2008.
- T. Bretz. <http://www.astro.uni-wuerzburg.de/results/ringmethod>, 2005.
- T. Bretz. http://www.astro.uni-wuerzburg.de/wiki/Image_Cleaning, 2007.

- T. Bretz, D. Dorner, and R. Wagner. The tracking system of the magic telescope. In *28th International Cosmic Ray Conference*, August 2003.
- T. Bretz, D. Dorner, and D. Höhne. Comparison of On-Off and Wobble mode observations for MAGIC. In *International Cosmic Ray Conference*, volume 4 of *International Cosmic Ray Conference*, pages 311–+, 2005.
- T. Bretz, M. Backes, W. Rhode, et al. Long-term vhe gamma-ray monitoring of bright blazars with a dedicated cherenkov telescope. In *30th International Cosmic Ray Conference*, July 2007.
- T. Bretz, D. Dorner, et al. Drive system of the magic telescope. *in preparation*, 2008.
- N. Carangelo, R. Falomo, J. Kotilainen, A. Treves, and M.-H. Ulrich. Spectroscopy of BL Lac Objects: New Redshifts and Mis-identified Sources. In L. O. Takalo and E. Valtaoja, editors, *High Energy Blazar Astronomy*, volume 299 of *Astronomical Society of the Pacific Conference Series*, pages 299–+, July 2003.
- Carlsberg Meridian Telescope. http://www.ast.cam.ac.uk/~dwe/SRF/camc_extinction.html, 2007.
- P. S. Chen, H. W. Fu, and Y. F. Gao. 2MASS observation of BL Lac objects. *New Astronomy*, 11:27–42, October 2005. doi: 10.1016/j.newast.2005.05.004.
- A. S. Cohen, W. M. Lane, W. D. Cotton, et al. The VLA Low-Frequency Sky Survey. *AJ*, 134:1245–1262, September 2007. doi: 10.1086/520719.
- S. Commichau. *Observation of Very High Energy Gamma-Rays from the Galactic Center with the MAGIC Telescope, considering Geomagnetic Field Effects on the Imaging Technique*. PhD thesis, Eidgenössische Technische Hochschule Zrich, Mar 2007.
- Condor Team. *Condor Version 7.0.1 Manual*, 2008. URL <http://www.cs.wisc.edu/condor/>.
- V. Curtef, M. Backes, D. Hadasch, and MAGIC Collaboration. Improvements of the energy reconstruction for the MAGIC telescope by means of analysis and Monte Carlo techniques. *Astronomische Nachrichten*, 328:622–+, July 2007.
- M. Dahlem. <http://www.atnf.csiro.au/people/mdahlem/pop/multi.html>, 2007.
- D. Dallacasa, C. Stanghellini, M. Centonza, and R. Fanti. High frequency peakers. I. The bright sample. *A&A*, 363:887–900, November 2000.
- B. L. Dingus. HAWC (High Altitude Water Cherenkov) Observatory for Surveying the TeV Sky. In S. Ritz, P. Michelson, and C. A. Meegan, editors, *American Institute of Physics Conference Series*, volume 921 of *American Institute of Physics Conference Series*, pages 438–439, July 2007. doi: 10.1063/1.2757390.

Bibliography

- D. Donato, R. M. Sambruna, and M. Gliozzi. Six years of BeppoSAX observations of blazars: A spectral catalog. *A&A*, 433:1163–1169, April 2005. doi: 10.1051/0004-6361:20034555.
- D. Dorner. System zum Ausrichten und Nachführen des MAGIC-Teleskops. Master's thesis, Bayerische Julius-Maximilians-Universität Würzburg, oct 2003.
- D. Dorner and T. Bretz. Automatische Datenanalyse für das MAGIC Teleskop - überblick und Ergebnisse, 2005. *Astroteilchenphysik in Deutschland*, Zeuthen.
- D. Dorner, K. Nilsson, and T. Bretz. A method to correct iact data for atmospheric absorption due to the saharan air layer. *A&A*, February 2008.
- J. N. Douglas, F. N. Bash, F. A. Bozyan, G. W. Torrence, and C. Wolfe. The Texas Survey of Radio Sources Covering -35.5 degrees $<$ declination $<$ 71.5 degrees at 365 MHz. *AJ*, 111:1945–+, May 1996. doi: 10.1086/117932.
- J.P. Dunion and C.S. Velden. The impact of the saharan air layer on atlantic tropical cyclone activity. *Bull. Amer. Meteor. Soc.*, 85:353–365, March 2004.
- R. Falomo and A. A. Treves. PG 1553+113: A Bright Optically Selected BL Lacertae Object. *PASP*, 102:1120–1125, October 1990.
- M. Fuchs. Untersuchung der atmspärischen Transmission mittels Pyroskop und Lidar zur Gamma-Astronomie mit dem MAGIC Cherenkov Teleskop auf La Palma. Master's thesis, Fachhochschule München, 2005.
- M. Garczarczyk. *First Observation of GRB Prompt and Early Afterglow Emission Phase at ~ 100 GeV Energy Regime with the 17 m \varnothing MAGIC Imaging Atmospheric Cherenkov Telescope*. PhD thesis, Universität Rostock, 2007.
- M. Gaug. *Calibration of the MAGIC Telescope and Observation of Gamma Ray Bursts*. PhD thesis, Universitat Autònoma de Barcelona, March 2006.
- P. Giommi. <http://www.asdc.asi.it/blazars>, 2008.
- P. Giommi, M. Capalbi, M. Fiocchi, et al. A Catalog of 157 X-ray Spectra and 84 Spectral Energy Distributions of Blazars Observed with BeppoSAX. In P. Giommi, E. Massaro, and G. Palumbo, editors, *Blazar Astrophysics with BeppoSAX and Other Observatories*, pages 63–+, 2002.
- F. Goebel, K. Mase, M. Meyer, et al. Absolute energy scale calibration of the MAGIC telescope using muon images. In *29th International Cosmic Ray Conference*, volume 5, pages 179–182, August 2005.
- F. Goebel, H. Bartko, E. Carmona, others, and for the MAGIC Collaboration. Upgrade of the MAGIC Telescope with a Multiplexed Fiber-Optic 2 GSamples/s FADC Data Acquisition system. *ArXiv e-prints*, 709, September 2007.

- A. G. Gorshkov, V. K. Konnikova, and M. G. Mingaliev. Spectra, optical identifications, and statistics of a complete sample of radio sources at declinations $10^{\circ} 12' 30''$. *Astronomy Reports*, 47:903–915, November 2003. doi: 10.1134/1.1626193.
- R.F. Green, M. Schmidt, and J. Liebert. The Palomar-Green Catalog of Ultraviolet-Excess Stellar Objects. *ApJ*, 61:305–352, June 1986.
- M. Griffith, M. Heflin, S. Conner, B. Burke, and G. Langston. The fourth MIT-Green Bank 5 GHz survey. *ApJS*, 75:801–833, March 1991. doi: 10.1086/191549.
- D. Hadasch. Observations of PKS 2155-304 with the MAGIC telescope. Master’s thesis, Universität Dortmund, 2008. in preparation.
- M. Haffke. Atmosphere Is Magic - Berechnung und Implementierung neuer Atmosphärenmodelle in die MAGIC-Monte-Carlo-Kette. Master’s thesis, Universität Dortmund, Mrz 2007.
- A. M. Hillas. Cerenkov light images of EAS produced by primary gamma. In *19th International Cosmic Ray Conference*, pages 445–448, August 1985.
- S. Huber. Spektrale Modellierung von AGN unter besonderer Berücksichtigung von binären Schwarzslochsystemen. Master’s thesis, Bayerische Julius-Maximilians-Universität Würzburg, 2007.
- J. V. Jelley and N. A. Porter. Cerenkov Radiation from the Night Sky. *QJRAS*, 4:275–+, March 1963.
- Y. Kaneko, R. D. Preece, M. S. Briggs, et al. The Complete BATSE Spectral Catalog of Bright Gamma-Ray Bursts. *ArXiv Astrophysics e-prints*, May 2006.
- A. D. Kerrick, C. W. Akerlof, S. D. Biller, et al. Outburst of TeV photons from Markarian 421. *ApJ*, 438:L59–L62, January 1995. doi: 10.1086/187715.
- H. V. Klapdor-Kleingrothaus and K. Zuber. *Teilchenastrophysik*. Teubner Studienbücher: Physik. Teubner, 1997.
- J. Knapp and D. Heck. *EAS Simulation with CORSIKA: A Users Manual (Version 6.023)*, 2004.
- T. M. Kneiske. Gamma-ray background: a review. *ArXiv e-prints*, 707, July 2007.
- T. M. Kneiske, K. Mannheim, and D. H. Hartmann. Implications of cosmological gamma-ray absorption. I. Evolution of the metagalactic radiation field. *A&A*, 386:1–11, April 2002. doi: 10.1051/0004-6361:20020211.
- T. M. Kneiske, T. Bretz, K. Mannheim, and D. H. Hartmann. Implications of cosmological gamma-ray absorption. II. Modification of gamma-ray spectra. *A&A*, 413:807–815, January 2004. doi: 10.1051/0004-6361:20031542.

Bibliography

- C. Kolodziejcki. Klassifikation von astronomischen Daten mit Neuronalen Netzen. Master's thesis, Bayerische Julius-Maximilians-Universität Würzburg, 2005.
- A. Lawrence. Classification of active galaxies and the prospect of a unified phenomenology. *PASP*, 99:309–334, May 1987.
- F. Lebrun, J. P. Leray, P. Lavocat, et al. ISGRI: The INTEGRAL Soft Gamma-Ray Imager. *A&A*, 411:L141–L148, November 2003. doi: 10.1051/0004-6361:20031367.
- T.-P. Li and Y.-Q. Ma. Analysis methods for results in gamma-ray astronomy. *ApJ*, 272: 317–324, September 1983. doi: 10.1086/161295.
- K. Mannheim. The proton blazar. *A&A*, 269:67–76, March 1993.
- E. Massaro, M. Perri, P. Giommi, and R. Nesci. Log-parabolic spectra and particle acceleration in the BL Lac object Mkn 421: Spectral analysis of the complete BeppoSAX wide band X-ray data set. *A&A*, 413:489–503, January 2004a. doi: 10.1051/0004-6361:20031558.
- E. Massaro, M. Perri, P. Giommi, R. Nesci, and F. Verrecchia. Log-parabolic spectra and particle acceleration in blazars. II. The BeppoSAX wide band X-ray spectra of Mkn 501. *A&A*, 422:103–111, July 2004b. doi: 10.1051/0004-6361:20047148.
- E. Massaro, A. Tramacere, M. Perri, P. Giommi, and G. Tosti. Log-parabolic spectra and particle acceleration in blazars. III. SSC emission in the TeV band from Mkn501. *A&A*, 448:861–871, March 2006. doi: 10.1051/0004-6361:20053644.
- D. Mazin and F. Goebel. Break in the Very High Energy Spectrum of PG 1553+113: New Upper Limit on Its Redshift? *ApJ*, 655:L13–L16, January 2007. doi: 10.1086/511751.
- C. A. Meegan, W. S. Paciesas, G. N. Pendleton, et al. The 4b BATSE Gamma-Ray Burst Catalog. In C. A. Meegan, R. D. Preece, and T. M. Koshut, editors, *American Institute of Physics Conference Series*, volume 428 of *American Institute of Physics Conference Series*, pages 3–+, 1998.
- M. Meyer. *Observations of a systematic selected sample of high frequency peaked BL Lac objects with the MAGIC telescope*. PhD thesis, Bayerische Julius-Maximilians-Universität Würzburg, 2008.
- H. R. Miller and R. F. Green. Optical/UV Observations of the BL Lac Object, PG 1553+11. In *Bulletin of the American Astronomical Society*, volume 15 of *Bulletin of the American Astronomical Society*, pages 957–+, September 1983.
- H.R. Miller, M.T. Carini, B.J. Gaston, and Hutter D.J. The Ultraviolet/Optical Variability of PG 1553+113. In *A Decade of UV Astronomy with IUE*, volume 2, June 1988.

- A. Moralejo, C. Baixeras, D. Bastieri, et al. The MAGIC telescope for gamma-ray astronomy above 30 GeV. *Chinese Journal of Astronomy and Astrophysics Supplement*, 3:531–538, December 2003.
- J. E. Morrison, S. Röser, B. McLean, B. Bucciarelli, and B. Lasker. The Guide Star Catalog, Version 1.2: An Astrometric Recalibration and Other Refinements. *AJ*, 121: 1752–1763, March 2001. doi: 10.1086/319383.
- MySQL AB. *MySQL 5.0 Reference Manual*, 1997–2008. URL <http://dev.mysql.com/doc>.
- M. Neumann, W. Reich, E. Fuerst, et al. Multifrequency observations of ROSAT selected radio sources. *A&AS*, 106:303–326, August 1994.
- E. Nieppola, M. Tornikoski, and E. Valtaoja. Spectral energy distributions of a large sample of BL Lacertae objects. *A&A*, 445:441–450, January 2006. doi: 10.1051/0004-6361:20053316.
- M. A. Osterman, H. R. Miller, A. M. Campbell, et al. Multiwavelength Observations of the Extreme X-Ray-selected BL Lacertae Object PG 1553+11 (1ES 1553+113). *AJ*, 132: 873–882, August 2006. doi: 10.1086/505565.
- D. Paneque et al. A method to enhance the sensitivity of photomultipliers for air cherenkov telescopes. *Nuclear Instruments and Methods in Physics A*, 504:109, 2003.
- R. Paoletti et al. The Trigger System of the MAGIC Telescope. March 2007.
- R. Pegna, R. Cecchi, R. Paoletti, et al. The DRS VME Board: a Low Power Digitizing System in the GHz Range. *Nuclear Physics B Proceedings Supplements*, 150:70–73, January 2006. doi: 10.1016/j.nuclphysbps.2004.07.002.
- M. Punch, C. W. Akerlof, M. F. Cawley, et al. Detection of TeV photons from the active galaxy Markarian 421. *Nature*, 358:477–+, August 1992. doi: 10.1038/358477a0.
- T. A. Rector, D. C. Gabuzda, and J. T. Stocke. The Radio Structure of High-Energy-Peaked BL Lacertae Objects. *AJ*, 125:1060–1072, March 2003. doi: 10.1086/367802.
- A. Reimer, L. Costamante, O. Reimer, G. Madejski, and D. Dorner. The hard x-ray view to the distant vhe blazars 1es 1101-232 and 1es 1553+113, 2008. submitted to ApJ.
- B. Riegel. Systematische Untersuchung der Bildparameter für das MAGIC-Teleskop. Master's thesis, Bayerische Julius-Maximilians-Universität Würzburg, 2005.
- B. Riegel and T. Bretz. A systematic study of the interdependence of the IACT image parameters. In *29th International Cosmic Ray Conference*, volume 5, pages 215–218, August 2005.
- S. Rosswog and M. Brüggen. *Introduction to High-Energy Astrophysics*. Cambridge University Press, 2007.

Bibliography

- S. Rügamer. Systematische Studien der Verwendung der Zeitstruktur von Luftschauern zur Reduktion des Untergrundes in MAGIC-Daten. Master's thesis, Bayerische Julius-Maximilians-Universität Würzburg, July 2006.
- M. Rieger. Modellierung der Gamma-Emission in Jets von aktiven Galaxienkernen an Hand des Synchrotron-Self-Compton Modells. Master's thesis, Bayerische Julius-Maximilians-Universität Würzburg, February 2007.
- B. Sbarufatti, A. Treves, and R. Falomo. Imaging Redshifts of BL Lacertae Objects. *ApJ*, 635:173–179, December 2005. doi: 10.1086/497022.
- B. Sbarufatti, A. Treves, R. Falomo, et al. ESO Very Large Telescope Optical Spectroscopy of BL Lacertae Objects. II. New Redshifts, Featureless Objects, and Classification Assessments. *AJ*, 132:1–19, July 2006. doi: 10.1086/503031.
- R. Scarpa, C. M. Urry, R. Falomo, J. E. Pesce, and A. Treves. The Hubble Space Telescope Survey of BL Lacertae Objects. I. Surface Brightness Profiles, Magnitudes, and Radii of Host Galaxies. *ApJ*, 532:740–815, April 2000. doi: 10.1086/308618.
- M. Sikora and G. Madejski. Blazars. In F. A. Aharonian and H. J. Völk, editors, *American Institute of Physics Conference Series*, volume 558 of *American Institute of Physics Conference Series*, pages 275–+, 2001.
- STACEE Collaboration: S. Oser, D. Bhattacharya, L. M. Boone, et al. High Energy Gamma-Ray Observations of the Crab Nebula and Pulsar with the Solar Tower Atmospheric Cherenkov Effect Experiment. *ArXiv Astrophysics e-prints*, June 2000.
- D. Tescaro, H. Bartko, N. Galante, others, and for the MAGIC Collaboration. Study of the performance and capability of the new ultra-fast 2 GSample/s FADC data acquisition system of the MAGIC telescope. *ArXiv e-prints*, 709, September 2007.
- A. Tramacere. http://www.asdc.asi.it/ssc_at, 2008.
- A. Tramacere, P. Giommi, E. Massaro, et al. SWIFT observations of TeV BL Lacertae objects. *A&A*, 467:501–508, May 2007. doi: 10.1051/0004-6361:20066226.
- A. Treves, R. Falomo, and M. Uslenghi. On the distance of PG 1553+11. A lineless BL Lacertae object active in the TeV band. *A&A*, 473:L17–L19, October 2007. doi: 10.1051/0004-6361:20078290.
- C. M. Urry and P. Padovani. Unified Schemes for Radio-Loud Active Galactic Nuclei. *PASP*, 107:803–+, September 1995.
- W. Voges, B. Aschenbach, T. Boller, et al. The ROSAT all-sky survey bright source catalogue. *A&A*, 349:389–405, September 1999.
- S. Wakely and D. Horan. <http://tevcat.uchicago.edu>, 2008.

- T. C. Weekes. *Very high energy gamma-ray astronomy*. Astronomy and Astrophysics. Institute of Physics Publishing, 2003.
- T. C. Weekes, M. F. Cawley, D. J. Fegan, et al. Observation of TeV gamma rays from the Crab nebula using the atmospheric Cerenkov imaging technique. *ApJ*, 342:379–395, July 1989. doi: 10.1086/167599.
- M. Weiss. <http://chandra.harvard.edu/resources/illustrations/quasar.html>, 2006. Credit: NASA/CXC, Melissa Weiss.
- R. L. White and R. H. Becker. A new catalog of 30,239 1.4 GHz sources. *ApJS*, 79:331–467, April 1992. doi: 10.1086/191656.
- www-01. <http://www.physics.adelaide.edu.au/astrophysics/cangaroo>, 2007.
- www-02. <http://icrhp9.icrr.u-tokyo.ac.jp/c-iii.html>, 2007.
- www-03. <http://veritas.sao.arizona.edu/content/blogsection/6/40>, 2008.
- www-04. <http://www.astro.ucla.edu/~stacee/index.html>, 2008.
- www-05. <http://www.icrr.u-tokyo.ac.jp/em/index.html>, 2008.
- www-06. <http://www.mpi-hd.mpg.de/hfm/HESS/HESS.html>, 2007.
- www-07. http://gamma1.astro.ucla.edu/agis/index.php/Main_Page, 2008.
- www-08. <http://www.mpi-hd.mpg.de/hfm/CTA>, 2008.
- www-09. <http://root.cern.ch>, 2007.
- www-10. <http://de.wikipedia.org>, <http://en.wikipedia.org>, 2007.
- www-11. <http://www-hegra.desy.de/hegra>, 2008.
- www-12. <http://coss.gsfc.nasa.gov/docs/cgro>, 2008.
- www-13. <http://www.astro.uni-wuerzburg.de/wiki/MARS:NEWS>, 2008.
- www-14. http://www.cgspace.it/index.php?option=com_content&task=view&id=143&Itemid=66, 2008.
- www-15. <http://www.astroteilchenpyhsik.de>, 2007.
- www-16. <http://ibas.iasf-milano.inaf.it>, 2008.
- www-17. <http://db.astro.uni-wuerzburg.de>, 2008.

Bibliography

A. PG 1553+113

A.1. The source

Table A.1 gives an overview of various names under which PG 1553+113 is known from different catalogs and compilations.

A.2. Selection of MAGIC data

Table A.2 lists all data of PG 1553+113 taken with the MAGIC telescope between April 16th 2005 and April 25th 2007. Excluded sequences are given in parenthesis and reasons for the exclusion are listed in the last column. Apart from that, night, i.e. date of sunrise, observation mode, duration, zenith distance range and identifier of the set in this thesis are given. For Off data the source name is given in the last column. Also other remarks on the data selection are listed there. For some sequences, runs have been excluded or added. Those are listed in table A.3 and A.4.

More information on the data selection can be found in section 4.1.

A. PG 1553+113

Object Name	Catalog/Details
[HB89] 1553+113	Hewitt+Burbidge QSO compilation
PG 1553+113 PG 1553+11	Palomar-Green Bright Quasar Catalog
RBS 1538	ROSAT Bright Survey
MG1 J155545+1110	First MIT-Green Bank 5 GHz Survey
87GB 155321.5+112002	1987 Green Bank Radio Survey
87GB[BWE91] 1553+1120	Becker+White+Edwards 1978 Green Band Radio Survey
[WB92] 1553+1120 NED02	White+Becker
EGO 1553+113	ExtraGalacticObject
TXS 1553+113	Texas Survey of Radio Sources Covering $-35.5^\circ < \delta < 71.5^\circ$
EF B1553+1119	Effelsberg Radio Sources
IVS B1553+113	International VLBI Service for Geodesy and Astrometry
JVAS J1555+1111 JVAS B1555+113	Jodrell Bank-VLA Astrometric Survey
VCSI J1555+1111	VLBA Calibrator Survey - 1
RGB J1555+111 RGB J1555.7+111	ROSAT-Green Bank sources
RX J1555.7+1111	ROSAT X-Ray source
1RXS J155543.2+111114	ROSAT All-Sky Survey Bright Source Catalog
1ES 1553+11.3	EINSTEIN Slew Survey Source Catalog
[KMB96] 09	Kock+Meisenheimer+Brinkmann
[KMB96] J1555+111	Kock+Meisenheimer+Brinkmann
[VCV2001] J155543.1+1111124	Veron-Cetty+Veron 2001 edition of A Catalog of Quasars and Active Nuclei other years: [VV2000b] [VV2003b] [VV2006b] [VV98b]
[SRM2005] J155543.04+111124.3	Sowards-Emmerd+Romani+Michelson
[JBB2007] J155543.04+111124.3	Jackson+Battye+Browne
QSO B1553+113	Quasi Stellar Object
BWE 1553+1120	Becker+White+Edwards
2E 3529 2E 1553.3+1120	EINSTEIN, 2nd version
INTREF 662	Integral Reference catalog
NVSS J155543+111124	NRAO VLA Sky Survey
[DGT2001] B1553+113	Donato+Ghisellini+Tagliaferri, 2001
[IN88] 1553+113	Impey+Neugebauer, 1988 (IRAS observations)

Table A.1.: List of identifiers of PG 1553+113.

Table A.2.: List of sequences of the observations of PG 1553+113 for the years 2005 to 2007 including also the Off data chosen for the On-Off observations.

The excluded (excl.) sequences are given in parenthesis. In the remarks, the reasons for the exclusions are given. In addition, problems (pb) of the data are listed there. More information on the datacheck can be found in section 4.1. For the Off sequences the source name of the chosen data is given.

Sequence	Night	Mode	Duration	ZD	Set	Remark
(53162)	2005-04-17	On	9.45 min	18 - 18	1	different psf, added runs (≈ 50 min)
(53223)	2005-04-18	On	28.23 min	18 - 22	1	different psf, added runs (≈ 5 min)
54499	2005-05-03	On	52.03 min	18 - 21	1	various pb
54521	2005-05-03	On	51.07 min	18 - 23	1	various pb
55116	2005-05-09	On	56.65 min	18 - 24	1	various pb
55256	2005-05-10	On	86.85 min	18 - 25	1	various pb, excl. runs due to bad weather
55288	2005-05-10	On	45.97 min	18 - 23	1	various pb, excl. runs due to bad weather
55598	2005-05-13	On	94.68 min	18 - 28	1	various pb
(55635)	2005-05-13	On	43.33 min	18 - 22	1	various pb, excl. due to bad weather
(81024)	2006-01-29	On	11.92 min	32 - 34	2	excl. due to broken pixel
81256	2006-01-30	On	22.13 min	30 - 33	2	-
81471	2006-01-31	On	22.17 min	30 - 34	2	-
(81627)	2006-02-01	On	25.85 min	29 - 33	2	excl. due to bad weather
81840	2006-02-02	On	35.55 min	28 - 35	2	-
82059	2006-02-03	On	31.37 min	29 - 34	2	-
82218	2006-02-04	On	129.83 min	29 - 34	2	excl. runs with ZD (zenith distance) $> 35^\circ$
82467	2006-02-06	On	10.65 min	49 - 50	2	added runs (≈ 1 h), excl. runs with ZD $> 35^\circ$
(83690)	2006-02-24	On	53.52 min	32 - 42	2	excl. due to bad weather
83876	2006-02-25	On	60.73 min	32 - 44	2	excl. runs with ZD $> 35^\circ$
84107	2006-02-27	On	149.32 min	18 - 43	2	excl. runs with bad weather or ZD $> 35^\circ$
84369	2006-03-03	On	92.92 min	18 - 29	2	-
84568	2006-03-04	On	4.13 min	23 - 24	2	-
84720	2006-03-05	On	98.43 min	18 - 29	2	-

Table A.2 – Continued

Sequence	Night	Mode	Duration	Zd	Set	Remark
85061	2006-03-08	On	145.70 min	18 - 37	2	excl. runs with ZD > 35°
85170	2006-03-09	On	45.58 min	21 - 28	2	-
85240	2006-03-24	On	17.42 min	26 - 28	2	-
85467	2006-03-25	On	42.68 min	22 - 28	2	-
85485	2006-03-25	On	23.18 min	19 - 21	2	-
(86884)	2006-03-27	On	59.90 min	20 - 28	2	excl. due to calima
(86904)	2006-03-27	On	59.85 min	18 - 19	2	excl. due to calima
(86924)	2006-03-27	On	31.47 min	19 - 22	2	excl. due to calima
87090	2006-03-28	On	59.87 min	20 - 28	2	-
87113	2006-03-28	On	35.30 min	18 - 19	2	-
87541	2006-03-30	On	23.65 min	24 - 27	2	-
87552	2006-03-30	On	66.13 min	18 - 22	2	-
(87700)	2006-03-31	On	104.32 min	18 - 28	2	excl. due to calima
(88021)	2006-04-02	On	51.42 min	19 - 27	2	excl. due to calima
(88044)	2006-04-02	On	34.82 min	18 - 18	2	excl. due to calima
(88149)	2006-04-03	On	59.92 min	19 - 27	2	excl. due to calima
(88168)	2006-04-03	On	34.35 min	18 - 18	2	excl. due to calima
(88756)	2006-04-23	Wobble	0.12 min	22 - 22	3	pb, excl. due to short duration
88759	2006-04-23	Wobble	62.57 min	18 - 21	3	pb
(88816)	2006-04-23	On	26.58 min	18 - 21	3	pb, excl. due to different observation mode
(88831)	2006-04-23	On	3.42 min	23 - 23	3	pb, added \approx 1h; excl. due to different obs. mode
(89051)	2006-04-24	On	10.60 min	34 - 36	3	pb, excl. due to different observation mode
89690	2006-04-27	Wobble	18.45 min	18 - 20	3	pb
89716	2006-04-27	Wobble	18.50 min	18 - 18	3	pb
89740	2006-04-27	Wobble	18.63 min	18 - 18	3	pb
89759	2006-04-27	Wobble	18.60 min	19 - 21	3	pb
89994	2006-04-28	Wobble	18.65 min	18 - 22	3	pb
90007	2006-04-28	Wobble	60.65 min	18 - 19	3	pb
90218	2006-04-29	Wobble	67.60 min	18 - 21	3	pb, written manually

Table A.2 – Continued

Sequence	Night	Mode	Duration	Zd	Set	Remark
90404	2006-04-30	Wobble	13.55 min	18 - 19	3	pb
90412	2006-04-30	Wobble	23.77 min	18 - 18	3	pb
90429	2006-04-30	Wobble	18.62 min	18 - 18	3	pb
90439	2006-04-30	Wobble	18.62 min	18 - 20	3	pb
(90456)	2006-04-30	Wobble	0.77 min	21 - 21	3	pb, excl. due to short duration
90592	2006-05-01	Wobble	18.75 min	18 - 19	3	pb
90599	2006-05-01	Wobble	18.67 min	18 - 18	3	pb
90607	2006-05-01	Wobble	18.65 min	18 - 18	3	pb
90616	2006-05-01	Wobble	18.68 min	19 - 21	3	pb
(90682)	2006-05-04	On	39.62 min	20 - 25	3	pb, excl. due to hardware pb
(90691)	2006-05-04	Wobble	18.68 min	18 - 19	3	pb, excl. due to hardware pb
(90697)	2006-05-04	Wobble	18.72 min	18 - 18	3	pb, excl. due to hardware pb
(90702)	2006-05-04	Wobble	18.70 min	18 - 19	3	pb, excl. due to hardware pb
(90707)	2006-05-04	Wobble	18.83 min	19 - 20	3	pb, excl. due to hardware pb
(90712)	2006-05-04	Wobble	0.72 min	21 - 21	3	pb, excl. due to hardware pb
93746	2006-06-22	Wobble	18.68 min	23 - 25	3	pb
93950	2006-06-23	Wobble	18.63 min	19 - 21	3	pb
93961	2006-06-23	Wobble	18.62 min	18 - 18	3	pb
93969	2006-06-23	Wobble	18.57 min	18 - 18	3	pb
93978	2006-06-23	Wobble	18.65 min	18 - 19	3	pb
(93987)	2006-06-23	Wobble	7.08 min	20 - 21	3	pb, moon, excl. due to rate drop
(93996)	2006-06-23	Wobble	0.62 min	20 - 21	3	pb, moon, excl. due to short duration
94425	2006-06-27	Wobble	18.65 min	20 - 21	3	pb
94434	2006-06-27	Wobble	18.73 min	18 - 20	3	pb
94443	2006-06-27	Wobble	18.68 min	18 - 18	3	pb
94451	2006-06-27	Wobble	18.68 min	18 - 18	3	pb
94459	2006-06-27	Wobble	18.68 min	19 - 20	3	pb
(94467)	2006-06-27	Wobble	4.67 min	21 - 21	3	pb, excl. due to short duration and closing camera
94471	2006-06-27	Wobble	11.48 min	23 - 24	3	pb

Table A.2 – Continued

Sequence	Night	Mode	Duration	Zd	Set	Remark
94563	2006-06-28	Wobble	18.67 min	20 - 22	3	pb
94571	2006-06-28	Wobble	7.98 min	19 - 19	3	pb
(95036)	2006-07-02	Wobble	59.17 min	18 - 26	3	pb, excl. due to higher pedestal rms (1.3)
95461	2006-07-15	Wobble	42.02 min	18 - 21	4	excl. due to missing calibration events, calima
95485	2006-07-16	Wobble	57.80 min	18 - 24	4	calima
95505	2006-07-16	Wobble	30.70 min	25 - 30	4	calima
95524	2006-07-17	Wobble	58.10 min	18 - 25	4	calima
95542	2006-07-17	Wobble	26.93 min	26 - 30	4	calima
95602	2006-07-18	Wobble	53.73 min	22 - 30	4	calima
96108	2006-07-22	Wobble	38.58 min	23 - 30	4	calima
96228	2006-07-24	Wobble	7.12 min	19 - 20	4	calima
96245	2006-07-24	Wobble	18.65 min	22 - 24	4	calima
96251	2006-07-24	Wobble	18.67 min	26 - 28	4	calima
96258	2006-07-24	Wobble	10.00 min	29 - 30	4	calima
96336	2006-07-25	Wobble	18.27 min	22 - 24	4	calima
96344	2006-07-25	Wobble	50.07 min	26 - 34	4	calima
96411	2006-07-26	Wobble	57.70 min	21 - 30	4	calima
96429	2006-07-26	Wobble	23.40 min	32 - 35	4	calima
96524	2006-07-27	Wobble	57.33 min	21 - 31	4	calima
229147	2007-03-23	Wobble	60.62 min	19 - 29	5	excl. runs due to bad weather
(235050)	2007-04-19	Wobble	92.75 min	18 - 29	5	excl. due to bad weather
(235152)	2007-04-19	Wobble	56.32 min	18 - 23	5	excl. due to bad weather
235673	2007-04-20	Wobble	56.20 min	20 - 29	5	-
235765	2007-04-20	Wobble	55.75 min	18 - 20	5	-
235857	2007-04-20	Wobble	36.62 min	19 - 23	5	-
236418	2007-04-21	Wobble	55.95 min	18 - 21	5	-
236505	2007-04-21	Wobble	56.13 min	18 - 24	5	-
236903	2007-04-22	Wobble	55.83 min	20 - 30	5	-
236992	2007-04-22	Wobble	55.88 min	18 - 21	5	-

Table A.2 – Continued

Sequence	Night	Mode	Duration	Zd	Set	Remark
237083	2007-04-22	Wobble	43.20 min	18 - 23	5	-
237452	2007-04-23	Wobble	85.95 min	18 - 27	5	-
237586	2007-04-23	Wobble	56.67 min	18 - 23	5	-
(237769)	2007-04-24	Wobble	4.38 min	19 - 20	5	excl. due to missing calibration events
237778	2007-04-24	Wobble	36.65 min	18 - 19	5	-
237838	2007-04-24	Wobble	52.38 min	18 - 23	5	-
238023	2007-04-25	Wobble	15.33 min	18 - 20	5	excl. due to higher pedestal rms (1.56)
79481	2006-01-01	Wobble	21.23 min	33 - 36	2	M87-W1
79488	2006-01-01	Wobble	18.98 min	29 - 32	2	M87-W2
79497	2006-01-01	Wobble	25.98 min	20 - 24	2	M87-W1
79506	2006-01-01	Wobble	15.30 min	19 - 20	2	M87-W2
79512	2006-01-01	Wobble	14.62 min	17 - 18	2	M87-W1
79584	2006-01-02	On	48.00 min	9 - 17	2	OffCrab13
79691	2006-01-02	Wobble	19.57 min	33 - 37	2	M87-W1
79702	2006-01-02	Wobble	16.82 min	30 - 33	2	M87-W2
79709	2006-01-02	Wobble	17.48 min	26 - 29	2	M87-W1
79717	2006-01-02	Wobble	17.73 min	23 - 25	2	M87-W2
79725	2006-01-02	Wobble	24.27 min	19 - 22	2	M87-W1
79736	2006-01-02	Wobble	22.52 min	17 - 18	2	M87-W2
79782	2006-01-03	On	34.55 min	23 - 24	2	Off3c120-1
79920	2006-01-03	Wobble	21.58 min	25 - 29	2	M87-W2
79931	2006-01-03	Wobble	22.28 min	21 - 24	2	M87-W1
79940	2006-01-03	Wobble	20.47 min	18 - 20	2	M87-W2
79948	2006-01-03	Wobble	14.82 min	17 - 17	2	M87-W1
80119	2006-01-06	Wobble	20.70 min	34 - 37	2	M87-W2
80127	2006-01-06	Wobble	20.15 min	29 - 32	2	M87-W1
80135	2006-01-06	Wobble	18.68 min	26 - 28	2	M87-W2
80143	2006-01-06	Wobble	20.00 min	21 - 24	2	M87-W1
80155	2006-01-06	Wobble	17.27 min	18 - 20	2	M87-W2

A.2. Selection of MAGIC data

Table A.2 – Continued

Sequence	Night	Mode	Duration	Zd	Set	Remark
80163	2006-01-06	Wobble	18.27 min	17 - 18	2	M87-W1
80171	2006-01-06	Wobble	15.30 min	16 - 17	2	M87-W2
80211	2006-01-08	Wobble	18.92 min	33 - 36	2	M87-W1
80220	2006-01-08	Wobble	17.43 min	29 - 33	2	M87-W2
80229	2006-01-08	Wobble	17.63 min	25 - 28	2	M87-W1
80237	2006-01-08	Wobble	17.92 min	22 - 25	2	M87-W2
80245	2006-01-08	Wobble	19.18 min	19 - 21	2	M87-W1
80299	2006-01-19	On	29.25 min	17 - 23	2	OffCrab13
80621	2006-01-23	On	57.85 min	15 - 27	2	OffCrab13
80639	2006-01-23	On	38.83 min	28 - 36	2	OffCrab13
81404	2006-01-31	Wobble	21.28 min	25 - 28	2	M87-W1
81414	2006-01-31	Wobble	61.33 min	17 - 24	2	M87-W
81773	2006-02-02	Wobble	19.57 min	27 - 30	2	M87-W1
81782	2006-02-02	Wobble	70.00 min	17 - 26	2	M87-W
81992	2006-02-03	Wobble	19.93 min	27 - 30	2	M87-W2
82001	2006-02-03	Wobble	59.78 min	17 - 26	2	M87-W
82182	2006-02-04	Wobble	27.90 min	25 - 30	2	M87-W1
82194	2006-02-04	Wobble	58.58 min	17 - 24	2	M87-W
82346	2006-02-05	Wobble	19.93 min	24 - 26	2	M87-W2
82355	2006-02-05	Wobble	59.75 min	16 - 22	2	M87-W
82380	2006-02-05	On	119.85 min	24 - 47	2	OffHB1553-1
82421	2006-02-06	Wobble	19.85 min	27 - 30	2	M87-W1
82433	2006-02-06	Wobble	79.72 min	16 - 26	2	M87-W
83165	2006-02-22	On	80.58 min	7 - 19	2	OffCrab5
83263	2006-02-22	Wobble	19.78 min	22 - 25	2	M87-W1
83284	2006-02-22	Wobble	19.95 min	19 - 22	2	M87-W2
83444	2006-02-23	Wobble	14.95 min	24 - 26	2	M87-W1
83452	2006-02-23	Wobble	89.60 min	16 - 24	2	M87-W
83839	2006-02-25	Wobble	17.95 min	20 - 22	2	M87-W1

Table A.2 – Continued

Sequence	Night	Mode	Duration	Zd	Set	Remark
83849	2006-02-25	Wobble	62.72 min	16 - 19	2	M87-W
84067	2006-02-27	Wobble	8.43 min	25 - 26	2	M87-W2
84073	2006-02-27	Wobble	89.67 min	16 - 22	2	M87-W
84301	2006-03-03	Wobble	19.92 min	22 - 25	2	M87-W1
84311	2006-03-03	Wobble	149.35 min	16 - 28	2	M87-W
84446	2006-03-04	On	15.28 min	35 - 35	2	Off3c279-6
84499	2006-03-04	Wobble	19.93 min	20 - 23	2	M87-W2
84510	2006-03-04	Wobble	106.00 min	16 - 28	2	M87-W
84558	2006-03-04	On	17.93 min	23 - 27	2	OffHB1553-1
84669	2006-03-05	Wobble	19.92 min	16 - 17	2	M87-W1
84680	2006-03-05	Wobble	79.43 min	17 - 28	2	M87-W
84829	2006-03-06	Wobble	8.13 min	20 - 21	2	M87-W2
84895	2006-03-07	Wobble	19.93 min	16 - 17	2	M87-W2
84905	2006-03-07	Wobble	59.78 min	17 - 25	2	M87-W
84937	2006-03-07	On	108.25 min	18 - 28	2	OffHB1553-1
85543	2006-03-21	Wobble	19.95 min	24 - 28	2	M87-W1
85554	2006-03-21	Wobble	19.95 min	21 - 24	2	M87-W2
85716	2006-03-22	Wobble	19.90 min	25 - 28	2	M87-W2
85728	2006-03-22	Wobble	15.08 min	22 - 24	2	M87-W1
85736	2006-03-22	Wobble	19.93 min	18 - 19	2	M87-W2
85747	2006-03-22	Wobble	14.95 min	16 - 17	2	M87-W1
85755	2006-03-22	Wobble	9.77 min	16 - 16	2	M87-W2
85876	2006-03-23	Wobble	19.92 min	26 - 29	2	M87-W1
85885	2006-03-23	Wobble	19.92 min	23 - 26	2	M87-W2
85894	2006-03-23	Wobble	19.92 min	19 - 21	2	M87-W1
85903	2006-03-23	Wobble	19.88 min	17 - 19	2	M87-W2
85916	2006-03-23	Wobble	25.60 min	16 - 17	2	M87-W1
85928	2006-03-23	Wobble	13.32 min	17 - 17	2	M87-W2
85935	2006-03-23	Wobble	14.93 min	18 - 19	2	M87-W1

A.2. Selection of MAGIC data

Table A.2 – Continued

Sequence	Night	Mode	Duration	Zd	Set	Remark
86181	2006-03-24	Wobble	19.90 min	17 - 19	2	M87-W1
86190	2006-03-24	Wobble	19.87 min	16 - 17	2	M87-W2
86200	2006-03-24	Wobble	19.92 min	16 - 17	2	M87-W1
86209	2006-03-24	Wobble	19.88 min	17 - 19	2	M87-W2
86394	2006-03-25	Wobble	19.88 min	17 - 18	2	M87-W1
86405	2006-03-25	Wobble	19.88 min	16 - 17	2	M87-W2
86415	2006-03-25	Wobble	19.83 min	16 - 18	2	M87-W1
86434	2006-03-25	Wobble	18.20 min	18 - 19	2	M87-W2
86622	2006-03-26	Wobble	19.88 min	17 - 19	2	M87-W1
86632	2006-03-26	Wobble	19.90 min	16 - 17	2	M87-W2
86642	2006-03-26	Wobble	19.93 min	16 - 17	2	M87-W1
86651	2006-03-26	Wobble	19.90 min	17 - 19	2	M87-W2
86664	2006-03-26	On	58.98 min	36 - 41	2	Off3c279-5
86686	2006-03-26	On	59.90 min	18 - 26	2	OffHB1553-1
87029	2006-03-28	Wobble	23.85 min	17 - 19	2	M87-W1
87042	2006-03-28	Wobble	18.68 min	16 - 17	2	M87-W2
87051	2006-03-28	Wobble	19.90 min	16 - 17	2	M87-W1
87060	2006-03-28	Wobble	19.95 min	18 - 19	2	M87-W2
87234	2006-03-29	Wobble	19.88 min	17 - 18	2	M87-W1
87244	2006-03-29	Wobble	19.88 min	16 - 17	2	M87-W2
87253	2006-03-29	Wobble	19.90 min	16 - 17	2	M87-W1
87262	2006-03-29	Wobble	19.87 min	17 - 19	2	M87-W2
87271	2006-03-29	On	56.20 min	36 - 41	2	Off3c279-5
87292	2006-03-29	On	59.83 min	18 - 26	2	OffHB1553-1
87314	2006-03-29	On	59.82 min	18 - 20	2	OffHB1553-1
87338	2006-03-29	On	40.58 min	20 - 26	2	OffHB1553-1
87476	2006-03-30	Wobble	18.68 min	18 - 19	2	M87
87485	2006-03-30	Wobble	18.67 min	16 - 17	2	M87
87494	2006-03-30	Wobble	18.63 min	16 - 17	2	M87

Table A.2 – Continued

Sequence	Night	Mode	Duration	Zd	Set	Remark
87504	2006-03-30	Wobble	18.70 min	17 - 19	2	M87
87513	2006-03-30	Wobble	5.88 min	19 - 19	2	M87
54263	2005-05-02	On	110.60 min	1 - 17	1	OffW-Comae-1
54468	2005-05-03	On	51.93 min	3 - 12	1	Off2E1415-1
54564	2005-05-04	On	29.52 min	17 - 21	1	Off1ES1426-1
54579	2005-05-04	On	50.05 min	14 - 16	1	Off1ES1426-1
54678	2005-05-06	On	76.00 min	17 - 27	1	OffM87-1
54748	2005-05-06	On	83.63 min	5 - 14	1	OffArp-220-1
54815	2005-05-07	On	113.72 min	3 - 25	1	Off2E1415-1
54855	2005-05-07	On	128.53 min	18 - 23	1	OffHB1553-1
55333	2005-05-11	On	112.93 min	14 - 25	1	Off1ES1426-1
55376	2005-05-11	On	148.57 min	5 - 17	1	OffArp-220-1
55710	2005-05-14	On	40.57 min	14 - 17	1	Off1ES1426-1

A. PG 1553+113

Seq. Number	Run Numbers	Night	Reason for Exclusion
55256	55278 - 55281	2005-05-10	bad weather, clouds
55288	55298 - 55304	2005-05-10	bad weather, clouds
82218	82220 - 82245	2006-02-04	ZD (zenith distance) > 35°
82467	82469 - 82493	2006-02-06	ZD > 35°
83876	83878 - 83891	2006-02-25	ZD > 35°
84107	84112 - 84117	2006-02-27	bad weather
	84109 - 84121	2006-02-27	ZD > 35°
85061	85063 - 85065	2006-03-08	ZD > 35°
229147	229244, 229245	2007-03-23	excluded runs due to bad weather

Table A.3.: For the sequences which have only partly a bad quality or too high zenith angles, some runs have been excluded. In this table the sequence number, the runs, the night and the reason are listed.

Seq. Number	Run Numbers	Night	OnTime	Reason for previous exclusion
53162	53168 - 53197	2005-04-17	≈ 50 min	calibration script NONE
53223	53240	2005-04-18	≈ 5 min	calibration script NONE
82467	82492 - 82513	2006-02-06	≈ 60 min	GRB inbetween
88831	88836 - 88864	2006-04-23	≈ 60 min	different HV settings
90218	all	2006-04-29	≈ 80 min	calibration run not in DB

Table A.4.: As the automatic building of sequences can not handle some technical problems, few runs have to be added manually to sequences or sequences have to be written manually. This table summarizes this for the analysis of the data of PG 1553+113.

A.3. Additional Results from Single Data Sets

In the following for each data set a χ^2 plot (upper plot) and a spectrum (lower plot) are shown (figures A.1, A.2, A.3, A.4, A.5 and A.6). For the data set 4, i.e. the one suffering from atmospheric absorption, two are shown, one before and one after the correction. For all spectra the spectral points including the errors and energy bins are given in tables A.5, A.6, A.7, A.8 and A.9.

A.3. Additional Results from Single Data Sets

E[GeV]	Emin	Emax	F	stat	sys
91	74	112	$6.4 \cdot 10^{-5}$	$6.4 \cdot 10^{-5}$	$6.4 \cdot 10^{-5}$
139	112	171	$1.6 \cdot 10^{-5}$	$0.4 \cdot 10^{-5}$	$0.4 \cdot 10^{-5}$
211	171	260	$1.6 \cdot 10^{-6}$	$0.5 \cdot 10^{-6}$	$0.5 \cdot 10^{-6}$
320	260	395	$2.7 \cdot 10^{-7}$	$1.5 \cdot 10^{-7}$	$1.2 \cdot 10^{-7}$
486	395	600	$2.8 \cdot 10^{-8}$	$2.8 \cdot 10^{-8}$	$2.8 \cdot 10^{-8}$

Table A.5.: Spectral points for Set 1.

E[GeV]	Emin	Emax	F	stat	sys
60	49	74	$7.6 \cdot 10^{-5}$	$2.0 \cdot 10^{-5}$	$2.0 \cdot 10^{-5}$
91	74	112	$3.9 \cdot 10^{-5}$	$0.6 \cdot 10^{-5}$	$0.6 \cdot 10^{-5}$
139	112	171	$2.7 \cdot 10^{-6}$	$2.1 \cdot 10^{-6}$	$2.1 \cdot 10^{-6}$
211	171	260	$1.8 \cdot 10^{-6}$	$0.4 \cdot 10^{-6}$	$0.4 \cdot 10^{-6}$
320	260	395	$1.6 \cdot 10^{-7}$	$0.9 \cdot 10^{-7}$	$0.9 \cdot 10^{-7}$
486	395	600	$3.2 \cdot 10^{-8}$	$2.9 \cdot 10^{-8}$	$2.5 \cdot 10^{-8}$

Table A.6.: Spectral points for Set 2.

E[GeV]	Emin	Emax	F	stat	sys
91	74	112	$6.3 \cdot 10^{-5}$	$2.1 \cdot 10^{-5}$	$2.1 \cdot 10^{-5}$
139	112	171	$9.5 \cdot 10^{-6}$	$1.9 \cdot 10^{-6}$	$1.1 \cdot 10^{-6}$
211	171	260	$1.3 \cdot 10^{-6}$	$0.3 \cdot 10^{-6}$	$0.2 \cdot 10^{-6}$
320	260	395	$1.3 \cdot 10^{-7}$	$1.0 \cdot 10^{-7}$	$0.4 \cdot 10^{-7}$
486	395	600	$3.5 \cdot 10^{-8}$	$3.5 \cdot 10^{-8}$	$1.5 \cdot 10^{-8}$
739	600	911	$1.2 \cdot 10^{-8}$	$1.2 \cdot 10^{-8}$	$0.7 \cdot 10^{-8}$

Table A.7.: Spectral points for Set 3.

E[GeV]	Emin	Emax	F	stat	sys
60	49	74	$4.3 \cdot 10^{-5}$	$2.0 \cdot 10^{-5}$	$1.7 \cdot 10^{-5}$
91	74	112	$3.6 \cdot 10^{-5}$	$0.8 \cdot 10^{-5}$	$0.8 \cdot 10^{-5}$
139	112	171	$7.8 \cdot 10^{-6}$	$2.9 \cdot 10^{-6}$	$2.9 \cdot 10^{-6}$
211	171	260	$2.1 \cdot 10^{-6}$	$0.7 \cdot 10^{-6}$	$0.6 \cdot 10^{-6}$
320	260	395	$9.5 \cdot 10^{-8}$	$9.5 \cdot 10^{-8}$	$9.5 \cdot 10^{-8}$
486	395	600	$9.2 \cdot 10^{-8}$	$4.5 \cdot 10^{-8}$	$4.5 \cdot 10^{-8}$
739	600	911	$1.5 \cdot 10^{-8}$	$1.5 \cdot 10^{-8}$	$0.7 \cdot 10^{-9}$

Table A.8.: Spectral points for Set 4.

A. PG 1553+113

E[GeV]	Emin	Emax	F	stat	sys
60	49	74	$5.8 \cdot 10^{-5}$	$2.5 \cdot 10^{-5}$	$1.8 \cdot 10^{-5}$
91	74	112	$3.3 \cdot 10^{-5}$	$0.8 \cdot 10^{-5}$	$0.8 \cdot 10^{-5}$
139	112	171	$6.0 \cdot 10^{-6}$	$1.9 \cdot 10^{-6}$	$1.3 \cdot 10^{-6}$
211	171	260	$9.3 \cdot 10^{-7}$	$3.1 \cdot 10^{-7}$	$2.9 \cdot 10^{-7}$
320	260	395	$2.2 \cdot 10^{-7}$	$1.0 \cdot 10^{-7}$	$0.9 \cdot 10^{-8}$
486	395	600	$8.9 \cdot 10^{-8}$	$3.9 \cdot 10^{-8}$	$3.1 \cdot 10^{-8}$
739	600	911	$1.7 \cdot 10^{-8}$	$1.6 \cdot 10^{-8}$	$1.0 \cdot 10^{-8}$
1124	911	1385	$4.2 \cdot 10^{-9}$	$4.2 \cdot 10^{-9}$	$2.0 \cdot 10^{-9}$
1708	1385	2105	$7.9 \cdot 10^{-10}$	$7.9 \cdot 10^{-10}$	$7.9 \cdot 10^{-10}$

Table A.9.: Spectral points for Set 5.

E[GeV]	Emin	Emax	F	stat
60	49	74	$9.0 \cdot 10^{-5}$	$1.9 \cdot 10^{-5}$
91	74	112	$4.2 \cdot 10^{-5}$	$4.8 \cdot 10^{-6}$
139	112	171	$6.2 \cdot 10^{-6}$	$1.2 \cdot 10^{-6}$
211	171	260	$1.5 \cdot 10^{-6}$	$2.2 \cdot 10^{-7}$
320	260	395	$1.7 \cdot 10^{-7}$	$5.1 \cdot 10^{-8}$
486	395	600	$5.5 \cdot 10^{-8}$	$1.8 \cdot 10^{-8}$
739	600	911	$7.5 \cdot 10^{-10}$	$7.4 \cdot 10^{-10}$

Table A.10.: Spectral points for the combined data set.

A.3. Additional Results from Single Data Sets

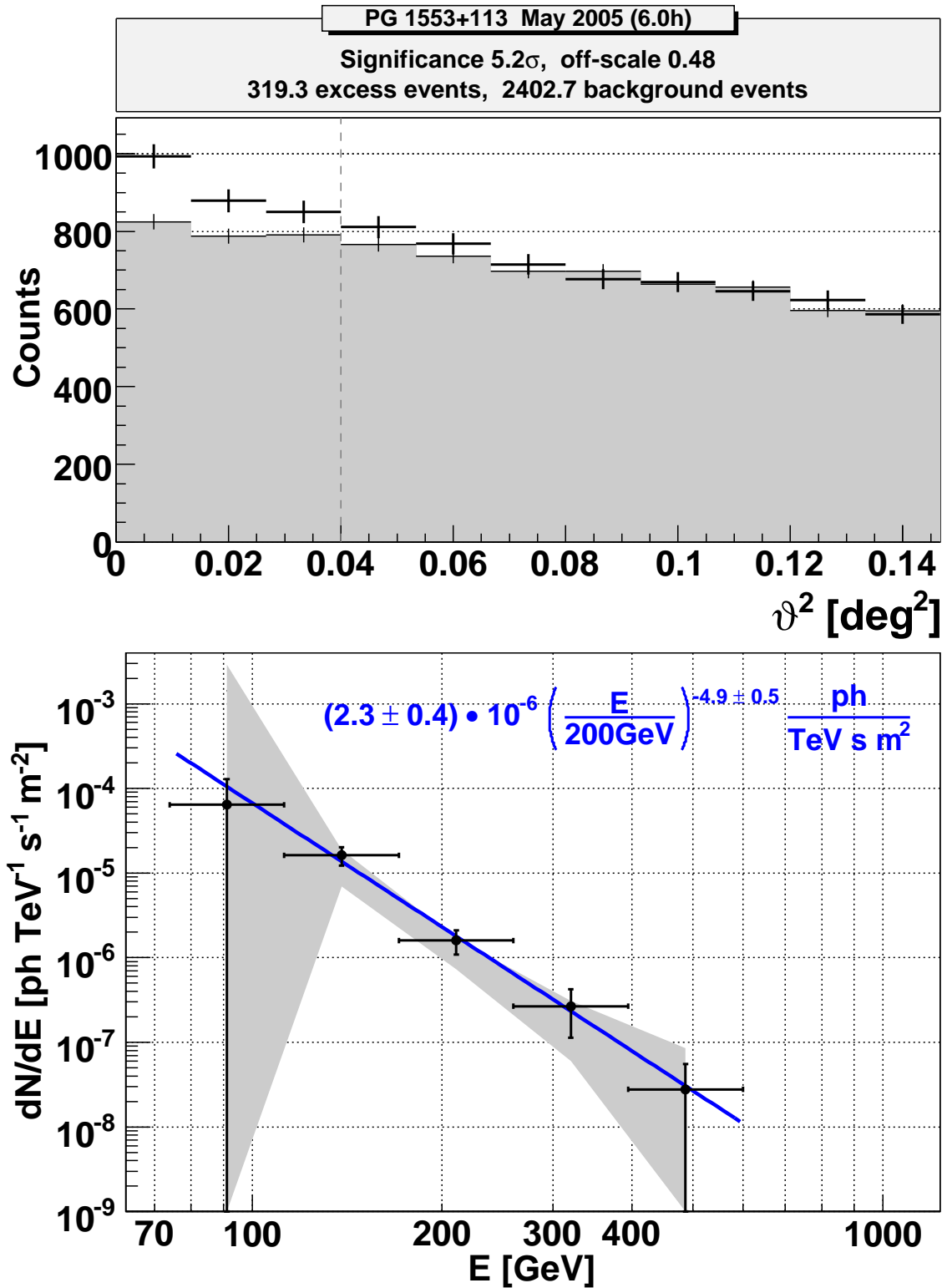


Figure A.1.: Results for the data set of May 2005.

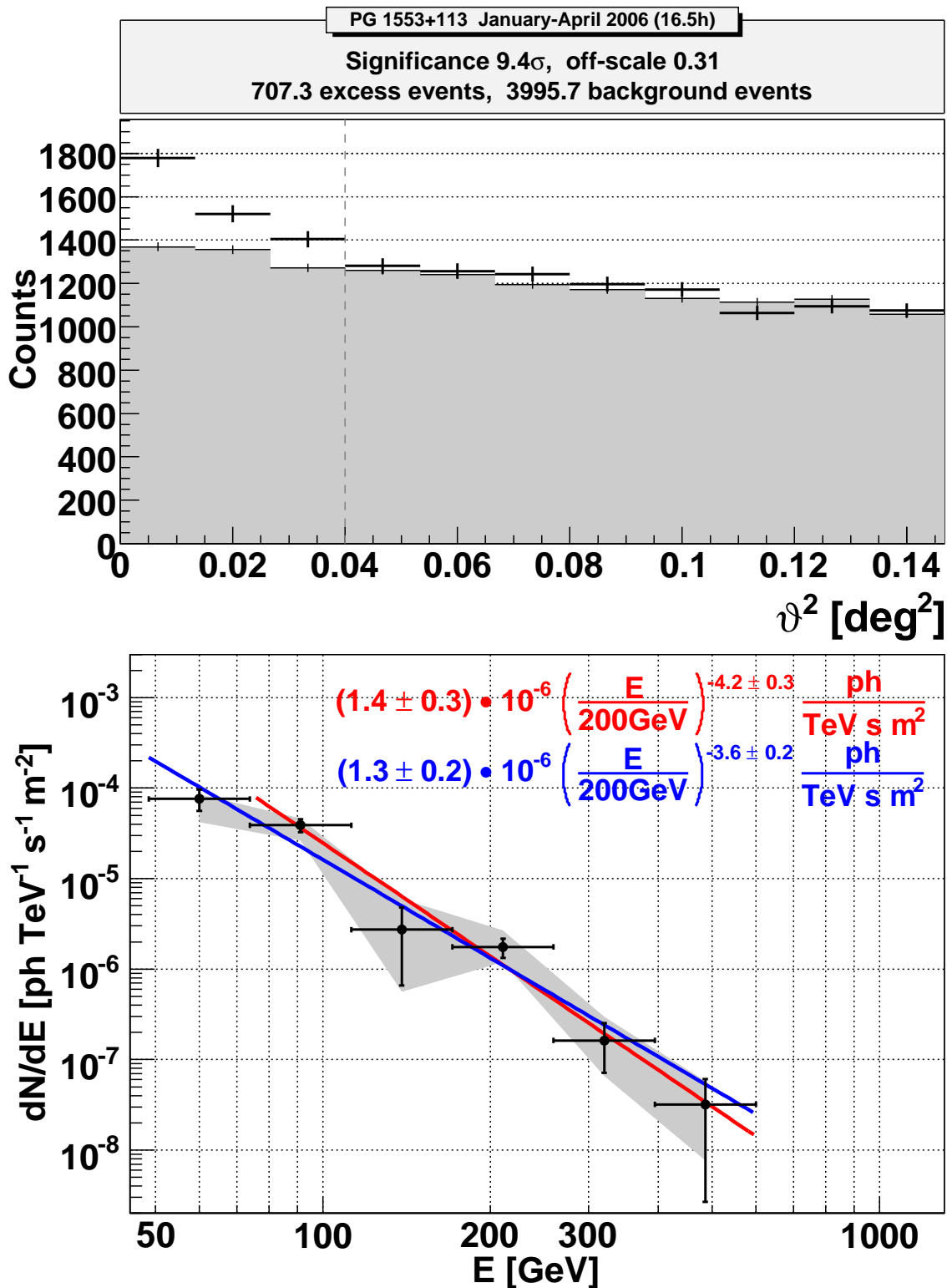


Figure A.2.: Results for the data set from January to April 2006.

A.3. Additional Results from Single Data Sets

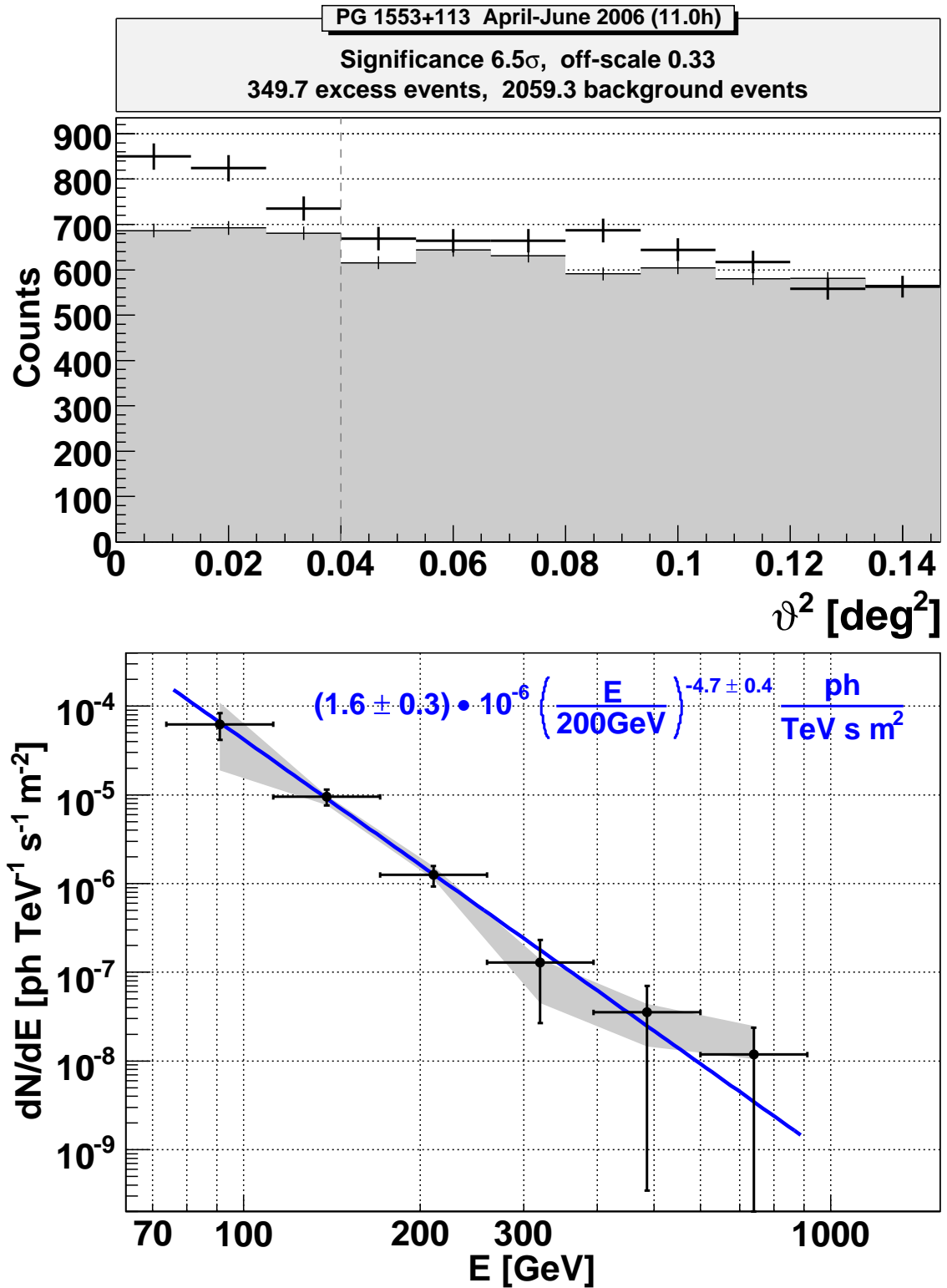


Figure A.3.: Results for the data set from April to June 2006.

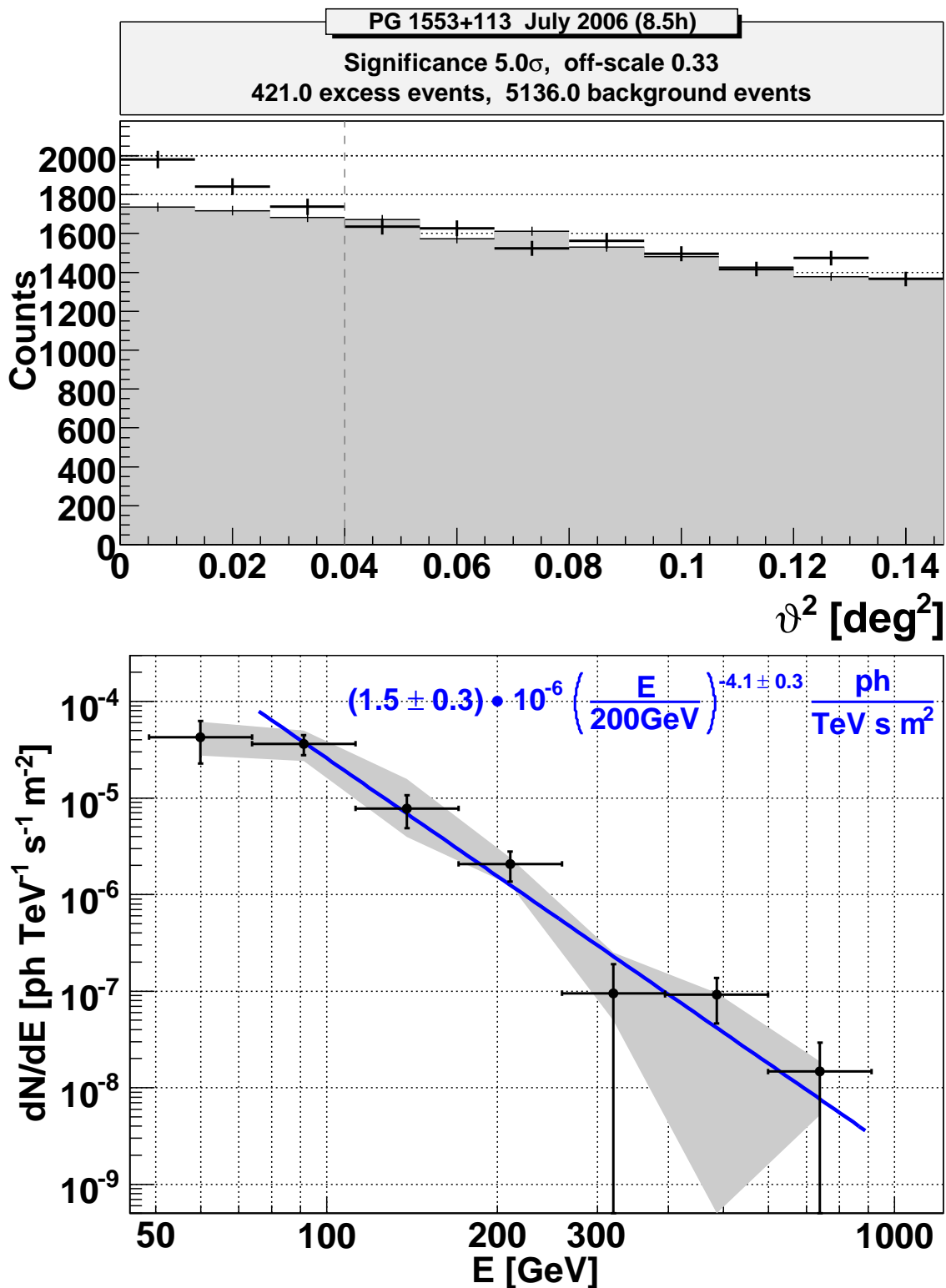


Figure A.4.: Results for the data set of July 2006.

A.3. Additional Results from Single Data Sets

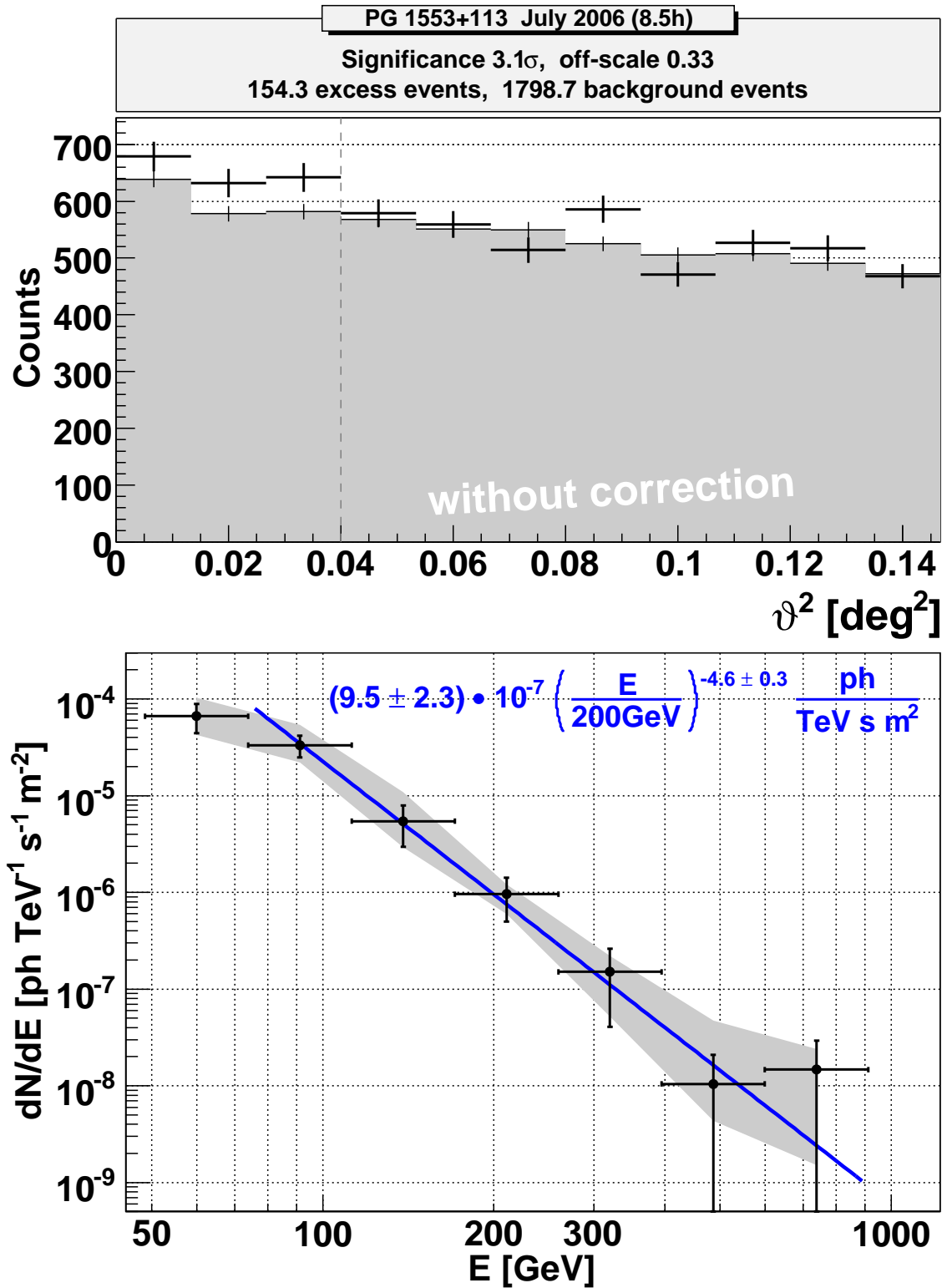


Figure A.5.: Results for the data set of July 2006 without applying a correction.

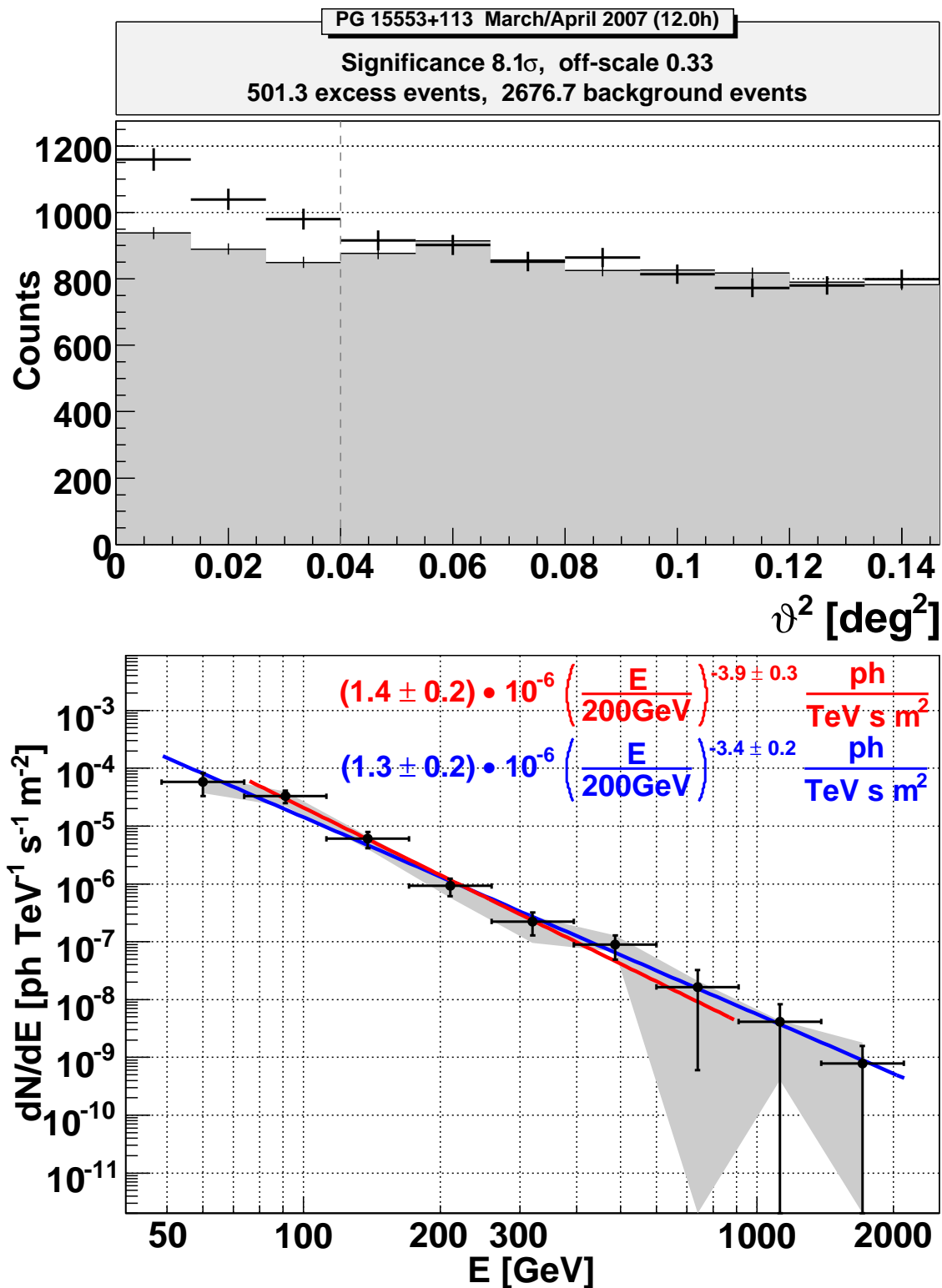


Figure A.6.: Results for the data set of March and April 2007.

B. Additional Information on the Automation Package

Here some additional information on the automatic analysis and the automation concept is provided.

In figure B.1 a scheme of the data flow in the automatic analysis is drawn. The structure of the automation package is not shown completely, but the most important parts of the database and the relevant scripts and their interaction are displayed. The data flow after the arrival of the files in the data center until the result of the background suppression is shown. The interaction between the scripts and the database and the data storage is specified in a diagram.

Then the components of the automation package including the software and the database are presented in several tables. The software package consists of several shell scripts, listed in table B.1, several root macros, listed see table B.2, and for completeness the programs from the MARS package used in the automatic analysis, listed in table B.3. In addition the files needed for the analysis are given in the tables B.4 and B.5.

In table B.6 it is listed which subsystem produces which files a which rate.

In table B.7 an overview of the database tables and its content is given. In section 3.2.3 more information on the different types of tables can be found. The detailed structure of the database follows in the consecutive tables (mysqldump from February 23th 2007).

B. Additional Information on the Automation Package

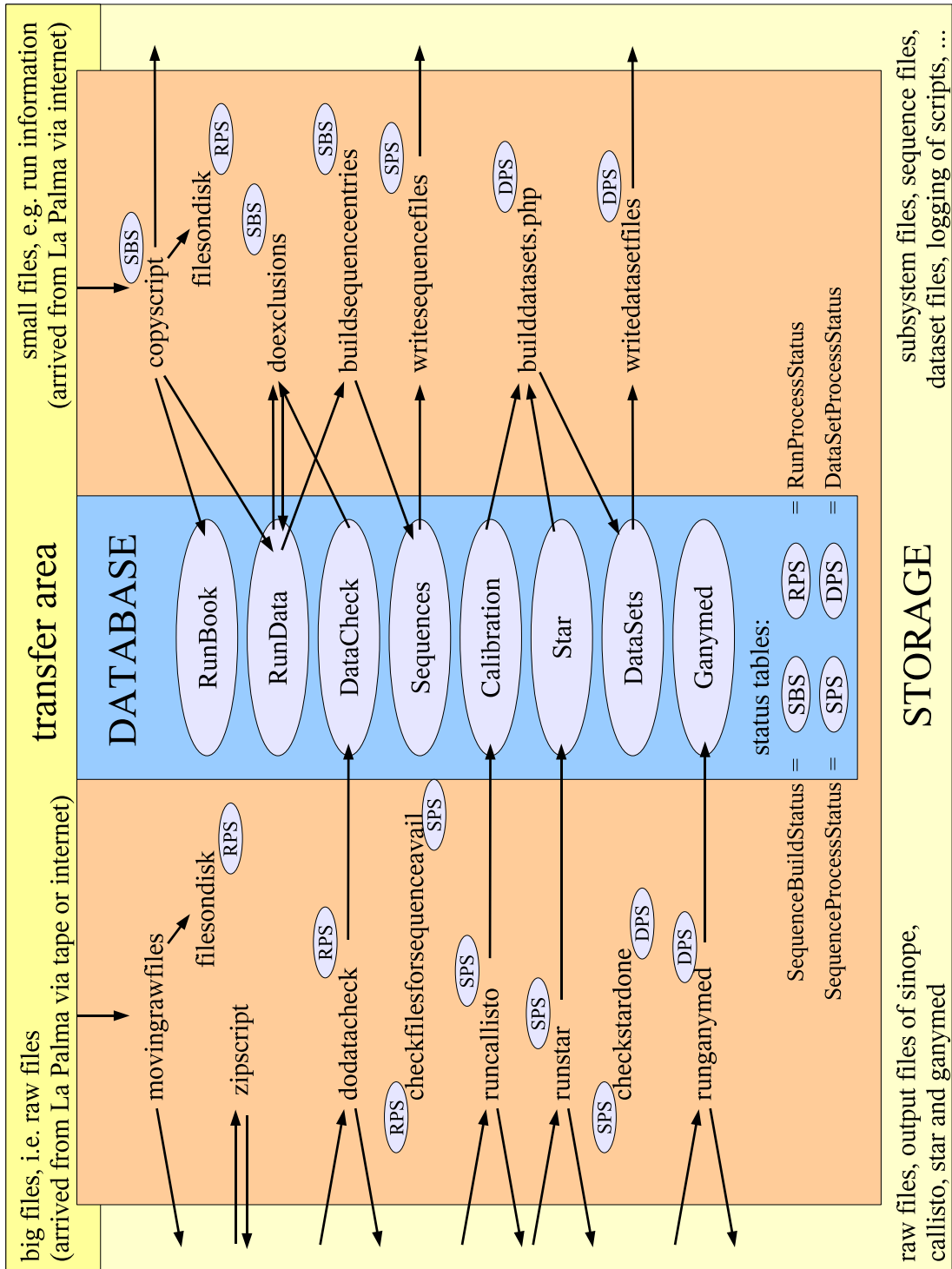


Figure B.1.: Scheme of the data flow in the automatic analysis, including the most important scripts and tables in the database.

Table B.1.: Alphabetical list of the scripts of the automation package. Some of the scripts call programs (B.3) or macros (B.2), which is given in the second column, while the third column explains the task of the script.

shell script	launches	task
buildsequenceentries	buildsequencentries.C	build sequences from the run information
checkfilesforsequenceavail	checkfileavail.C	check if all files needed for calibration are available
checklogs	-	provide warnings and errors from all logfiles
checkstardone	checkstardone.C	check if all files needed for ganymed are available
checktransfer	-	check if the transfer from La Palma and PIC is running
copyscript	filldotrun.C filldotrbk.C insertdate.C filloptical.C	insert run information into database insert runbook entries into database insert date into database, needed for further processing insert optical data into database and move all files to the data center structure
correcttime	correct_raw_time	correct timing of raw files
dodatacheck	filldotraw.C sinope fillsinope.C resetcolumn.C	insert additional information from rawfiles into database run data check for C and D runs fill results from sinope into database reset exclusions
doexclusions	doexclusions.C	exclude runs from the analysis
doqualityplots	plotdb.C	plot quality parameter from the database: for all data, for all data sets
dowebplots	showplot	produce ps and png from all status display root files
filesondisk	resetallruns.C findcacofiles.C insertcacofile.C	reset entries in the database for all files (raw, caco and cc) search appropriate caco files for raw files insert found caco files into database
fillcallisto	fillcalib.C fillsignal.C	read information from calib*.root files and insert it into database read information from signal*.root files and insert it into database
fillstar	fillstar.C	read information from star*.root files and insert it into database
jobmanager	runcallisto,	launch all scripts running the main steps (calibration, calculation

Table B.1 – Continued

shell script	launches	task
	runstar, runganymed, dodatacheck	of image parameter, background suppression and datacheck) and make sure that the computing system is used efficiently
linkmc	-	link montecarlo camera files to structure needed by Mars
makecallistolinks	- resetcolumn.C	link callisto.rc files for sequences with problems reset callisto in the database
mcsequences	-	build montecarlo sequences for processing and write sequence files
movingrawfiles	-	move transferred raw files to data center structure
movingsubsystemfiles	-	move transferred (via tape) subsystem files to data center structure
processmcsequences	callisto, star	calibrate montecarlo sequences calculate image parameter for montecarlo sequences
rmlocks	-	remove lockfiles in case of power failure of the computer system
runcallisto	callisto merpp	calibrate raw files and merge subsystem files into calibrated files
runganymed	ganymed	do background suppression for data sets
runstar	star	calculate image parameter for sequences
scriptlauncher	-	launch database interaction scripts and scripts started preferably in a special order
setup	-	setup file for variables and jobmanager
sourcefile	-	collection of functions used in all scripts
webupdate-callisto	dowebplots	produce callisto plots and copy them to the web
webupdate-ganymed	dowebplots	produce ganymed plots and copy them to the web
webupdate-sinope	dowebplots	produce sinope plots and copy them to the web
webupdate-star	dowebplots	produce star plots and copy them to the web
writedatasetfile	writedataset.C	write data set files
writesequencefiles	writesequencefile.C	write sequence files
zipscript	-	zip rawf files

root macro	task
buildsequenceentries.C	read run information from database [RunData], group runs to sequences, insert sequence information [Sequences, SequenceProcessStatus]
checkfileavail.C	check from database [RunProcessStatus] if all files (*.raw, *.rep, *.txt) needed for calibration of sequence are available
checkstardone.C	check from database [SequenceProcessStatus] availability star files for sequences
doexclusions.C	read exclusions from setup file, insert exclusion flag into database [RunData] for bad runs
fillcalib.C	read parameter from calib*.root insert them into database [Calibration]
filldotraw.C	read information from raw file and insert it into database [RunData]
filldotrbk.C	read runbook entries from *.rbk and insert it into database [RunBook]
filldotrun.C	read information from *.run and insert it into database [RunData, DataCheck]
fillganymed.C	read information from ganymed file and insert it into database [Ganymed]
filloptical.C	read information from *.instr and insert it into database [OpticalData]
fillsignal.C	read information from signal*.root and insert it into database [Calibration]
fillsinope.C	read information from sinope file and insert it into database [DataCheck]
fillstar.C	read information from star file and insert it into database [Star]
findcacofiles.C	check the database [RunProcessStatus] for missing caco files and write list
insertcacofile.C	insert found caco file into database [RunProcessStatus]
insertdate.C	insert date into database [SequenceBuildStatus]
plotdb.C	query quality parameter from database [Calibration,Star] and plot them
resetallruns.C	reset status of file availability in database [RunProcessStatus]
resetcolumn.C	reset status of one step in database [*Status]
writedatasetfile.C	query data set information from database [DataSets,DataSetSequenceMapping] and write data set file
writesequencefile.C	query sequence information from database [Sequences] and write sequence file

Table B.2.: List of root macros provided by the automation package including an explanation of their usage. In [] the tables in the database are given with which the macros interact.

program	task
callisto	calculate calibration constants, extract signal and calibrate data
ganymed	background suppression
mars-config	check root or mars version
mars	display events
merpp	preprocessing raw to root files, merpp report and currents files
showlog	display log file
showplot	show status display
sinope	data check
sponde	spectrum and flux calculation
star	image cleaning, bad pixel treatment, software trigger, calculation of image parameter

Table B.3.: List of the programs and their tasks in the MARS package. Most of them are also used in the automation package.

filetype	extension	identifier	content
files from La Palma			
rawfiles	.raw	run #	rawdata
ccfiles	.rep, .run, .run.html, .rbk	run #, time	data of central control, i.e. reports of subsystem, runbook, ...
cacofiles	.txt	run #, timestamp	data of camera control, i.e. dc currents, ...
other input files			
mcfiles	.raw	run #	simulated data
setup files for the analysis:			
sequence files	.txt	sequence #	setup file grouping runs together
dataset files	.txt	dataset #	setup file grouping sequences together
output files of the analysis:			
calibrated files	*Y*.root	sequence #, run #	output files of the calibration
star files	*I*.root	sequence #, run #	output files of the calculation of the image parameter
ganymed files	.root	dataset #	output files of the back ground suppression

Table B.4.: Overview of input and output files in the analysis.

filetype	analysis step	purpose
rawfiles	callisto	calibrate rawdata
ccfiles (.rep)	callisto	merpp subsystem information into calibrated files, e.g. starguider information
cacofiles	callisto	to merpp caco information into calibrated files
sequence files	callisto, star	contains information which runs belong to sequence
calibrated files	star	calculation of image parameter
dataset files	ganymed, sponde	contains information which sequences belong to the dataset
star files	ganymed	background suppression
mc files	ganymed	train cuts
ganymed files	sponde	spectrum
mc files	sponde	energy reconstruction

Table B.5.: Overview, which files are needed for which step in the analysis.

file	subsystem	frequency	content	usage
*.rbk	cc	1 per cc start	electronic runbook	filldotrbk.C
*.run	cc	1 per cc start	set of run information	filldotrun.C
*.run.html	cc	1 per cc start	reduced set of run information	archive, web
*.rep	cc	1 per cc start 1 per run	reports from all subsystems	archive merpp
*.dbg	cc	1 per cc start	logging information	archive
*.edb	cc	2 per night	current catalogfiles	archive, ganymed
*.txt	caco	1 per run 1 per between runs	currents	merpp archive
*.log *.errlog *.err	caco	several per night	logging	archive
*.log *.out *.Out	amc	1 per amc start	logging	archive
*.lut *.info	amc	1 laser adjust	information from laser adjust	archive
*.star	amc	1 per LUT adjust	information from LUT adjust	archive
*.log	drive	1 per drive start	logging	archive
*.rep	drive	1 per drive start	starguider and drive reports	archive
*.txt	drive	2 per drive start (when taking data for pointing models)	data for pointing models (telescope and starguider)	pointing model, mispointing correction
*.log	daq	1 per daq start	logging	archive
*.raw	daq	1 per run	raw data	callisto

Table B.6.: Overview, which files are generated on the site in La Palma listing from which subsystem the file is written and at which frequency. Apart from that, the content and the later usage is given.

Table B.7.: This table gives the information which table in the MAGIC database contains which information. The type given in the second column pursues the following notation:

I: information

i: initial information, i.e. coming directly from the site

p: processing information, i.e. obtained during the processing of the data

K: information that reappears and is outsourced in extra tables for technical reasons

R: analysis results from the various analysis steps

a: additional information i.e. not needed for and not coming from the analysis

S: information about the status of the analysis

More on the different types of tables in the MAGIC database can be found in section 3.2.3.

name	type	content
Band	iIK	information on different filter bands of the optical data
CCD	iIK	information on different CCDs of the optical data
Calibration	pR	results of calibration
CalibrationScript	iIK	information on different calibration scripts
DataCheck	pR	results from the data check
DataSetProcessStatus	S	status of the data set processing
DataSetSequenceMapping	pI	information which data set contains which sequences
DataSets	pI	information on data sets
DiscriminatorThresholdTable	iIK	information on different discriminator threshold settings
ExcludedFDA	pIK	list of reasons to exclude runs from the analysis
FitsFile	iIK	information on different fitsfiles of the optical data
Ganymed	pR	results from the background suppression
HvSettings	iIK	information on different HV settings
L1TriggerTable	iIK	information on different configurations of level 1 of the trigger
L2TriggerTable	iIK	information on different configurations of level 2 of the trigger
LightConditions	iIK	information on different light conditions
MagicNumber	iIK	information on different file states
MarsVersion	aI	information when which Mars release was used in the data center

Table B.7 – Continued

name	type	content
Object	aIK	information on the observed objects
ObservationMode	iIK	information on different observation modes
OpticalData	iI	optical data
Project	iIK	information on different project names
RunBook	iI	entries of the electronical runbook
RunData	iI	run information
RunProcessStatus	S	status of the run processing
RunType	iIK	information on different run types
SequenceBuildStatus	S	status of the steps on night basis
SequenceProcessStatus	S	status of the sequence processing
Sequences	pI	sequence information
Source	iIK	information on different source names
SourceType	aIK	information on different source types
Star	pR	results from the calculation of the image parameter
Status	iIK	information on different states of the optical data
Telescope	iIK	information on different telescopes of the optical data
TestFlag	iIK	information on different flags (of the runs)
TriggerDelayTable	iIK	information on different trigger delays
User	aIK	user administration for dataset building

B. Additional Information on the Automation Package

Table B.8.: Structure of table Band

Field	Type	Null	Default
<i>fBandKEY</i>	smallint(5)	No	
fBandName	varchar(255)	No	
fBand	varchar(255)	Yes	NULL

Table B.9.: Structure of table CCD

Field	Type	Null	Default
<i>fCCDKEY</i>	smallint(5)	No	
fCCDName	varchar(255)	No	
fCCD	varchar(255)	Yes	NULL

Table B.10.: Structure of table Calibration

Field	Type	Null	Default
<i>fSequenceFirst</i>	int(10)	No	0
fUnsuitableInner	smallint(5)	No	0
fUnsuitableOuter	smallint(5)	No	0
fUnreliableInner	smallint(5)	No	0
fUnreliableOuter	smallint(5)	No	0
fIsolatedInner	smallint(5)	No	0
fIsolatedOuter	smallint(5)	No	0
fIsolatedMaxCluster	smallint(5)	No	0
fLastUpdate	timestamp(14)	Yes	NULL
fMeanPedRmsInner	float(6,2)	No	0.00
fMeanPedRmsOuter	float(6,2)	No	0.00
fArrTimeMeanInner	float(5,1)	No	0.0
fArrTimeMeanOuter	float(5,1)	No	0.0
fArrTimeRmsInner	float(6,2)	No	0.00
fArrTimeRmsOuter	float(6,2)	No	0.00
fConvFactorInner	float(6,3)	No	0.000
fConvFactorOuter	float(6,3)	No	0.000
fMeanSignalOuter	float(6,2)	No	0.00
fMeanSignalInner	float(6,2)	No	0.00
fPulsePosMean	float(6,2)	No	0.00
fPulsePosRms	float(6,2)	No	0.00
fPulsePosCheckMean	float(6,2)	Yes	NULL
fPulsePosCheckRms	float(6,2)	Yes	NULL
fPulsePosOffMed	float(7,4)	Yes	NULL

Table B.10.: Structure of table Calibration (continued)

Field	Type	Null	Default
fPulsePosOffDev	float(7,4)	Yes	NULL
fHiLoGainRatioMed	float(6,2)	Yes	NULL
fHiLoGainRatioDev	float(6,2)	Yes	NULL

Table B.11.: Structure of table CalibrationScript

Field	Type	Null	Default
<i>fCalibrationScriptKEY</i>	smallint(5)	No	
fCalibrationScriptName	varchar(255)	No	
fCalibrationScript	varchar(255)	Yes	NULL

Table B.12.: Structure of table DataCheck

Field	Type	Null	Default
<i>fRunNumber</i>	int(10)	No	0
fEvents	int(10)	Yes	NULL
fPositionSignal	tinyint(3)	Yes	NULL
fPositionFWHM	tinyint(3)	Yes	NULL
fHeightSignal	smallint(5)	Yes	NULL
fHeightFWHM	smallint(5)	Yes	NULL
fHasSignal	enum('yes', 'no')	Yes	NULL
fHasPedestal	enum('yes', 'no')	Yes	NULL
fPositionAsym	enum('yes', 'no')	Yes	NULL
fHeightAsym	enum('yes', 'no')	Yes	NULL
fEventsInterlaced	int(10)	Yes	NULL
fPositionSignalInterlaced	tinyint(3)	Yes	NULL
fPositionFWHMInterlaced	tinyint(3)	Yes	NULL
fHeightSignalInterlaced	smallint(5)	Yes	NULL
fHeightFWHMInterlaced	smallint(5)	Yes	NULL
fHasSignalInterlaced	enum('yes', 'no')	Yes	NULL
fHasPedestalInterlaced	enum('yes', 'no')	Yes	NULL
fPositionAsymInterlaced	enum('yes', 'no')	Yes	NULL
fHeightAsymInterlaced	enum('yes', 'no')	Yes	NULL

Table B.13.: Structure of table DataSetProcessStatus

Field	Type	Null	Default
<i>fDataSetNumber</i>	int(10)	No	0

B. Additional Information on the Automation Package

Table B.13.: Structure of table DataSetProcessStatus (continued)

Field	Type	Null	Default
fDataSetInserted	datetime	Yes	NULL
fGanymed	datetime	Yes	NULL
fStarFilesAvail	datetime	Yes	NULL
fFillGanymed	datetime	Yes	NULL
fStartTime	datetime	Yes	NULL
fFailedTime	datetime	Yes	NULL
fFailedCode	smallint(5)	Yes	NULL
fReturnCode	smallint(5)	Yes	NULL
fFailedCodeAdd	int(10)	Yes	NULL
fDataSetFileWritten	datetime	Yes	NULL

Table B.14.: Structure of table DataSetSequenceMapping

Field	Type	Null	Default
<i>fSequenceFirst</i>	int(11)	No	0
<i>fDataSetNumber</i>	int(11)	No	0
fOnOff	tinyint(4)	No	0

Table B.15.: Structure of table DataSets

Field	Type	Null	Default
<i>fDataSetNumber</i>	int(10)	No	0
fSourceKEY	smallint(5)	No	0
fLastUpdate	timestamp(14)	Yes	NULL
fComment	varchar(255)	Yes	NULL
fDataSetName	varchar(20)	Yes	NULL
fRunTime	smallint(6)	No	0
fZenithDistanceMax	tinyint(4)	Yes	NULL
fZenithDistanceMin	tinyint(4)	Yes	NULL
fRunStop	datetime	No	0000-00-00 00:00:00
fRunStart	datetime	No	0000-00-00 00:00:00
fObservationModeKEY	smallint(6)	No	0
fUserKEY	smallint(6)	No	0

Table B.16.: Structure of table DiscriminatorThresholdTable

Field	Type	Null	Default
<i>fDiscriminatorThresholdTableKEY</i>	smallint(5)	No	

Table B.16.: Structure of table DiscriminatorThresholdTable (continued)

Field	Type	Null	Default
fDiscriminatorThresholdTableName	varchar(255)	No	
fDiscriminatorThresholdTable	varchar(255)	Yes	NULL

Table B.17.: Structure of table ExcludedFDA

Field	Type	Null	Default
fExcludedFDAKEY	smallint(5)	No	
fExcludedFDAName	varchar(255)	No	
fExcludedFDA	varchar(255)	Yes	NULL
fExcludedFDAImportance	smallint(5)	Yes	NULL
fExcludedFDAAutomatic	enum('yes', 'no')	Yes	NULL

Table B.18.: Structure of table Filter

Field	Type	Null	Default
fFilterKEY	smallint(5)	No	
fFilterName	varchar(255)	No	
fFilter	varchar(255)	Yes	NULL

Table B.19.: Structure of table FitsFile

Field	Type	Null	Default
fFitsFileKEY	smallint(5)	No	
fFitsFileName	varchar(255)	No	
fFitsFile	varchar(255)	Yes	NULL

Table B.20.: Structure of table Ganymed

Field	Type	Null	Default
fDataSetNumber	int(10)	No	0
fExcessEvents	int(10)	No	0
fBackgroundEvents	int(10)	No	0
fSignalEvents	int(10)	No	0
fSignificance	float(5,1)	Yes	NULL
fScaleFactor	float(5,2)	Yes	NULL
fEffOnTime	int(10)	No	0
fLastUpdate	timestamp(14)	Yes	NULL

B. Additional Information on the Automation Package

Table B.20.: Structure of table Ganymed (continued)

Field	Type	Null	Default
fStandard	enum('no', 'yes')	No	no

Table B.21.: Structure of table HvSettings

Field	Type	Null	Default
<i>fHvSettingsKEY</i>	smallint(5)	No	
fHvSettingsName	varchar(255)	No	
fHvSettings	varchar(255)	Yes	NULL

Table B.22.: Structure of table L1TriggerTable

Field	Type	Null	Default
<i>fL1TriggerTableKEY</i>	smallint(5)	No	
fL1TriggerTableName	varchar(255)	No	
fL1TriggerTable	varchar(255)	Yes	NULL

Table B.23.: Structure of table L2TriggerTable

Field	Type	Null	Default
<i>fL2TriggerTableKEY</i>	smallint(5)	No	
fL2TriggerTableName	varchar(255)	No	
fL2TriggerTable	varchar(255)	Yes	NULL

Table B.24.: Structure of table LightConditions

Field	Type	Null	Default
<i>fLightConditionsKEY</i>	smallint(5)	No	
fLightConditionsName	varchar(255)	No	
fLightConditions	varchar(255)	Yes	NULL

Table B.25.: Structure of table MagicNumber

Field	Type	Null	Default
<i>fMagicNumberKEY</i>	tinyint(3)	No	
fMagicNumber	smallint(5)	No	0
fMagicNumberName	varchar(255)	No	

Table B.26.: Structure of table MarsVersion

Field	Type	Null	Default
<i>fMarsVersion</i>	smallint(5)	No	
fStartDate	datetime	Yes	NULL
fMarsVersionName	varchar(12)	No	

Table B.27.: Structure of table Object

Field	Type	Null	Default
<i>fObjectKEY</i>	smallint(5)	No	
fObjectName	varchar(255)	No	
fObject	varchar(255)	Yes	NULL
fMagnitude	float(5,2)	Yes	NULL
fVRColour	float(4,2)	Yes	NULL
fSourceKEY	smallint(5)	No	0
fRightAscension	double	Yes	NULL
fDeclination	double	Yes	NULL
fEpoche	smallint(5)	Yes	NULL

Table B.28.: Structure of table ObservationMode

Field	Type	Null	Default
<i>fObservationModeKEY</i>	smallint(5)	No	
fObservationModeName	varchar(255)	No	
fObservationMode	varchar(255)	Yes	NULL

Table B.29.: Structure of table OpticalData

Field	Type	Null	Default
<i>fOpticalDataKEY</i>	int(11)	No	
fTimestamp	datetime	No	0000-00-00 00:00:00
fExposure	smallint(5)	No	0
fFitsFileKEY	smallint(5)	No	0
fObjectKEY	smallint(5)	No	0
fSkyLevel	float(6,1)	Yes	NULL
fFWHM	float(4,2)	Yes	NULL
fApertureRadius	float(3,1)	Yes	NULL
fInstrumentalMag	float(7,4)	Yes	NULL
fInstrumentalMagErr	float(6,4)	Yes	NULL
fStatusKEY	smallint(5)	No	0

B. Additional Information on the Automation Package

Table B.29.: Structure of table OpticalData (continued)

Field	Type	Null	Default
fZenithDistance	float(4,1)	Yes	NULL
fBandKEY	smallint(5)	No	0
fFilterKEY	smallint(5)	No	0
fTelescopeKEY	smallint(5)	No	0
fCCDKEY	smallint(5)	No	0

Table B.30.: Structure of table Project

Field	Type	Null	Default
fProjectKEY	smallint(5)	No	
fProjectName	varchar(100)	No	
fProject	varchar(255)	Yes	NULL

Table B.31.: Structure of table RunBook

Field	Type	Null	Default
fRunBookKEY	int(10)	No	
fRunBookDate	datetime	No	0000-00-00 00:00:00
fRunBookText	text	No	

Table B.32.: Structure of table RunData

Field	Type	Null	Default
fRunDataKEY	int(10)	No	
fRunNumber	int(10)	No	0
fMagicNumberKEY	tinyint(3)	No	0
fFormatVersion	smallint(5)	No	0
fRunTypeKEY	tinyint(3)	No	0
fProjectKEY	smallint(5)	No	0
fSourceKEY	smallint(5)	No	0
fNumEvents	mediumint(8)	No	0
fRunStart	datetime	No	0000-00-00 00:00:00
fRunStop	datetime	Yes	NULL
fZenithDistance	tinyint(4)	Yes	NULL
fAzimuth	smallint(6)	Yes	NULL
fTriggerTableKEY	smallint(5)	No	0
fHvSettingsKEY	smallint(5)	No	0
fDaqStoreRate	smallint(5)	Yes	NULL

Table B.32.: Structure of table RunData (continued)

Field	Type	Null	Default
fDaqTriggerRate	smallint(5)	Yes	NULL
fMeanTriggerRate	smallint(5)	Yes	NULL
fL2RatePresc	smallint(5)	Yes	NULL
fL2RateUnpresc	smallint(5)	Yes	NULL
fExcludedFDAKEY	smallint(5)	No	0
fSequenceFirst	int(10)	No	0
fLastUpdate	timestamp(14)	Yes	NULL
fTestFlagKEY	smallint(5)	No	0
fLightConditionsKEY	smallint(5)	No	0
fCalibrationScriptKEY	smallint(5)	No	0
fDiscriminatorThresholdTableKEY	smallint(5)	No	0
fTriggerDelayTableKEY	smallint(5)	No	0
fL1TriggerTableKEY	smallint(5)	No	0
fL2TriggerTableKEY	smallint(5)	No	0
fObservationModeKEY	smallint(5)	No	0

Table B.33.: Structure of table RunProcessStatus

Field	Type	Null	Default
<i>fRunNumber</i>	int(10)	No	0
fCCFileAvail	datetime	Yes	NULL
fCaCoFileAvail	datetime	Yes	NULL
fCaCoFileFound	int(10)	Yes	NULL
fRawFileAvail	datetime	Yes	NULL
fDataCheckDone	datetime	Yes	NULL
fTimingCorrection	datetime	Yes	NULL
fMerpp	datetime	Yes	NULL
fMerppCCUpdate	datetime	Yes	NULL
fMerppCaCoUpdate	datetime	Yes	NULL
fStartTime	datetime	Yes	NULL
fFailedTime	datetime	Yes	NULL
fFailedCode	smallint(5)	Yes	NULL
fReturnCode	smallint(5)	Yes	NULL
fFailedCodeAdd	int(10)	Yes	NULL

B. Additional Information on the Automation Package

Table B.34.: Structure of table RunType

Field	Type	Null	Default
<i>fRunTypeKEY</i>	tinyint(3)	No	
fRunType	smallint(5)	No	0
fRunTypeName	varchar(255)	No	

Table B.35.: Structure of table SequenceBuildStatus

Field	Type	Null	Default
<i>fDate</i>	date	No	0000-00-00
fCCFilled	datetime	Yes	NULL
fExclusionsDone	datetime	Yes	NULL
fSequenceEntriesBuilt	datetime	Yes	NULL
fStartTime	datetime	Yes	NULL
fFailedTime	datetime	Yes	NULL
fFailedCode	smallint(5)	Yes	NULL
fReturnCode	smallint(5)	Yes	NULL
fFailedCodeAdd	int(10)	Yes	NULL

Table B.36.: Structure of table SequenceProcessStatus

Field	Type	Null	Default
<i>fSequenceFirst</i>	int(10)	No	0
fSequenceFileWritten	datetime	Yes	NULL
fAllFilesAvail	datetime	Yes	NULL
fCallisto	datetime	Yes	NULL
fFillCallisto	datetime	Yes	NULL
fStar	datetime	Yes	NULL
fFillStar	datetime	Yes	NULL
fStartTime	datetime	Yes	NULL
fFailedTime	datetime	Yes	NULL
fFailedCode	smallint(5)	Yes	NULL
fReturnCode	smallint(5)	Yes	NULL
fFailedCodeAdd	int(10)	Yes	NULL

Table B.37.: Structure of table Sequences

Field	Type	Null	Default
<i>fSequenceFirst</i>	int(10)	No	0
fSequenceLast	int(10)	Yes	NULL

Table B.37.: Structure of table Sequences (continued)

Field	Type	Null	Default
fProjectKEY	smallint(5)	No	0
fSourceKEY	smallint(5)	No	0
fNumEvents	mediumint(8)	No	0
fRunStart	datetime	No	0000-00-00 00:00:00
fTriggerTableKEY	smallint(5)	No	0
fHvSettingsKEY	smallint(5)	No	0
fManuallyChangedKEY	smallint(5)	No	0
fLastUpdate	timestamp(14)	Yes	NULL
fRunTime	smallint(5)	No	0
fTriggerDelayTableKEY	smallint(5)	No	0
fDiscriminatorThresholdTableKEY	smallint(5)	No	0
fTestFlagKEY	smallint(5)	No	0
fLightConditionsKEY	smallint(5)	No	0
fAzimuthMin	smallint(6)	Yes	NULL
fAzimuthMax	smallint(6)	Yes	NULL
fZenithDistanceMin	tinyint(4)	Yes	NULL
fZenithDistanceMax	tinyint(4)	Yes	NULL
fL1TriggerTableKEY	smallint(5)	No	0
fL2TriggerTableKEY	smallint(5)	No	0
fObservationModeKEY	smallint(5)	No	0
fRunStop	datetime	Yes	NULL

Table B.38.: Structure of table Source

Field	Type	Null	Default
fSourceKEY	smallint(5)	No	
fSourceName	varchar(80)	No	
fSourceTypeKEY	smallint(5)	No	0
fRightAscension	double	Yes	NULL
fDeclination	double	Yes	NULL
fEpochChar	char(1)	Yes	NULL
fEpochDate	smallint(4)	Yes	NULL
fMagnitude	smallint(6)	Yes	NULL
fTest	enum('no', 'yes')	No	no
fRealSourceKEY	smallint(6)	Yes	NULL

B. Additional Information on the Automation Package

Table B.39.: Structure of table SourceType

Field	Type	Null	Default
<i>fSourceTypeKEY</i>	smallint(5)	No	
fSourceTypeName	varchar(255)	No	

Table B.40.: Structure of table Star

Field	Type	Null	Default
<i>fSequenceFirst</i>	int(10)	No	0
fMeanNumberIslands	float(6,2)	No	0.00
fPSF	float(5,1)	No	0.0
fLastUpdate	timestamp(14)	Yes	NULL
fRatio	float(5,1)	No	0.0
fMuonRate	float(6,2)	No	0.00
fMuonNumber	int(10)	No	0
fEffOnTime	int(10)	No	0
fDataRate	int(10)	No	0
fMaxHumidity	float(6,1)	No	0.0
fInhomogeneity	float(5,1)	No	0.0
fNumStarsMed	float(5,1)	No	0.0
fNumStarsRMS	float(5,1)	No	0.0
fBrightnessRMS	float(5,1)	No	0.0
fBrightnessMed	float(5,1)	No	0.0
fNumStarsCorMed	float(5,1)	No	0.0
fNumStarsCorRMS	float(5,1)	No	0.0

Table B.41.: Structure of table Status

Field	Type	Null	Default
<i>fStatusKEY</i>	smallint(5)	No	
fStatusName	varchar(255)	No	
fStatus	varchar(255)	Yes	NULL

Table B.42.: Structure of table Telescope

Field	Type	Null	Default
<i>fTelescopeKEY</i>	smallint(5)	No	
fTelescopeName	varchar(255)	No	
fTelescope	varchar(255)	Yes	NULL

Table B.43.: Structure of table TestFlag

Field	Type	Null	Default
<i>fTestFlagKEY</i>	smallint(5)	No	
fTestFlagName	varchar(255)	No	
fTestFlag	varchar(255)	Yes	NULL

Table B.44.: Structure of table TriggerDelayTable

Field	Type	Null	Default
<i>fTriggerDelayTableKEY</i>	smallint(5)	No	
fTriggerDelayTableName	varchar(255)	No	
fTriggerDelayTable	varchar(255)	Yes	NULL

Table B.45.: Structure of table User

Field	Type	Null	Default
fUserKEY	smallint(6)	Yes	NULL
fUserName	varchar(20)	Yes	NULL

B. Additional Information on the Automation Package

C. Correction of atmospheric absorption due to the Saharan Air Layer

For completeness, the publication mentioned in section 4.2.3 is appended here.

A method to correct IACT data for atmospheric absorption due to the Saharan Air Layer

D. Dorner¹, K. Nilsson², and T. Bretz¹

¹ Universität Würzburg, D-97074 Würzburg, Germany

² Tuorla Observatory, University of Turku, FI-21500 Piikkiö, Finland

Received ... / Accepted ...

ABSTRACT

Context. Using the atmosphere as a detector volume, Imaging Air Cherenkov Telescopes (IACTs) depend highly on the properties and the condition of the air mass above the telescope. On the Canary Island of La Palma, where the Major Atmospheric Gamma-ray Imaging Cherenkov telescope (MAGIC) is situated, the Saharan Air Layer (SAL) can cause strong atmospheric absorption affecting the data quality and resulting in a reduced gamma flux.

Aims. To correlate IACT data with other measurements, e.g. long-term monitoring or Multi-Wavelength (MWL) studies, an accurate flux determination is mandatory. Therefore, a method to correct the data for the effect of the SAL is needed.

Methods. Three different measurements of the atmospheric absorption are performed on La Palma. From the determined transmission, a correction factor is calculated and applied to the MAGIC data.

Results. The different transmission measurements from optical and IACT data provide comparable results. MAGIC data of PG 1553+113, taken during a MWL campaign in July 2006, have been analyzed using the presented method, providing a corrected flux measurement for the study of the spectral energy distribution of the source.

Key words. Methods: data analysis – Atmospheric effects – Techniques: photometric – Gamma rays: observations

1. Introduction

For all ground based observations, the atmosphere plays an important role, as the light of the observed objects passes through it. Scattering and absorption in this air mass, having variable properties, reduce the flux measured by the telescope. On the Canary Island of La Palma, very strong atmospheric absorption can take place in case of the occurrence of the meteorologic phenomenon Saharan Air Layer (SAL): A warm air mass, consisting of mineral dust, is moving from the Sahara westward and becomes the so-called SAL, when it is undercut by a cool and moist air layer from the sea. Located between 1.5 km and 5.5 km a.s.l., the SAL, also known as Calima, can extend in the North Atlantic Ocean as far as the United States and the western Caribbean Sea (Dunion & Velden 2004).

Variable absorption can cause apparent flux variations, and the absolute flux level is reduced. To be able to correct for this, the atmospheric absorption is measured. On La Palma, three measurements are available: The Carlsberg Meridian Telescope (CMT) provides nightly values of extinction. From the optical data of the KVA and also from the MAGIC data itself, the atmospheric transmission can be determined. The results of these measurements are discussed and compared for the nights between July 15th 2006 and July 28th 2006.

A correction method has been developed for the MAGIC telescope: From the absorption measurements, a factor is calculated and used in the analysis to correct for the effect of SAL.

2. Feasibility Study

Before the development of the method, the feasibility of a correction based on the transmission measurement has to be checked. After explaining shortly the principle of the Imaging Air Cherenkov Technique, the effect of the SAL on the Cherenkov data is explained, discussing in particular the vertical shower development.

2.1. Imaging Air Cherenkov Technique

Particles enter the atmosphere and interact there with nuclei, producing electromagnetic or particle cascades. The Cherenkov light emitted by these secondary particles passes the rest of the atmosphere and is measured in a camera equipped with photon detectors. The morphology of the recorded shower images is used to distinguish the images of gamma induced showers from those initiated by other particles, e.g. protons. Therefore the shower images are parameterized (Hillas 1985), and cuts in the corresponding distributions are used to suppress the background (Riegel & Bretz 2005). The energy spectrum is calculated by comparing the parameters of the measured to those of the simulated data, for which the energy is known. The most important parameter to reconstruct the energy of a primary photon is SIZE, i.e. the total amount of light in the shower image. Apart from minor dependences on other properties, the energy is mainly proportional to the SIZE.

Send offprint requests to: Daniela Dorner e-mail: daniela.dorner@astro.uni-wuerzburg.de

2.2. Effect of Atmospheric Absorption

The atmospheric absorption reduces the number of measured photons and therefore the SIZE of the shower images. Consequently, the energy of the primary particle is underestimated when comparing the SIZE of affected data to that of showers simulated for an ideal atmosphere. For an accurate energy reconstruction, the shower images have to be corrected for the loss of light due to absorption, or the atmospheric absorption has to be included in the simulation. As different amounts of atmospheric absorption in the single nights would require different sets of simulated data, a correction method for the data is preferred.

2.3. Dependence on the Height in the Atmosphere

Based on optical data, the values for transmission provided by CMT and KVA correspond to light passing the whole atmosphere. The Cherenkov light of a shower originates in a height between 20 km a.s.l. and the ground. While the first interaction takes place at about 20 km a.s.l., the shower maximum is at around 10 km a.s.l. Figure 1 shows the number of produced Cherenkov photons (upper plot) and the fraction of produced light (lower plot) versus height. From the integral fraction of light (lower plot), it can be concluded that for primary particles with an energy below 500 GeV more than 90% of the shower light is produced above 5.5 km a.s.l. Consequently, less than 10% of the overall emitted light is absorbed slightly less as it does not pass the complete SAL. In a first order approximation, this small effect can be neglected, meaning that a factor calculated from the measured atmospheric transmission can be used to correct the affected data.

3. Measurements of the Atmospheric Absorption

Absorption measurements are available from three different instruments at the Observatorio del Roque de los Muchachos (ORM).

3.1. CMT - Extinction Measurements

The CMT (Evans et al. 2002) is one of the optical telescopes in the ORM. Since 1984, it provides a value for the atmospheric extinction for each night. Since April 1999, the measurement is done in the r'-band at an effective wavelength of 625 nm (CMT 2007). For a dust-free night, the extinction for the passband r' has been determined to be 0.09 mag. The atmospheric transmission $\frac{I}{I_0}$ can be calculated with the following formula, where m_0 is the extinction in a dust-free night and m the observed one:

$$\frac{I}{I_0} = 10^{\frac{m-m_0}{-2.5}} \quad (1)$$

While the Cherenkov spectrum extends between 280 nm and 700 nm and has its maximum at about 320 nm, the optical measurements are above 600 nm. As the effect of SAL is dominated by Mie scattering, i.e. being independent of the wavelength, the measured absorption can be used for the correction.

As the values of the CMT are given for zenith, i.e. airmass $X = 1$, they have to be corrected for the larger airmass when using them for data with higher zenith distance.

For the IACT data presented here, the zenith distance is between 18° and 35° ($1.05 < X < 1.22$) resulting in a difference for the atmospheric transmission of less than 5% for the range of extinction values shown here.

3.2. KVA - Optical Data

The KVA telescope¹ consists of two telescopes with 60 cm and 35 cm apertures. The latter is used for photometric observations of TeV blazars in the R-band (effective wavelength 640 nm). The flux of the blazar is determined by measuring the counts inside a circular aperture and comparing this to several calibrated comparison stars in the field of the blazar, measured with the same aperture radius. In this way, any influence of atmospheric extinction is effectively eliminated. However, the comparison stars can also be used to estimate the atmospheric extinction during the night. In principle, the extinction could be determined by fitting a straight line to an airmass-magnitude plot, but for this the photometric accuracy of the comparison stars in the literature (0.02 mag-0.05 mag) is not sufficient. Instead, only stars observed at low airmass ($X < 1.2$) were selected and for each star the zero point value $z_0 = R_{instr} - R_{cal}$ was determined, where R_{instr} is the measured magnitude (scaled to an exposure time of one second) and R_{cal} is the calibrated R-band magnitude. Averaging z_0 for each night, 5.16 is found to describe well a photometric night. During nights affected by the SAL, z_0 is higher. The transmission relative to a dust-free night is computed with formula 1, where m_0 is 5.16 and m the average z_0 for the night.

3.3. MAGIC Data

In addition to the optical measurements, the atmospheric transmission can be determined directly from the IACT data.

A simple way is to use the absolute light yield measure obtained from muon images as described in Goebel et al. (2005). This method is based on the fact that the spectral shape and flux of muons at the telescope are well known. For a well determined muon sample, only showers where the telescope is inside the Cherenkov light cone are selected. As these showers produce ring-like images in the camera, the background can be completely suppressed. Comparing the measured light yield distribution to that of a corresponding simulated sample, gives a ratio which is then used for an absolute light calibration to correct for changes in the light efficiency of the telescope, e.g. mirror degradation. As this correction is done on monthly basis, short time variations of the atmosphere are not taken into account. Consequently, the effect of SAL is still visible from the measured muons. Having an impact parameter smaller than the diameter of the mirror (17 m), the selected muons produce their light between 700 m above the telescope and the ground, i.e. between 2900 m and 2200 m a.s.l. in case of the MAGIC telescope. To account for the fact that this light passes only part of the SAL, the determined ratio is multiplied by a factor of ten to estimate the absorption, assuming an effective production height of 350 m for Cherenkov light. Without any additional measurements, the layering of the SAL is unknown. Accordingly, the results from the muons are not very precise and should therefore not be used for

¹ <http://tur3.tur.iac.es/>

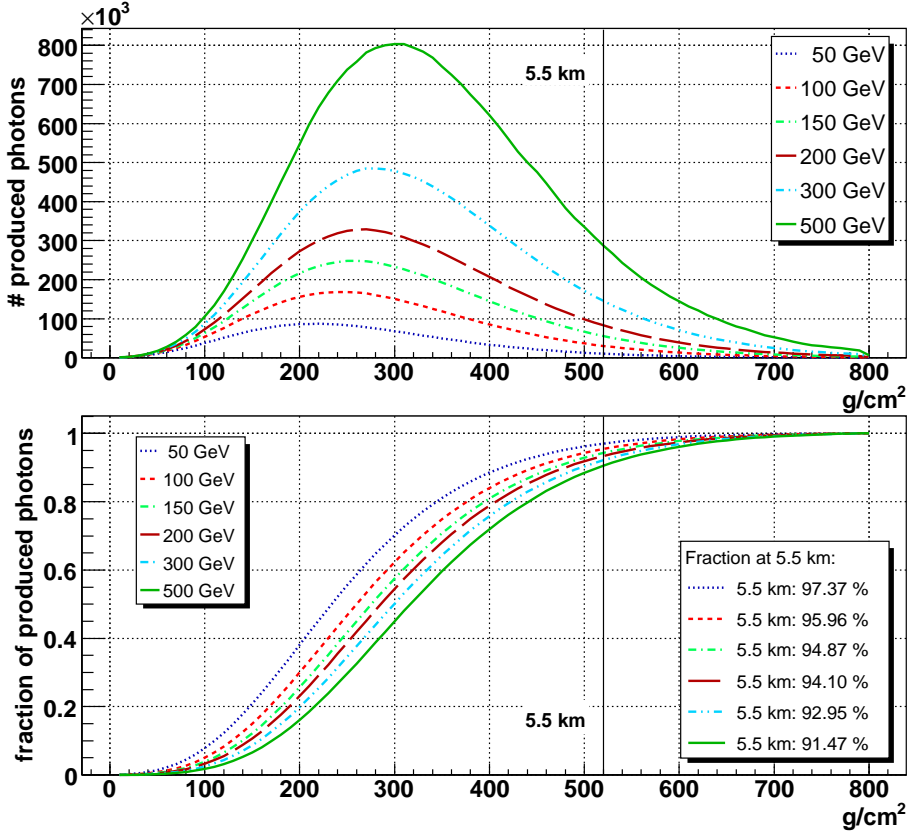


Fig. 1. In the upper plot, the number of produced photons (generated with CORSIKA (Knapp & Heck 2004)) is shown versus height (airmass in g/cm^2) for monoenergetic showers with energies between 50 GeV and 500 GeV in different colors. Below, the integral fraction of produced photons is plotted versus height for the same showers. In addition, for each graph it is listed which fraction of the altogether emitted light is already produced at 5.5 km indicating the upper border of the Saharan Air Layer.

correction, but can serve as an independent crosscheck and first order approximation.

Instead, the absorption can be directly determined from the images of the showers themselves by comparing the SIZE distributions of the affected data to those of a dust-free night. The transmission is calculated from the shift of the peak of these distributions, where p is the position of the peak either for a dust-free night ($p_{dustfree}$) or for a night affected by the SAL ($p_{affected}$):

$$\frac{I}{I_0} = \frac{p_{dustfree} - p_{affected}}{p_{dustfree}} \quad (2)$$

For each night of affected data, one value $\frac{I}{I_0}$ is determined. As the used observations have almost the same zenith angle distributions and the zenith distance is only between 18° and 35° , the dependence on the zenith angle can be neglected here.

A similar method has been studied for the Whipple telescope (Lebohec & Holder 2003) using the measured cosmic ray background for a relative calibration of the detector response.

4. Correction Method

In the analysis of MAGIC, there are several levels at which possible corrections can be applied:

1. the factor for absolute light calibration is adapted to correct for the additional absorption.
2. the SIZE of the shower is increased according to the absorption
3. the correction is included in the energy reconstruction

The last two cases do obviously not correct for changes in the shower morphology. Losses of light at the shower margin might change the shape of the image after cleaning. Consequently, common background-suppression cuts, normally applied to all data, will give worse results, as the morphology of the showers is different from the one assumed by the cuts. Inter-night changes of the atmospheric absorption complicate adapting the cuts to the changing shower shape. In contrast to this, a correction applied before cleaning, i.e. to the raw signal of all pixels, also correctly recovers the image shape and parameters accordingly.

For this approach, an additional factor is applied in the conversion from FADC counts to photo-electrons (phe). The correction is done according to the following formula:

$$\text{signal[phe]} = \text{signal[FADCcounts]} \cdot c_{cal} \cdot \frac{I_0}{I} \quad (3)$$

Applying this correction, obviously non-detected showers cannot be recovered, but they can be assumed to be well below the used cleaning levels anyhow. Furthermore, the fluctuations of the signals, e.g. from night-sky background light, increase. Comparing corrected dark time observations to data taken with strong moon light (Albert et al. 2007), it turns out that the fluctuations after correction stay well below those with extreme light conditions. Apart from that, it could be shown (Tescaro et al. 2007) that including arrival time information in the image cleaning, even data with strong fluctuations are properly handled. Hence, no further correction is necessary to account for this effect if the correction is applied to data taken under normal light conditions. Consequently, the calculated image parameters are not skewed by increased fluctuations and thus do not influence the efficiencies obtained from simulated showers.

5. Results

In July 2006, the MAGIC telescope observed the Active Galactic Nucleus PG 1553+113 simultaneously with the X-ray satellite Suzaku, the IACT array H.E.S.S. and the optical telescope KVA during a MWL campaign. Due to the SAL, the absorption for the single nights from July 15th to July 28th was varying between 5 % and 40 % according to the SIZE measurement. Therefore, the discussed correction has been applied to the MAGIC data.

5.1. Measurements of the Atmospheric Transmission

With the atmospheric transmission $\frac{I}{I_0}$ determined from the presented measurements, comparable results are achieved for the eight nights of observation of PG 1553+113 in July 2006 (figure 2). From the MAGIC, data the transmission has been determined only for the nights in which data of PG 1553+113 are available. During some nights, the atmospheric transmission was changing, seen both by the CMT and KVA. The KVA reports considerable changes even within a few minutes. Consequently, the different measurements agree less than in nights with stable extinction, as they were very likely not completely simultaneous. Unstable conditions during the observation worsen the accuracy of the correction. The remaining differences between the values of the KVA and the CMT can be explained by the fact that the intrinsic errors in magnitude for the comparison stars are larger in the case of KVA. Deviations of the SIZE may come from the limited accuracy of the method. For the muon measurements, the systematic uncertainties of the values are higher due to the strong dependence on the vertical distribution of the sand-dust in the SAL. Apart from small deviations and the differences in the nights with variable extinction, the measurements agree well.

As the CMT measurements are the most accurate, they were used for the calculation of the correction factors.

5.2. SIZE Distributions

As explained in section 2.1, the atmospheric extinction mainly influences the SIZE of the showers. Figure 3 shows the SIZE distributions in the range used for the analysis before (left) and after (right) applying the correction with the values from the CMT. For the shown distributions, special cuts have been applied to remove non-physical and muon events. Each curve corresponds to the data of one night.

Before the correction, the SIZE distributions spread between 2.8 a.u. and 7 a.u. at 200 phe. After the correction, it reduces to a spread between 4.7 a.u. and 7 a.u. apart from one outlier, corresponding to one of the nights with variable extinction (red dotted line, 22.7.2006). Apart from this and a second curve (black dotted line, 17.7.2006) with a deviation at around 300 phe, the SIZE distributions agree well after the correction for SIZE > 200 phe, i.e. in the range used in the analysis.

5.3. Signal Reconstruction

The cuts for the background suppression mentioned in section 2.1 include an intrinsic lower cut in SIZE, i.e. events with small SIZE are removed. Consequently, events having reduced SIZEs due to atmospheric absorption are cut

away, resulting in a lower significance of the signal if the same standard cuts are applied.

For PG 1553+113 a large number of events are expected at low energies due to the measured steep spectrum of the source. The expected effect of reduced significance due to the SAL is observed for the data taken in July 2006: Without correction, a signal is obtained with 3.2 σ significance, improving to 5.0 σ with correction, using identical cuts for the background suppression in both cases.

5.4. Flux Determination

Applying the correction as explained in section 4, the 8.5 hours of MAGIC data of PG 1553+113 from July 2006 were analyzed. Fitting a power law to the differential spectrum, a flux of $(1.4 \pm 0.3) \cdot 10^{-6}$ ph TeV⁻¹s⁻¹m⁻² at 200 GeV and a spectral index of -4.1 ± 0.3 were determined. A daily light curve shows a flux consistent with a constant flux within the errors. The results are shown in detail in Albert et al. (2008) and have been used for MWL studies in Reimer et al. (2008).

Correcting the flux for the effect of the SAL, the systematic uncertainty of the method of 5 % results in an additional error of $0.2 \cdot 10^{-6}$ ph TeV⁻¹s⁻¹m⁻² in the absolute flux.

6. Conclusion and Outlook

The different measurements of the atmospheric transmission from stellar photometry (KVA, CMT) and IACT data (MAGIC) agree well for nights with stable extinction. As more than 90 % of the shower light originates above the SAL, the measurements can be directly used to correct the IACT data. By applying a correction factor in the calibration, for example the data of PG 1553+113 taken during the MWL campaign in July 2006 have been successfully corrected. This shows that the loss of observation time due to atmospheric absorption can be reduced.

The correction should not be blindly applied to data suffering from atmospheric absorption of other origin. For those, the vertical distribution of the atmospheric conditions should be studied e.g. with a Lidar (light detection and ranging), i.e. a device shooting a laser beam into the atmosphere and measuring the backscattered light. The possibilities as how to exploit the information provided by a Lidar still have to be investigated.

Acknowledgements. We would like to thank the IAC for the excellent working conditions at the Observatorio del Roque de los Muchachos in La Palma. The support of the German BMBF is gratefully acknowledged. We thank Dafydd Wyn Evans for his help and the fruitful discussions about the data of the Carlsberg Meridian Telescope and Dorota Sobzynska for her help with the simulated showers.

References

- Albert, J., Aliu, E., Anderhub, H., et al. 2007, Very high energy gamma-ray observations during moonlight and twilight with the MAGIC telescope
- Albert, J., Aliu, E., Anderhub, H., et al. 2008, MAGIC Observations of PG 1553+113 during a Multi-Wavelength Campaign in July 2006 CMT. 2007, http://www.ast.cam.ac.uk/~dwe/SRF/camc_extinction.html
- Dunion, J. & Velden, C. 2004, Bull. Amer. Meteor. Soc., 85, 353
- Evans, D., Irwin, M., & Helmer, L. 2002, A&A, 395, 347
- Goebel, F., Mase, K., Meyer, M., et al. 2005, in 29th International Cosmic Ray Conference, Vol. 5, 179–182

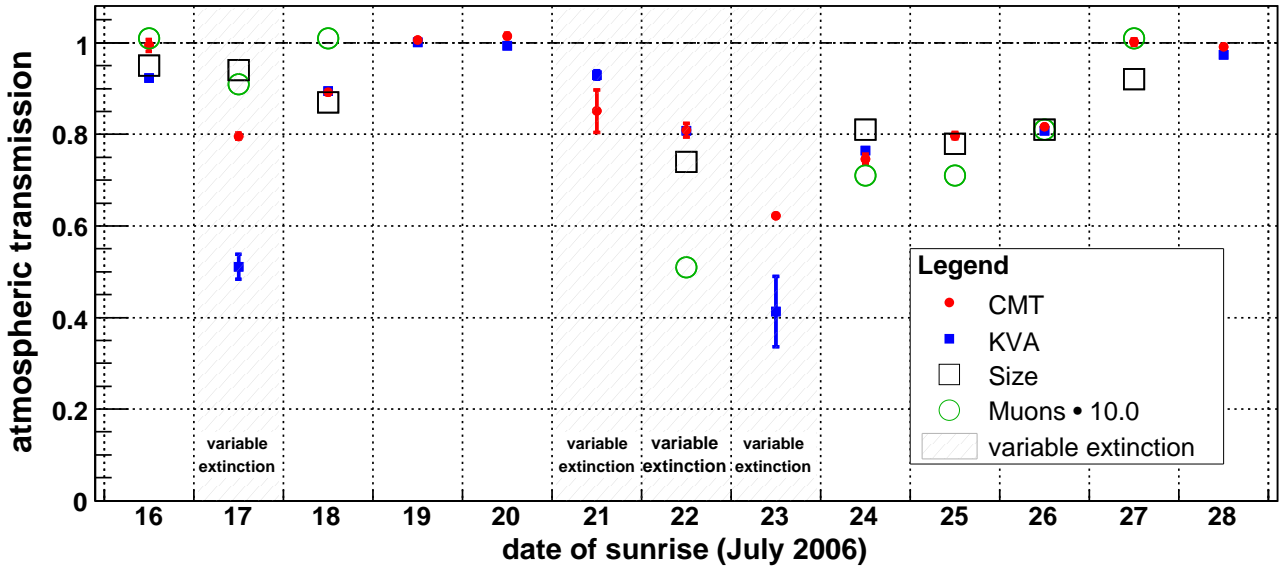


Fig. 2. Atmospheric Transmission for the nights between July 16th and 28th 2006 from the measurements of the CMT (red dots), the KVA (blue full squares) and MAGIC. From the latter, not only the SIZE measurement (black open squares) is shown, but also the values derived from muon rings (green circles) where the value is scaled by a factor ten to account for the smaller absorption for muons. Nights with unstable extinction are marked with gray shaded background.

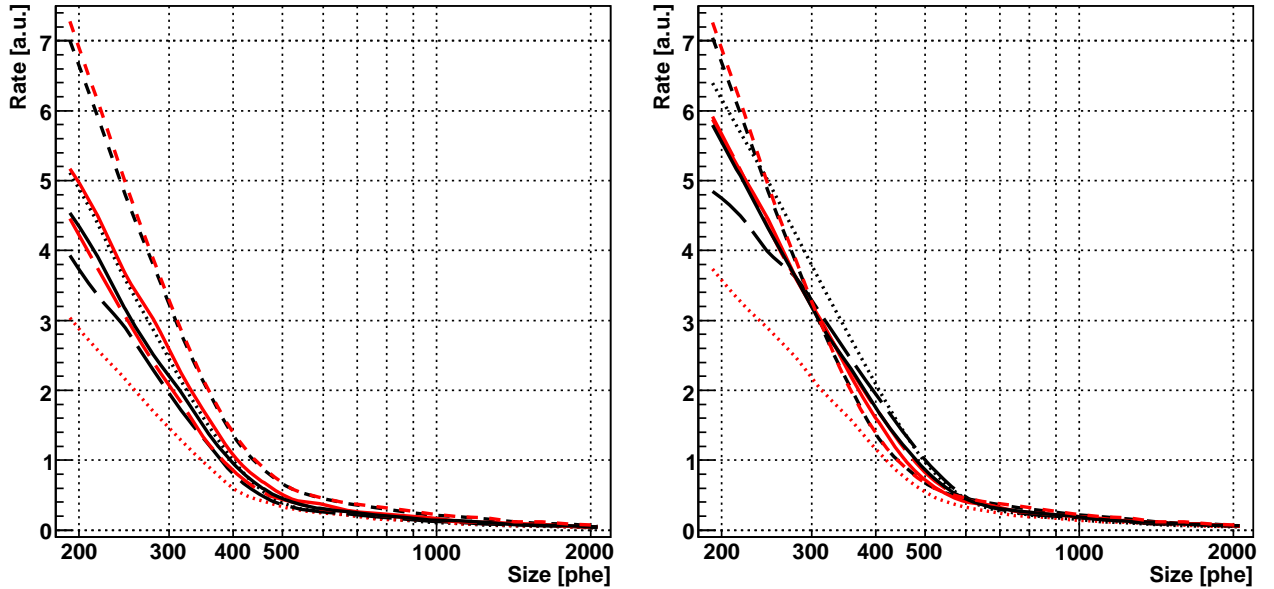


Fig. 3. SIZE distributions between 200 phe and 2000 phe (i.e. approximately from 100 GeV to 1 TeV) before (left) and after (right) correcting for the effect of SAL. Each line corresponds to one night and is scaled by the observation time. The color and style of each line is different to distinguish the nights from each other.

- Hillas, A. M. 1985, in 19th International Cosmic Ray Conference, 445-448
- Knapp, J. & Heck, D. 2004, EAS Simulation with CORSIKA: A Users Manual (Version 6.023)
- Lebohec, S. & Holder, J. 2003, Astroparticle Physics, 19, 221
- Reimer, A., Costamante, L., Reimer, O., Madejski, G., & Dorner, D. 2008, The hard X-ray view to the distant VHE blazars 1ES 1101-232 and 1ES 1553+113
- Riegel, B. & Bretz, T. 2005, in 29th International Cosmic Ray Conference, Vol. 5, 215-218
- Tescaro, D., Bartko, H., Galante, N., et al. 2007, in 30th International Cosmic Ray Conference